Winds of Opportunity

Intertidal Flat Hydrodyanmics & Morphodynamics

Colosimo, I.

DOI
10.4233/uuid:706d31e7-3a50-49bb-bb08-328a67cbb938

Publication date
2024

Document Version
Final published version

Citation (APA)
Colosimo, I. (2024). *Winds of Opportunity: Intertidal Flat Hydrodyanmics & Morphodynamics*. [Dissertation (TU Delft), Delft University of Technology]. https://doi.org/10.4233/uuid:706d31e7-3a50-49bb-bb08-328a67cbb938

WINDS OF OPPORTUNITY

INTERTIDAL FLAT HYDRODYNAMICS & MORPHODYNAMICS

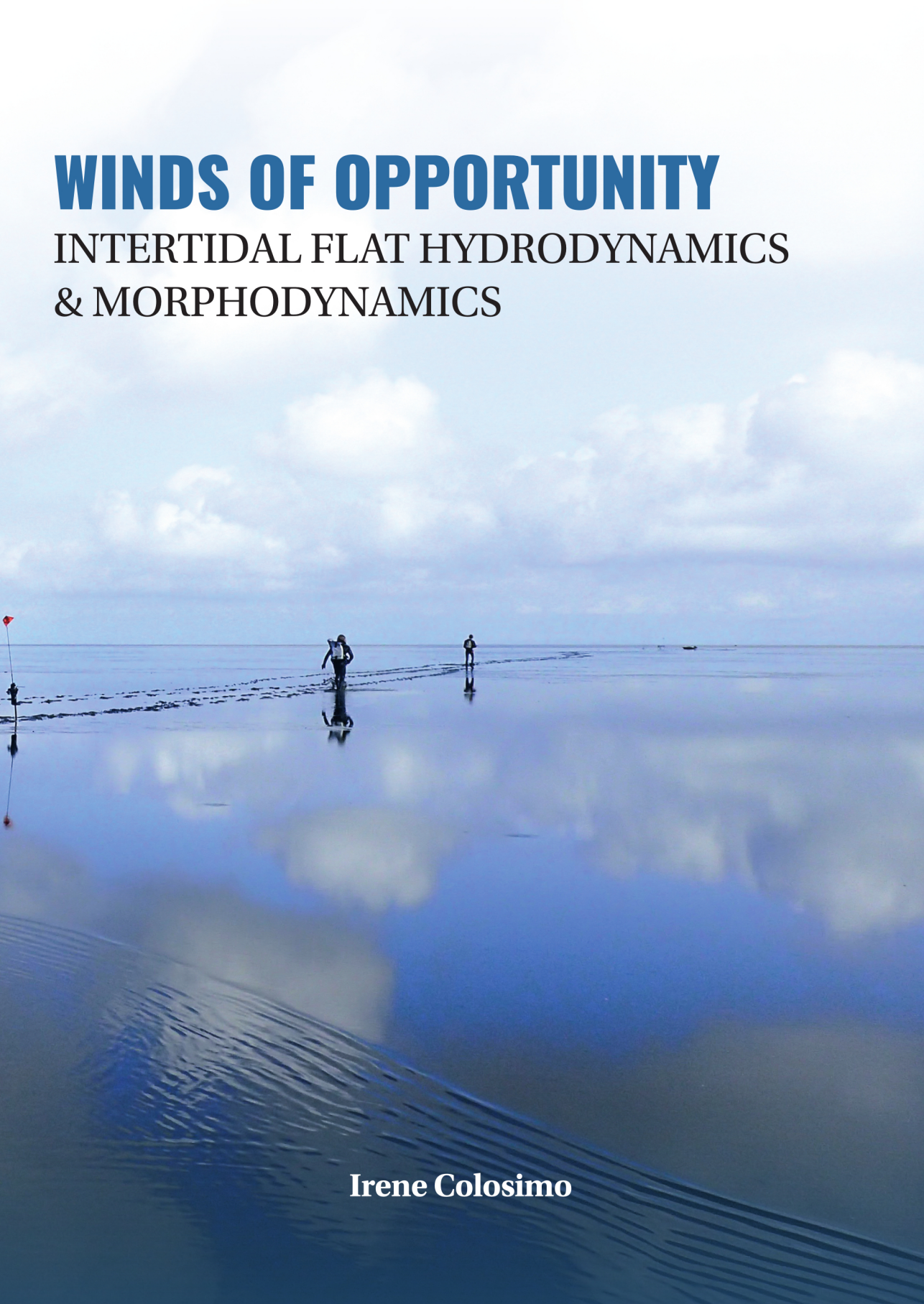

Irene Colosimo

WINDS OF OPPORTUNITY

INTERTIDAL FLAT HYDRODYNAMICS & MORPHODYNAMICS

Irene COLOSIMO

WINDS OF OPPORTUNITY

INTERTIDAL FLAT HYDRODYNAMICS & MORPHODYNAMICS

Proefschrift

ter verkrijging van de graad van doctor
aan de Technische Universiteit Delft,
op gezag van de Rector Magnificus Prof. dr. ir. T.H.J.J. van der Hagen,
voorzitter van het College voor Promoties,
in het openbaar te verdedigen op maandag 16 december om 10.00 uur

door

Irene COLOSIMO

Ingenieur in milieu- en territoriale techniek,
Universiteit van *Alma Mater Studiorium Bologna*
geboren in Catanzaro, Italië.

Dit proefschrift is goedgekeurd door de promoteren.
Samenstelling promotiecommissie:

Rector Magnificus,	voorzitter
Dr. ir. B. C. van Prooijen,	Technische Universiteit Delft, promotor
Dr. D. S. van Maren,	Technische Universiteit Delft, promotor
Prof. dr. ir. A. J. H. M. Reniers,	Technische Universiteit Delft, promotor
Onafhankelijke leden:	
Prof. dr. D. van der Wal,	Universiteit Twente
Prof. dr. ir. J. A. Roelvink,	IHE Delft/Technische Universiteit Delft
Prof. dr. ir. Z. B. Wang,	Technische Universiteit Delft
Dr. T. Gerkema,	Royal Netherlands Institute for Sea Research
Dr. C. Chassagne,	Technische Universiteit Delft, reservelid

Prof. dr. ir. J. C. Winterwerp heeft in belangrijke mate aan de totstandkoming van het proefschrift bijgedragen.

This study is part of the Research Program "*Sediment for Salt Marshes: Physical and Ecological Aspects of a Mud Motor*" with project number 13888, which is partly financed by The Netherlands Organization for Scientific Research (NWO).

Keywords:	Intertidal Flats, Sediment Transport, Wind-driven Transport, Coastal Morphology, Tidal Flat Accretion, Mud Consolidation.
Printed by:	Ridderprint
Front & Back:	The cover features a photograph of the Koehool intertidal flat (NL), taken in May 2016.

ISBN 978-94-6384-700-1

An electronic version of this dissertation is available at
`http://repository.tudelft.nl/`.

To Leonardo and Vittorio.
May you always nurture a spirit of curiosity.
May you feel free to be who you want to be,
never cease dreaming,
and approach the world with open minds
and courageous hearts.

CONTENTS

Summary **xi**

Samenvatting **xiii**

1 Introduction **5**
- 1.1 Intertidal Flats . . . 6
- 1.2 Ecosystem Services . . . 9
- 1.3 The Impact of Anthropogenic Pressure . . . 10
- 1.4 Intertidal Systems Restoration . . . 11
- 1.5 Beneficial Use of Sediment for Salt Marshes Restoration: the Mud Motor Study Case . . . 14
- 1.6 Research Set Up . . . 17
- 1.7 Structure of the Dissertation . . . 18

2 The Study Area **23**
- 2.1 The Wadden Sea . . . 24
- 2.2 Koehool and Westhoek Intertidal Flats . . . 29

3 Field Measurements **39**
- 3.1 Introduction . . . 40
- 3.2 Measurement sites . . . 40
- 3.3 Instrumentation . . . 41
- 3.4 The 2016 Field Campaign . . . 45
- 3.5 The 2017 Field Campaign . . . 47
- 3.6 The 2018 Field Campaign . . . 50
- 3.7 Data Processing . . . 52
- 3.8 Public Data . . . 60

4 Wind Effects on Intertidal Flats Hydrodynamics **65**
- 4.1 Introduction . . . 67
- 4.2 Methodology . . . 67
  - 4.2.1 General Approach . . . 67
  - 4.2.2 Bed Shear Stress Induced by Wave–Current Interaction . . . 68
- 4.3 Results . . . 69
  - 4.3.1 Full-Period Time Series . . . 69
  - 4.3.2 Wind-Induced Tidal Flow Reversal . . . 72
  - 4.3.3 Flow Reversal Observed with Current Profilers . . . 72

4.4 Analytical Model Development . . . 76
4.4.1 Determination of Leading Order Terms in the Momentum Balance Equation . . . 76
4.4.2 Tide–Wind Interaction Model . . . 78
4.4.3 Effect of Wind on Tide-Averaged Flow: Model and Data Comparison . . . 80
4.4.4 Model Validation . . . 81
4.4.5 Applicability of the Model . . . 82
4.5 Conclusions . . . 83

5 Wind Effects on Intertidal Flats Sediment Transport 87
5.1 Introduction . . . 89
5.2 Methodologies . . . 90
5.3 Results . . . 90
5.3.1 SSC at Varying Water Depths . . . 90
5.3.2 Tide Averaged SSC . . . 92
5.3.3 SSC and SSF Variations at Intra-Tidal Timescale . . . 93
5.3.4 SSF Variation at Monthly Timescale . . . 94
5.3.5 The Effect of Wind Direction on Residual Transport . . . 98
5.4 Discussion . . . 101
5.4.1 Resuspension and Advection by Currents and Waves . . . 101
5.4.2 Conceptual Model of Wind-Induced Sediment Transport and Storage in Intertidal Areas . . . 103
5.5 Conclusions . . . 104

6 Wind Effects on Intertidal Flats Morphodynamics 109
6.1 Introduction . . . 111
6.2 Methodology . . . 112
6.3 Results . . . 112
6.3.1 Bed Level Changes Over Tidal to Yearly Timescales . . . 112
6.3.2 Storm-Induced Erosion and Post-Storm Recovery . . . 114
6.3.3 Deposition Events . . . 116
6.3.4 Wind-Induced Effects on Inundation and Consolidation . . . 119
6.3.5 Impact of Aerial Exposure on Consolidation . . . 123
6.4 Discussion . . . 124
6.5 Conclusions . . . 126

7 Discussion 131
7.1 Part 1: Improved Understandings of Hydro- & Morphodynamics of Intertidal Flats . . . 132
7.1.1 Wind-Driven Flows in Intertidal Areas . . . 132
7.1.2 Sediment transport over Intertidal Areas . . . 132
7.1.3 Turbid Fringes in Intertidal Systems . . . 133
7.1.4 Short-Term and Long-Term Dynamics of Muddy Beds . . . 134
7.2 Part 2: Implications . . . 136
7.2.1 Implications of Wind on Vegetation Establishment . . . 136
7.2.2 Implications for the design of a Fine Sediment Nourishment . . . 138

8 Conclusions **143**
8.1 General Conclusions 144
8.2 Implications 146
8.3 Suggestions for Future Studies 146

References **149**

A Annex-A: Calibration Curves Optical Back Scatter Sensors **169**

B Annex-B: Wind Climate **173**

Acknowledgements **181**

List of Publications **185**

Curriculum Vitæ **187**

SUMMARY

Intertidal flats and salt marshes are ecologically important areas providing major ecosystem services. These areas undergo exploitation beyond their natural resilience, and their fast degradation requires coastal managers to undertake restoration efforts. Ideally, such restoration efforts serve multiple purposes. Beneficial use of sediments is a concept where sediment is removed from a place where it is undesired, to a place where it is needed. A potential restoration measure called the "Mud Motor" is to dispose fine sediments dredged from a port into a nearby tidal channel on a location chosen to maximally nourish the nearby intertidal area and salt marsh. Such a measure has two benefits, strengthening ecological development of the salt marshes while reducing maintenance dredging requirements. The Mud Motor Pilot Project was carried out in the Dutch Western Wadden Sea in the years 2016-2017, and involved an intense research program, including the PhD work presented in this dissertation.

The success of fine sediment nourishments requires a thorough understanding of the mechanisms controlling the sediment dynamics and the morphological evolution of intertidal flats. These mechanisms are directly influenced by the combined action of tides, waves, and wind. Unravelling these mechanisms forms the core of this thesis.

Numerous studies have been focusing on the contrasting effects of tidal currents and wind waves. Where every day tidal currents contribute to the building up of intertidal flats, wind waves (during events) tend to erode the tidal flats. Much less scientific attention has been paid to the role of wind, affecting the intertidal flats hydro–morphodynamics via three main processes. Wind is responsible for (i) the generation of wind waves; (ii) it induces water level set–up/–down (especially in closed/semi–enclosed estuarine systems); and(iii) it generates wind–driven currents. Moreover, the combination of these processes can lead to enhanced sediment transport.

In order to assess and quantify the role of wind in the hydro–morphodynamics of intertidal areas, we conducted three field campaigns in the Dutch Wadden Sea: the intertidal flats of Koehool and Westhoek (i.e. the targeted intertidal flats of the Mud Motor nourishments). Frames were installed during for an overall period of four months during the years 2016, 2017 and 2018. Water levels, suspended sediment concentrations, waves, currents and bed level changes were monitored, at four sites, via the deployment of Acoustic Doppler Velocimeters, Optical Back Scatter sensors, Acoustic Doppler Current Profilers and Wave Gauges.

We first quantified the role of wind in the hydrodynamics of intertidal flats. A clear effect of wind was found. Winds directed opposite to the main flood (ebb) current direction are able to reverse the tidal flow, such that the flow is ebb–(flood–) directed during

the full tidal cycle or even during consecutive tidal cycles. This control exerted by wind is more pronounced at the higher intertidal zone, where the contribution of the tidal flow progressively decreases. Through a newly developed analytical model, based on the Momentum Balance Equation, we determined the non-linear interaction between the wind-driven component and the tide-driven component of the flow. The field data was used to calibrate and validate the model.

Second, the sediment fluxes are addressed. Fine sediment is easily resuspended by wind-waves and mainly transported by currents as suspended load (advection). Our field observations attest the key-role of wind direction in determining the amount of sediment advected during one tidal cycle, overall controlling the fate of the residual sediment flux. Low to moderate winds (timescales of weeks to months) in the same direction as the tide-induced residual transport promote an accumulation of sediment in relatively low-energy environments of the tidal basin (e.g. the higher intertidal zone) which temporarily work as a "sediment storage". This accumulated sediment is resuspended and transported back into the basin by fairly short windy periods (timescales of hours-days) from the opposite direction. Wind-driven sediment fluxes are therefore a crucial part of short- and long-term sediment dynamics in muddy systems such as the Wadden Sea.

The third part of our research focuses on the effect of wind on the long-term morphological development of intertidal flats. A window of opportunity for long–term tidal flat accretion is identified as the temporal sequence of sediment deposition and over–consolidation. Bed level change data evidences that sediment may deposit for several tidal cycles during conditions with relatively large supply and mild hydrodynamic conditions. However, on longer timescales (weeks-months) the combined forcing of waves and currents easily erodes this relatively fresh material. We show that although sediment may deposit it does not gain sufficient strength to withstand even minor wave–induced resuspension events. Underwater (self weight) consolidation is too slow to generate sufficient strength in the bed to withstand even a mild storm event; sufficient strength is only attained through over-consolidation resulting from a low water table, evaporation and drying. These conditions are largely driven by the wind, that is able to provide the "opportunity" for tidal flats accretion (hereby the title of this dissertation: "Winds of Opportunity").

In conclusion, the dissertation illustrates the importance of wind on the hydrodynamics and sediment dynamics of tidal flats. Restoration projects that rely on natural processes therefore have to account for the effects of wind. This complicates the predictions, but it might also bring new opportunities.

SAMENVATTING

Getijdenplaten en kwelders zijn ecologisch belangrijke gebieden die cruciale ecosysteemdiensten leveren. Deze gebieden worden zwaarder belast dan hun natuurlijke veerkracht aankan, en hun snelle achteruitgang vraagt kustbeheerders om herstelmaatregelen te nemen. Idealiter dienen dergelijke herstelmaatregelen meerdere doelen. Een mogelijke maatregel is het concept van het hergebruik van sediment. Dit houdt in dat sediment wordt verplaatst van een plek waar het ongewenst is naar een plaats waar het nodig is. Een mogelijke herstelmaatregel genaamd de "Mud Motor ïs het storten van fijn sediment dat is gebaggerd uit een haven in een nabijgelegen getijdengeul, op een locatie die is gekozen om de nabije getijdengebieden en kwelders optimaal te voeden. Zo'n maatregel heeft twee voordelen: het bevordert de ecologische ontwikkeling van de kwelders en vermindert de onderhoudsvereisten voor baggeren. Het Mud Motor Pilot Project werd uitgevoerd in de Nederlandse westelijke Waddenzee in de jaren 2016-2017 en omvatte een intensief onderzoeksprogramma, inclusief het promotieonderzoek dat in dit proefschrift wordt gepresenteerd. Het succes van fijn sedimentbeheer vereist een grondig begrip van de mechanismen die de sedimentdynamiek en de morfologische evolutie van getijdenplaten beheersen. Deze mechanismen worden direct beïnvloed door de gecombineerde werking van getijden, golven en wind. Het ontrafelen van deze mechanismen vormt de kern van dit proefschrift.

Talrijke studies hebben zich gericht op de tegengestelde effecten van getijdestromingen en windgolven. Waar dagelijkse getijdestromingen bijdragen aan de opbouw van getijdenplaten, neigen windgolven (tijdens stormen) de getijdenplaten te eroderen. Er is veel minder wetenschappelijke aandacht voor de rol van wind, die de hydro-morfodynamiek van getijdenplaten op drie manieren beïnvloedt. Wind is verantwoordelijk voor (i) het genereren van windgolven; (ii) verandering van het waterpeil door opwaaiing (vooral in gesloten of half-gesloten estuariene systemen); en (iii) het genereren van windgedreven stromingen. Bovendien kan de combinatie van deze processen leiden tot vergroting van het sedimenttransport.

Om de rol van wind in de hydro-morfodynamiek van getijdengebieden te beoordelen en te kwantificeren, hebben we drie veldcampagnes uitgevoerd in de Nederlandse Waddenzee: de getijdenplaten van Koehool en Westhoek (d.w.z. de doelgebieden van de Mud Motor). Frames werden geïnstalleerd gedurende een totale periode van vier maanden in de jaren 2016, 2017 en 2018. Waterstanden, concentraties van gesuspendeerd sediment, golven, stromingen en veranderingen in het bodemniveau werden op vier locaties gemeten met behulp van akoestische Dopplervelocimeters, optische backscattersensoren, akoestische Doppler-stroomprofilers en golfmeters.

Allereerst hebben we de rol van wind in de hydrodynamica van getijdenplaten gekwanti-

ficeerd. Een duidelijk effect van wind werd waargenomen. Wind die tegengesteld is aan de dominante vloed- (eb-) stromingsrichting kan de getijdenstroom omkeren, waardoor de stroom gedurende de volledige getijdencyclus of zelfs gedurende opeenvolgende getijdencycli eb- (vloed-) gericht blijft. Deze invloed van wind is sterker in het hogere deel van het intergetijdengebied, waar de bijdrage van de getijdenstroom geleidelijk afneemt. Door middel van een nieuw ontwikkeld analytisch model, gebaseerd op de impulsvergelijking, hebben we de niet-lineaire interactie bepaald tussen de windgedreven en getijgedreven component van de stroming. De veldgegevens werden gebruikt om het model te kalibreren en te valideren.

Ten tweede worden de sedimentfluxen behandeld. Fijn sediment wordt gemakkelijk door windgolven opgewerveld en voornamelijk door stromingen als gesuspendeerde last (advectie) vervoerd. Onze veldwaarnemingen bevestigen de cruciale rol van de windrichting bij het bepalen van de hoeveelheid sediment die tijdens één getijdencyclus wordt afgevoerd, wat uiteindelijk de bestemming van de residuele sedimentflux bepaalt. Lage tot matige winden (tijdschalen van weken tot maanden) in dezelfde richting als het getijgedreven residuele transport bevorderen een accumulatie van sediment in relatief energiearme gebieden van het getijdenbekken (bijv. de hogere getijdenzone) die tijdelijk als "sedimentopslag" fungeren. Dit opgehoopte sediment wordt weer opgewerveld en terug het bekken in getransporteerd door korte periodes met hogere windsnelheden (tijdschalen van uren tot dagen) uit de tegenovergestelde richting. Windgedreven sedimentfluxen zijn dus een cruciaal onderdeel van zowel de korte- als de langetermijnsedimentdynamiek in modderige systemen zoals de Waddenzee.

Het derde deel van ons onderzoek richt zich op het effect van wind op de langetermijnmorfologische ontwikkeling van getijdenplaten. Een "window of opportunity" voor langetermijn-getijdenopbouw wordt geïdentificeerd als de temporele volgorde van sedimentafzetting en overconsolidatie. Bodemhoogteveranderingen tonen aan dat sediment gedurende meerdere getijdencycli kan worden afgezet tijdens omstandigheden met een relatief groot aanbod en rustige hydrodynamische omstandigheden. Op langere tijdschalen (weken-maanden) kan het gecombineerde effect van golven en stromingen echter dit relatief verse materiaal gemakkelijk eroderen. We tonen aan dat, hoewel sediment kan bezinken, het niet voldoende sterkte ontwikkelt om zelfs een kleine forcering door golven te weerstaan. Als er water op de platen staat, verloopt consolidatie door eigen gewicht te traag om voldoende sterkte in het sediment te creëren om zelfs een geringe storm te weerstaan. Voldoende sterkte wordt pas bereikt door overconsolidatie, veroorzaakt door een laag waterpeil, verdamping en uitdroging. Deze omstandigheden worden grotendeels door wind gedreven, die daarmee de "opportunity" biedt voor getijdenaangroei (vandaar de titel van dit proefschrift: "Winds of Opportunity").

Samenvattend illustreert het proefschrift het belang van wind voor de hydrodynamiek en sedimentdynamiek van getijdenplaten. Herstelprojecten die afhankelijk zijn van natuurlijke processen moeten daarom rekening houden met de effecten van wind. Dit maakt voorspellingen ingewikkelder, maar kan ook nieuwe kansen bieden.

About the Photo

A human footprint in soft mud, surrounded by the delicate tracks of birds. Photo taken on May 15, 2017, at the Westhoek intertidal flat.

1

INTRODUCTION

Why are intertidal flats and salt marshes important? What are the main engineering solutions used to protect and restore them? And what knowledge is necessary to enhance the success of such engineering interventions? Our scientific research, focused on the hydrodynamics and morphodynamics of intertidal flats, is presented within the broader context of intertidal system creation and restoration. This chapter also introduces the Mud Motor Project, an experimental fine sediment nourishment conducted in the Netherlands along the years 2016 and 2017. The research presented in this dissertation is framed in the context of this Project. Eventually, this chapter delves into the research questions addressed in this dissertation.

1

1.1. INTERTIDAL FLATS

Intertidal flats are mildly sloped coastal environments originating from the action of tides. The tidal forcing is generated by the gravitational force of the Moon and Sun on the Earth's water body. This leads to the alternation of high and low water levels and a consequent flooding and ebbing flow. Intertidal flats are identified as those areas with elevations between the low water level and the high water level and hence provide a transition zone between aquatic and terrestrial environments.

Intertidal flats develop especially in low-energy environments, where waves are gentle, allowing for sedimentation (*Friedrichs and Perry*, 2001). As a consequence, intertidal flats are typically found in sheltered environments, such as estuaries and coastal lagoons. They furthermore develop in areas with sufficient sediment supply. Two main types of tidal flats exist: fringing intertidal flats, which are attached to the shore, and intertidal shoals, which are surrounded by water. Fringing tidal flats are found in bays (e.g. sheltered by barrier islands, left panel in Figure 1.1), but also on open coasts (right panel in Figure 1.1). In most cases these intertidal environments are characterized by a high percentage of fine sediment (i.e. clayey-silty sediments, also referred to as mud), rich in organic matter. Examples are the broad tidal flats fringing the Yangtze Estuary or Yellow River Delta in China (e.g. *Wang et al.*, 2014; *Chen et al.*, 2016), the intertidal coast of Indonesia (the country with the greatest extent of tidal flats worldwide (e.g. *Murray et al.*, 2019; *Winterwerp et al.*, 2020) or the Guyana's and Suriname's fringing flats, influenced by the Amazon River dynamics (e.g. *Anthony et al.*, 2019).

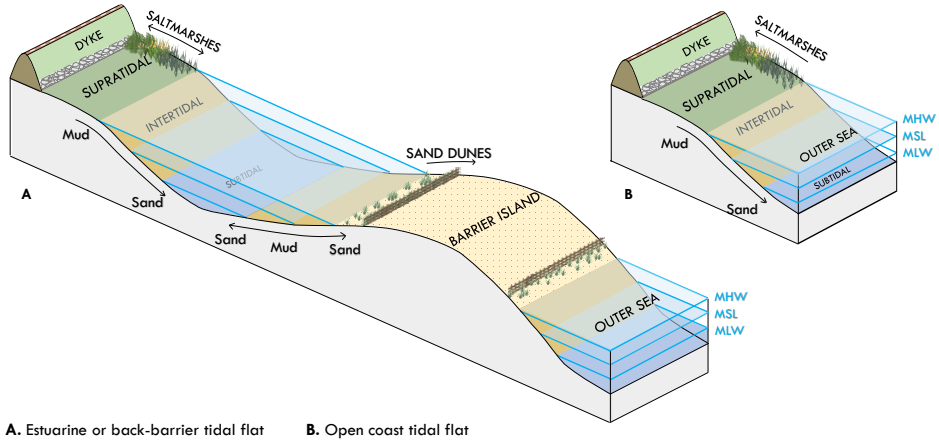

Figure 1.1: Sketch of intertidal flats found on estuarine or back-barrier systems (e.g. the Wadden Sea, The Netherlands, Germany, Denmark) and on open coast (e.g. Yangtze mouth, China). Redrawn from *Friedrichs* (2012).

Figure 1.1 illustrates, in its left panel, a sketch of the succession of subtidal, intertidal and supratidal areas across back-barrier fringing intertidal flats. Barrier islands defend the inner coast from the action of waves generated in the open sea. A well-known example of intertidal back barrier systems is the Wadden Sea. With about 40 islands, the

Dutch-German-Danish Wadden Sea is the world's largest unbroken system of intertidal flats, running along a 500 kilometer's coastline and covering about 1 million hectares (e.g. *Frazier*, 1999; *Dankers et al.*, 2012; *Elias et al.*, 2012). Additional information related to the Wadden Sea intertidal system is provided in Chapter 2. Another example is the Virginia's back barrier system (USA Atlantic coast, Figure 1.2), with 23 barrier islands stretching along a 122 km coastline (e.g. *Deaton et al.*, 2017). Intertidal shoals are especially found in estuaries and, being largely exposed to the hydrodynamic action, the morphology of these areas can be particularly dynamic. Extensive intertidal shoals are found in the Yangtze Estuary in China (*Gao et al.*, 2010; *Wei et al.*, 2017), and in numerous estuaries in New Zealand (e.g. *Hume and Herdendorf*, 1988) but also in back–barrier systems, such as the above mentioned Wadden Sea (GE, NL, DK), and Virginia's barrier islands (USA). Examples of a low-lying chain of barrier islands, intertidal shoals and tidal marshes, located along the coast of Delmarva Peninsula (Virginia, USA) are visualized in Figure 1.2.

The morphological evolution of intertidal flats is mainly influenced by the action of hydrodynamic forcings (i.e. tides, waves, wind), and by the availability of sediment. Furthermore, biological components can play a key role in sediment transport (*Le Hir et al.*, 2007, e.g.). The interaction between biotic and abiotic processes, and the positive–negative feedback related to such interactions, contribute to a long–term morphodynamic (quasi) equilibrium of intertidal flats (*Fagherazzi et al.*, 2007; *Friedrichs*, 2012; *Coco et al.*, 2013; *Zhou et al.*, 2017; *Maan*, 2019). Given the large number of processes affecting the morphological evolution of intertidal flats, simplifications have been adopted to understand how intertidal flats are shaped by the diverse hydrodynamic forcings. According to a generally accepted dichotomy, tidal currents promote accretion, whereas wind waves lead to degradation of the tidal flats. The contrasting consequences of tide-dominated conditions versus wave-dominated conditions have been studied by means of numerical modelling and arise from field observations as well. Tide-dominated conditions result in the accretion (and seaward progradation) of tidal flats. Oppositely, wave-dominated conditions, e.g. storms, lead to the erosion of the tidal flat with sediment export in the offshore direction (e.g. *Friedrichs and Aubrey*, 1996; *Janssen-Stelder*, 2000; *Le Hir et al.*, 2000; *Friedrichs*, 2012). *Van Straaten and Kuenen* (1957) emphasized the difference in time scales: on the one hand weak net sediment import by tidal currents occurs during relatively long periods of predominant calm conditions and, on the other hand, large but brief export of sediment occurs during storms, when sediments are washed off the intertidal flats. The net effect of these two mechanisms ultimately determines the long-term evolution of the flats.

Although hydrodynamics play a key role in the development of tidal flats, it has been known for decades as well that biogenic processes provide additional mechanisms shaping the flats. Tidal flats are in fact identified as 'bio–geomorphic systems', as their morphological evolution relates to the interaction between physical (abiotic) and biotic processes (e.g. *Reed et al.*, 2018). In temperate zones, upper tidal flats are typically colonized by salt marsh plant species, differing from tropical zone where mangrove forests are found along the intertidal coasts. Colonisation by salt marsh vegetation takes place whenever the mudflat reaches a sufficiently high level in relation to the tidal regime (e.g. *Boorman et al.*, 2002; *Marani et al.*, 2004; *Balke et al.*, 2016; *Boorman and Hazelden*,

Figure 1.2: Virginia's back barrier islands and shoals (USA). Top left satellite picture: Virginia back barrier islands top view (source: Google Earth, Image Landsat Copernicus). Top right picture: Conn Island, Virginia (credits to *Gordon Campbell, At Altitude Atlas*). Bottom pictures: Myrtle and Ship Shoals, Virginia (credits to *Gordon Campbell, At Altitude Atlas*), with its branching channel system and tidal marsh.

2017). The tolerance of salt marshes to sea water inundation differs between species, so that a succession of plant species exists across the flat (*Brereton*, 1971; *Davy et al.*, 2000). According to *Boorman and Hazelden* (2017) vegetation generally develops where the inundation period is lower than 50% of the time. However, several other studies deduced different elevation thresholds for salt marshes establishment from local analyses. To provide a few examples: *McKee and Patrick* (1988) indicates mean low water level as elevation of the border between tidal flat and salt marshes, at some macro-tidal estuaries along the USA Atlantic coast; *Marani et al.* (2004) reports that, at elevations of 30 cm above mean sea level, salt marshes develop within the Northern Venice Lagoon (Italy); in the Dutch Wadden Sea *Bakker et al.* (2002) suggests the 20-40 cm below mean high water level to be the local seaward limit for pioneer species development. This large variability is attributed to numerous factors, among which the tidal range (*Balke et al.*, 2016) – and its variation due to human interventions – and the positive/negative feedbacks between abiotic and biotic factors. Non-vegetated mudflats are also influenced by biological processes. Benthic species activity, such as cockles (*Cerastoderma edule*), or lugworms (*Arenicola marina*),lead to bioturbation, biostabilisation, bio-irrigation, or direct resuspension by their fouraging behaviour and locomotion (e.g. *Gibson et al.*, 2001; *Murray et al.*, 2002; *Le Hir et al.*, 2007; *Mariotti and Fagherazzi*, 2012; *Van Regteren et al.*, 2017). The abundance of these organisms can be so large that their presence and activ-

ities affect the characteristics of the substrate hosting them. On the other side, also the physical processes occurring on the tidal flat affect the biological activities (e.g. *Mariotti and Fagherazzi*, 2012; *Cozzoli et al.*, 2021; *Holzhauer et al.*, 2022): e.g. waves can disrupt the biofilm produced by benthos, that would act as a sediment stabilizer, ultimately affecting the evolution of the tidal flat.

Several studies highlighted the 'bi-stable nature' of intertidal elevations, with low-lying bare flats and elevated vegetated marshes being two alternative stable states (*Fagherazzi et al.*, 2007; *Carniello et al.*, 2009; *Wang and Temmerman*, 2013). Rapid shifts occur from the vegetated state to the bare state (e.g. *Kirwan et al.*, 2011) and vice versa (e.g. *Wang and Temmerman*, 2013). Large-scale losses of vegetated marshes have been documented in relation to decreased sediment supply, limiting the ability of marsh to cope with sea level rise (*Kirwan et al.*, 2011). Oppositely, the transition from a bare to a vegetated flat may occur due to increased sediment supply (*Yang et al.*, 2001; *Kirwan et al.*, 2011). *Wang and Temmerman* (2013) demonstrated that an elevation threshold exists, above which the vegetation patches colonize the pioneer zone, and the positive feedback between sediment and vegetation drive the rapid shift to the vegetated state.

The prediction of the morphological evolution of intertidal flats is hence complex, due to the high number of biotic and physical processes simultaneously contributing to it. A thorough system understanding is needed to support coastal managers in planning interventions that protect such valuable environments.

1.2. ECOSYSTEM SERVICES

Intertidal flats and salt marshes are ranked among the most valuable habitats regarding to the benefits provided to human life (*Temmerman et al.*, 2013). The positive contribution of these ecosystems to our health and society are numerous, and result in a wide range of services (the so-called 'ecosystem services'), from production and regulating services to cultural and supporting services (e.g. *Groot et al.*, 2018).

Salt marsh ecosystems contribute to maintaining a high water quality, especially in regions where high suspended sediment concentrations would result in euthrophication-related issues (e.g. *Sanger and Parker*, 2016). The vegetation, in particular its root system, captures sediments and pollutants, filtering them out of the water, hereby guaranteeing a natural water treatment (*Mudd et al.*, 2010; *Lin and Yu*, 2018). Moreover, benthic species, inhabiting the tidal flat bed, play a key role in the food web, both locally and on global scale (*Christianen et al.*, 2017).

Intertidal flats and salt marshes act as a natural barrier, minimizing damage from storm surges (*Barbier et al.*, 2008; *Gedan et al.*, 2011; *Suykerbuyk et al.*, 2012). The vegetation augments the rate of sedimentation by intercepting and trapping the sediment transported by the tides. With its roots system, vegetation reduces sediment erosion and enhances sediment consolidation (*Barbier et al.*, 2008; *Mudd et al.*, 2010; *Temmerman et al.*, 2013; *Li et al.*, 2014; *Möller et al.*, 2014). Both laboratory and field studies have demonstrated that wave impact is significantly attenuated in presence of a vegetated flat compared to the case of a bare flat (e.g. *Vuik et al.*, 2019; *Blackmar et al.*, 2014; *Kobayashi*, 1993). For this reason, salt marshes in temperate areas - as much as mangroves in tropical areas - are considered as natural flood defenses, and appointed as 'bio-engineers'. The accelerated rise in mean sea level, and the more extreme meteo-

rological events posed by climate change, amplify the importance of these natural flood defenses in protecting coastal cities and communities (*Temmerman et al.*, 2013).

Intertidal flats and salt marshes also contribute to the carbon sequestration. The reduction of carbon dioxide captured by marsh species is considered 30-50 times more efficient than the one for forest plants (e.g. *Pendleton et al.*, 2012; *Ouyang and Lee*, 2013; *Malak et al.*, 2021).

The societal and economical values of these ecosystems also relate to the widely applied production services. Intertidal areas are largely used for commercial fisheries and shell-fisheries (e.g. *Barbier et al.*, 2011), providing an important source of food and income (e.g. *Adam*, 2002; *Taylor et al.*, 2018; *Wang et al.*, 2022). Reclamation of the vegetated intertidal areas to accommodate the continuously increasing demand for habitable and agriculture or aquaculture land resulted in massive coastal erosion end ecosystem degradation (*Groot et al.*, 2018). An example is the case of Demak, Indonesia, were massive coastal erosion (about 100 m/yr) followed the disruption of mangrove forests (*Winterwerp et al.*, 2020). These mangrove forests were removed for aquaculture and agriculture, wood production, and urban infrastructure (*Winterwerp et al.*, 2005; *Marfai*, 2011; *Van Wesenbeeck et al.*, 2015; *Winterwerp et al.*, 2020).

1.3. THE IMPACT OF ANTHROPOGENIC PRESSURE

In the current era of climate change and anthropogenic pressure, coastal ecosystems are among the most vulnerable areas of our planet (*Day and Rybczyk*, 2019). The human pressure on coastal areas resulted in an increasing demand for a fixed coastline, and, through the process of land reclamation, the coastal defence structures (dikes and other embankments) have been gradually moved seaward. Under natural conditions, in response to sea level rise, intertidal flats and salt marshes would migrate land inwards (e.g. *Rezaie et al.*, 2020). The artificial land boundaries though, hamper such natural migration, and intertidal habitats are lost due to the so called 'coastal squeeze' (*Yang et al.*, 2011; *Pontee*, 2013). Human activities resulting in land subsidence, such as sub-surface water withdrawals and drainage (*M. Parry et al.*, 2007), and in the reduction of sediment supply to river deltas (*Yang et al.*, 2003; *Besset et al.*, 2019) can locally increase the relative rise in sea level. The health and functioning of coastal ecosystems are further challenged by those engineering interventions required to maintain navigation channels and ports operational, i.e. dredging activities (*PIANC*, 2011).

Land reclamation is the human activity that majorly reduced the intertidal area over the last century worldwide (*Kirwan et al.*, 2016). Extensive salt marshes and mangrove forests have been claimed and converted into agricultural lands, aquaculture ponds and fisheries (*Valiela*, 2006; *Li et al.*, 2018; *Friess et al.*, 2019). Over the past 30 years, the Yellow Sea (China) and the Yangtze Estuary (China) lost, respectively, 28% (*Murray et al.*, 2014), and 36% of their surrounding tidal flats (*Chen et al.*, 2016). Europe, in the last 300 years, was the area with the highest rate of wetland degradation, with Ireland losing more than 90% of its wetlands, Germany, Lithuania and Hungary more than 80% and the UK, the Netherlands and Italy more than 75% (*Fluet-Chouinard et al.*, 2023). However, during the 20th century and early 21th century, the degradation of wetlands in Europe has slowed down, with a rate loss of approximately 1% of the total area per year (*Davidson*, 2014). In the Netherlands, land reclamation is the main reason for tidal flats loss (*Mai*

and Bartholomä, 2000). The story of the country closely relates to the land reclamation process, starting already back in the 16^{th} century (*De Mulder et al.*, 1994; *M. Parry et al.*, 2007). The Dutch polders have been the largest and most effective land reclamation works in the world (*Hoeksema*, 2007), and the polderization process acted pivotal for the existence of the country: about 17% of the current land is formed by land reclaimed from either sea or lakes (*Damen*, 2004).

In absence of coastal protection works a rising mean sea level leads to longer and more frequent flooding (*Reed*, 1990; *Friedrichs and Perry*, 2001). Whether intertidal systems are able to keep pace with the increasing inundation regime depends on several factors, primarily the sediment availability in the system (e.g. *Friedrichs and Perry*, 2001). Recent modelling-based studies demonstrate that, if sediment is available, intertidal flats and salt marshes will likely be able to keep pace with the increase in mean sea level (e.g. *Kirwan et al.*, 2016). However, other studies predict major losses due to the *accelerated* sea level rise. According to *Crosby et al.* (2016), 60% of the salt marshes will gain elevation at a rate insufficient to keep pace with the sea-level rise predicted by 2100. Similarly, *Huismans et al.* (2022) predicts up to 10% loss of intertidal flats in the Dutch Wadden Sea tidal basins in the coming 40 years, considering the scenario of sea level rise accelerating from the current rate of 2 mm/yr up to 6 mm/yr in 2060.

The loss of intertidal areas directly impacts the biodiversity, compromising the natural food-web functioning. In the Yellow Sea a 30% of mudflat loss corresponds to a 5% of bird population decrease per year (*Studds et al.*, 2017). At twelve of the most productive estuaries worldwide, human impacts caused loss of 65% of seagrass and wetland habitat (*Lotze et al.*, 2006). On the long term, models predict that this ecosystem loss will have consequences for human health as well (*Crosby et al.*, 2016).

Overall, the impact of human activities (including those enhancing climate change) on intertidal systems far outweighs the pressure induced by natural variations (*Valiela*, 2006). As a result, numerous intertidal systems worldwide undergo exploitation beyond their natural resilience (*Frazier*, 1999).

1.4. INTERTIDAL SYSTEMS RESTORATION

To counteract the loss of wetlands, restoration measures are being proposed. We focus, in the following, on measures adopted for salt marsh restoration, but most of the concepts have been applied for mangrove forest restoration as well. Restoration initiatives involve the creation of new marshes, the re-creation of marshes on areas which had previously been claimed from the sea, and the restoration of degraded existing salt marshes or intertidal flats. To create or restore marshes where a coastal dyke exists, managed realignment methods (in the past named also as 'managed retreat', 'setback' or 'depolderization') are adopted. In managed realignment schemes, the sea defence line is moved landward and sediment is released nearby in concert (or not) with the constructions of permeable dams or embankments favouring sedimentation, so that a buffer of intertidal habitat establishes (*Boorman and Hazelden*, 2017). Managed realignment schemes allow both a creation/restoration of coastal habitats and a renewing of sea defenses as well. The formation of the new vegetated buffer between the sea and the dyke reduces the flood risk (e.g. *Möller et al.*, 2014; *Boorman and Hazelden*, 2017; *Vuik et al.*, 2019). With this approach, coastal dykes can be reduced in size, with a significant drop in con-

struction costs (*Wolanski and Elliott*, 2015).

A noted successful managed realignment experiment in Europe was carried out in Tollesbury (Essex, England), where in 1997 new sea defences (low embankments) were constructed behind the existing sea wall around an area of circa 21 ha. Following the completion of the new sea defences, the existing sea wall was breached and the enclosed area was exposed to tidal inundation for the first time after about 150 years. After 10 years the restored salt marshes covered 62% of the former bare flat, and after another 9 years (2016), the vegetation cover increased further by 18%, reaching a total 80% marsh restoration (*Reading et al.*, 2008; *Boorman and Hazelden*, 2017). Restoration initiatives can further include the spreading of salt marsh seeds and/or the plantation of vegetation plugs, to fasten the recovery (*Winterwerp et al.*, 2005). As an example, we show in Figure 1.3 the case of Prime Hook marsh restoration project (Delaware Bay, USA), which involved the usage of dredged sand over a surface of about 4000 ha. As evident from the figure, this combination of beach nourishments, fences' construction and plugs' plantation, resulted in a relatively fast and successful habitat recovery.

Figure 1.3: Wetland restoration project in Prime Hook (Delaware, USA). Three pictures are taken from the same spot onto a sandy tidal flat (credit to *U.S. Fish and Wildlife Service*, https://e360.yale.edu/features/the-science-and-art-of-restoring-a-damaged-wetland)

.

The great majority of the salt marshes in the Wadden Sea (about 350 km^2) were created artificially by means of the so called 'Schleswig-Holstein method', largely applied already back at the end of the 19^{th} century (*Hofstede*, 2003). With this method, interconnected sedimentation basins (each measuring from 100x100 m^2 up to 400×400 m^2) were realized in front of the higher intertidal flats via the construction of permeable dams (e.g. *Dijkema et al.*, 1988; *Bakker et al.*, 2002; *Adam*, 2019; *Winterwerp et al.*, 2020), see Figure 1.4. The permeable dams (consisting of brushwood groins) allow sediment-rich water to enter the basin. Wave energy is however reduced, leading to settling of the sediment, and sediment poor water leaves the basin during ebb. This leads ultitmately to accumulation of sediment and hence vegetation expansion. The contextual creation of draining channels optimized the functioning of the method (*Winterwerp et al.*, 2020).

As above mentioned, the focus here is on salt marshes system, but it is important to highlight that permeable dams have also been adopted in mangrove restoration projects in Guyana, Indonesia, Suriname, Thailand and Vietnam (e.g. *Schoonees et al.*, 2019; *Winterwerp et al.*, 2005, 2013, 2020; *Mancheño et al.*, 2021).

Despite the progress in the success of restoration methods (both for salt marshes and mangroves ecosystems), there are still several critical aspects that hamper the recreation/restoration of fully healthy and functioning ecosystems. It takes a long time (usu-

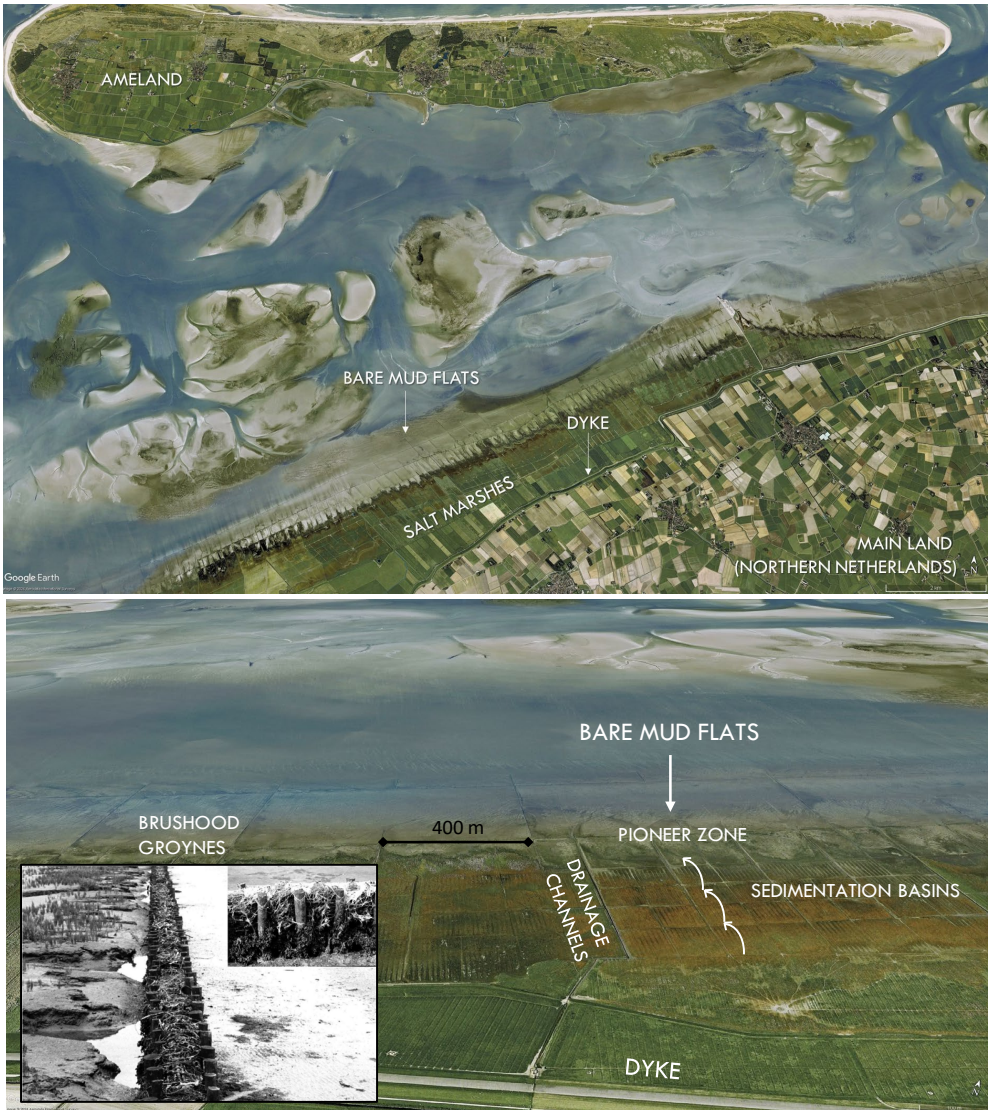

Figure 1.4: Salt marshes created through the development of sedimentation basins, realized with brushwood groins (Zwarte Haan, Northern Netherlands). The background figure is captured from Google Earth while the sketches are re-drawn from *Winterwerp et al.* (2020); the brushwood groyne picture is from *Hofstede* (2003).

ally more than 15 years according to *Burden et al.* (2013)) for artificial marshes to reach biological characteristics that are comparable to those of a natural marsh. A fully functional anthropogeneic alternative for a salt marsh is difficult to develop (*Streever*, 2000; *Mossman et al.*, 2012). The robustness and hence the resilience of an artificially created marsh is often not sufficient to dissipate the wave-induced energy of a major storm (*Fagherazzi et al.*, 2013). Moreover, the sediment used to feed the intertidal areas re-

quires similar characteristics as the local existing sediment, not only in terms of grain size but also in its bulk density, pH, nutrients level and organic matter content, the latter affecting the cohesiveness of the bed material, a key factor to achieve plant colonisation (*Hazelden and Boorman*, 2001; *Barkowski et al.*, 2009; *Kadiri et al.*, 2011).

While coastal ecosystems are being progressively more restored, lack of funding and/or time frequently leads to restoration efforts, insufficiently building on a solid scientific basis. The restoration of an ecosystem obeys the timescale of the natural system, so that a long–term vision is key in this perspective (*Winterwerp et al.*, 2020). A robust system understanding in terms of sediment dynamics, tidal regime, wave climate and biological features, is key to successfully apply restoration methods, such that gathering site specific data and information, before defining a certain restoration strategy, is compelling.

1.5. BENEFICIAL USE OF SEDIMENT FOR SALT MARSHES RESTORATION: THE MUD MOTOR STUDY CASE

For coastal systems where sediment availability is a limiting factor, restoration techniques involve the nourishment of sediments. Dredging operations, needed to maintain harbour and navigational channels operational, are an interesting potential source of sediment for such interventions.

Back in the 1973, the *United States Army Corps of Engineers (USACE)* initiated a number of pilot projects (part of the broader *Dredged Material Research Program (DMRP)*) aimed at experimenting the usage of dredged sediment to enhance wildlife habitats in salt marshes environments (e.g. *Landin et al.*, 1989; *LaSalle et al.*, 1991). Several following experiments provided recommendation to optimize and expand the usage of dredged material for beneficial purposes (*Yozzo et al.*, 2004). Dredged material has since then not only been used to promote marsh habitat restoration, but also to e.g. restore oyster reefs, create spits and bars, re-contour the coastline or remediate upland habitats (*Solanki et al.*, 2023). The beneficial use of dredged material lead to multiple positive outcomes (*Suedel et al.*, 2022). An economic benefit arises from the reduction of dredging operations and a reduced flooding risk, an environmental benefit results from habitat creation/restoration, while a social benefit eventually comes by providing recreational opportunities (*Laboyrie et al.*, 2018).

Nowadays, the increasing size of commercial vessels is demanding increasing depths of channels and harbours (*De Vriend et al.*, 2011; *Wang and van der Spek*, 2015; *Chen et al.*, 2016) so that even the amount of available dredged material continuously increases. The disposal location of dredged material is generally selected based on two contradicting criteria: far enough to avoid direct return of the sediment, and close enough to reduce transportation costs.

Since 2007, an innovative design approach in coastal hydraulic engineering named *"Building with Nature" (BwN)* started being promoted in the Netherlands by the 'Echoshape' consortium (*Baptist et al.*, 2019). According to its definition, the BwN approach 'harnesses the forces of nature to benefit environment, economy and society'. The natural forces (tides, wind, waves) are hence part of the hydraulic engineering solution, and contribute to the achievements of the diverse goals.

Since the start, various projects have shown the potential of this approach (e.g. *Laboyrie*

et al., 2018). One show case project is the 'Sand Engine' (or 'Sand Motor') i.e. a mega sand nourishment (about 20 millions m^3) realized in 2011 nearby Den Haag, aiming on one side at optimizing nourishment operations and on the other side at creating recreational areas (e.g. *Stive et al.*, 2013; *Herman et al.*, 2021). This Pilot Project further provided opportunity for a better understanding of sediment transport processes, encouraging similar initiatives worldwide.

In line with this approach the 'Mud Motor' Pilot Project was initiated at the North Holland coast. Within the Mud Motor initiative, fine sediment dredged from a harbour basin was disposed in a channel to feed nearby low-lying tidal flats. The increased sediment availability introduced in the channel was expected to accelerate accretion of the targeted mudflats, hereby promoting the salt marshes development. The "win-win" solution foresees the reduction of dredging volumes in the harbour basins (and so a related reduction in dredging costs) and the concurrent creation of salt marshes (enhancing the related ecosystem services). The concept is visualized in Figure 1.5.

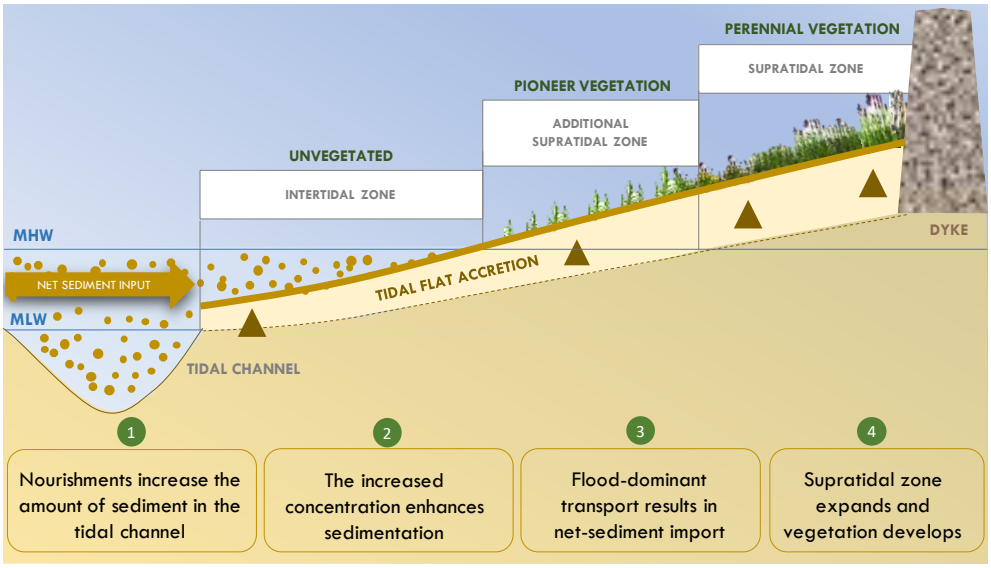

Figure 1.5: 2D conceptual scheme of Mud Motor functioning. Fine sediments are released in the channel and the tide-dominant regime result in net sediment import onto the intertidal flat. The increased mud concentration enhances the sedimentation, such that the bed level vertically increases. The consequent tidal flat progradation is followed by the lateral vegetation expansion.

Where traditional approaches release sediment directly on the salt marsh itself, (e.g. *Scott et al.*, 2017), within the Mud Motor nourishment the sediment is released directly from the hopper's bottom doors into the channel (*Baptist et al.*, 2019). The underlying assumption of the Mud Motor is that an increase in sediment availability in the channel would lead to additional sediment transport towards the tidal flats. A potential other approach would have been to rainbow the sediment on the tidal flats, however such method is more costly and may potentially damage existing habitats (*Scott et al.*, 2017). Overall, compared to the traditional salt marshes restoration methods (mostly applied

in the United States (*Welp et al.*, 2003) and the United Kingdom (*Scott et al.*, 2017)), less sediment reaches the target area, but the sediment that does reach the target area creates more robust and healthy marshes.

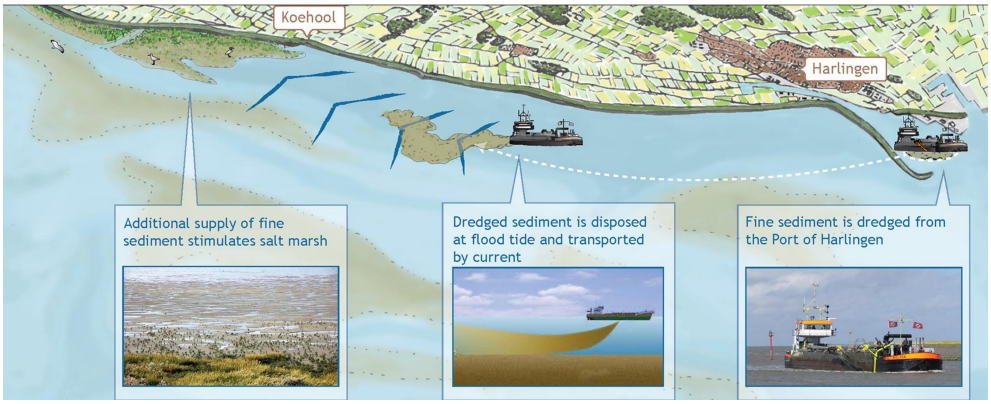

Figure 1.6: Graphical visualization of the Mud Motor applied in Harlingen. The dredging barge releases the sediment dredged from the Port of Harlingen at the new disposal site. The tidal flow transports the sediment towards the tidal flats of Koehool and Westhoek. The salt marshes are expected to expand due to the increased amount of mud feeding the intertidal flats. (Source: *Baptist et al.*, 2019)

The Mud Motor Pilot Project was initiated in the Dutch Wadden Sea in 2016. Dredged sediment from the harbour basins of the Port of Harlingen was disposed in the Kimstergat Channel for the restoration of the tidal flats fringing the coast of Koehool and Westhoek (Figure 1.6). In the Port of Harlingen, on average 1.3 million m^3 of fine sediment ($D_{50} \sim 10\mu$) is annually dredged (*Baptist et al.*, 2019). This sediment is usually disposed at two sites, located in the two tidal channels (named K1 and K2 in Figure 1.7): the *Kimstergat Channel* (K1) and the *Pollendam Channel* (K2). The latter connects the Port of Harlingen with the island of Terschelling, whereas the Kimstergat forms a connection between the Port of Harlingen and the eastern part of the Wadden Sea.

A considerable (but unknown) amount of the material disposed at K1 and K2 flows quickly back to the harbour basins (*Baptist et al.*, 2019). Dredging activities are therefore needed at daily or weekly timescales. Within the Mud Motor Pilot Project, new disposal locations were selected, and a volume of about 300.000 $m^3/year$ has been disposed at these sites. The experiment was carried out in the period September-January of 2016 and 2017. Specific information on the nourished volumes and timing are reported by *Baptist et al.* (2019).

The strategic disposal site, located in the Kimstergat tidal channel, has been selected via a numerical study reported by *Van Weerdenburg R.* (2019). The disposal location was selected on various criteria: a residual tidal flow directed towards the tidal flats; a relatively small cross-shore distance to the upper intertidal zone (i.e. the target area) and a sufficient water depth for operating the hopper (minimum depth of 3 m).

The Pilot Project was accompanied by an extensive research program, aiming at understanding the physical and biological processes within the channel–mudflat–salt marshes system. Transport processes within the tidal channel were elaborated by *Schulz and*

Gerkema (2018) and those related to the salt marshes were investigated by *van Regteren* (2020), while the transport processes over the intertidal flat areas are analyzed in this dissertation.

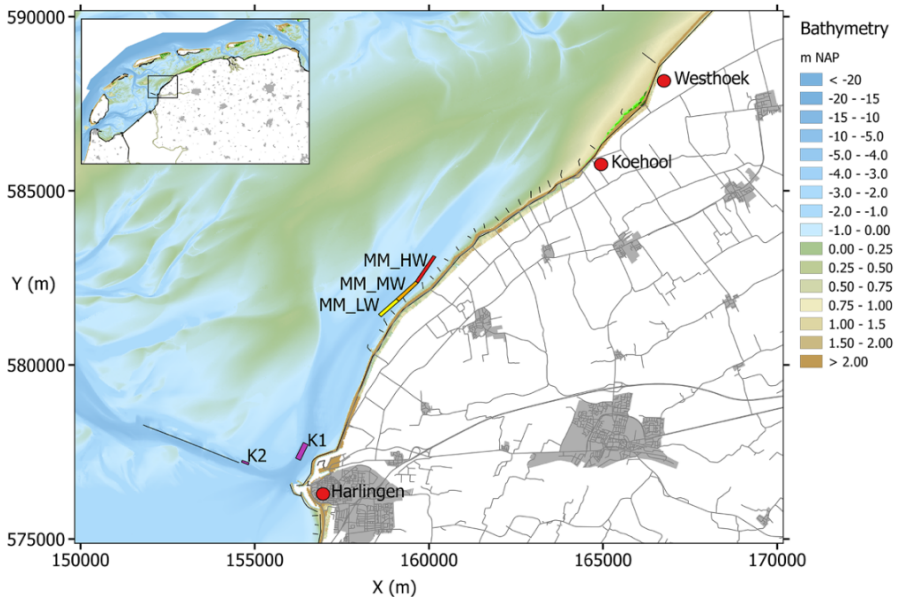

Figure 1.7: Disposal locations prior to Mud Motor application: K1, K2, respectively found in the Kimstergat and the Pollendam tidal channels. The Mud Motor disposal locations depends on the local water depth: at low water (LW), mid water (MW) and high water (HW) (Source: *Baptist et al.*, 2019).

1.6. RESEARCH SET UP

In the sections above, we described the importance of salt marshes to provide ecosystem services, as well as the pressure they face. Effective restoration projects are therefore needed, based on a solid system understanding. Despite the progress over the last decades, there is still a knowledge gap in how sediment is transported over tidal flats, and especially under the influence of waves.

The main scope of this dissertation is therefore to improve the understanding of the mechanisms controlling the transport of fine (muddy) sediments over intertidal flats and the consequent accretion–erosion processes. We focus on the role of the wind-driven processes influencing sediment transport and bed level variability. The focus on wind does not exclude accounting for the effect of tides (tidal flow and water level fluctuations). We structured our analyses along three main research questions:

Research Questions

Research Question 1:

What is the role of wind on residual and tidal flows over intertidal flats?

Research Question 2:

How do tides and winds influence sediment transport over intertidal flats?

Research Question 3:

How are phases of accretion and erosion of intertidal flats influenced by wind?

1.7. STRUCTURE OF THE DISSERTATION

The present **Chapter 1** introduces the context of intertidal systems, highlighting the need for restoration initiatives for habitat preservation and recreation. Moreover, this chapter aims at framing our scientific research into the broader context of the 'Mud Motor' Pilot Project, executed in the Netherlands in the years 2016-2017. Within the present dissertation, chapters related to the scientific theoretical understanding are integrated with reflections on the application of these findings to the Mud Motor study case, and in general to the functioning of fine sediment nourishments.

Chapter 2 describes the Wadden Sea study area, from a large (tidal basin) scale, to the small (intertidal flats) scale and concludes with the description of the two transects where intensive field work was carried out.

Chapter 3 presents the applied research methodology. This includes the field campaigns design, the installed instrumentation, the calibration methods and the data post-processing procedures.

Chapter 4 focuses on the hydrodynamic conditions on intertidal systems, exploring the effect of the intermittent action of wind on the wind-driven flows and tidal flows.

Chapter 5 investigates how the hydrodynamic conditions affect sediment transport, and formulates a conceptual model for wind-induced sediment transport and storage in intertidal systems.

Chapter 6 focuses on the morphological evolution of intertidal flats. More specifically, it dives into the effect of wind on the local conditions required for an intertidal flat to accrete, highlighting the importance of sequences of energetic and calm conditions.

The scientific outcomes are placed in perspective of the available knowledge on in-

tertidal systems in **Chapter 7** where the implications for the beneficial (re-)use of fine sediments in intertidal systems are further discussed.

Chapter 8 presents the conclusions of this dissertation and includes recommendations for future studies.

About the Photo

Pioneer vegetation at the intertidal flat of Westhoek (NL). The picture was taken on September 15, 2017.

2

THE STUDY AREA

The findings presented in this dissertation are the outcome of intensive fieldwork carried out in the Dutch Wadden Sea, and more precisely the intertidal areas of Koehool and Westhoek (Province of Friesland). This is the area where the Mud Motor Pilot Project was carried out. In this chapter, the Wadden Sea and the tidal flats are described from a hydrodynamic and morphodynamic perspective.

2.1. THE WADDEN SEA

GENERAL INTRODUCTION

The Wadden Sea is a lagoonal system situated along the north-west coast of Europe, running from The Netherlands, passing through Germany, and reaching Denmark (Figure 2.1). The lagoon spans along 500 km coastline, and covers a surface of about 11.000 km^2, half of which consist of intertidal areas (*De Jonge et al.*, 1993). The German Wadden Sea is the largest section, consisting of about 50% of the total area (*Dankers et al.*, 2012). A barrier of about 40 islands separates the Wadden Sea from the North Sea. The distance between the mainland and the barrier islands spans between 2 and 30 km. Inlets separating individual barrier islands, connect the North Sea and the Wadden Sea.

HISTORICAL DEVELOPMENT

The Wadden Sea has always been a very dynamic tidal system in which the morphology of the landscape continuously changed. Driving factors of the morphological changes have been sea-level rise (e.g. *Huismans et al.*, 2022), intense storm events (e.g. *Fruergaard et al.*, 2013), development of accommodation space for sedimentation (e.g. *Bauer et al.*, 2001), natural sediment transport processes (e.g. *Wang et al.*, 2012) and human interference in the landscape (e.g. *Oost et al.*, 2017). Human interventions in the Wadden Sea started many centuries ago, with land reclamation starting around 900-1000 AD (*Oost*, 1995; *Van der Spek*, 1995). The first small dykes along the coasts, aiming at protecting lands from flooding, were built around 1500 AD (e.g. *Bazelmans et al.*, 2012). About one century later, 1600 AD, wooden groins were built to complement the role of dykes, boosting sedimentation and promoting coastal vegetation development along the mainland and the outer barrier islands (*Van der Spek*, 1995). At that time the Wadden Sea was very different compared to the present-day Wadden Sea. Figure 2.2 shows a map drawn in 1641 AD visualizing the previously existing Zuiderzee (separating the North-Holland and the Friesland provinces) and the Lauwerzee (separating the Friesland and the Groningen provinces). The bottom panel of the figure illustrates the differently shaped estuary of the Ems river (including several islands in the Dollard basin) as well as the extended German Jade Bight (shaped by storm floods, according to *Graber* (2010), during the 13^{th} and 16^{th} centuries). Several measures were also taken, over time, to limit the erosion of the barrier islands, e.g. by reinforcing existing dunes, nourishing the coast with sand or building seawall, jetties and groins (*Elias et al.*, 2012). Moreover, the Dutch Government prescribed (with the 1^{st} Coastal Policy Document issued by the Ministry of Transport, Public Works and Water Management, titled "*Coastal Defence after 1990, a Policy Choice for Coastal Protection*") that the Dutch coastline – including the barrier islands coastline – should not retreat landward of a reference line that is based on its 1990 position (*Van Koningsveld and Mulder*, 2004).

CLOSURE OF THE ZUIDERZEE

Intense storms provided pivotal moments for decisions regarding the coastal management in the Netherlands. The storm surge that occurred in 1916 was such a pivotal moment. Various dikes along the Zuiderzee breached, with catastrophic consequences, like a total of 51 deaths (e.g. *Bouwer and Vellinga*, 2007). There were already plans for a large dam to close the Zuiderzee to create new land for agriculture. The storm accelerated the

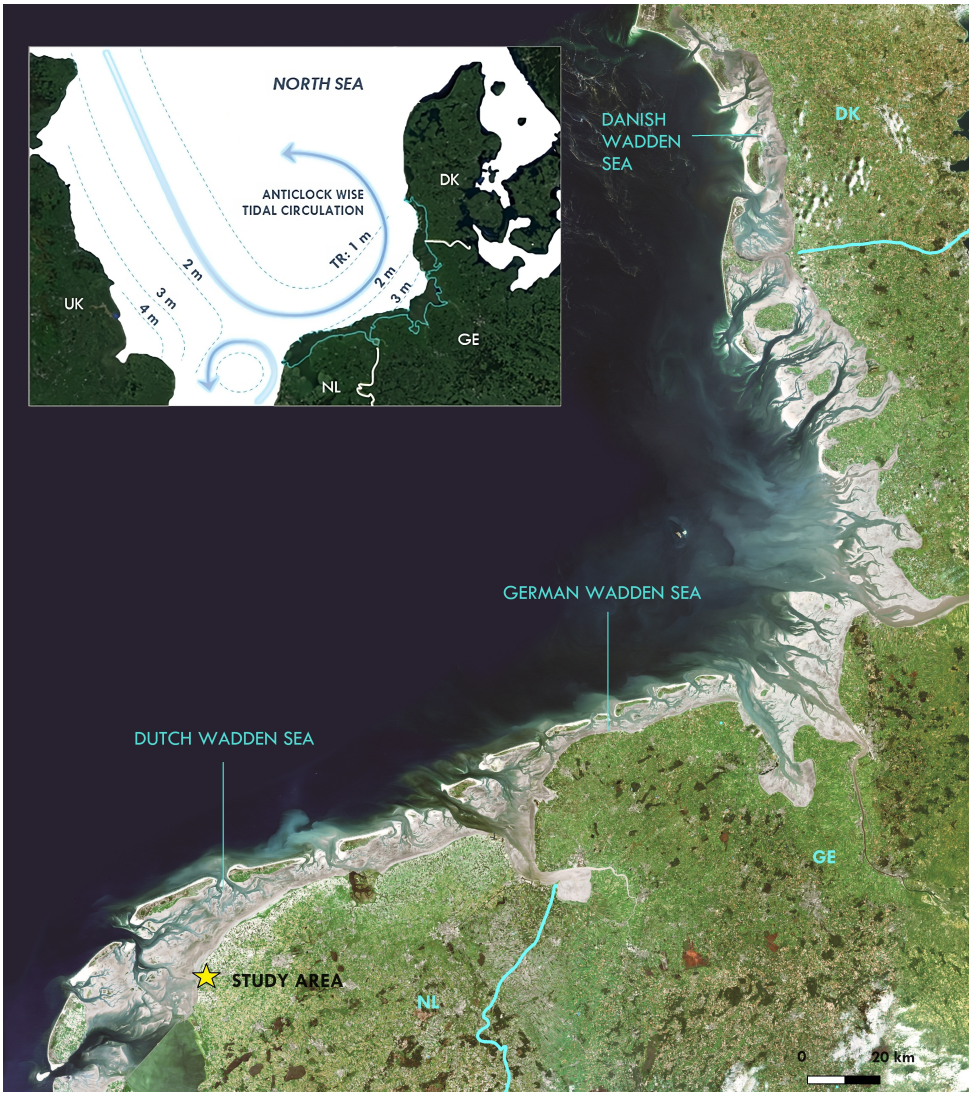

Figure 2.1: The Dutch, German and Danish Wadden Sea (about 500 km coastline). Background figure is modified from a satellite image of the Wadden Sea (Copyright: Satellite image, Albedo39 Satellitenbildwerkstatt e.K., image processing). Top panel figure, illustrating the anti-clockwise direction of the tidal wave, is modified from *Dyke* (2007).

decision making. The Dutch Government hence decided, with large political consensus, to build the largest human intervention ever in the Wadden Sea, i.e. the closure of the Zuiderzee, via the construction of the 32 km-long Afsluitdijk. With the completion of this massive work in 1932, the Zuiderzee became a freshwater lake (the 'IJsselmeer'), and large areas of water were reclaimed for agricultural use. In 1976, the IJsselmeer was

Figure 2.2: Antique sea chart of the Dutch and German Wadden Sea drawn by *Henricus Hondius* in 1641 and reported by *van der Krogt* (2000). In the top panel the illustrated area spans from North-Holland, through the Zuiderzee and Friesland, up to the Groningen province (NL). The bottom panel illustrates the area spanning from the Ems Dollard estuary (border between the current Dutch and German Wadden Sea) through the Jade Bight and the Elbe estuary, up to the Eiderstedt province (GE). The different size and shape of the barrier islands is noticeable compared to the current one (see also next figure for comparison with the current (2020) Dutch Wadden Sea coast).

split by the construction of the Houtribdijk, and the southern section became the Markermeer. In 1953 another intense storm surge hit the Netherlands (as well as Belgium and the United Kingdom). Water levels reaching 5.6 m above mean sea level caused multiple dike breaches and the death of 1836 people in the Netherlands (*De Kraker*, 2006). As a response to this event, a *Delta Works Commission* was called to develop a *Delta-Plan* aiming at preventing such disasters in future. This plan included an extensive system of dams and storm surge barriers, such as the Maeslantkering, built on the Nieuwe Waterweg (near Rotterdam, South-Holland) and completed in 1997 (e.g. *Bol*, 2005). Moreover, the *Delta Work Commission* set the 'acceptable risk' for complete failure of every dike ring in the country at 1 in 10.000 years. Specifically, for the Wadden region, flood risk measures included a preferred strategy, including on one hand the strengthening of the

existing coastal dykes, and on the other hand the maintenance of the intertidal areas (consisting of islands, mudflats, salt marshes and channels). According to such strategy, the maintenance of this buffer and dike reinforcement will ensure a safe living on the mainland and on the barrier islands (e.g. *Kabat et al.*, 2009; *Van Buuren et al.*, 2016).

HYDRODYNAMICS

The semidiurnal tides generated in the North Sea result in a flooding and ebbing flow aligned in the north-east (flood) and south-west (ebb) direction, following the anticlockwise direction of the tidal wave (Figure 2.1). The tidal range varies between about 1.5 m and 4 m. About $3*10^{10} m^3$ of water penetrates in between the barrier islands during each tidal cycle (*Oost et al.*, 2017). The water flows through a branching channel system that conveys the water to the intertidal flats, fringing the mainland (Figure 2.3). The Wadden Sea is generally defined as a series of interconnected tidal basins, with each basin bordered by the mainland, the barrier islands and the tidal divides (*Wang et al.*, 2012). The tidal divides can be defined in different ways (*Vroom*, 2011): hydrodynamic divide (based on the smallest velocities) or morphological divide (based on the maximum bed level). The simulations of *Duran-Matute et al.* (2014) and the measurements of *Van Weerdenburg et al.* (2021) indicate that there is quite some flow over the tidal divides during storm conditions, leaking water and likely sediment. Furthermore, morphological changes also lead to migration of the tidal divides, partly caused by human interventions like the Afsluitdijk. As a consequence, the understanding of the Wadden Sea system requires the understanding of processes at multi-basin scale.

In addition to the tidal flow, waves play a key role in the Wadden Sea. The tidal basins are sheltered by barrier islands (Figure 2.3) hence offshore-generated waves only partially penetrate the lagoon. Tidal currents, within the lagoon, mainly interact with locally-generated short-period wind waves. At the tidal inlets the hydrodynamic energy is higher, with more energetic flows and waves compared to the inner intertidal flats.

Concerning density driven flow in the Dutch Wadden Sea, the main freshwater discharges (indicated in Figure 2.3) are at Den Oever ($\sim 240 m^3/s$), at the Kornwerderzand sluice ($\sim 200 m^3/s$), at the Lauwers Lake ($\sim 37 m^3/s$) and, at the boundary with the German Wadden Sea, the Ems River ($\sim 80 m^3 h/s$) (*Dankers et al.*, 2012; *Duran-Matute et al.*, 2014; *Gräwe et al.*, 2016). Although the volume of these discharges is small compared to the volume of seawater exchanged with the North Sea, it is relevant for water exchange because of density-driven exchange flows (*Duran-Matute et al.*, 2014; *Gräwe et al.*, 2016) but also for the existence of important habitats (*Frazier*, 1999).

SEDIMENT TRANSPORT AND AND DISTRIBUTION

The water motion, the consequent sediment transport, and the seabed features (also affected by biological processes) result into an intricate morphodynamic development of the Wadden Sea lagoon. The inlets are the main source of sediment in the Wadden Sea. About 12 million ton/year of mud is transported through the Wadden Sea and the North Sea. The amount of mud entering the Dutch Wadden sea from its southwest inlets is transported towards the northeast (following the anticlockwise direction of the tidal flow), and constitutes a valuable resource for intertidal areas and supra-tidal marshes (*Colina Alonso et al.*, 2024) which face the challenges imposed by accelerated sea level

Figure 2.3: Satellite image of the Dutch Wadden Sea (Credit: European Union, Copernicus Sentinel-2, image taken on 22 September 2020). The picture visualizes the north Dutch mainland and five barrier islands (from East to West: Texel, Vlieland, Terschelling, Ameland and Schiermonnikoog). The closure dam ('Afsluitdijk') separates the Wadden Sea from the artificial lake IJssel. Sandy intertidal flats fringe the outer border of the barrier islands, whereas muddy intertidal shoals and fringing flats are found along the mainland coast. The red spots indicate freshwater discharges, from East to West: the Kornwerderzand sluice in proximity of the Afsluitdijk, the Lauwersmeer and the Ems-Dollard estuary, the latter representing the eastern border of the Dutch Wadden Sea.

rise. The amount of available mud in the Wadden Sea seems sufficient for the intertidal areas to cope with the present-day sea level rise rates. However, this amount is influenced by anthropogenic pressures (e.g. dredged material is disposed on land or offshore), whose effects are prolonged in time (*Van Maren et al.*, 2016) and a decrease in sedimentation rates will likely occur (*Colina Alonso et al.*, 2024).

The sediment grain size gradually decreases from the inlets (mainly sandy) towards the tidal flats fringing the mainland (mainly muddy), due to the decreasing transport capacity of the tidal currents. Sand and mud are both vertically (in the seabed), and horizontally (within the basins) unequally distributed. The sediment distribution in the lagoon is the result of gradual, and relatively slow, natural processes (such as sea level rise) and of abrupt changes in the system caused by human interventions (*Colina Alonso et al.*, 2021). The latter include land reclamation, the realization of hard coastal protection structures (such as dykes) and the construction of closure dams. From 1927 to 1932, the 32 km long closure dam *Afsluitdijk* (Figure 2.3) was built with the aim of reducing the flooding risk and of creating large polders for agricultural use. The main channels of Marsdiep and Vlie were interrupted by the dam, resulting in a large amount of fine sediments becoming available in the Wadden Sea (*Gerkema et al.*, 2014; *Colina Alonso et al.*, 2021). The timescales associated with such human interventions typically varies from decades to centuries (*Van Maren et al.*, 2023).

IMPACT OF SEA LEVEL RISE

An important question is whether the Wadden Sea is importing sediment from the North Sea (*Gerkema et al.*, 2014). A comparison between bathymetric surveys from 1935 and 2005 suggests that, as long as the change in mean sea level is gradual, the Wadden Sea will be able to keep pace with sea level rise (*Elias et al.*, 2012). According to the recent numerical study of *Huismans et al.* (2022), doubling the rate of sea level rise will lead to doubling of the loss of intertidal areas as well. This study also shows that the response of different tidal basins to sea level rise depends on their size (and tidal prism), with the larger tidal basins facing harder challenges compared to smaller basins. On the other hand, the analysis of *Van Maren et al.* (2023) suggests only the fringing flats in the Marsdiep inlet are accreting and not so much the deeper parts of the basin, and only with fine-grained sediments. But even more, this sedimentation appears to be a response to closure of the South Sea rather than to rising sea levels.

BIODIVERSITY

The Wadden Sea consists of a large variety of habitats, ranging from salt marshes to bare intertidal flats and intertidal shoals, islands, barrier islands, gullies, tidal creeks and channels. About 50% of the Wadden Sea remains emerged at low tide: the ~ 5000 km^2 of emerged land forms the world's largest system of interconnected intertidal flats. The alternation of emerged and submerged conditions creates an ideal environment for a wide variety of living species. The Wadden Sea is a *Unesco World Heritage* site, and it is further listed into the *Natura 2000* network. One of the criteria that resulted in the selection of the Wadden Sea as *World Heritage Property* in 2009, is the unique richness of its ecosystems, hosting around 10.000 species of flora and fauna (*Reise et al.*, 2010). This intertidal system is considered one of the most important areas for migratory birds worldwide, being a stopover location both in the context of the East Atlantic Flyway (*Blew et al.*, 2005) and of the African-Eurasian migratory way (*Colin A. et al.*, 2014). Up to 6.1 million birds can be present at the same time in the lagoon, with an average of 10-12 million specimen passing through it each year (*Blew et al.*, 2005). Moreover, intertidal areas are also vital to some mammals species, such as the grey seals (*Frazier*, 1999). The variety of landscapes and of flora and fauna species, along the intertidal Friesland coast, is illustrated with some pictures, reported in Figure 2.4, which were taken during field work in 2016-2017. Salt marshes perennial species cover the higher tidal flat zone ([a]). Through a tidal creek system ([b]) water and sediment are transported up to (and from) the higher mudflat zone, where the pioneer vegetation specie, *Salicornia procumbens*, colonizes the bed (panel [c]). Patches of other vegetation species (e.g. *Spartina aglica* [d]) are evident at elevation higher than the Mean High Water level. A large variety of fauna inhabits these muddy coastal areas, ranging from numerous birds species (e.g. the Ruddy Turnstone, *Arenaria interpres*, in panel [e]), to several molluscs and shall fishes species ([f],[g]). Benthos species, living the muddy substrate (such as the *Oligochates*, panel [h]) are a key element of the food-web. These species significantly affect the characteristic of the bed itself, as shown in panel [f], where the micro-tunnels in the mud are well visible.

2.2. KOEHOOL AND WESTHOEK INTERTIDAL FLATS

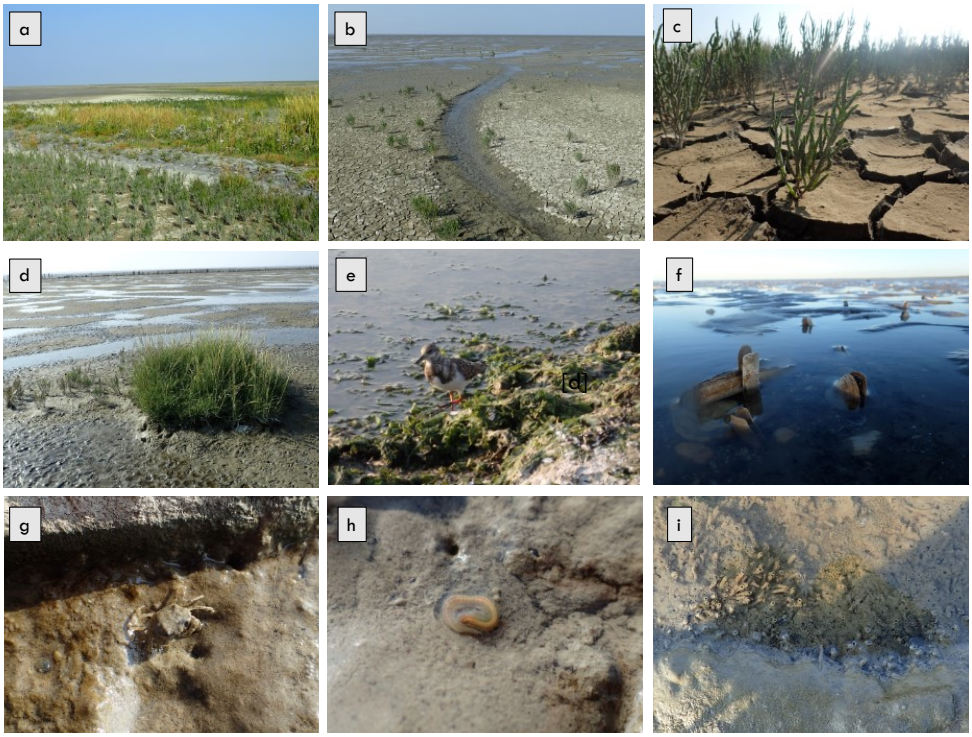

Figure 2.4: Some flora and fauna species photographed during the field campaigns (2016 to 2018) at Koehool and Westhoek. **[a]** Salt marshes perennial species at Westhoek; **[b]** and **[c]** *Salicornia Procumbens* at the vegetation edge and higher on the Westhoek mudflat; **[d]** Patches of *Spartina Anglica* at Westhoek; **[e]** Ruddy Turnstone (*Arenaria Interpres*) at Koehool; **[f]**, **[g]** molluscs and fish species at Koehool; **[h]** *Oligohocates* that bioturbate the substrate **[i]** at Koehool.

GENERAL INTRODUCTION

Two adjacent intertidal flats fringing the Dutch Frisian coast were investigated. The intertidal flats, named after the two adjacent municipalities 'Koehool' and 'Westhoek', are located on the opposite site of the Terschelling barrier island. The bathymetry of the Dutch Wadden Sea presents a system of branching channels, which are deeper in proximity of the tidal inlets, and become shallower when approaching the mainland coast (Figure 2.5). The Kimstergat tidal channel runs parallel to the coast, and transports water and sediments back and forth from the Harlingen Harbour to the investigated flats. Bed elevations at the investigated tidal flats range between -1 m MSL (i.e. Mean Low Water Level) and +1 m MSL (i.e. Mean High Water Level). At Koehool, bed elevations are lower compared to Westhoek.

MORPHOLOGICAL EVOLUTION

During the last century this area went through remarkable changes in bed elevation. Figure 2.6 indicates that, from 1926 to 2016, accretion and erosion larger than 3 m occurred both at the outer inlet and within the tidal basin, with evident channels migration. Along

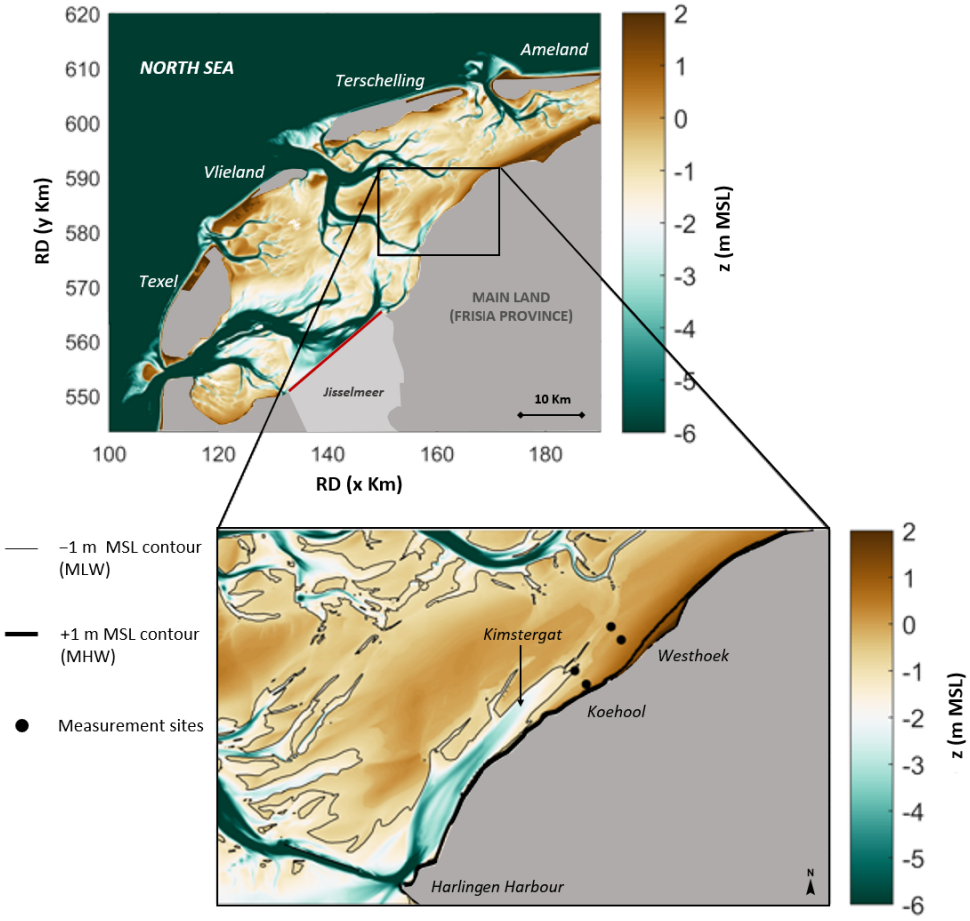

Figure 2.5: Top panel: 2017 Bathymetry of the Dutch Wadden Sea with its barrier islands separating the lagoon from the North Sea *(Vaklodingen dataset, Rijkswaterstaat)*. The coordinates RD (x) and RD (y) in kilometers refers to the RD (*Rijks-Driehoek*) reference system, i.e. the coordinate system used by the Dutch geographical service. The red line represents the Asfluitdijke. Dark gray represents land (mainland and islands), whereas light gray represents the Jisselmer. Bottom panel: zoom on the studied area. The Kimstergat becomes shallower towards the north-east direction, i.e. approaching the investigated flats. The intertidal areas are limited by the Mean Low Water (MLW) and Mean High Water (MHW), respectively illustrated with thin and thick black lines. Four measurements locations are indicated with black markers. More details about these specific sites are provided in the following chapter.

the mainland coast, including at the intertidal areas of Koehool and Westhoek, sediment deposition promoted a vertical accretion in the order of 1-2 m. Along the two investigated transects though, a difference in the bed level evolution is noticed. Already back in 1926, the bed elevation at Westhoek was higher than Koehool, especially within the first kilometer from the shore. The permanent accretion at Westhoek allowed, since the late 80's, to overcome the threshold of +1 m MSL (i.e. the Mean High Water Level). Differently, at Koehool, the bed level increase was less pronounced, so that this threshold has

not been reached yet.

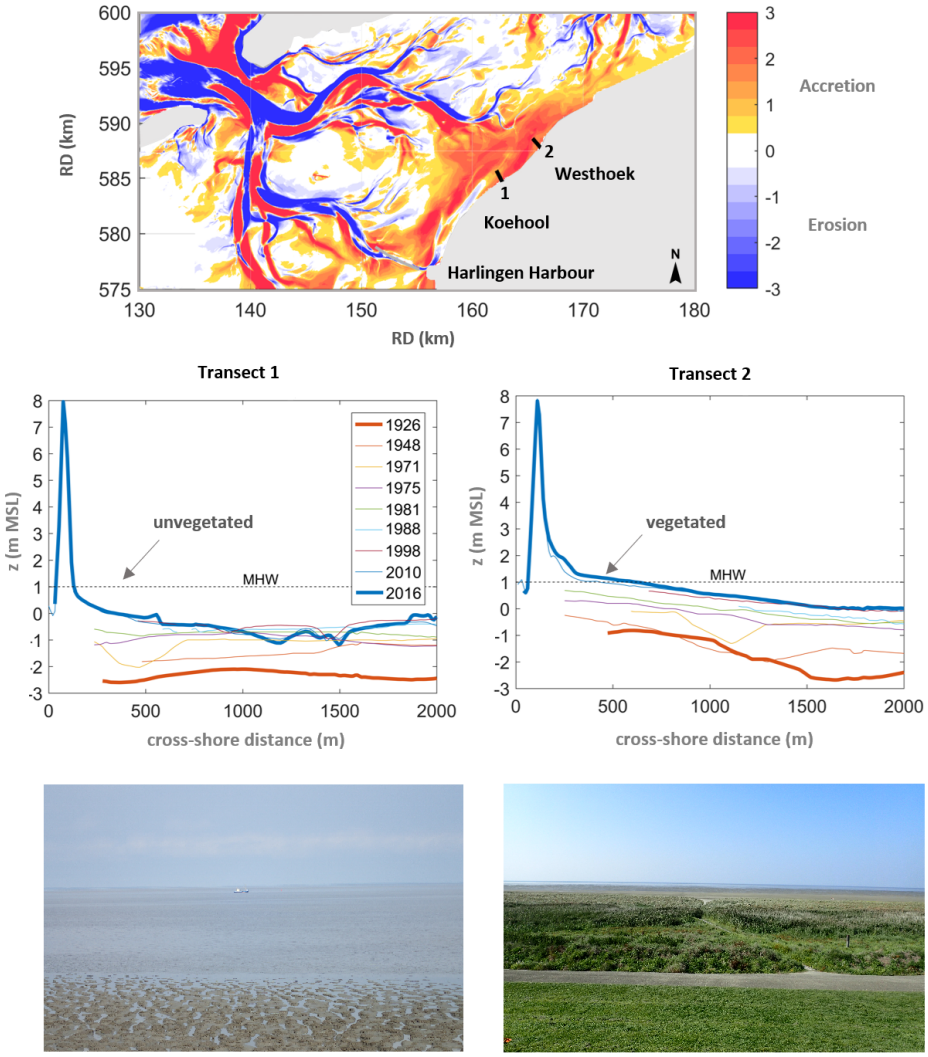

Figure 2.6: Top panel: Comparison of bed elevations in 1926 and 2017 *(Vaklodingen dataset, Rijkswaterstaat)*. Positive values indicate bed accretion, negative values bed erosion. Central panels: the evolution of two kilometer-long transects, one at Koehool and one at Westhoek, reveal that since the 80's the bed elevation at Westhoek overcame the MHW level. Bottom panels: the outlook of the two mudflats, pictured from the coastal dyke in September 2017 indicated that the lack of right conditions for vegetation development at Koehool.

KOEHOOL VS. WESTHOEK

This difference in bed levels resulted in different bio-morphological evolution of the two intertidal flats. Since the beginning of the 90's salt marshes developed a Westhoek. The lateral expansion of salt marshes was such that in 2015 the maximum distance of vegetation from the coastline was about 160 m. Figure 2.7 shows that such development started, and was more pronounced, at the more sheltered side of the coast. Likely, the concave shape favoured the deposition of sediment, making the area more suitable for the establishment of vegetation. During our field campaign at Westhoek, we observed the pioneer specie *Salicornia procumbens* at the seaward edge of the vegetated area (pictured in panel 1) but also at higher mudflat zones (pictured in panel 2). Furthermore, in Figure 2.7, the bed elevation of +0.95 m NAP in 2016 indicates the potential area in which the salt marsh may still expand at Westhoek (*Van Weerdenburg R.*, 2019). The vegetation width decreases towards the south and towards the north of Westhoek. At Koehool the vegetation is completely absent, as the bed level is still about 40 cm below MHW level in proximity of the coastline.

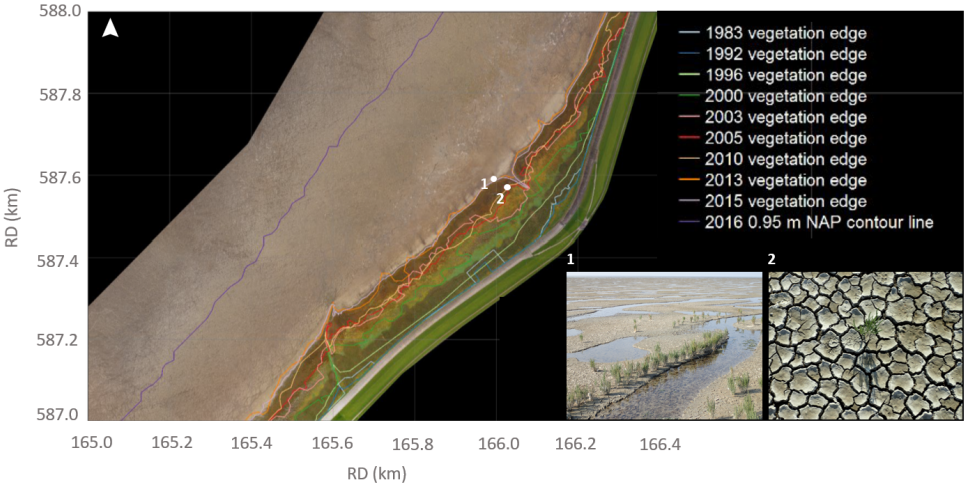

Figure 2.7: Aerial picture of Westhoek realized in 2015, indicating the vegetation edge in 2015, and in previous time steps starting in 1983. The figure is modified from the one presented in the Deltares report dedicated to the Mud Motor study case, we refer to *Van Weerdenburg R.* (2019). The two field pictures, taken during the 2017 field campaign at Westhoek, were provided of latitude and longitude coordinates in the WGS84 reference system, which have been converted to RD coordinates and indicated over the map.

BEDFORMS AT KOEHOOL

Although the bedform topic has not been addressed in our scientific research, we find interesting to report the diversity and variability of the tidal flat bedforms at Koehool. The lower and sandy (median grain size $D_{50} \sim 125\mu m$, see next chapter for details) intertidal flat bed (near the Mean Low Water level, i.e. in proximity of the Kimstergat tidal channel edge) is characterized by ripples. The observed ripple wave length was typically 5-10 cm, with a width of ~10 cm and a crest height of ~0.5-1 cm. During different seasons of ob-

servations, the orientation of the ripples was elongated towards the shore direction (as indicated in Figure 2.8).

Higher on Koehool mudflat, a dense network of ridges and runnels periodically exists (Figure 2.8). Ridges were 50-60 cm long, 20-30 cm wide and 10 cm height; the runnels were of similar size. Differently from the ripples, we observed a variation in size and orientation of the ridge-runnel system during the various field visits. The pictures in Figure 2.8 were taken during spring 2017 and a similar ridge-runnel system was observed in winter (with iced ridge crests as well). Sedimentation occurring during summer filled up the runnels with very soft mud. This process was accompanied by algae mat formation and intense biological activities (noticeable also by a bubbling mud surface). As specified in the following chapter, sediment grain size at this area showed a D_{50} of ~ 30μm.

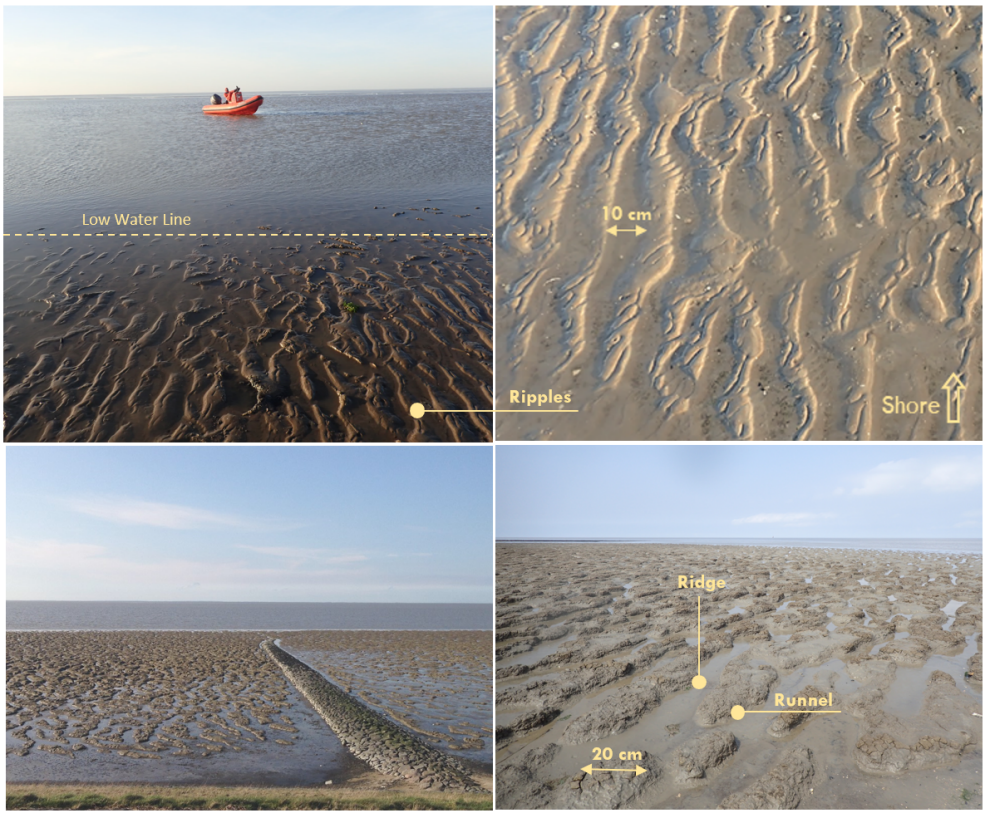

Figure 2.8: Top panels: Ripples observed at the investigated site located at the lower Koehool mudflat (bed elevation -1 m MSL) during Winter 2018. These pictures were taken at low water, hence the submerged area is subtidal. Bottom panels: ridge-runnel system observed at higher Koehool mudflat during Spring 2017. These pictures were not taken at the investigated site, but at higher tidal flat elevation (bed elevation +0.20 m MSL).

Whitehouse et al. (2000) reported the formation of similar bed forms at *Peterstone Wentlooge (Severn estuary, UK)*, with a size comparable to the ones observed at Koehool (0.4-0.7 m wide and 0.1 m high ridges, and 0.3-0.35 wide runnels). The formation of

runnels and ridges – not investigated in this dissertation – relates to a combination of wave-induced stress and biological activities (*O'Brian,* 1998; *Whitehouse et al.*, 2000).


XCEL

About the Photo

This photo, taken on May 15, 2017, captures the walk toward the frame located 1 km from the coastline on the Westhoek intertidal flat. The fieldwork aimed to retrieve the instruments and dismantle the frame.

3

FIELD MEASUREMENTS

We carried out field measurements during spring and winter seasons of the years 2016, 2017 and 2018, at the intertidal flats of Koehool and Westhoek (Dutch Western Wadden Sea). High resolution data were obtained via the deployment of Acoustic Doppler Velocimeters, Acoustic Doppler Current Profilers, Optical Back Scatters and Wave Gauges. These instruments were installed for one or two-month long periods, providing information on water levels, waves, currents, suspended sediment concentrations and bed level changes. This chapter reports on the technical aspects of these field measurements, including a description of the deployed instrumentation, their working principles and the main configuration settings needed to extract the desired data. We provide details on the eight frames that were installed, the data collected during their deployment and the key post-processing steps carried out to create the dataset used in this dissertation.

3.1. INTRODUCTION

Field measurements are carried out to improve the knowledge on the mechanisms controlling the hydrodynamics and sediment transport on intertidal areas. Beside this, as detailed in Chapter 1, the results can be used for understanding and optimizing the design of fine sediment nourishments for ecological purposes (such as the Mud Motor study case). Hence, we measured: (a) the hydrodynamics in the tidal channel - tidal flat areas; (b) the suspended sediment concentrations; (c) the bed level changes.

We defined four sites located along two transects, one trasect on the Koehool and one on the Westhoek intertidal flats (see Chapter 2). The monitoring activities were carried out during two seasons: the spring and the winter season. During spring time, measurements were realized at Koehool transect in 2016, and at Westhoek transect in 2017. The two transects were instead simultaneously monitored during winter time in 2018. This monitoring design allowed the analysis of hydrodynamics, sediment transport and morphological processes – and of their relative importance – at different tidal flat elevations, under different meteorological conditions. In the following sections, the measurement sites, the deployed instruments, their main settings, and the post-processing performed on the raw data, are described.

3.2. MEASUREMENT SITES

With the aim of investigating the hydrodynamics and morphodynamics at two intertidal flats fringing the Dutch Wadden Sea, (Figure 3.1[a]), two transects were monitored: one at Koehool and one at Westhoek (Figure 3.1[b]). Two sites were investigated along each transect (Figure3.1[c]). The coordinates of the installation sites are reported in Table 3.1. The subscripts 'H' and 'L' are used to indicate the 'Higher' and 'Lower' relative positioning of the measurement sites along each transect. Site K_L was the lowest investigated site, being located at a bed elevation of -1 m MSL. Sites K_H and W_L were located, respectively, at -20 cm and -13 cm MSL. Despite the similar bed elevation, the two sites are differently exposed to hydrodynamic forcing and sediment sources. W_L, similarly to K_L, is located near the tidal channel edge, at 1.6 km distance from the shoreline. K_H instead, lies in between the tidal channel and the shoreline, at 350 m distance from it. Also the sediment grain size (D_{50}, see 3.2) is different, being finer at K_H (30 μm) compared to W_L(99 μm). Site W_H, with a bed elevation of +10 cm MSL, was the highest investigated site and it was located at a distance of about 1 km from the (vegetated) shoreline. At this site, the finest sediment is observed (D_{50}=13μm). The reciprocal distance between the investigated sites along the transect, is 620 m at Koehool and 650 m at Westhoek, whereas the difference in bed elevation is 0.87 m and 0.30 m, respectively. This implies that the Koehool transect is three times steeper than the Westhoek transect (Table3.2). This difference in slope is indicated in Figure 3.1[d].

Site	*RD (x)*	*RD (y)*	*WGS84 (E)*	*WGS84 (N)*
K_L	162.5	585.6	53.256905	5.499590
K_H	162.9	585.0	53.251508	5.505569
W_L	163.8	587.4	53.273059	5.519118
W_H	164.2	586.9	53.268559	5.525100

Table 3.1: Local coordinates of the four installation sites in the RD (*Rijks Driehoeken*) reference system (x,y) and in the WGS84 reference system (East, North).

During a time period of 6 years (2011-2017) the Kimstergat tidal channel was subject to pronounced bed level dynamics, with erosion and accretion larger than 0.5 m, as illustrated in Figure 3.1[c]. As noticed from Figure3.1[d], during this time period, vertical accretion occurred both at

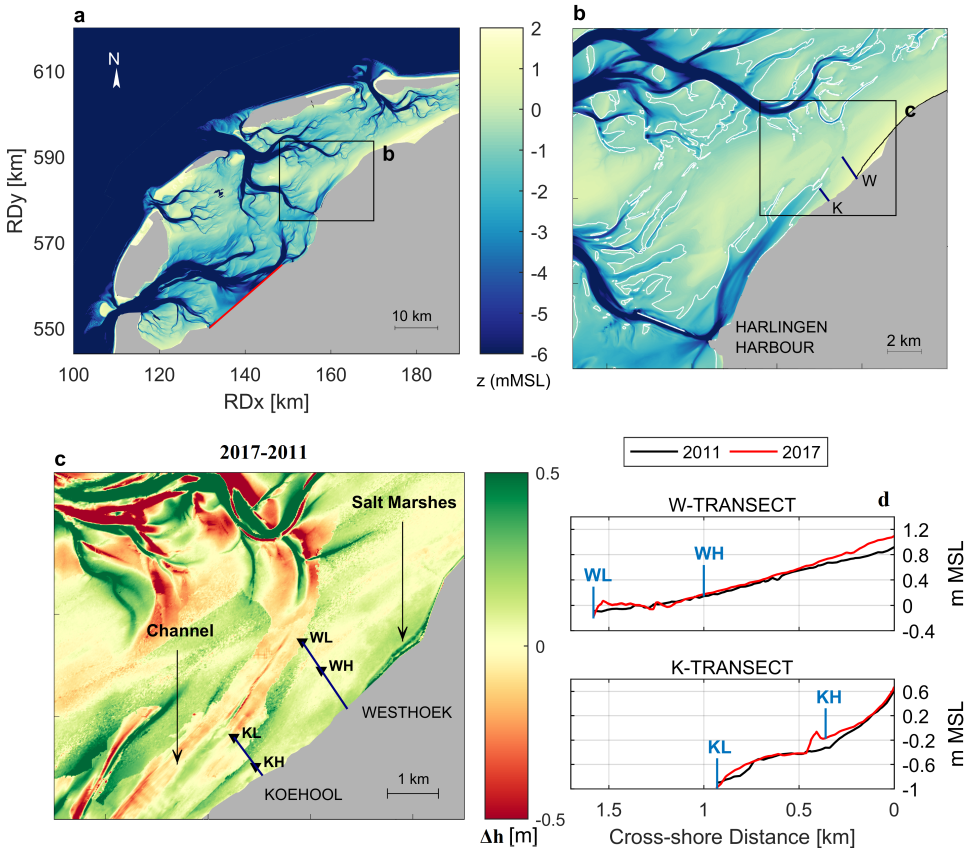

Figure 3.1: **[a]**: 2017 Western Wadden Sea Bathymetry with grey colour indicating the barrier islands, the IJsselmeer and the mainland. The red line indicates the closure dam (Afsluitdijk). The coordinates RD (x) and RD (y) in kilometers refers to the RD (*Rijks Driehoeken*: Dutch Triangles) reference system. **[b]**: The two investigated transects named 'K' and 'W' are sited at Koehool and Westhoek, respectively. The white lines indicate the Mean Low Water (MLW) level (i.e. -1 m MSL), while the black lines (in proximity of the coastline) indicates the Mean High Water (MHW) level (i.e. +1 m MSL). **[c]**: K_L, K_H, W_L, W_H indicate the position of the measurement frames over an erosion-deposition map of the study area referred to the time period 2011-2017. Positive values indicate increase in bed elevation. **[d]**]: Bed levels of the two transects referred to the years 2011 and 2017 (note that the y-axis is different but the interval 1.8 km is the same in both the sub-figures.

Westhoek and at Koehool. At Westhoek the maximum accretion (~20 cm, i.e. from 0.9 m MSL to 1.13 m MSL) occurred in proximity of the most elevated salt marshes, whereas at Koehool the maximum accretion (~30 cm, i.e. from -0.4 m MSL to -0.1 m MSL) occurred at 0.4 km from the shoreline, which is in proximity of our measuring frame K_H.

3.3. INSTRUMENTATION

In this Section, the instrumentation deployed in the monitoring campaigns is described, with a special focus on three main instruments which provided the core data used in our research: *Acoustic Doppler Velocimeter*, *Acoustic Doppler Current Profiler* and *Optical Back Scatter*. The configu-

Site	z_b	D_{50}	*Dist. from shore*	*Period*
K_L	MSL-1 m	123 μm	970m	Apr-May2016, Dec2017-Feb2018
K_H	MSL-13 cm	30 μm	350 m	Apr-May2016, Dec2017-Feb2018
W_L	MSL-20 cm	99 μm	1650 m	Apr-May2017, Dec2017-Feb2018
W_H	MSL+10 cm	13 μm	1000 m	Apr-May2017, Dec2017-Feb2018

Table 3.2: Local coordinates in the RD Reference System, Bed elevations (z_b), median grain size (D_{50}), distance from shore and periods of measurement at the four investigated sites: K_L,K_H, W_L, W_H. Data of grain size is provided after in situ-field measurements, as detailed in Section 3.7.

ration settings that required major attention are detailed hereafter, together with the accuracy of the data extracted from the sensors.

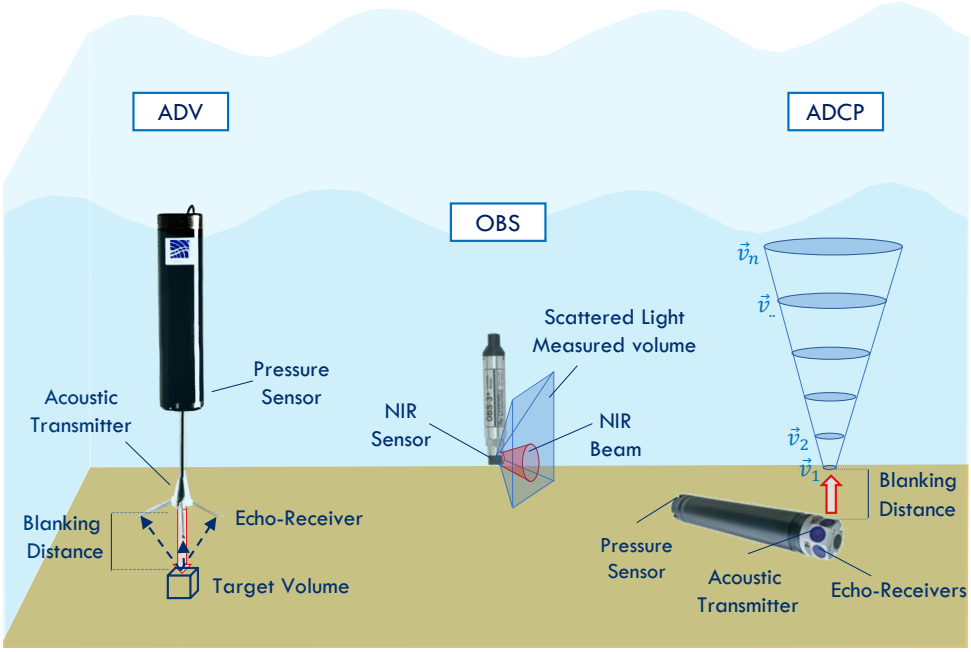

Figure 3.2: Illustration of the instruments' working principle which provided the core data of this dissertation. From left to right: *Acoustic Doppler Velocimeter* (ADV), *Optical Back Scatter* (OBS) and *Acoustic Doppler Current Profiler* (ADCP).

ACOUSTIC DOPPLER VELOCIMETER (ADV)

The *Acoustic Doppler Velocimeter* (*Nortek Vector*, in our campaigns) uses the Doppler principle to perform point-measurements of the 3D flow velocity vector. The working principle is visualized in Figure 3.2. The instrument transmitter sends a pulse of sound (at 6 MHz frequency), listens to its echo (via three receiving beams) and measures the change in frequency of the echo. The sound is not reflected by the water itself but rather from particles suspended in the water (typically suspended sediment). Therefore, the working principle of this instruments is based on the

assumption that water and suspended sediment move with the same speed. The accuracy of the so-obtained flow velocity measurements is, by default, the largest between 0.1 cm/s and the 0.5% of the measured value. As an example, at flow velocities of 1 m/s, the former option results in 0.1 cm/s, whereas the latter in 0.5 cm/s accuracy. As noticed from Figure 3.2, the sampling volume, i.e. the measured water volume, is located at a certain distance from the transmitter. This distance is named *blanking distance* and equals 15 cm. The sampling volume is a cylinder with 1.5 cm diameter and height between 0.5 to 2 cm. We set a sampling volume of 1.5 cm height.

A part from measuring the flow velocity, the ADV includes several additional sensors, among which a compass and a pressure sensor. The compass (having an accuracy of 2°) was crucial to extract flow velocities along specific compass directions (North and East direction). In our campaigns the challenging installation conditions in the (often very soft) mud, did not allow to be accurate in the alignment of the main beam with the North direction. The alignment discrepancy (range 10-to-25°) was hence corrected within the data post-processing. The pressure sensor data (having an accuracy of 1 mm with the settings applied in our studies, i.e. maximum water depths of 4 m) was used to extract water levels and wave height. The data post-processing was a key step to correct and calibrate the pressure data (as detailed in Section 3.7).

The output sampling rate of the ADVs installed in our campaigns (i.e. the frequency of the output data) was set as 8 Hz, in the available range 1-64 Hz. This value was selected as a convenient compromise to obtain high-frequency data (high enough for wave analysis) and reasonable battery consumption.

The ADV operates in *continuous* or *burst* mode. The choice of the instrument's operational mode is essential, as it affects not only the quality, but also the quantity of data. Continuous mode have the advantage of providing more data (the full submergence period of the transmitter sensor), but it requires a relatively large memory to store the data, and battery to supply the power. For this reason, long term deployments rather require the configuration in burst mode. When configuring the instrument in burst mode, two parameters have to be set: the duration of the burst interval (BI), and the number of samples per burst interval (SpB). The selection of BI and the SpB must result in a sufficiently high number of waves to perform a consistent wave analysis; consequently the wave period has to be then taken into account (albeit often unknown at this stage). Moreover, in case of ADVs installed vertically, the instrument provides the distance between the transmitter and the bed at the end of each burst. The choice of the burst interval therefore dictates also the frequency of bed level changes data. In morphological studies this is of utmost importance. At our study site the averaged mean wave period was acknowledged to be about 3 seconds. The ADVs that measured in burst mode were configured to operate with burst intervals of 20 minutes, and numbers of samples per burst of 2400 to 4800. A burst interval of 20 min at 8 Hz, equals 9600 data per burst interval. A number of 4800 samples per burst implies that, out of the 9600 data gathered within the interval, only the half (i.e. 4800 samples) is stored in memory. This eventually means that, out of the 20 minutes burst interval, 10 minutes of data are stored, while the following 10 minutes are discarded. The bed level change is measured at the end of each burst interval, i.e. every 20 minutes. With these settings, per each 10 minutes data block, about 200 waves are expected to be available for the wave analysis. These instrument settings have to be strategically selected when designing a field campaign. Pursuing strategic choices to save memory and battery, while getting good data quality for a prolonged time period, is especially key for long term (week-to-months) filed measurements.

Eventually, the ADV works as "parent-instrument" for those probes which are not provided of power supply and/or data storage volume. In our field campaigns the ADVs were configured to supply battery and memory storage to one or multiple Optical Back Scatter (OBS) sensors.

ACOUSTIC DOPPLER CURRENT PROFILER (ADCP)

The *Acoustic Doppler Current Profiler (ADCP)* (*Nortek Aquadopp – AQDP –* in our field campaigns) uses the Doppler principle to measure the 3D flow velocity along the full water column (Figure 3.2).

This instrument has a data output frequency of maximum 1 Hz, which is significantly lower than the ADVs. The accuracy of the velocity data is the largest between ±0.5 cm/s and ±1% of the measured value. As an example, with flow velocities of 1 m/s the largest value between 0.5 cm/s and 1 cm/s is automatically selected. Compared to the ADVs therefore, the current profiler provides more spatial information (full water column vs a point-measurement) at a lower output frequency (1 Hz vs 8 Hz) and with a smaller accuracy (1% vs 0.5% of the measured value). The instruments can be installed downward (i.e. with the transmitter pointing towards the bed) or upward looking (i.e. with the transmitter pointing towards the water surface). The latter configuration have been adopted in our campaigns. As for the ADVs a *blanking distance* of 15 cm exists between the transmitter and the first measurement volume, which in this case is a cone with increasing diameter towards the water surface (Figure 3.2). The resolution of the measurements along the vertical can be selected in the range 10 cm – 2 m. In our measurements, the AQDPs were configured to measure flow velocity at resolution of 10 cm along the vertical. Similarly to the ADVs, the AQDP operates either in *continuous* or *burts* mode. Being upward looking installed though, the sensors do not provide the bed level changes tracking. The AQDPs in our campaigns were configured to operate with burst intervals (BI) of 20 minutes and number of samples per burst (SpB) of either 300 or 600. Also similarly to the ADVs, the AQDP instruments include other sensors, providing, e.g. the geographical orientation of the instrument's beams (i.e. the compass) and the pressure signal. The latter was used to validate the water levels obtained from the ADVs.

OPTICAL BACK SCATTER (OBS)

The turbidity sensors typically use the *Optical Back Scatter (OBS)* working principle to measure suspended solid concentration in natural environments. In our field campaigns eight *OBS-3+ Campbell* sensors were deployed. The working principle is illustrated in Figure 3.2. A laser diode emits the light source (Near-InfraRed light, NIR) converting the input electrical current to optical power. The light is scattered by the suspended sediments and detected by a photodiode with enhanced NIR responsivity. Water turbidity is not only related to suspended sediment, but also to dissolved matter such as plankton, bacteria or organic matter. Moreover, the OBS response depends on the composition, size and shape of suspended particles. For this reason a pre- or post-field campaign calibration process is fundamental for a correct data interpretation. The turbidity response is stored as Voltage values. Empirical correlations between Voltage values and physical concentration units (e.g. g/l) are established through the calibration procedure (described in Section 3.7). The sensor transmittance must remain constant in order to prevent calibration biases, so keeping the OBS window clean is the most important maintenance duty. For this reason, every two weeks the OBS windows were inspected; no bio-fouling was encountered during the inspections. The *OBS3+Campbell* can be set to operate at either *low* or *high* sediment concentration *mode*. The latter was selected. In muddy environment this result in an upper limit for sediment concentration detection of 10 g/l. The accuracy of sediment concentration data is, in this case, 1 mg/l. The OBS sensor were connected to ADVs or AQDPs providing power supply and flesh memory for data storage. The OBS operates in the same mode (continuous/burst) and with the same frequency (with a maximum of 10 Hz) as the connected "parent-instrument". During our field campaign, the OBSes were connected to the ADVs; the obtained suspended sediment concentration data therefore have a frequency of 8 Hz.

3.4. THE 2016 FIELD CAMPAIGN

During the period April 15 – May 22, 2016, two measuring frames were installed at the tidal flat fringing the coast of the municipality of Koehool (sites K_L and K_H, Figure 3.1). The frames installed at site K_L and K_H are showed in Figures 3.3 and 3.4. The figure includes a schematic view of the deployment, in which the distance of each sensor from the tidal flat bed is represented. The instruments installed at each frame are indicated in Table 3.3.

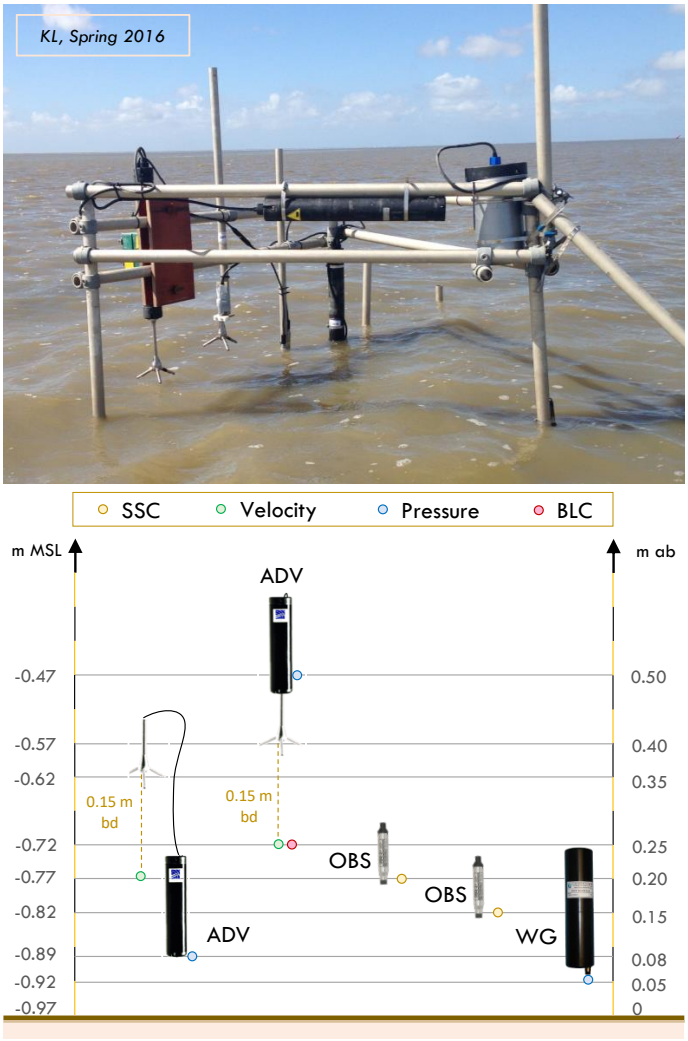

Figure 3.3: Picture and schematic representation of the equipped frame installed at site K_L (bed elevation -0.97 m MSL) during the spring **2016 field campaign**. The schematic representation includes the distance of each sensor from the tidal flat bed (with "m ab" indicating "meters above the bed") and the elevation with respect to Mean Sea Level ("m MSL"). Distances are linearly scaled (with each black/yellow bar on y–axes representing a length of 5 cm), whereas instruments size is not on scale.

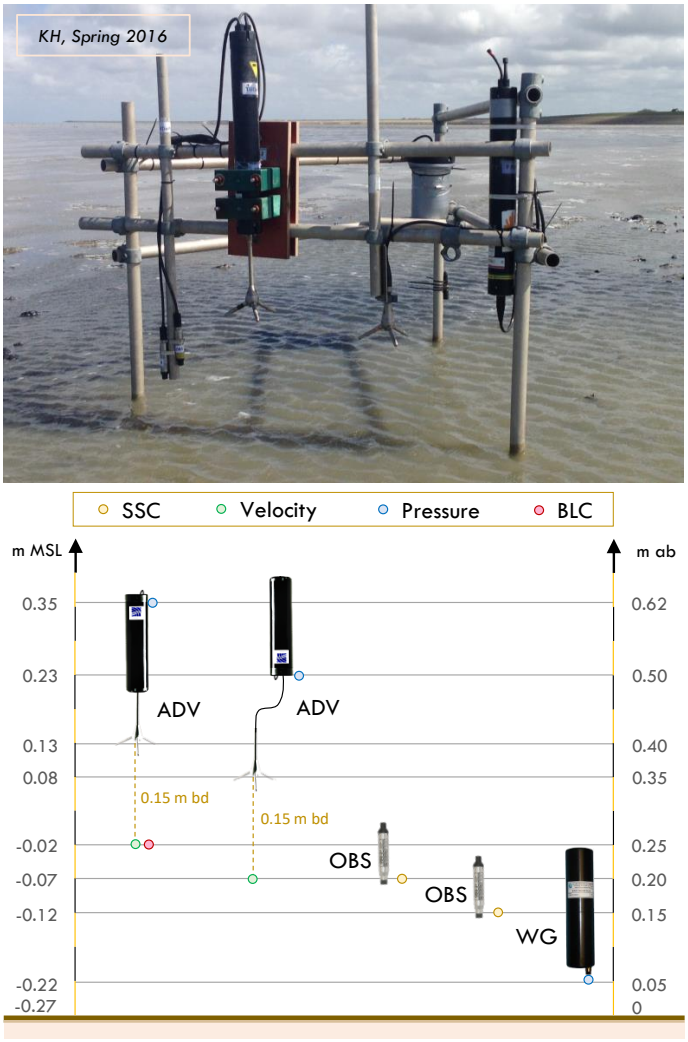

Figure 3.4: Picture and schematic representation of the equipped frame installed at site K_H (bed elevation -0.27 m MSL) during the spring **2016 field campaign**. The schematic representation includes the distance of each sensor from the tidal flat bed (with "m ab" indicating "meters above the bed") and the elevation with respect to Mean Sea Level ("m MSL"). Distances are linearly scaled (with each black/yellow bar on y–axes representing a length of 5 cm), whereas instruments size is not on scale.

At each frame, two ADVs were installed to perform 3D flow velocity at 20 cm and 25 cm above the bed. The data of the two ADVs were used for different purposes. The ADVs at 20 cm from the bed were used to measure the flow velocity in a continuous mode, whereas the ADVs at 25 cm from the bed were set to measure in burst mode. The latter, were configured to measure with a 20-minute burst intervals and 4800 samples/burst at K_L, and 2400 samples/burst at K_H. This implies that the ADV at K_L measured during 10 minutes out of the 20-minute long burst interval, whereas the ADV at K_H measured during 5 minutes out of the same interval. The ADVs configured in burst

Site	Type	Data	Freq.	Mode	Period	Tidal Cycles
K_L	ADV	$\vec{v}_{20}$, h, H	8 Hz	Continuous	April 14–May 22	73
	ADV	$\vec{v}_{25}$, h, H, BLC	8 Hz	BI 20 min SpB 4800	April 15–May 22	73
	OBS	SSC_{15}	8 Hz	Continuous	April 15–May 22	73
	OBS	SSC_{20}	8 Hz	BI 20 min SpB 4800	April 15–May 22	73
	WG	h, H	10 Hz	Continuous	April 15–May 22	73
K_H	ADV	$\vec{v}_{20}$, h, H	8 Hz	Continuous	April 15–May13	56
	ADV	$\vec{v}_{25}$, h, H, BLC	8 Hz	BI 20 min SpB 2400	April 15–May13	56
	OBS	SSC_{15}	8 Hz	Continuous	April 15–May13	56
	OBS	SSC_{20}	8 Hz	BI 20 min SpB 2400	April 15–May13	56
	WG	h, H	10 Hz	Continuous	April 15–May 13	56

Table 3.3: Instrumentation installed at sites K_L and K_H during the **2016 Field Campaign**. Some of the configuration settings, such as the burst interval (BI), the duration and number of samples per burst (SpB) are included. The subscripts '20' and '25' indicate the distance from bed at which the measurements is performed. The symbols h and H refer to water level, water depth and wave height, obtained via pressure data obtained with ADVs, AQDPs, and WGs sensors. BLC indicates "Bed Level Changes".

mode therefore stored bed elevation data at a frequency of 20 minutes.

Two OBSes were mounted at each frame at 15 and 20 cm above bed. The OBSes at 15 cm from the bed were meant as duplicates for validation purposes, which explains the short vertical distance between the two sensors. The backup OBSes showed almost identical values to the OBSes installed at 20 cm above the bed; the latter were used in the data analysis. In order to perform the OBS calibration procedure, 10 liters of sediment laden water were gathered in proximity of site K_H, at the end of the field campaign.

In proximity of each frame one Wave Gauge (WG) *(OSSI-010-003C, Ocean Sensor System)* was installed, with the pressure sensor positioned at 5 cm above the bed, with the aim of providing further wave measurements (used to check and validate the ADV pressure measurements). These sensors were configured to measure in continuous mode with a frequency of 10 Hz. The frames were installed for totally 37 days. At K_L the battery was sufficient to measure for 36.5 days. At K_H the battery dropped after 28 days. The data were therefore processed for 73 tidal cycles at K_L and 56 tidal cycles at K_H.

Every two weeks the frames were inspected and no bio-fouling was detected on the sensors. At each inspection the bed elevation and the sensors' distances from the bed were monitored using a differential GPS (**DGPS**-Leica GS14). DGPS data have 0,01 m data accuracy.

3.5. THE 2017 FIELD CAMPAIGN

During the period April 18 – May 15, 2017, two measuring frames were installed at the tidal flat fringing the coast of the municipality of Westhoek (sites W_L and W_H). The frames were installed for totally 27 days. At W_L the data were obtained for 25.5 days (i.e. 51 tidal cycles), whereas at site W_H for 26 days (i.e. 52 tidal cycles). The frames installed at site W_L and W_H are showed in Figures 3.5 and 3.6. The figure includes a schematic view of the deployment with an indication of the distance of each sensor from the tidal flat bed. The instruments installed at each frame are

indicated in Table 3.4.

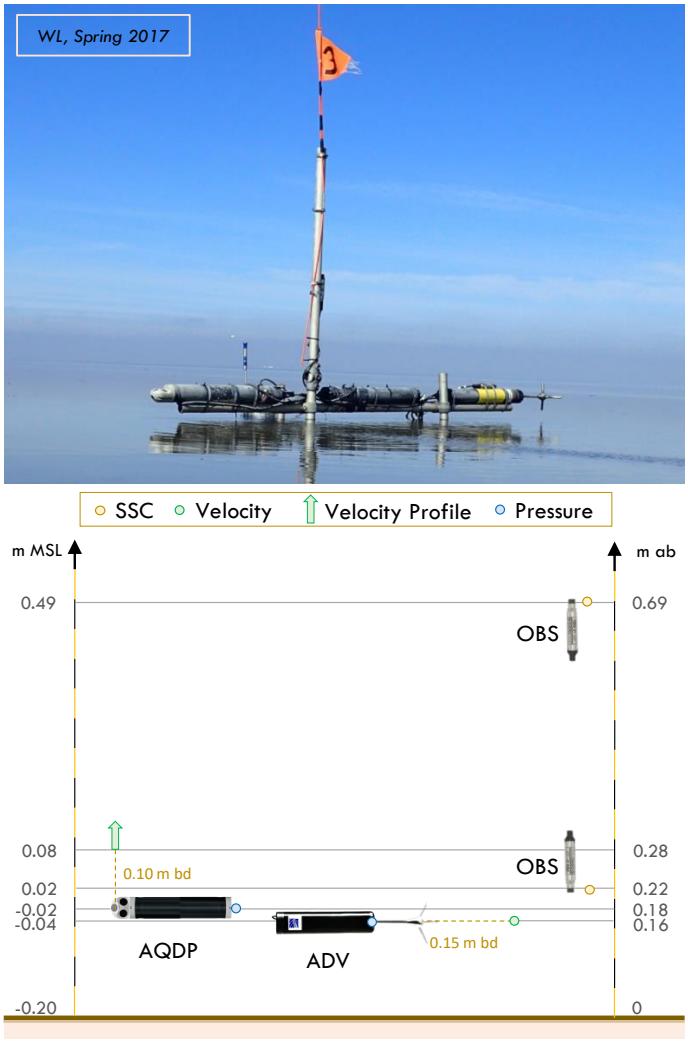

Figure 3.5: Picture and schematic representation of the equipped frame installed at site W_L (bed elevation -0.20 m MSL) during the spring **2017 field campaign**. The schematic representation includes the distance of each sensor from the tidal flat bed (with "m ab" indicating "meters above the bed") and the elevation with respect to Mean Sea Level ("m MSL"). Distances are linearly scaled (with each black/yellow bar on y–axes representing a length of 5 cm), whereas instruments size is not on scale.

Each frame included: one ADV, two OBSes and one ADCP. The frames installed in 2017 had a different design compared to the 2016's campaign, as the ADVs were installed horizontally. This choice was related to one main reason. Bed elevation at site W_H is relatively high compared to the other sites, and as a consequence the duration of inundation is on average the ~ 40% of the tidal cycle, with a mean high water depth of ~ 90 cm. Installing the instrument vertically, due to imposed blanking distance, about the 15% of the data would be lost, overall getting to less than

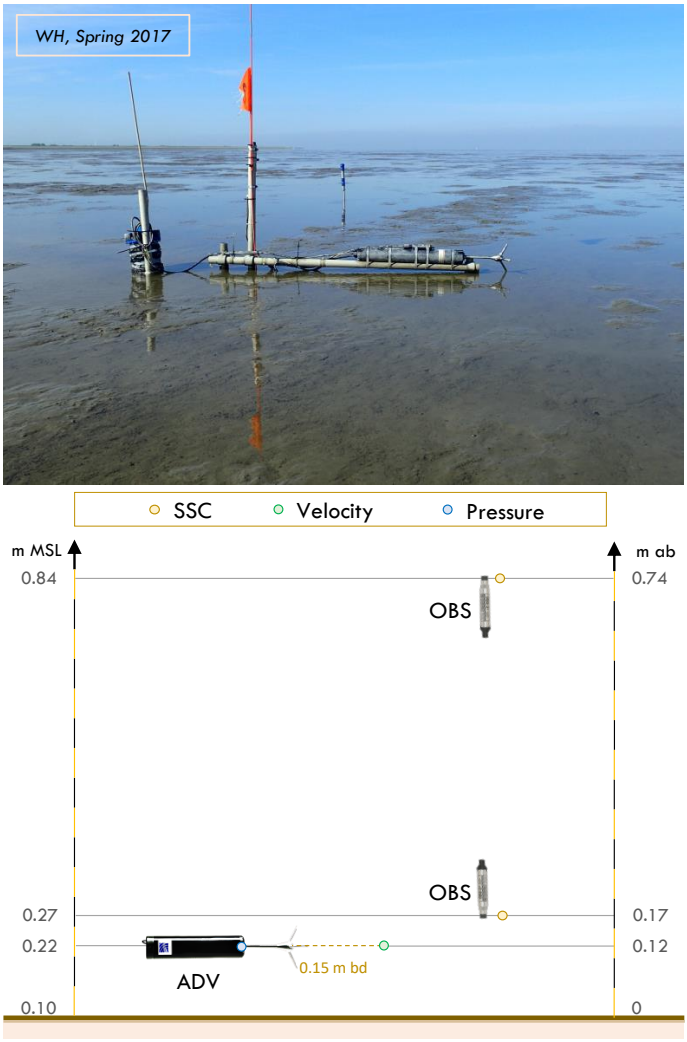

Figure 3.6: Picture and schematic representation of the equipped frame installed at site W_H (bed elevation +0.10 m MSL) during the spring **2017 field campaign**. The schematic representation includes the distance of each sensor from the tidal flat bed (with "m ab" indicating "meters above the bed") and the elevation with respect to Mean Sea Level ("m MSL"). Distances are linearly scaled (with each black/yellow bar on y–axes representing a length of 5 cm), whereas instruments size is not on scale.

25% of data, out of the full tidal cycle. Therefore the option of installing the ADVs horizontally was preferable, providing the advantage of measuring the flow velocity and the sediment concentration at 20 cm from the bottom (as in the previous campaign), still measuring the ~ 40% of the tidal cycle duration. This installation mode, did not allow for bed level measurements.

The frames included one up-ward looking AQDP. The instrument performed 3D flow velocity measurements with a resolution of 10 cm along the water column, at a frequency of 1 Hz. At each frame, two OBSes measured the SSC, respectively, at 20 cm and 60 cm above the bed. In order to

Frame	Type	Data	Freq.	Mode	Period	Tidal Cycles
W_L	ADV	$\vec{v}_{16}$, h, H	8 Hz	Continuous	Apr18–May15	51
	OBS	SSC_{22}	8 Hz	Continuous	Apr18–May15	51
	OBS	SSC_{69}	8 Hz	Continuous	Apr18–May15	51
	AQDP	$\vec{v}$, h, H	1 Hz	BI 20 min SpB 4800	Apr18–May15	51
W_H	ADV	$\vec{v}_{12}$, h, H	8 Hz	Continuous	Apr18–May15	52
	OBS	SSC_{17}	8 Hz	Continuous	Apr18–May15	52
	OBS	SSC_{74}	8 Hz	Continuous	Apr18–May15	52
	AQDP	$\vec{v}$, h, H	X Hz	BI 20 min SpB 4800	Apr18–May15	52

Table 3.4: Instruments installed at sites W_L and W_H during the **2017 Field Campaign**. Some of the configuration settings, such as the burst interval (BI) duration and number of samples per burst (SpB) are included. The subscripts '20' and '60' indicate the distance from bed at which the measurements is performed. The symbols h and H refer to water level, water depth and wave height, obtained via pressure data obtained with ADVs, AQDPs, and WGs sensors.

perform the OBS calibration procedure, 10 liters of sediment laden water were gathered in proximity of site W_H, at the end of the field campaign. After the field campaign, the OBS installed at site K_H was damaged, so that this instrument could not be calibrated. The calibration curve obtained for this instrument in the 2016 campaign, was therefore adopted (more details are provided in Section 3.7 and Annex A).

3.6. THE 2018 FIELD CAMPAIGN

During the period December 11 (2017) – February 14 (2018) one frame was installed at each investigated site: K_L and K_H at Koehool transect, W_L and W_H at Westhoek transect. The frames were hence installed for totally 61-63 days (depending on the site). The number of tidal cycles during which the measurements were performed ranges between 120 and 124 (see Table 3.5). The frames installed at Koehool and Westhoek transects are shown, respectively, in Figures 3.7 and 3.8 3.9 and 3.10. These figures include a schematic view of the deployment with representation of the sensors distances from the tidal flat bed.

The measuring frames contained one ADV, one or more (up to three) OBSes, and one ADCP. Moreover, one Wave Gauge *(OSSI-010-003C, Ocean Sensor System)* was installed in proximity of each frame. The ADVs measured the flow velocity at $\sim 20cm$ above the bed, with a frequency of 8Hz, in burst intervals of 20 minutes ad with a number of samples per burst of 4800 (equally to the 2016 campaign). The ADVs were installed vertically, therefore provided bed level changes record.

Multiple OBSes were installed at different elevations above the bed. At all sites two OBSes were installed at respectively 20 cm and 60 cm above the bed; at the less elevated site, K_L, one additional OBS was installed at 120 cm above the bed. At site W_L the OBS at 60 cm above the bed was replaced by one *Fluorometer*, performing optical measurements of turbidity using the same optical back scatter principle of OBSes. The instrument was in fact calibrated using the same procedure valid for OBSes, as detailed in Section 3.7.

The AQDPs were installed upward-looking, with the instrument transmitter close to the tidal flat bed (on average 15 centimeters above the bed). These acoustic instruments measured 3D flow velocity along the full water column, with a resolution of 10 cm.

In proximity of each frame one Wave Gauge was installed at 5 cm above the bed, with the aim

of providing further waves measurements (used to check and validate the ADV pressure measurements). These sensors were configured to measure in continuous mode with a frequency of 10 Hz.

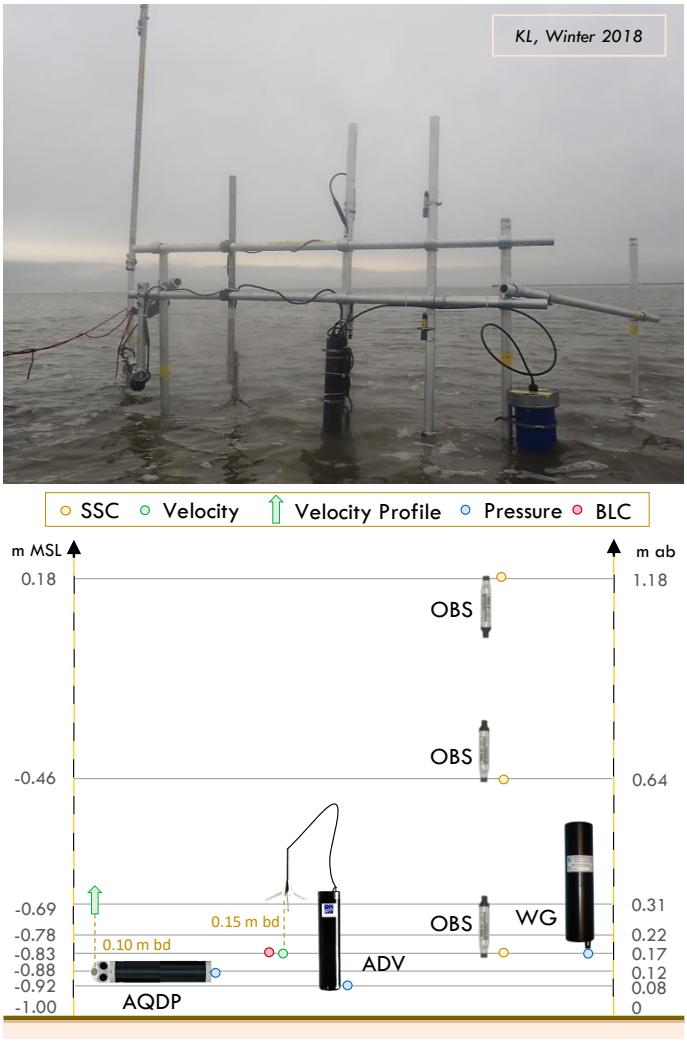

Figure 3.7: Picture and schematic representation of the equipped frame installed at site K_L (bed elevation -1.00 m MSL) during the winter **2018 field campaign**. The schematic representation includes the distance of each sensor from the tidal flat bed (with "m ab" indicating "meters above the bed") and the elevation with respect to Mean Sea Level ("m MSL"). Distances are linearly scaled (with each black/yellow bar on y–axes representing a length of 5 cm), whereas instruments size is not on scale.

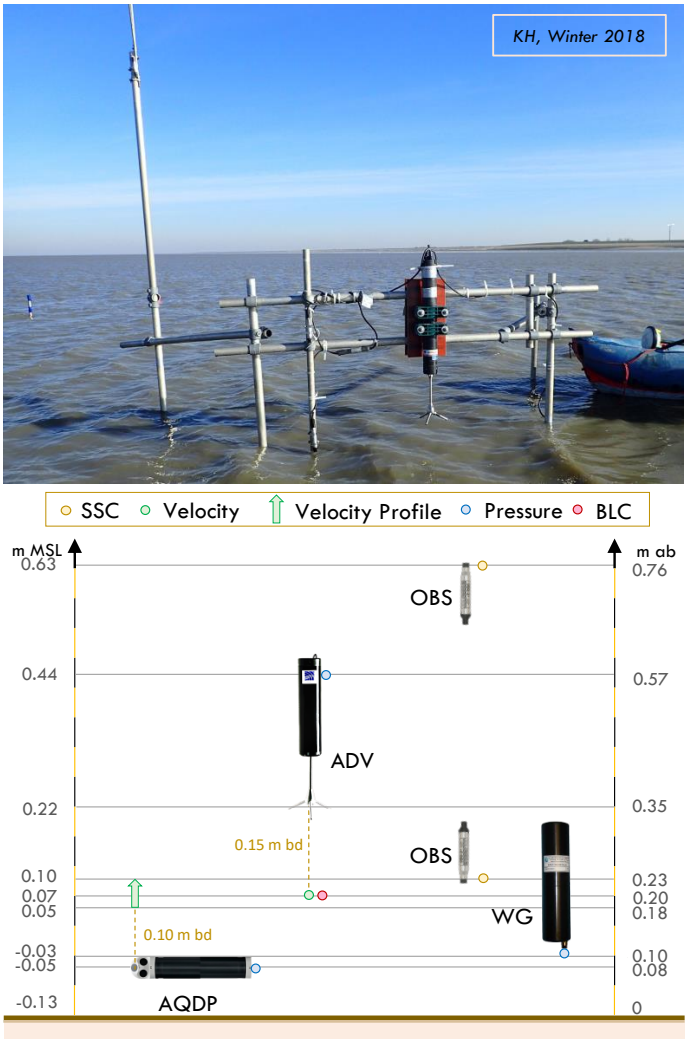

Figure 3.8: Picture and schematic representation of the equipped frame installed at site K_H (bed elevation -0.13 m MSL) during the winter **2018 field campaign**. The schematic representation includes the distance of each sensor from the tidal flat bed (with "m ab" indicating "meters above the bed") and the elevation with respect to Mean Sea Level ("m MSL"). Distances are linearly scaled (with each black/yellow bar on y–axes representing a length of 5 cm), whereas instruments size is not on scale.

3.7. DATA PROCESSING

This Section introduces the definitions and conventions adopted in our study, and describes the main steps that have been carried out in the post-processing of hydrodynamic, sediment concentration, and bed level changes data.

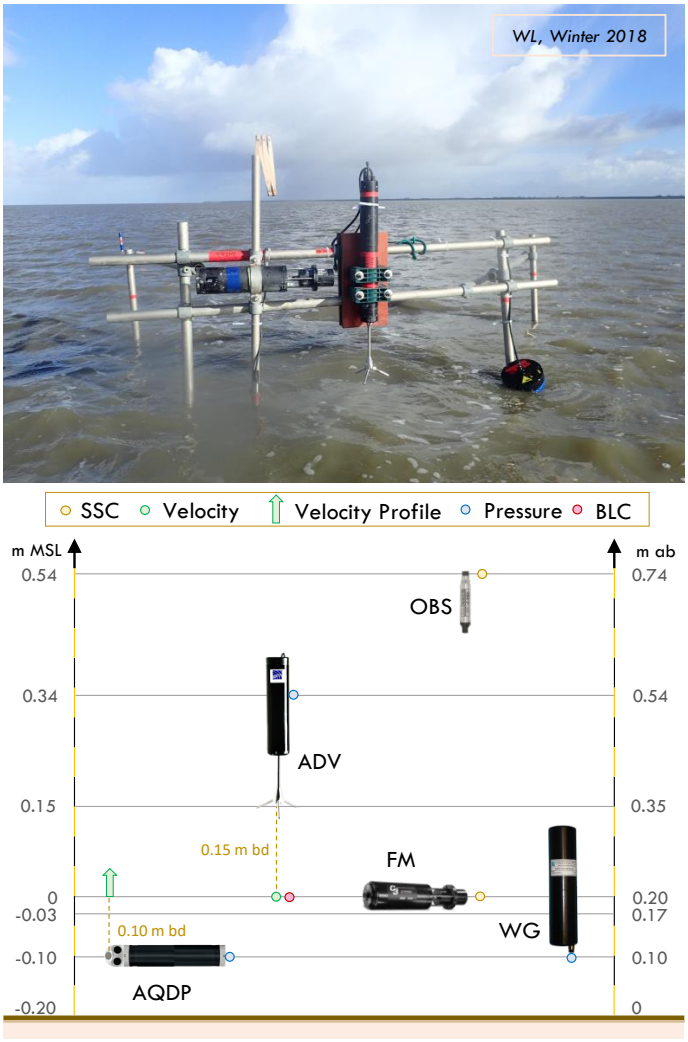

Figure 3.9: Picture and schematic representation of the equipped frame installed at site W_L (bed elevation -0.20 m MSL) during the winter **2018 field campaign**. The schematic representation includes the distance of each sensor from the tidal flat bed (with "m ab" indicating "meters above the bed") and the elevation with respect to Mean Sea Level ("m MSL"). Distances are linearly scaled (with each black/yellow bar on y–axes representing a length of 5 cm), whereas instruments size is not on scale.

DEFINITIONS AND CONVENTIONS

In this study the long-shore and cross-shore components of flow and sediment transport are estimated. We define the *long-shore* and *cross-shore* directions based on the topographic (contour) lines at the site locations (Figure 3.11).

At our sites the contour is oriented along the SW-NE axis direction (with deviations smaller than 10%at Koehool and 15% at Westhoek). Hence, we consider the flow in the SW-NE direction as long-shore flow, and the flow in the SE-NW direction as cross-shore flow. The local coordinate

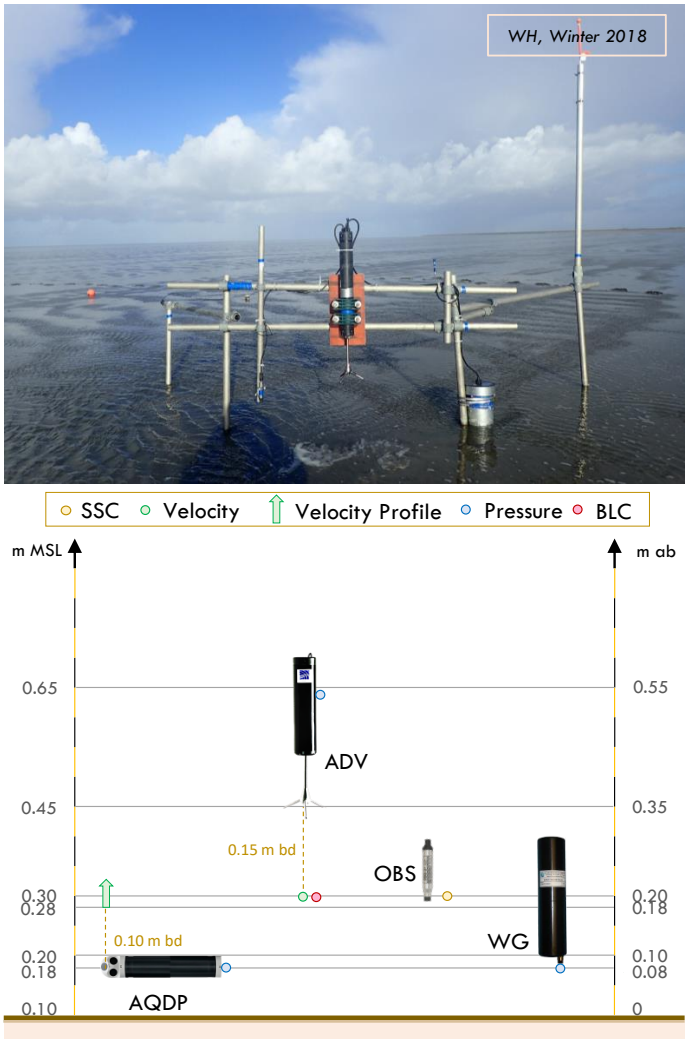

Figure 3.10: Picture and schematic representation of the equipped frame installed at site W_H (bed elevation +0.10 m MSL) during the winter **2016 field campaign**. The schematic representation includes the distance of each sensor from the tidal flat bed (with "m ab" indicating "meters above the bed") and the elevation with respect to Mean Sea Level ("m MSL"). Distances are linearly scaled (with each black/yellow bar on y–axes representing a length of 5 cm), whereas instruments size is not on scale.

system is shown in the upper left panel of Figure 3.11. In the long-shore direction, the flow is up-channel during flood and down-channel during ebb. In the cross-shore direction, the flow is onshore-directed during flood and offshore-directed during ebb.

In the following sections we use the terms "reversed flood" and "reversed ebb". We define a "reversed flood" as a period with rising water and with down-channel long-shore flow and offshore-directed cross-shore flow. Vice versa, we define a "reversed ebb" as a falling-water period with up-channel long-shore flow and onshore-directed cross-shore flow.

Frame	Type	Data	Freq.	Mode	Period	Tidal Cycles
K_L	ADV	$\vec{v}_{17}$, h, H, BLC	8 Hz	BI 20 min SpB 4800	Dec12-Feb14	124
	OBS	SSC_{17}	8 Hz	Continuous	Dec12-Feb14	124
	OBS	SSC_{64}	8 Hz	BI 20 min SpB 4800	Dec12-Feb14	124
	OBS	SSC_{118}	8 Hz	BI 20 min SpB 4800	Dec12-Feb14	124
	AQDP	$\vec{v}$, h, H	X Hz	BI 20 min SpB 4800	Dec12-Feb14	124
	WG	h, H	10 Hz	Continuous	Dec12-Feb14	124
K_H	ADV	$\vec{v}_{20}$, h, H, BLC	8 Hz	BI 20 min SpB 2400	Dec12-Feb14	122
	OBS	SSC_{23}	8 Hz	Continuous	Dec12-Feb14	122
	OBS	SSC_{76}	8 Hz	BI 20 min SpB 2400	Dec12-Feb14	122
	AQDP	$\vec{v}$, h, H	X Hz	BI 20 min SpB 4800	Dec12-Feb14	122
	WG	h, H	10 Hz	Continuous	Dec12-Feb14	122
W_L	ADV	$\vec{v}_{20}$, h, H, BLC	8 Hz	BI 20 min SpB 2400	Dec12-Feb14	120
	OBS	SSC_{20}	8 Hz	Continuous	Dec12-Feb14	120
	FM	SSC_{74}	8 Hz	BI 20 min SpB 2400	Dec12-Feb14	120
	AQDP	$\vec{v}$, h, H	X Hz	BI 20 min SpB 4800	Dec12-Feb14	120
	WG	h, H	10 Hz	Continuous	Dec12-Feb14	120
W_H	ADV	$\vec{v}_{25}$, h, H, BLC	8 Hz	BI 20 min SpB 2400	Dec12-Feb14	120
	OBS	SSC_{20}	8 Hz	BI 20 min SpB 2400	Dec12-Feb14	120
	AQDP	$\vec{v}$, h, H	X Hz	BI 20 min SpB 4800	Dec12-Feb14	120
	WG	h, H	10 Hz	Continuous	Dec12-Feb14	120

Table 3.5: Instruments deployed at the four measuring sites during the **2018 Field Campaign**. Some of the configuration settings, such as the burst interval (BI) duration and number of samples per burst (SpB) are included. The subscripts '20' and '25' indicate the distance from bed at which the measurements were performed. The symbols h and H refer to water level, water depth and wave height, obtained via pressure data obtained with ADVs, AQDPs, and WGs sensors. SSC indicates "Suspended Sediment Concentration", whereas "BLC" indicates "Bed Level Changes".

The standard nautical definition is used for the wind direction, e.g. SW wind indicates wind blowing from the SW towards the NE direction.

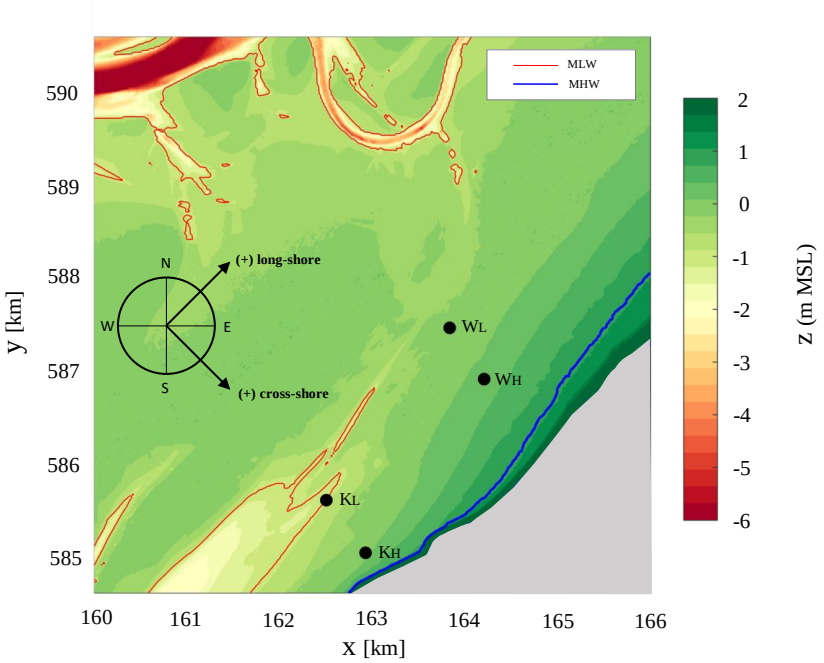

Figure 3.11: Definition of local long-shore and cross-shore direction adopted for flow and sediment transport. The land colour in the bathymetry indicates land. The MLW and MHW lines are indicated in red and blue colour, respectively. The provided coordinates refer to the RD-System.

FLOW VELOCITIES

Flow velocity measurements were performed using ADVs and ADCPs. The data were first despiked using the methodology proposed by *Goring and Nikora* (2002), applying threshold values of 70% for beam correlation and 100 counts for signal amplitude. Both the ADV and the ADCP measure the flow velocity along the direction of the three receiving beams. The orientation of the receiving beams with respect to the North direction has been measured in the field. With a change in coordinate system, the flow velocity in the ENU (East-North-Up) system was computed.

WATER DEPTHS

The pressure variation – detected by ADVs, ADCPs and Wave Gauges – includes the pressure related to changes in water levels, as well as changes in local air pressure. The signals were hence corrected using the air pressure variation measured at the KNMI (*Koninklijk Nederlands Meteorologisch Instituut*) meteorological station of Leuwaarden, situated about 20 km inland from the study site. An harmonic analysis (with the methodology proposed by *Codiga* (2011)) has been performed on the water levels measured at the tidal gauge installed at the Port of Harlingen.

WAVES

The pressure signals obtained with the ADV, combined with the flow velocity signals, were used to perform a *directional wave spectral analysis*. The pressure signals obtained from the Wave Gauges were used instead to perform a *non-directional wave spectral analysis*. Although the first analysis provides more detailed information (such as the direction between currents and waves), it is

only available for a reduced part of the tidal cycle. In fact, the ADV pressure sensors were located at relatively large distance from the seabed (up to 55 cm), due to the constraint of measuring the velocity at 20 cm from the seabed (see Figure 3.2). In contrast, the Wave Gauges provide less information but, given the reduced distance of the sensors from the bed (i.e. 5 cm) this information is available almost for the full period in which the bed is submerged. Therefore, the wave heights and wave periods resulting from the directional analysis were used only were strictly needed for specific analysis (e.g. the combined wave-current bed shear stress). The wave parameters obtained from the non-directional wave spectral analysis, more specifically the significant wave height and the mean period of the 33% highest waves, are used in our analysis.

BED LEVEL CHANGES

The ADVs measured the flow velocity, at a frequency of 8 Hz, either continuously or in burst intervals of 5-20 minutes. When the ADV operates in burst mode, the distance of the probe from the seabed at the end of each burst is recorded, providing a bed level observation once every 5-20 minutes. This bed level change track method applies only if the acoustic signal transmitter points the bed, i.e. when the ADV is installed vertically (2016, 2018 field campaigns). The bed level change signals were smoothed using a 40 minutes running mean.

SEDIMENT GRAIN SIZE

Sediment samples were gathered nearby each measuring frame during the 2018 winter field campaign. The upper 5 cm samples were analyzed to extract bed sediment grain size using a Malvern Mastersizer 2000. This instrument uses laser diffraction to measure particle sizes in the range 0.1 μm - 3 mm. The D_{50} resulting from the granulometric analysis have been reported in Table 3.2.

SUSPENDED SEDIMENT CONCENTRATIONS

Suspended sediment concentration was measured at several elevations above the tidal flat bed using *Optical Back Scatter* (OBS) sensors. The OBS sensors were calibrated in laboratory, using sediment-laden water samples collected in the field. The 10 l samples were collected:

- in proximity of site K_H after the completion of the 2016 field campaign;
- in proximity of site W_H after the completion of the 2017 field campaign;
- in proximity of site K_H after the completion of the 2018 field campaign.

The samples were collected while holding a sample at $\sim 30cm$ above the bed, and simultaneously inducing sediment resuspension by eroding the upper seabed layers. The procedure in laboratory included synchronized OBS measurements (in a 8 litres calibration bowl) and sample filtration through 0.45 μm pore filters (*Merckelbach*, 2006). From 20 to 30 dilution steps were carried out. At each step a sample of 500 ml of the sediment-laden water was extracted from the calibration bowl and replaced by 600 ml of clear water. Through this process, the initial sediment-laden water was reduced to an almost clear-water. After each dilution step the OBS signals (stored as *Voltage*) were collected for a 5-minute period and during this period, a 100 ml sample was taken in proximity of the optical sensors. These samples were filtered and the filters were dried for 24 h in an oven at 105 °C. The filters were weighted before and after the filtration procedure so that, given the volume of the sample (100 ml) the sediment concentration (in g/l) was estimated. The so obtained calibration curves are shown in Figure 3.13 for the calibration performed in May 2016 (directly after the instruments' retrieve). The relation between SSC (in g/l) and OBS signal (in mV) shows a linear relationship up to 1 g/l (averaged $R^2 \approx 0.97$); a quadratic regression instead, can better describe the relationship for SSC higher than this threshold (averaged $R^2 \approx 0.94$). In Annex A the calibration curves obtained for the optical instruments installed in the 2017 and 2018 field campaigns are reported.

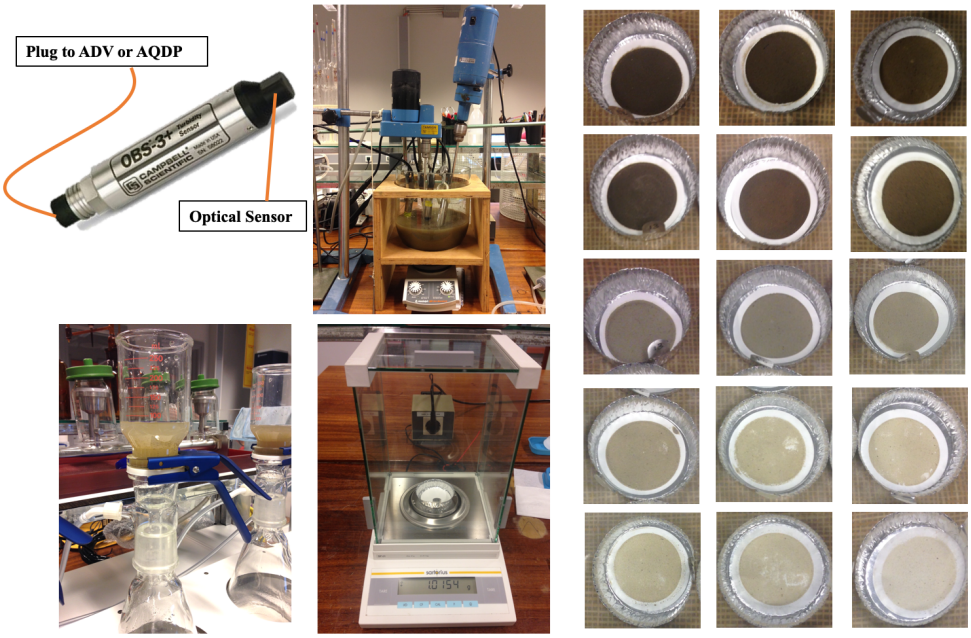

Figure 3.12: Photographs from OBS Calibration procedure carried out in laboratory. On the top left, OBS sensor with indication of its connecting plug and optical sensor position. On its right, the calibration bowl, where sediment is stirred up and OBS sensors are submerged into the sediment-laden water. Bottom panels: filtering system and precision balance. Right panels: some of the filtered sediments, at decreasing concentrations, after the oven-induced drying process.

The uncertainty of the SSC obtained with OBS sensors, i.e. the ±10% of the measured data (Scientific Campbell OBS-3+), is related to several factors. Firstly, the optical sensors responds differently to different sediment sizes (e.g. *Conner and De Visser*, 1992; *Merten et al.*, 2014; Scientific Campbell OBS-3+; *Fettweis et al.*, 2019; *Pearson et al.*, 2021). At the investigated mudflats, the sediment is finer - as expected - at the more elevated sites (the smallest D_{50} = 13μm measured at site W_H), and increases in size for decreasing bed elevations (the highest D_{50} = 123μm measured at site K_L). For the 2016, 2018 measurement campaigns, the calibration procedure was realized using sediment-laden water samples collected at site K_H (D_{50} = 30μm), whereas for the 2017 field campaign the samples were collected at size W_L. As a consequence, the OBS installed at the lower mudflats (K_L, W_L) and those installed at the most elevated site (W_H) were calibrated using sediments that were, respectively, finer and coarser compared to the sediment actually found at those sites. As the OBS sensors "see" better the fine compared to the coarse sediments, the SSC reported for sites K_L and W_L (or K_H) might be larger (or smaller) than the obtained data.

Secondly, the OBS sensors are sensitive to other sediment properties, such as particle shape, flocks' density and sediment "color" (the latter, affecting the near-infrared reflectivity (e.g. *Druine et al.*, 2018; Scientific Campbell OBS-3+)). This variability of the sensor's output with sediment proprieties results in an intra-tidal variability of the uncertainty on SSC data related to e.g. advection, resuspension and flocculation (*Lin et al.*, 2020). Eventually, the presence of phytoplankton blooms (*Downing*, 2006) and of organic matter (*Bunt et al.*, 1999) are also captured by the optical

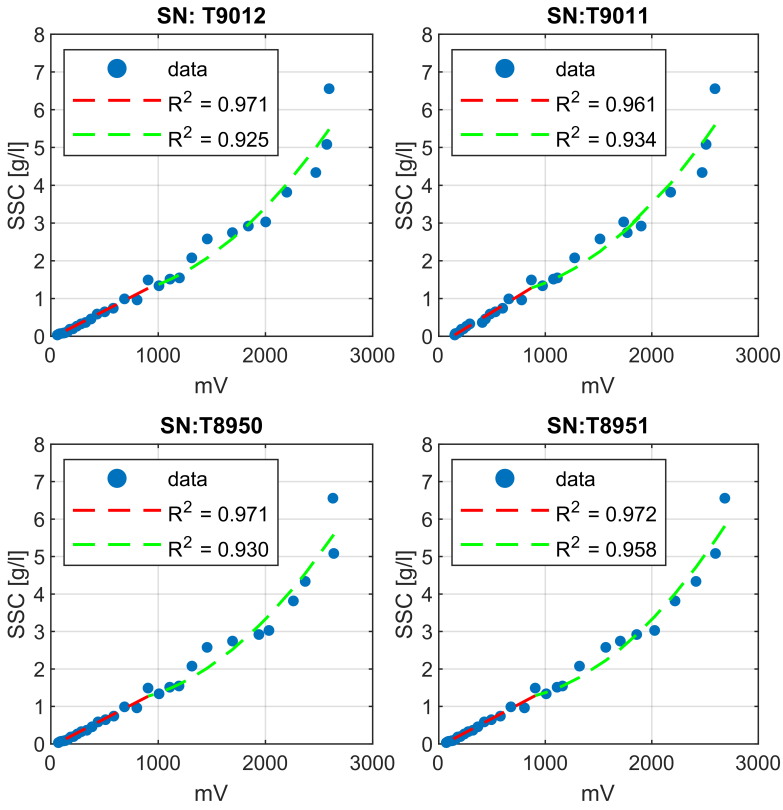

Figure 3.13: OBSes Calibration curves, **Field Campaign 2016**. The panel's title indicate the Serial Number (SN) of the OBS sensors. A linear fit is adopted for SSC< 1g/l, whereas a quadratic fit is adopted for SSC higher than this threshold.

sensors. Additional measurements, aimed at quantifying the relative importance of each of these factors, in the specific setting, would imply reduced inaccuracies in the SSC data.

The OBS calibration procedure requires specific attention to avoid further sources of error. The instrument has to be preferably calibrated directly before or after the field investigation, as these instruments change "behaviour" - even in relatively short time periods (e.g. months) - due to a number of factors, including a decreasing efficiency of the receiving sensors (*Downing*, 2006). It is further required that the mechanical mixing in the calibration bowl is efficient enough to avoid sediment accumulation at its bottom. The OBS sensors should be positioned, in the calibration bowl, in such a way that the interference's among them are minimized. Eventually, each OBS, during the calibration procedure, is advised to be connected to the same analog-door of the Datalog (i.e. the ADV) as the one used during the field measurements (Scientific Campbell OBS-3+).

The OBS-3+ Campbell sensors are limited to deployments in sites where the SSC is lower than 10 g/l in case of muddy environments, and lower than 100 g/l in case of sandy environments, corresponding to a maximum turbidity of ~ 4000NTU. In mixed environments, the combination of optical and acoustic instruments is preferred to quantify the contribution of the different grain

sizes to the SSC (e.g. *Pearson et al.*, 2021). In the 2017 field campaign, we calibrated the OBS up to a maximum SSC of ~ 30 g/l, to check the response of our optical sensors to sediment concentrations higher than the 10 g/l threshold. The results are shown in Figure 3.14. The same relation between SSC and NTU was found by *Lin et al.* (2020). The backscatter intensity decreases exponentially, with increasing SSC, when a certain voltage threshold is reached. This values differs per instrument; the instrument manual (i.e. Scientific Campbell OBS-3+) indicates turning points at 10 g/l corresponding to 4000 mV. In our cases the calibration curves reaches the 10 g/l, and hence turn, around 2500-3000 mV. As indicated by *Lin et al.* (2020) the combination of acoustic and optical measurements allows to overcome this ambiguity. In this work such combination between signal and acoustic signals was not performed. The OBS signals during our field measurements however, did overcome the 3000 mV during less than 2% of the total measurement time. The corresponding SSC values in g/l have been extrapolated using the linear or quadratic fits obtained using the calibration data-points up to 10 g/l.

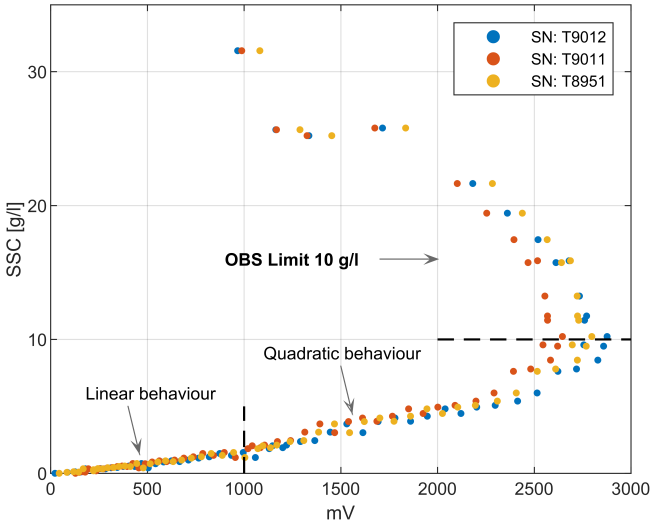

Figure 3.14: OBS Calibration curves, **Field Campaign 2017**. The calibration was pushed above the OBS limit of 10 g/l to check the sensor's behaviour beyond such threshold.

3.8. PUBLIC DATA

Publicly available data were also used to support the analyses. Wind data have been widely used in this dissertation. We analysed data from two meteorological stations. The first is *Noorderbalgen* meteorological station, located in the Wadden Sea (Lat: 53.365742°N; Long: 5.384852°E – WGS84), approximately 20 km offshore to the study site, in proximity of Terschelling barrier island. This data was available from November 2008 until March 2018, with a frequency of 10 minutes. The second is *Leeuwarden* meteorological station (Lat: 53.216667°N; Long: 5.766667°E – WGS84) located about 20 km inland to the study sites. These data were available for a much longer period (1990 to 2019) with a one hour frequency. The analyses on the two dataset provided almost identical results, so we present, in this thesis, the wind data obtained from the *Leeuwarden*, as we used also other types of data gathered at this meteorological station. Air pressure data from the meteorolog-

ical station of *Leeuwarden*, have been used to correct the signal gathered by the pressure-sensors from the local air pressure variations (as detailed in Section 3.7). Processed bathymetry data were available via the *Vaklodingen* dataset. Eventually, the water level data gathered at Harlingen tidal gauge (situated in the Harbour, Lat: 53.166667°N; Long: 5.4°E – WGS84) have been used to validate our water level data. The publicly available data used in this dissertation were made available by the by *Koninklijk Nederlands Meteorologisch Instituut, KNMI* and by *Rijskwaterstaat*, i.e. the *Dutch Ministry of Water and Environment.*

About the Photo

The photo shows a micro ridge-runnel system on the upper Westhoek intertidal flat, near the groins. It was taken on May 14, 2017, during a field visit to check the instrumentation.

Explore more media content using the following QR-code.

4

WIND EFFECTS ON INTERTIDAL FLATS HYDRODYNAMICS

The hydrodynamic forcing on intertidal flats is a combination of a deterministic tidal (astronomical) component and a stochastic (meteorological) component. The former induces the daily and spring-neap variations in water levels and flow velocities. The latter includes the wind forcing, interacting through diverse processes with the tidal forcing. Field observations show that wind-driven flows interact with tide-induced flows, overall controlling the direction of residual flows also at relatively low wind speeds. Based on field data, in this chapter, we formulate the first analytical model that predicts the residual flow velocity resulting from the interaction between tide– and wind– driven currents across intertidal flats. The presented results show that the effect of wind-driven flows over the residual flow increases for decreasing tidal flow amplitudes. Model and observations demonstrate that, overall, the wind-induced reversal of the tidal flow is a relatively common phenomenon in (especially shallow) intertidal areas.

Parts of this chapter have been published as: *Colosimo et al. (2020).* The Impact of Wind on Flow and Sediment Transport over Intertidal Flats. Journal of Marine Science and Engineering.
Co–authors: P.L.M. de Vet, D.S. van Maren, Ad J.H. Reniers, J.C. Winterwerp, B.C. van Prooijen

Ch 4: Wind Effects on Intertidal Flats Hydrodynamics

Main Research Question

RQ 1: What is the role of wind on residual and tidal flows over intertidal flats?

Keypoints

Keypoint 1: The effect of wind on the tidal flow increases (decreases) for decreasing (increasing) tidal flow amplitudes.

Keypoint 2: The effect of the wind on the tidal flow depends on the Eulerian asymmetries in the astronomical signal and affects the Eulerian asymmetries in the meteorological signal.

Keypoint 3: Wind-induced reversal of the tidal flow is a relatively common phenomenon.

Implications for Fine Sediment Nourishments

A model-based residual flow prediction is key when designing fine sediment nourishments. An accurate modeling of the horizontal residual flow should include, among other processes, the non-linear interaction between tidal currents and wind–driven flows.

4.1. INTRODUCTION

Sustainable application of soft engineering methods for coastal protection, such as a Mud Motor type of nourishment, requires a thorough understanding of its effectiveness (i.e. morphological change). Morphological changes are a consequence of spatial gradients in sediment fluxes (*Wang et al.*, 2012; *Daidu et al.*, 2013) and result from a number of interacting sediment transport processes. These processes depend on hydrodynamic forcing, sediment properties, and biogenic influences (*Van Straaten*, 1961). Forecasting the effectiveness of a Mud Motor (or even understanding the executed pilot) therefore requires detailed knowledge of the hydrodynamic processes.

The hydrodynamic forcing is a combination of a deterministic tidal (astronomical) component and a stochastic (meteorological) component. The former induces the daily variation and spring-neap variations in water level and flow velocity. The latter includes the wind forcing. The action of wind on the sea surface results in water level gradients (set-up/down) inducing large-scale circulation patterns (especially in enclosed or semi-enclosed systems such as coastal lagoons or estuaries). Wind blowing on the sea surface also generates wind-waves, which induce turbulence resulting in sediment resuspension from the seabed. Wind waves interact with the (tide- and wind-induced) currents, modifying the bed roughness and ultimately affecting the bed shear stress induced by the flow (*Faria et al.*, 1998; *Soulsby and Clarke*, 2005). Furthermore, wind-driven flows are related to wind induced shear stress penetrating the water column.

While the combined effect of wind events and tides has received significant attention in the scientific literature, e.g. *Le Hir et al.* (2000); *Bassoullet et al.* (2000); *Carniello et al.* (2011); *Friedrichs* (2012); *Mariotti and Fagherazzi* (2013); *Green and Coco* (2014); *Zhu et al.* (2017), the studies focused primarily on the relative impacts of wave-induced erosion and tide-induced deposition. However, the role of wind-driven flows, and especially the interaction between tidal currents and wind-driven flow, has received much less attention in the scientific literature. It has been demonstrated that wind-driven flows affect the tide-induced velocities and suspended sediment concentrations on the Belgian inner shelf (thereby influencing the position of the turbidity maximum (*Baeye et al.*, 2011)). Observations by *Christiansen et al.* (2006), *Talke and Stacey* (2008) and *Mariotti and Fagherazzi* (2011), demonstrate that different meteorological conditions generate asymmetries in the intratidal sediment transport. In multi-inlet lagoons such as the Wadden Sea, the wind-induced fluxes result in water and sediment exchange over the tidal divides, leading to an inter-connected morphodynamic evolution of the adjacent tidal basins (*Duran-Matute et al.*, 2014; *Sassi et al.*, 2015). However, even though these studies demonstrate the importance of wind-driven flows, it remains unclear how wind-driven flows interact with tidal currents, and how this interaction subsequently impacts residual sediment transport.

In this chapter, field data is used to develop an analytical model that predicts the horizontal flow velocity resulting from the interaction between tide- and wind-generated currents across an intertidal flat. The following chapter (Chapter 5), unravels the consequences of such interaction on the suspended sediment concentration and suspended sediment transport.

4.2. METHODOLOGY

4.2.1. GENERAL APPROACH

Chapter 3 described the three extensive fieldwork campaigns carried out on two adjacent mudflats (Koehool, Westhoek) fringing the Dutch Western Wadden Sea (from 2016 to 2018). In this chapter, the interaction between the hydrodynamic forcing at sites K_L and K_H is first analyzed during spring weather conditions based on data collected in 2016. This data is used to develop an analytical model that simulates the interaction of hydrodynamic forcing(s) at different tidal flat elevations, published in *Colosimo et al.* (2020).

This chapter expands on the published results by validating the developed model with data

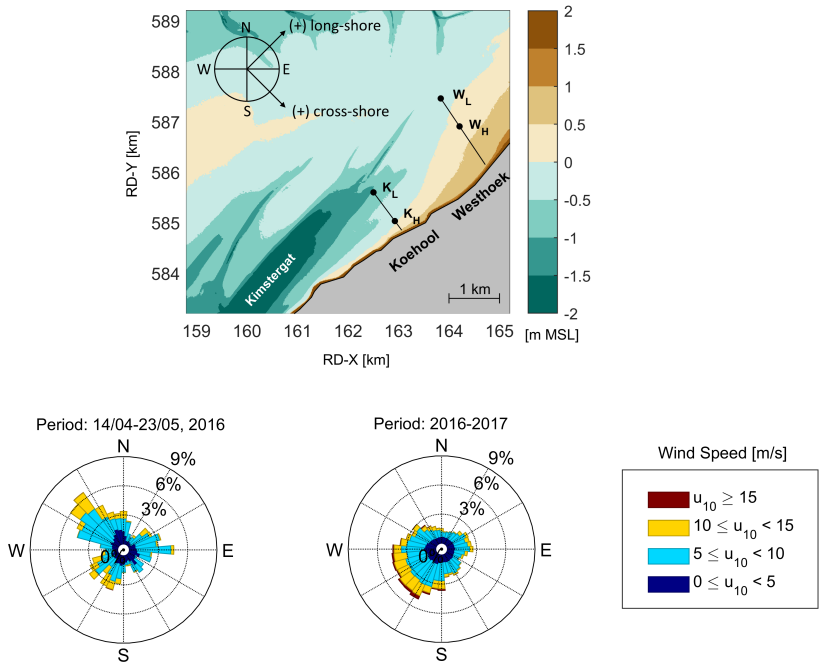

Figure 4.1: Study sites and wind forcing.**[a]** Measuring sites along the two transects: lower and higher Koehool mudflat frames (K_L, K_H), lower and higher Westhoek mudflat frames (W_L,W_H). The 2017 data is used for the bathymetry map. Sign convention adopted for long-shore and cross-shore flow and transport direction is included. **[b]** Wind roses referring to the 2016 deployment period (April 14, May 22) and to the period January 2016 – December 2017.

collected during the 2017 and 2018 field campaigns, more specifically the flow velocity point measurements gathered with ADVs. Moreover, as the 2017 and 2018 dataset included also flow velocity observations through the full water depth (AQDP data), the results presented in *Colosimo et al.* (2020) were further updated. Sections 3.4, 3.5 and 3.6, provided pictures and schematic views of the frames' instrumentation set-up. In this section we provide, with Figure 4.1, the indication of the four measurement sites over the bathymetry map and, because wind data is broadly used in this chapter, we include here the wind roses of the spring 2016 measurement period and of the two year-long period 2016–2017.

4.2.2. BED SHEAR STRESS INDUCED BY WAVE–CURRENT INTERACTION

The analytical model (detailed in Section 4.4.2) is forced by a bed shear stresses generated by waves and currents. In this dissertation the bed shear stress resulting from the combined action of waves and currents is estimated using the wave-current-interaction (WCI) model proposed by *Soulsby* (1995). The mean bed shear stress resulting from the interaction of currents and waves is defined as:

$$\tau_m = \tau_c \left[1 + 1.2 \left(\frac{\tau_w}{\tau_c + \tau_w} \right)^{3.2} \right] \tag{4.1}$$

with τ_c current-induced shear stress, and τ_w wave-induced shear stress. The usage of the mean bed shear stress as expressed in Equation 4.1 is suitable when estimating the effect of waves on the

current-induced flow, (e.g. *Faria et al.*, 1998).

The current-induced shear stress is estimated as:

$$\tau_c = \rho_w c_{f_c} u^2 \tag{4.2}$$

with c_{f_c} the current-related friction coefficient and $u = (u_x, u_y)$ the flow velocity magnitude. The bed friction coefficient depends on the roughness height z_0:

$$\frac{1}{\sqrt{c_{f_c}}} = \frac{1}{\kappa}\left(\ln\left(\frac{h}{z_0}\right) - 1\right) \tag{4.3}$$

The estimation of the roughness height z_0 is not straightforward, as it depends on the skin friction (sediment diameter), on the presence of bed forms (e.g., current and wave induced ripples), on the hydrodynamics, and among other factors, on sediment stratification (e.g. *Soulsby et al.*, 1993; *Faria et al.*, 1998; *Fan et al.*, 2019). Values of the current related friction coefficient c_{f_c} available in literature suggest a variability of the parameter in the range 0.001–0.004, (e.g. *on Hydromechanics of the Hydraulics Division*, 1963; *Sternberg*, 1968; *Soulsby et al.*, 1993; *Soulsby*, 1995; *Faria et al.*, 1998; *Verney et al.*, 2006; *Pascolo et al.*, 2018; *Fan et al.*, 2019). A value of 0.002 has been selected, based on which the roughness length z_0 has been estimated along the full measurement period, as a function of water depth (Equation 4.3). The so-estimated z_0 values are one order of magnitude higher than the values obtained from a definition based on the grain size only (e.g., $z_0 = \frac{k_s}{30} = D_{50}/12$).

The wave-induced shear stress is estimated based on the wave-friction factor f_w and the wave orbital velocity at the bottom U_δ:

$$\tau_w = \frac{1}{2}\rho_w f_w {U_\delta}^2 \tag{4.4}$$

The wave orbital velocity is estimated using the linear wave theory:

$$U_\delta = \frac{\pi H}{T} \cdot \frac{1}{\sinh(kh)} \tag{4.5}$$

The wave number k is obtained by resolving the dispersion relationship using a polynomial approximation, based on the measured water depth and mean wave period following *Hunt et al.* (2015). The wave friction factor f_w is estimated using the formulation proposed by *Soulsby and Clarke* (2005):

$$f_w = min\left[0.3, 1.39\left(\frac{U_\delta T}{2\pi z_0}\right)^{-0.52}\right] \tag{4.6}$$

where z_0 is the bed roughness.

4.3. RESULTS

4.3.1. FULL-PERIOD TIME SERIES

The time series of wind speed and direction, water depth, long-shore and cross-shore flow velocity and significant wave height are shown in Figure 4.2 for the lower mudflat (K_L) and in Figure 4.3 for the higher mudflat (K_H).

The average wind speed (Figure 4.2[a] or Figure 4.3[a]) was 7 m/s, and the mean of the 5% highest values was 14 m/s. The maximum wind speed was 16 m/s and it occurred in SW wind direction. The dominant wind direction during the measurement period was NW, and the maximum wind speeds (16.4 m/s) had SW wind direction. Based on the wind roses in Figure 4.1, it is noticed that along a year instead, the dominant wind direction is SW.

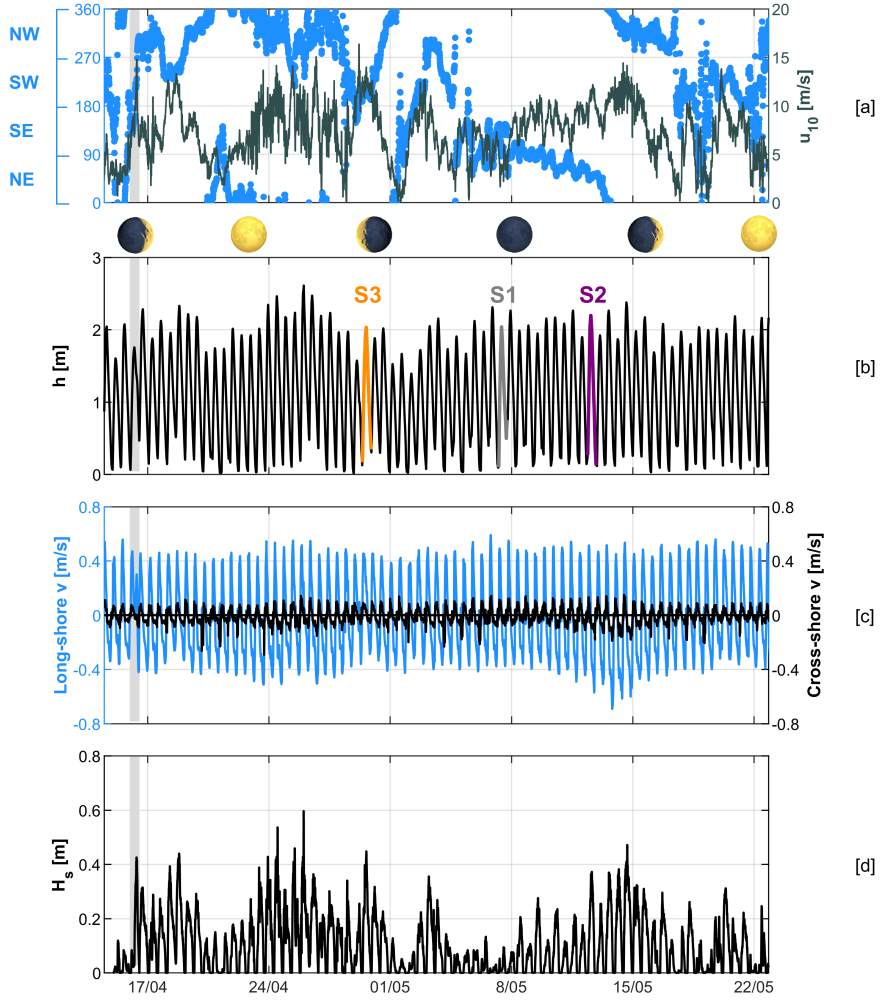

Figure 4.2: Time series at the lower mudflat (K_L): [**a**] Wind speed and direction; [**b**] Water depth (moving mean over 10-min intervals); [**c**] Long-shore and cross-shore flow velocities; [**d**] Significant wave height. Spring-neap variations are indicated by the moon phases. The gray bands indicate the tides affected by the wind-induced reversal of ebb flow. The tides indicated by S1, S2, and S3 are used in Section 4.3.2 to analyze the intratidal variations during three different wind scenarios.

The water depth (Figures 4.2[b] and 4.3[b]) depends on the tide and on a wind-induced water level set-up. Increased water levels occur for example in the period 24–28 April for NW wind of ~13 m/s.

The tidal flow amplitude (Figures 4.2[c] and 4.3[c]) is ~0.5 m/s at K_L and ~0.25 m/s atK_H. The flow at K_L is mainly directed in the long-shore direction (NE–SW). The cross-shore component magnitude (SE–NW) is ~20% of the long-shore flow. At K_H, the cross-shore component is much larger (both relatively and absolutely), with a magnitude comparable to the long-shore flow

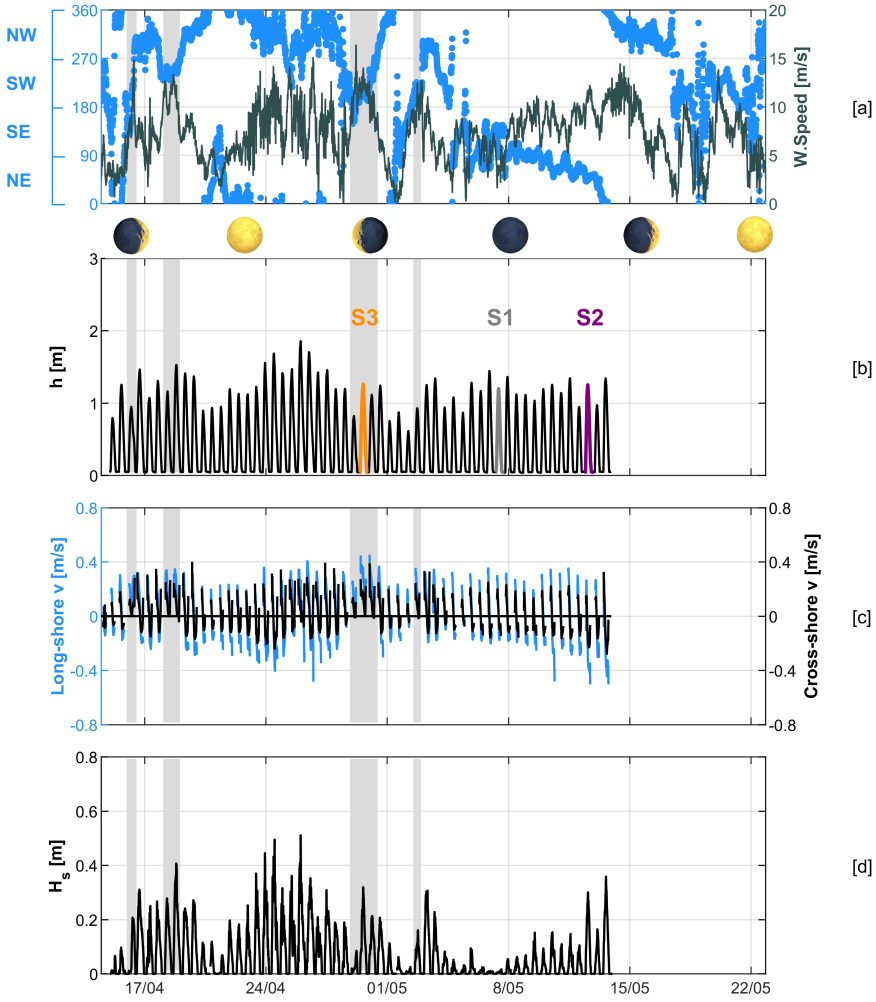

Figure 4.3: Time series at the higher mudflat (K_H): [**a**] Wind speed and direction; [**b**] Water depth (moving mean over 10-min intervals); [**c**] Long-shore and cross-shore flow velocities; [**d**] Significant wave height. Spring-neap variations are indicated by the moon phases. The gray bands indicate the tides affected by the wind-induced reversal of ebb flow. The tides indicated by S1, S2, and S3 are used in Section 4.3.2 to analyze the intratidal variations during three different wind scenarios.

velocity component. In Figure 4.3[c] the large variations in flow velocity are evident: the flow is not necessarily flood-directed (positive) and then ebb-directed (negative) during each tidal cycle. During several periods of falling water (i.e., during ebb), the flow remains up-channel (i.e., flood-directed). These reversed ebb flow conditions are caused by wind-driven flow and occur during wind from the SW (i.e., wind parallel and opposite to the ebb flow). The reversal conditions are highlighted in Figures 4.2[a],[c] and 4.3[a],[c] by gray colored bands. In particular, Figure 4.3[c] shows that the tidal flow was up-channel during three consecutive tidal cycles (29–30 April). This

wind-induced reversal of the ebb flow occurred during 17% of the monitored period at the higher mudflat (K_H) but only once (1.3% of the time) at the lower mudflat (on 16 April).

Maximum wave heights were observed during maximum water levels (Figures 4.2[d] and 4.3[d]), resulting from a larger fetch (related to the submergence of the shoals) and weaker bed friction at larger depths. The highest significant wave height was 0.6 m on both sites. The wave conditions are dominated by the local wind, because the barrier islands shelter the study area from North Sea (swell) waves.

4.3.2. WIND-INDUCED TIDAL FLOW REVERSAL

In order to isolate the effects of wind on the tide-induced flow, we selected three representative wind scenarios: one scenario with weak wind (S1, $u_{10} < 5$ m/s) and two scenarios with long-shore directed wind, i.e., NE wind (S2, ebb directed) and SW wind (S3, flood-directed). The latter two scenarios exhibit the wind-effects on the flow when the tidal and wind forcing(s) are aligned. These three scenarios occurred on May 7 (S1), May 12 (S2), and April 29 (S3), respectively, as indicated in Figures 4.2 and 4.3 and detailed at intratidal time scale in Figures 4.4 and 4.5. Scenario S1 is characterized by the formation of a standing wave, with maximum flow velocities during maximum gradients in water level (generally occurring when the water level is around MSL). Flood velocities are generally higher than ebb velocities and the falling water phase lasts longer (8 h) than the rising water phase (4 h). This implies a peak flow asymmetry in flood direction. This Eulerian asymmetry in peak flow velocities is modified when the wind enhances tidal flow velocities, as discussed in detail hereafter.

In scenario S1, the weak offshore directed wind resulted in significant wave heights smaller than 0.1 m (Figures 4.4[b] and 4.5[b]). The tide-averaged wind speed during scenario S3 was slightly higher (12 m/s) compared to S2 (10.6 m/s). In scenario S3 this high wind speed persisted for 12 consecutive hours, whereas in scenario S2 the wind speed was above 10.6 m/s during the 67% of the tidal cycle. As a consequence, the significant wave height peaks were ~10 cm higher during scenario S3 than S2.

During scenario S2, wind from the NE enhances the ebb flow, increasing the peak long-shore flow velocity by more than 20 cm/s at both sites, thereby becoming ebb-dominant. During scenario S3 the flow generated by the opposing wind reverses the tidal flow: during part of the ebb phase at K_L and during the full cycle at K_H. The vertical dotted lines in Figures 4.4 and 4.5 indicate the moment of high water, which at K_L in scenarios S1 and S2 corresponds to slack water conditions. In scenario S3 at K_L the wind opposing ebb delays slack water and consequentially increases the length of flood directed flow by about three hours. At K_H in scenario S2 the flood phase is shortened by about one hour due to the opposite NE wind, whereas in scenario S3 the flood-directed flow persisted during the full tidal cycle.

4.3.3. FLOW REVERSAL OBSERVED WITH CURRENT PROFILERS

The analysis of flow velocity, carried out in Sections 4.3.1 and 4.3.2, showed that the tide-induced flow can be reversed by oppositely-directed wind-driven currents. The flow velocity used in the analysis is the flow velocity measured at ~ 20 cm above the tidal flat bed, using Acoustic Doppler Velocimeters, at sites K_L and K_H (Spring 2016).

In the present section we expand this analysis, providing the flow velocity obtained with Acoustic Doppler Current Profilers during wind conditions analogous to scenarios S2 and S3 (i.e. respectively NE and SW wind). Using Figure 4.6 we therefore look at the velocity variation over the full water depth during, respectively, SW wind (left panels) and NE wind (right panels).

Moderate SW wind (up to u_{10} of ~ 10 m/s, 2017 spring period) induces ebb flow reversal along the full water depth, for consecutive tidal cycles, at site W_L. During the entire tidal cycle the flow is relatively uniform along the (maximum 1.2 m) water depth. Stormy SW wind (up to u_{10}

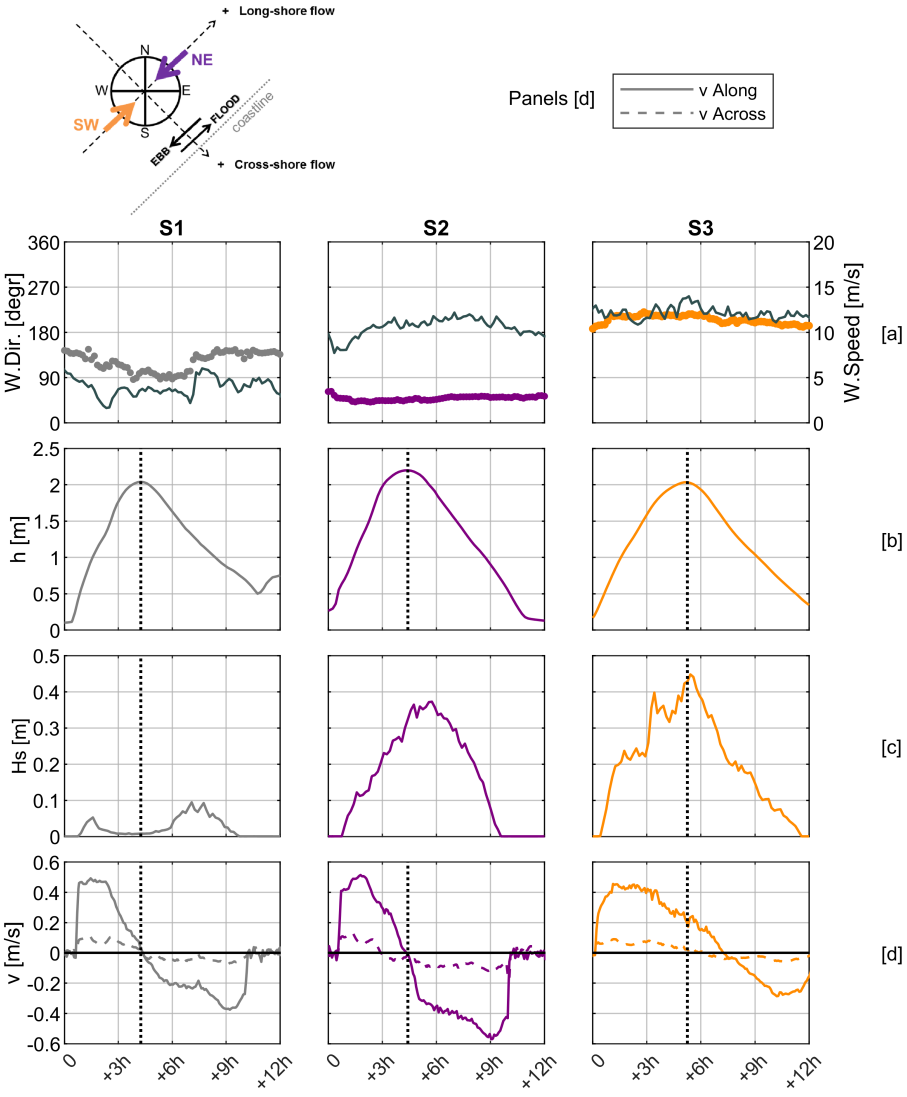

Figure 4.4: Intra-tidal variation at the lower mudflat K_L) in three wind scenarios: S1 (weak wind); S2 (ebb-directed wind); S3 (flood-directed wind). [**a**] Wind speed (solid line) and direction (markers); [**b**] Water depth; [**c**] Significant wave height; [**d**] Flow velocity in the long-shore direction (solid line) and cross-shore direction (dashed line).

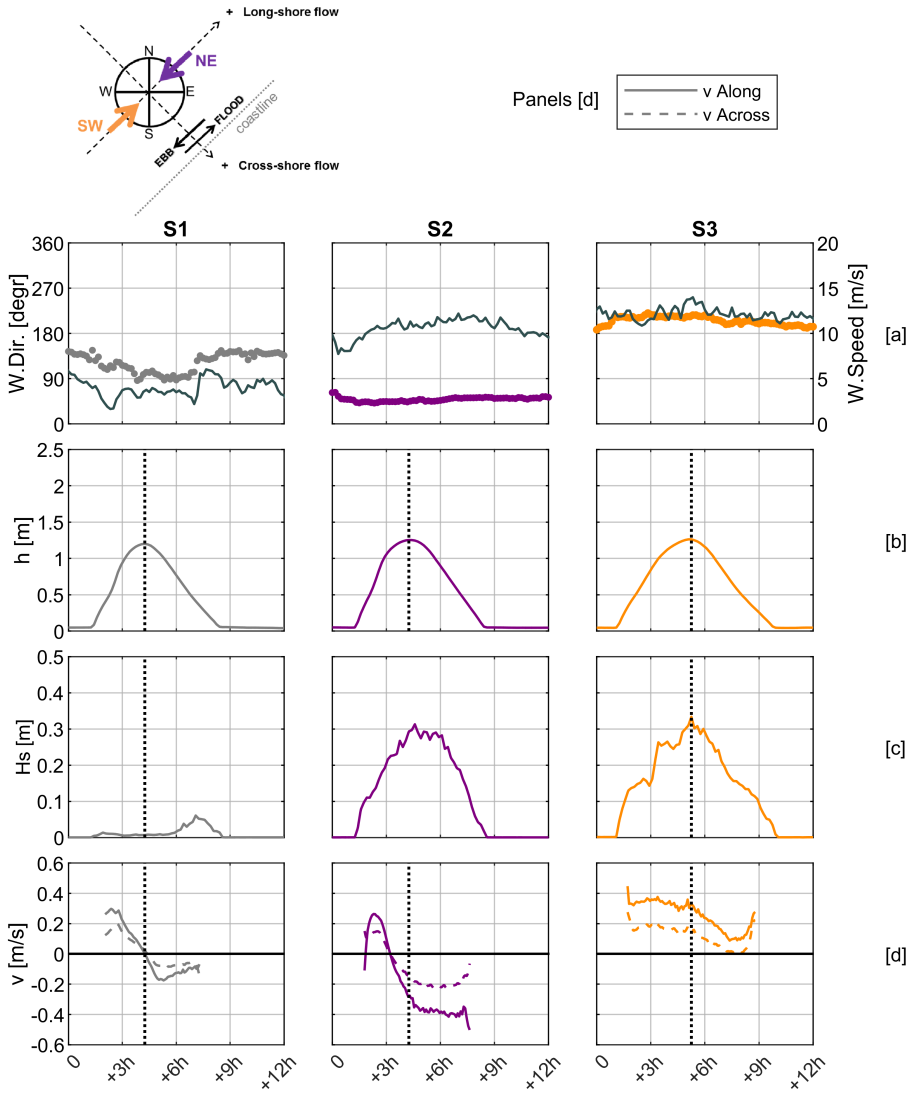

Figure 4.5: Intra-tidal variation at the lower mudflat (K_H) in three wind scenarios: S1 (weak wind); S2 (ebb-directed wind); S3 (flood-directed wind). [**a**] Wind speed (solid line) and direction (markers); [**b**] Water depth; [**c**] Significant wave height; [**d**] Flow velocity in the long-shore direction (solid line) and cross-shore direction (dashed line).

of ~ $25 m/s$, 2018 winter period) generates wind-driven currents resulting in flood-directed flows during decreasing water depths, with flow magnitude up to 0.7–1 m/s (even larger than 1 m/s at site W_L).

Relatively strong NE wind (up to u_{10} ~ 18 m/s, 2017 spring period), resulted in ebb-directed flow during consecutive tidal cycles. A full flood-reversal was not observed in the 2016 field cam-

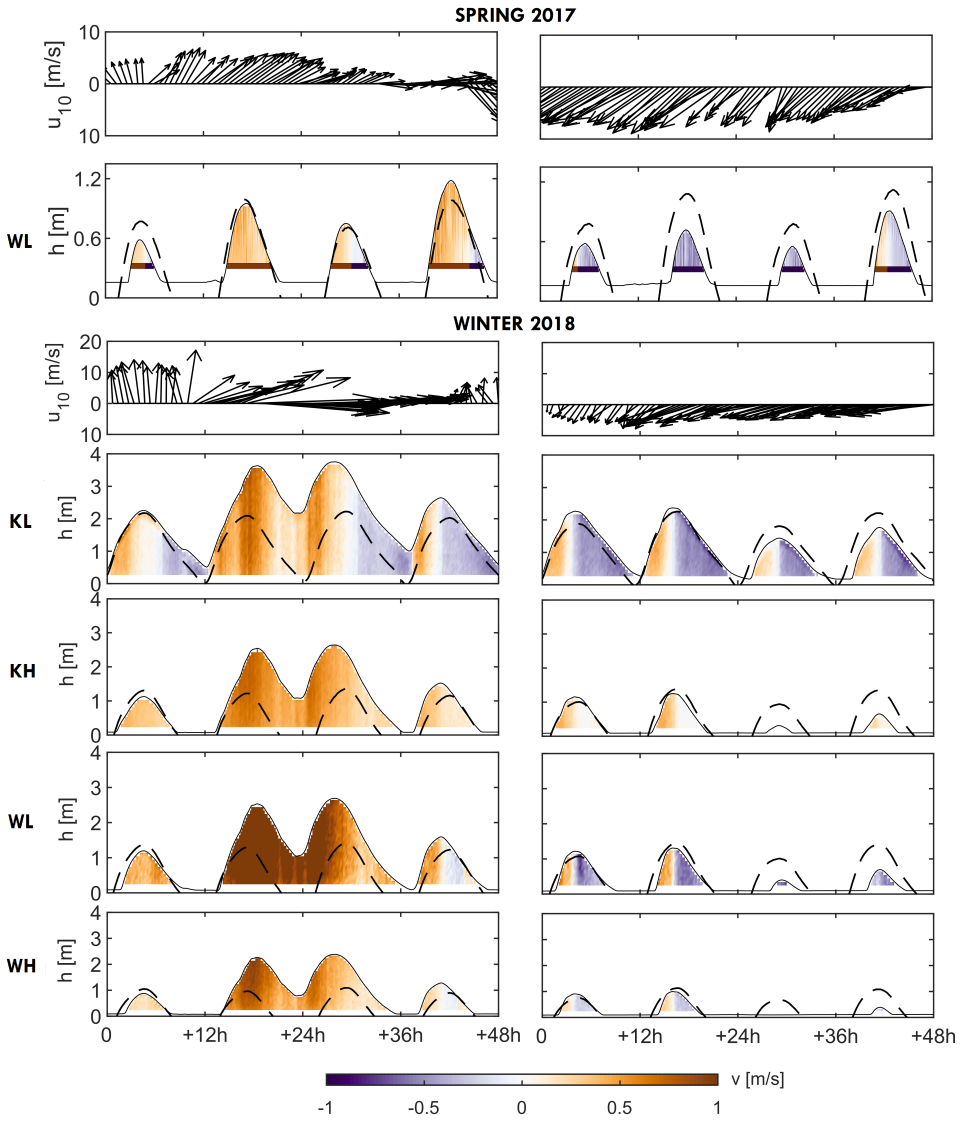

Figure 4.6: Flow reversal along the full water depth observed with Acoustic Doppler Current Profilers, during spring 2017 (site W_L) and during winter 2018 (all sites). Left and right column indicate SW and NE wind conditions inducing flow reversal, respectively, during the ebb and during the flood phase.

paign; scenario S2 in Figures 4.4 and 4.5 showed a partial flow reversal during floods. We observe, in fact, that moderate NE wind (up to $u_{10} \sim 10$, winter period) increases the duration of the ebb directed flow (e.g. sites K_L, W_L) and results in water level set-down, but it does not reverse fully the flow during flood.

4.4. ANALYTICAL MODEL DEVELOPMENT

4.4.1. DETERMINATION OF LEADING ORDER TERMS IN THE MOMENTUM BALANCE EQUATION

Section 4.3.2 revealed the prominent role of wind in modifying the flow velocity at the two study sites, especially on the higher mudflat. In this section, we quantify the mechanisms explaining this difference using the depth-averaged momentum balance equation (MBE) in the dominant flow direction:

$$\rho_w h \frac{\partial u_x}{\partial t} - \rho_a c_D u_{10} |u_{10}| + \rho_w c_{f_{wc}} u_x |u_x| + \rho_w g h \frac{\partial \eta}{\partial x} + \rho_w u_x h \frac{\partial u_x}{\partial x} = 0 \tag{4.7}$$

with the density of seawater $\rho_w = 1020$ kg/m^3; water depth h; long-shore flow velocity u_x; time t; density of air $\rho_a = 1.23$ kg/m^3; wind drag coefficient c_D; wind speed at 10 m above the surface u_{10}; bed friction coefficient related to waves and currents $c_{f_{wc}}$; gravitational acceleration g and water level η. The first three terms in Equation 4.7 can be determined from the time series of the variables measured at the two sites.

The first term in Equation 4.7 represents inertia and can be estimated using the time series of the water depth and the long-shore flow velocity measured at 20 cm from the seabed.

The second term is the stress induced by the wind on the sea surface, computed using the wind speed time-series. The dimensionless wind drag coefficient typically ranges between 0.001 and 0.002 for wind speed between 5 m/s and 20 m/s, (e.g. *Lin et al.*, 2002). This coefficient can be estimated from the wind speed (*Wu*, 1980, 1982):

$$c_D = \frac{\rho_a}{\rho_w} \cdot (a + b \cdot u_{10}) \tag{4.8}$$

with a and b coefficients as estimated by *Wu* (1982): $a = 0.8$, $b = 0.065$. The mean value of the drag coefficient obtained for the measurement period is 0.0015, which corresponds well to values found in literature. As we compute the momentum balance in the long-shore direction, we evaluate the case of wind in the same direction (positive when blowing in the flood direction).

The third term represents the current-induced bed shear stress. The coefficient c_{f_w} represents the exchange of momentum between the bed and the water, and depends on the combined effect of current and waves. Waves modify the vertical profile of the flow velocity resulting in a net bed shear stress in addition to the current-induced shear stress. The friction coefficient by waves and currents $c_{f_{wc}}$ is defined as *Soulsby* (1995) and *Faria et al.* (1998):

$$c_{f_{wc}} = \frac{\tau_m}{\rho_w u^2} \tag{4.9}$$

with τ_m the mean bed shear stress by currents and waves and u the depth-averaged flow velocity. The mean bed shear stress τ_m is estimated using the model proposed by *Soulsby* (1995), as elaborated in detail in Section 4.2.2. Its mean value during the field experiment was 0.0034 at K_L and 0.0025 at K_H, respectively.

The fourth term represents the barotropic pressure gradient, which is composed of two components: a time-averaged component (resulting in water level set-up/-down) and a time-varying component (related to the propagation of the tidal wave). The former cannot be established from

the local time-series, so it remains excluded from our balance. The latter can be estimated from the celerity $c = \sqrt{gh}$, so that the spatial water level gradient can be computed from its temporal gradient:

$$\rho_w g h \frac{\partial \eta}{\partial x} \approx -\rho_w \sqrt{gh} \frac{\partial \eta}{\partial t} \tag{4.10}$$

The fifth term represents advection and requires estimation of the spatial velocity gradient, for which we apply the approach of Equation 4.10 as well:

$$\rho_w u_x h \frac{\partial u_x}{\partial x} \approx -\rho_w u_x h \frac{1}{\sqrt{gh}} \frac{\partial u_x}{\partial t} \tag{4.11}$$

Advection in the cross-shore direction has been neglected as the cross-shore gradient of the long-shore velocity ($\partial u_x / \partial y$) is relatively small. Substituting these estimates into Equation 4.7 gives:

$$\rho_w h \frac{\partial u_x}{\partial t} - \rho_a c_D u_{10} |u_{10}| + \rho_w c_{f_{wc}} u_x |u_x| - \rho_w \sqrt{gh} \frac{\partial \eta}{\partial t} - \rho_w u_x h \frac{1}{\sqrt{gh}} \frac{\partial u_x}{\partial t} + \text{res} = 0 \tag{4.12}$$

with 'res' a residual term, representing errors in the estimations and the terms that could not be computed using the time series.

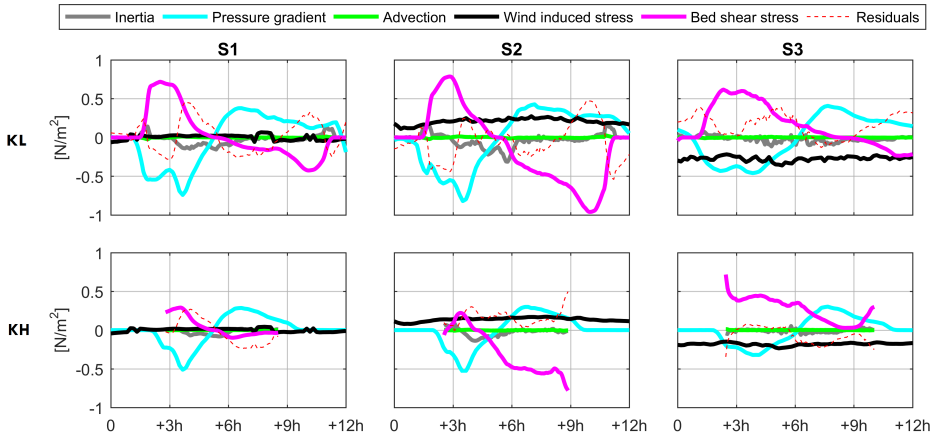

Figure 4.7: Terms of the momentum balance equation in the three wind scenarios (S1–S3 from left to right) at the lower mudflat (K_L, upper panels) and higher mudflat (K_H, bottom panels). The terms include the sign given in Equation 4.7.

In Figure 4.7 the five terms are presented for the three wind scenarios. Advection ($O(10^{-3})$) and inertia ($O(10^{-2})$) are small compared to the wind-induced stress, the bed shear stress, and the pressure gradient ($O(10^{-1})$).

Figure 4.7 suggests that three dominant terms in the MBE are: the wind induced stress, the bed shear stress, and the (time-varying) pressure gradient. Furthermore, comparing the scenarios S2–S3 with scenario S1, Figure 4.7 shows that an increase in wind-induced stress is mainly compensated by a higher bed shear stress. Differently from the bed shear stress, the pressure gradient does not show a clear variation with wind-shear stress.

Figure 4.7 also reveals that wind has a more pronounced effect in modifying the tide-induced flow at K_H than at K_L: the velocity at K_H is positive (i.e., flood-directed) during the full tidal cycle for S3, while the same wind conditions did not fully reverse the ebb flow at K_L. The mechanisms

responsible for this difference are explored in the next section via the development of a tide-wind interaction model (Section 4.4.2) which is subsequently compared to the data (Section 4.4.3).

The different terms do not result in a closure of the balance, leading to a residual. The residuals are also shown in Figure 4.7. These residuals reflect: (1) the terms that cannot be estimated from a point-measurement; (2) assumptions in the definitions of the bed shear stress term and wind shear stress term, including the uncertainties related to the coefficients $c_{f_{wc}}$ and c_D, and (3) measurement inaccuracies. The residuals have similar magnitudes as the dominant terms, implying that the excluded terms (especially the time-varying pressure gradient, given the relatively small advection values in the long-shore direction) play a role in the momentum balance. If we compare the residuals of S1 and S2 for K_L, a similar pattern is found. No clear influence of the wind can be identified. In S3, instead, the residuals partly compensate for the wind induced shear stress. This is, however, not the case for S3 at K_H: at this site, the residuals have the same sign as the wind shear stress. No particular general pattern could be deduced from the time variation of the residual. High resolution numerical modeling could provide more insights into the residual term.

4.4.2. TIDE–WIND INTERACTION MODEL

Figure 4.7 indicates that the time-varying pressure gradient, the bed shear stress, and the wind shear stress are three dominant terms in the momentum balance. In this section we elaborate on the balance of these three terms in windy and non-windy conditions. We especially aim at exploring the interaction between these terms and the implications for the flow velocity.

In absence of wind, a balance is assumed between the time-varying pressure gradient and the bed shear stress; i.e., the flow velocity is purely tide-induced, i.e., $u_x \equiv u_T$:

$$\rho_w g h \frac{\partial \eta}{\partial x} = -\rho_w c_{f_{wc}} u_T |u_T| \tag{4.13}$$

The wind (S2, S3) induces a considerable shear stress at the surface (up to 0.4 Pa in S3). The balance therefore requires an additional wind-induced shear stress and a bed shear stress generated by tides and wind (i.e., $u_x \equiv u_{TW}$):

$$\rho_w g h \frac{\partial \eta}{\partial x} = \rho_a c_D u_{10} |u_{10}| - \rho_w c_{f_{wc}} u_{TW} |u_{TW}| \tag{4.14}$$

The pressure gradient term due to the tide – first term in Equation 4.14 – follows from Equation 4.13, as this term is hardly influenced by the wind; see Figure 4.7:

$$-\rho_w c_{f_{wc}} u_T |u_T| = \rho_a c_D u_{10} |u_{10}| - \rho_w c_{f_{wc}} u_{TW} |u_{TW}| \tag{4.15}$$

Equation 4.15 is an approximation of the MBE in which u_T and u_{TW} are now explicit. We emphasize that the effect of water level set-up/-down is not included here. This implies that the flow velocity u_{TW} is to be considered as an upper limit.

Rearranging Equation 4.15 yields an expression for the velocity due to tides and wind, expressed as the sum of the two components:

$$u_{TW} |u_{TW}| = \underbrace{u_T |u_T|}_{\text{TIDE}} + \underbrace{\frac{\rho_a c_D}{\rho_w c_{f_{wc}}} u_{10} |u_{10}|}_{\text{WIND}} \tag{4.16}$$

This relation is explored for a sinusoidal tide $u_T = \hat{u} \sin\left(\frac{2\pi}{T} t\right)$, with velocity amplitude $\hat{u}$ and tidal period T. To keep the model simple, we use the mean time-invariant value of the friction coefficient $c_{f_{wc}} = 0.00285$. The velocity due to tide and wind u_{TW} can thus be computed for a given wind speed (Figure 4.8).

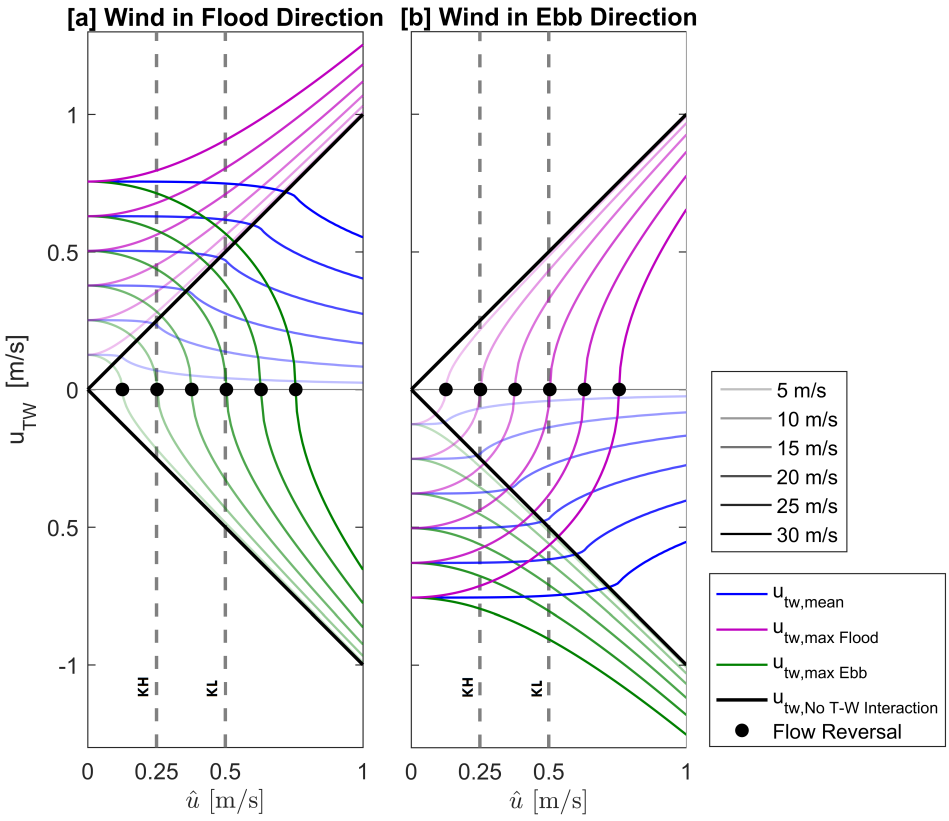

Figure 4.8: Tide-wind interaction model results. Tide-averaged flow velocity resulting from the interaction of tidal flow and wind-driven flow (u_{TW}) as a function of the tidal flow amplitude ($\hat{u}$). [**a**] Wind is in flood direction; [**b**] Wind is in ebb direction. The tide-averaged velocity (blue) and the maximum tide-averaged velocity during flooding (pink) and during ebb flow (green) are computed as functions of the tidal flow amplitude. The flow tidal amplitudes at the K_H and K_L are 0.25 and 0.5 m/s, respectively. The black markers indicate the turning points for wind-induced reversal of the tidal flow.

The two panels of Figure 4.8 present two contrasting cases of wind in flood direction (Figure 4.8[a]) and in ebb direction (Figure 4.8[b]). The mean u_{TW} decreases for increasing $\hat{u}$, implying that the effect of wind-driven flow is smaller when the "background" (pressure-induced) tidal flow is larger. Wind in flood direction (Figure 4.8[a]) leads to a non-linear summation of tidal and wind-driven flow during flood, and in the opposite direction during ebb. During both flood and ebb, u_{TW} is larger for higher wind speed. However, the wind-driven flow is less effective at larger tidal flow amplitude, so that u_{TW} tends to the value of u_T (black lines with 1:1 slope). In cases of opposing wind, the u_{TW} during ebb can be positive (i.e., reversed in flood direction). These results are confirmed by observations at the two sites, the tidal flow amplitudes of which are indicated by gray dashed lines. Figure 4.8 suggests flow reversal at K_H at wind velocities exceeding ~10 m/s, which corresponds to the observations in Figure 4.5. The figure suggests that a wind speed of

~20 m/s should reverse the ebb flow at the lower mudflat (K_L), but such a wind speed (and flow reversal) did not occur during our field campaign.

Two specific hydrodynamic conditions in the tide-wind interaction model require attention. The first is the absence of tidal flow ($\hat{u} = 0$ m/s). This condition equals the first order estimate derived in *De Vet et al.* (2018). The second is the zero-flow condition ($u_{TW} = 0$ m/s, indicated by black markers). Zero-flow corresponds to the turning point for wind-induced tidal flow reversal: the tidal flow and wind-driven flow are equal in magnitude. This condition implies that the wind shear stress equals the pressure gradient related to the tide. The two cases are therefore related: for a given wind velocity, u_{TW} at $u_T = 0$ m/s is equal to $\hat{u}$ at $u_{TW} = 0$ m/s. This implies that for constant wind conditions, the flow velocity u_{TW} at zero tidal flow is equal to the wind-driven flow $\hat{u}$ required to reverse the tidal flow. The circular-like shape of the ebb curves when wind blows in flood direction, and for the flood curves when wind blows in ebb direction, results from Equation 4.16 getting the form of a circumference equation: $x^2 + y^2 = r^2$. For $u_{10} > 0$ the circular-like shape exists for $u_T < 0$, i.e., during ebb; and for $u_{10} < 0$ the circular-like shape exists for $u_T > 0$, i.e., during flood.

The interaction between tidal and wind-driven flow also depends on the tidal asymmetry, which is only marginally important for our case. In case of flood dominance, the wind is more effective in modifying the ebb; and in cases of ebb-dominance the flow velocity during flood will be more sensitive to the wind-induced modifications (at the same wind speed). The tide–wind interaction results in modified asymmetries in peak flow velocity during flood and ebb. Therefore, the effect of the wind on the flow depends on the Eulerian asymmetries in the astronomical signal (being stronger for small tidal asymmetry) and affects the Eulerian asymmetries in the meteorological signal (possibly reversing the flow during flood or ebb).

4.4.3. EFFECT OF WIND ON TIDE-AVERAGED FLOW: MODEL AND DATA COMPARISON

This tide–wind interaction model was first verified using data from the full 2016 measurement period (Figure 4.9) and subsequently validated using spring 2017 and winter 2018 dataset. The validation is discussed in Section 4.4.4.

For wind speeds close to zero the observed tide-averaged flow velocity is close to zero, whereas tide-averaged flow velocities increase with higher wind speeds. Although the absolute flow velocity is larger at K_L than at K_H, the net flow is strongest at K_H. The direction of the net flow is determined by the wind direction: not only long-shore directed winds, but also wind non-parallel to the flow (e.g., NW or SE) enhance flood and ebb currents in their main direction (i.e., long-shore direction). This effect results from the bathymetry of the channel, forcing the flow to align with the main tidal channel flow.

The dashed lines in Figure 4.9 indicate the computed tide-averaged velocity by wind over a still body of water, i.e., without tide–wind interaction: $\langle u_{TW} \rangle = \frac{\tau_W}{\rho_w c_{fc\,w}}$. Including the tide–wind interactions (solid line) the net flow depends on the tidal amplitude also (for which we use typical values of $\hat{u} = 0.5$ m/s at K_L and $\hat{u} = 0.25$ m/s at K_H).

Both the solid and the dashed lines represent conditions where the wind is exactly in streamwise direction and persists during the full tidal cycle, and are therefore upper limits of the wind effect. At K_H the dashed and the solid lines are closer than at K_L. On the higher mudflat the tidal flow is small (0.25 m/s), and even weak winds are able to influence the net flow. On the lower mudflat, the lines diverge because of the larger tidal flow (0.5 m/s), resulting in stronger non-linear interactions between the two components, and therefore in weaker net flows.

The model shows good agreement with the observations, highlighting the difference in the tide–wind interaction at the different elevations of the mudflat. Contrary to previous works (i.e. mainly the approximation by *De Vet et al.* (2018)), this model predicts the flow velocity, including

the interaction between tidal flow and wind-driven flow. The contribution of such a mechanism is key for predicting net flow velocities at larger tidal flow velocities. The relative and absolute influence of the wind on the flow decreases with increasing tidal flow.

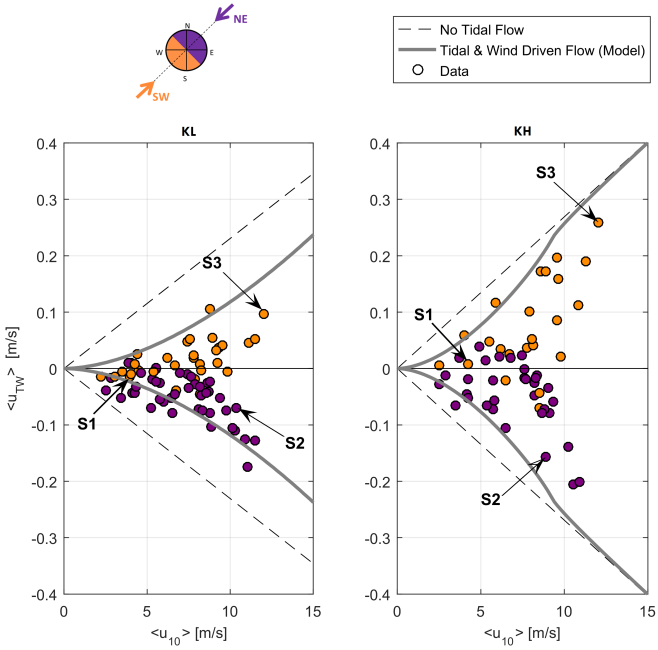

Figure 4.9: Flow velocity resulting from the interaction of tidal flow and wind driven flow as a function of wind speed. The dashed lines indicate u_{TW} in case of no interaction between tide and wind-driven flow; the solid lines represent u_{TW} accounting for the tide–wind interaction. The tidal flow amplitude was set as 0.5 m/s at K_L and 0.25 m/s at K_H. The drag coefficient was set as $c_D = 0.0015$, i.e., the mean value of the time-dependent drag coefficient during the full measurement period. The bed friction coefficients were set as $c_{f_{cw}} = 0.0034$ at K_L and $c_{f_{cw}} = 0.0025$ at K_H, i.e., the mean value of the time-dependent wave–current bed friction coefficient during the full measurement period. Each marker represents the long-shore flow velocity averaged during one tide. Positive values in the figure imply flood-directed net flow; negative values imply ebb-directed net flow. The color of the marker indicates the dominant wind direction during the tide. The tides representing the three wind scenarios are indicated.

4.4.4. MODEL VALIDATION

The goodness of the model was tested against the data of the 2017 and 2018 field campaigns. Figure 4.10 shows that the predicted flow velocities resulting from the interacting forcing, i.e. U_{TW} provides an envelope of the collected data (similar to the 2016 data). The deviation between U_{TW} and the wind-only flow (wind blowing over a still water body) increases for increasing tidal flow amplitudes. At site W_H the tidal flow amplitude is so small (around 0.1 m/s), that the U_{TW} envelopes approximate wind-only flow. At high wind velocities the effect of the tidal currents becomes progressively weaker.

The model application requires the estimation of the friction coefficient due to waves and currents, $c_{f_{wc}}$, for each site. This coefficient (computed using Equation 4.9) is a function of the (mean) bed shear stress (by currents and waves) and of the flow velocity magnitude, which differ during

spring and winter weather conditions. The model hence shows that in winter, strong winds result in a larger residual flow compared to spring time, and that the residual flow tends to increases at increasing bed elevations (upper flat), due a smaller tidal flow amplitude.

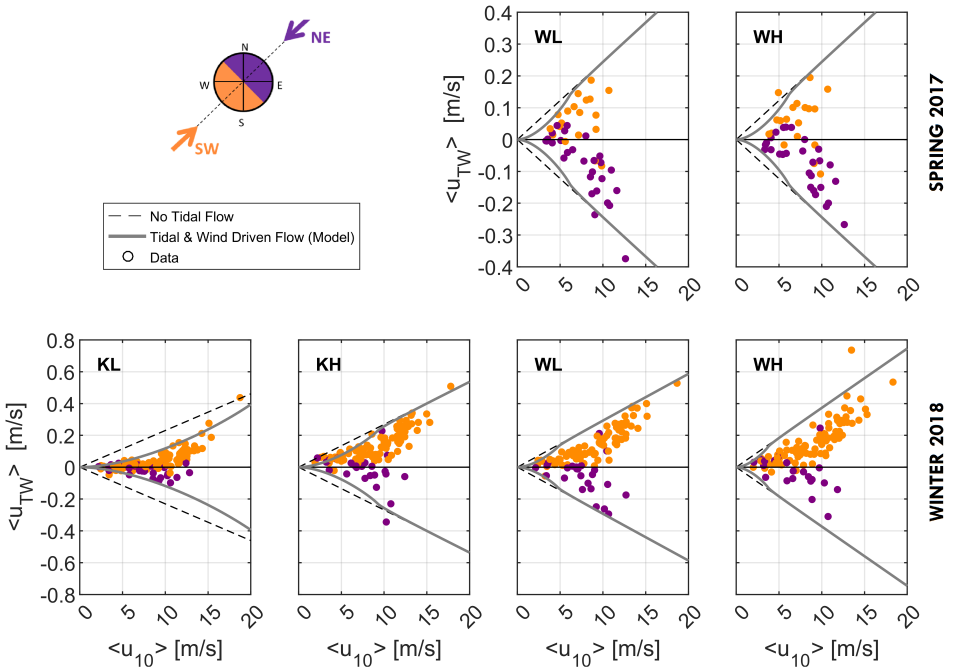

Figure 4.10: Flow velocity resulting from the interaction of tidal flow and wind driven flow as a function of wind speed. 2017 2018 Field campaign data.

4.4.5. APPLICABILITY OF THE MODEL

In order to asses the model's applicability to other locations and environments, the underlying assumptions made are discussed hereafter. Firstly, the model is based on Equation 4.16 in which we neglected the contribution by the residuals in the MBE, and especially the component related to the wind-induced pressure gradient. The model does include the barotropic pressure gradient related to the tide. It does not, however, include changes in the pressure gradient by wind, which would induce a time-averaged water level set-up/-down. We expect this contribution to be relevant at our site and in other semi-enclosed systems like coastal lagoons or in estuaries, where solid land boundaries allow the development of a spatial pressure gradient. In such systems, the wind shear stress is to a larger extent counterbalanced by a pressure gradient. The Wadden Sea tidal basin shape is elongated in the direction of the dominant wind direction (see Figure 2.5 in Chapter 3): the land boundaries in the NE and SW result in smaller set-up with wind blowing in the long-shore direction (e.g., the dominant wind direction, SW) compared to the boundaries in the cross-shore direction.

Secondly, a term excluded from the MBE was the advection of the long-shore velocity in cross-shore direction. Given the magnitude of advection in the main velocity direction, we do not expect

that this term plays an important role. However, this term is expected to have more relevance at tidal flats which are more elevated relative to MSL. In this case, refraction of the tidal wave on the coastal shelf would increase cross-shore flows on the higher flat.

Thirdly, a constant (time-averaged) value for the drag coefficient and the bed friction coefficients is used. This assumption was based on an assessment of the time-dependency of the drag and friction coefficients not reported here (see as a reference *Speerstra* (2018)), which showed consistency with values suggested in the literature. Even though this assessment suggests that the temporal variability of the drag and friction coefficients was sufficiently small to use values typical for the full observation period, the model might be further improved by including the time-dependence of these parameters.

We conclude that the representation of the momentum balance equation by three terms (pressure gradient term, bed friction, and wind forcing) shows that there is a strong non-linear interaction. The influence of the wind diminishes for increasing tidal flow. Furthermore, the model provides a simple algebraic formulation for the estimation of flow reversal.

4.5. CONCLUSIONS

This chapter presented the analysis of high resolution hydrodynamic data (flow velocities, waves and water levels) collected at the intertidal flats of Koehool and Westhoek during spring and winter seasons. This data revealed the existence of a non-linear interaction between tide-induced flow and wind-induced flow over intertidal flats. Using the observations collected in spring 2016, an analytical model describing the interaction between tide-induced and wind-induced flow was developed. This model was subsequently validated using the spring 2017 and winter 2018 observations.

The model shows that the magnitude of wind-driven flow decreases (increases) for increasing (decreasing) tidal flow amplitude. At sites characterized by a relatively weak tide-induced flow (~0.2 m/s) the wind is able to reverse the direction of the tidal flow also at moderate wind speeds (~10 m/s). This study hence reveals that wind-induced reversal of the tidal flow is a relatively common phenomenon in environments characterized by small tidal flow amplitudes. The model's prediction of the net tidal flow and of the wind speed at which the tidal flow is reversed by wind shows good agreement with data, both in calm (spring) weather and more energetic (winter) conditions.

About the Photo
Wind and tidal flow at the intertidal flat of Westhoek. The photo was taken on February 12, 2018.

Explore more media content using the following QR-code.

5

WIND EFFECTS ON INTERTIDAL FLATS SEDIMENT TRANSPORT

Wind–driven flows interact with tidal currents, affecting the residual water transport also at relatively low wind speeds, especially on the higher intertidal flat. But what are the implications of such hydrodynamic interaction for sediment transport? In this chapter we examine the variation in suspended sediment concentrations and fluxes over different spatial and time scales (from intra–tidal to monthly timescales). Field observations provide evidence that windy events (timescales of hours) following relatively calm weather periods (timescales of weeks) generate sediment fluxes which are several order of magnitudes larger than averaged fluxes. Based on our results, we propose a conceptual sediment transport–storage model in intertidal systems, accounting for the the crucial contribution of tide– and wind–induced sediment advection in fine-sediments intertidal environments.

Parts of this chapter have been published as: *Colosimo et al. (2020)*."The Impact of Wind on Flow and Sediment Transport over Intertidal Flats". Journal of Marine Science and Engineering.
Coauthors: P.L.M. de Vet, D.S. van Maren, Ad J.H. Reniers, J.C. Winterwerp, B.C. van Prooijen

Ch 5: Wind Effects on Intertidal Flats Sediment Transport

Main Research Question

RQ2: How do tides and winds influence sediment transport over intertidal flats?

Keypoints

Keypoint 1: Wind aligned in the flood (ebb) direction results in smaller ebb-(flood-) directed residual sediment fluxes.

Keypoint 2: Wind-driven sediment advection induce the storage of fine sediments in low energy areas of intertidal systems.

Keypoint 3: Sediment fluxes during windy conditions increase by several order of magnitudes compared to averaged conditions, due to resuspension and advection of poorly consolidated (or unconsolidated) sediment.

Implications for Fine Sediment Nourishments

When designing fine sediment nourishments, the interaction between the tide– and wind– driven horizontal flows, dictating the sediment advection, should be predicted via numerical models that include the existence of storage areas in the system.

5.1. INTRODUCTION

Previous studies indicated that the primary forces determining the morphological equilibrium of intertidal flats are wind-waves and tidal currents. Intertidal flats increase in elevation during tide-dominated conditions and erode during wave-dominated conditions (e.g. see *Bassoullet et al.*, 2000; *Carniello et al.*, 2011; *Friedrichs*, 2012; *Green and Coco*, 2014; *Le Hir et al.*, 2000; *Mariotti and Fagherazzi*, 2013; *Zhu et al.*, 2017). Especially relevant is the work of *Janssen-Stelder* (2000), a field study in the Dutch Wadden Sea (Groningen tidal flats), i.e. an environment very similar to our study sites. These observations confirmed that during storms, wind-waves are the controlling forcing, inducing bed erosion and sediment export from the tidal flat. During the following calm weather conditions, the sediment transport is controlled by the tidal forcing, resulting in an onshore sediment transport and deposition in the higher intertidal zone.

Erosion and deposition processes are controlled by net sediment transport occurring over the tidal cycle. Considering a cross-shore transect of a tidal flat, the net sediment transport associated to tides- and waves- dominated conditions is, respectively, landward and seaward directed (e.g. *Le Hir et al.*, 2000; *Bassoullet et al.*, 2000; *Friedrichs*, 2012). During tide-dominated conditions, the asymmetries driving net sediment transport across a tidal flat can be separated into Lagrangian (spatial) asymmetries and Eulerian (local) asymmetries. Lagrangian asymmetries are due to the spatial gradients in hydrodynamic forcing in combination with a finite critical bed shear stress for erosion and settling velocity (i.e. the so called 'scour lag' and 'settling lag').The combination of scour and settling lag result in a net sediment transport in the onshore direction (*Postma*, 1961). In contrast, the net sediment transport due to waves across an intertidal flat is seaward. Wind-waves favour sediment erosion and induce turbulence motions that keep sediment in suspension, even during high water slack. During the following ebb phase, the concentrated sediment fluxes lead to a net sediment export (e.g. *Janssen-Stelder*, 2000; *Le Hir et al.*, 2000; *Green and Coco*, 2014). The erosive effect of waves increases with a decreasing water depth, so that wave-dominated conditions generally prevail at the higher intertidal zone. However, the timing of the different hydrodynamic forcing can alter such conditions: *De Vet et al.* (2020b) observed, at a Western Scheldt estuary intertidal flat (the Netherlands) that a storm occurring during low water conditions can drastically affect the bed morphology (and its evolution on timescales of years) of the lower intertidal flats, while the higher flat, being emerged during the storm, remains unaffected. The spatio-temporal variability of wind-waves and tidal currents across intertidal flats therefore controls the morphological evolution both over short (storm-related, i.e. hours/days) timescales and long (post-storm recovery, i.e. days-months, even years) timescales. As illustrated above, the combined effect of waves and tides has received significant attention in the scientific literature. These studies focused primarily on the relative impact of wave-induced erosion and tide-induced sedimentation. However, wind-driven flows also play a role in the control of the sediment fluxes across intertidal areas (*Christiansen et al.*, 2006; *Mariotti and Fagherazzi*, 2011; *Talke and Stacey*, 2008; *De Vet et al.*, 2018), also over larger spatial scales. In multi-inlet lagoons such as the Wadden Sea, the wind driven fluxes result in water and sediment exchange over the tidal divides (*Gerkema et al.*, 2014; *Van Weerdenburg et al.*, 2021), leading to inter-connected morphodynamic evolution of the adjacent tidal basins (*Duran-Matute et al.*, 2014; *Sassi et al.*, 2015).

Despite these earlier studies, it remains unclear how the interaction between wind-driven flows, wind-waves and tidal currents impacts the residual sediment transport over intertidal areas and how this interaction affects tidal flat morphology. The previous chapter (Chapter 4) advanced on the impact of wind-induced effects on the hydrodynamics, revealing how wind-driven flows control the flow direction over intertidal flats. In this chapter, we investigate the consequences of such wind effect on the sediment transport over intertidal flats at different timescales (from hourly to seasonal) and spatial scales (from tidal flat transect to basin scale). In contrast with numerous previous studies, the focus is not on stormy events, but on averaged wind conditions. Special at-

tention is dedicated to the role of wind direction, playing a pivotal role in the sediment transport over large spatial scale. Within the present chapter we therefore aim at improving our understanding on:

- The effect of wind on the sediment concentrations at different tidal flat elevations;
- The different contribution of waves and currents to sediment transport at different tidal flat elevations;
- The effect of wind on the suspended sediment fluxes over intertidal flats;
- The different spatial and temporal timescales of sediment transport in muddy intertidal systems.

5.2. METHODOLOGIES

The analysis carried out in this chapter is based on field data gathered during the three field campaigns (2016-2017-2018). Flow velocity point measurements at 20 cm above the bed are available at each measured site during all field campaigns. Flow velocity profiles (AQDP data) are only available for the 2018 winter campaign and (only at one site) for the 2017 field campaign (see Chapter 3). Similarly, the SSC has been measured at 20 cm above the bed during all campaigns, whereas data at 60 and 120 cm above the bed is available only at some sites, during some campaigns. Where the flow and SSC profile were available (i.e. AQDP data and multiple OBSes along the depth), the SSF was estimated as:

$$SSF(t) = \int_0^H h(t) \cdot u(t) \cdot SSC(t) \tag{5.1}$$

With H maximum water depth (m), h the water depth (m), u the flow velocity along the water depth (m/s) and SSC the suspended sediment concentration along the water depth. Where the flow and SSC velocity profiles are not available, we approximate the SSF by assuming that the velocity and SSC measured at 20 cm above the bed are representative of the depth-averaged values:

$$SSF(t) = h(t) \cdot u_{20}(t) \cdot SSC_{20}(t) \tag{5.2}$$

with long-shore or cross-shore flow velocity u_{20} and suspended sediment concentration SSC_{20} at 20 cm above the bed and h water depth. The effects of the vertical distribution of the velocity and sediment concentration on the fluxes are therefore, in this case, not taken into account. A similar approach was followed by *Andersen and Pejrup* (2001).

The Suspended Sediment Flux has been integrated to estimate the residual fluxes over a time-period T*:

$$RT = \int_0^{T^*} SSF(t) = \int_0^{T^*} h(t) \cdot u_{20}(t) \cdot SSC_{20}(t) \tag{5.3}$$

When estimating the residual transport over a single tidal cycle, the time scale T^* depends on the submergence time per tide (hence not necessarily equal to the tidal period). The minimum water level was used to separate two subsequent tides in case the bed did not emerge.

5.3. RESULTS

5.3.1. SSC AT VARYING WATER DEPTHS

The suspended sediment concentration data, obtained at several elevations above the bed, is used in Figure 5.1 to examine the vertical distribution of sediments at changing water depths. The top right panel shows the logarithmic relation between water depth and SSC:

$$SSC_{max}(h) = SSC_{max,obs} \cdot e^{-h} \tag{5.4}$$

with h (m) water depth, SSC_{max} (g/l) the upper SSC limit at a certain water depth and $SSC_{max,obs}$ (g/l) the maximum SSC observed during field measurements. This implies that the SSC at a certain water depth, is below the threshold represented by the envelope:

$$SSC(h) \leq SSC_{max,obs} \cdot e^{-h} \tag{5.5}$$

Such relation implies that the maximum SSC decays exponentially with increasing water depth. This maximum SSC is independent from the height above the bed at which the SSC is measured. At 20 cm above the bed, SSC values up to 10 g/l are observed at depths smaller than 70 cm, whereas SSC larger than 10 g/l are observed at depths smaller than 40 cm.

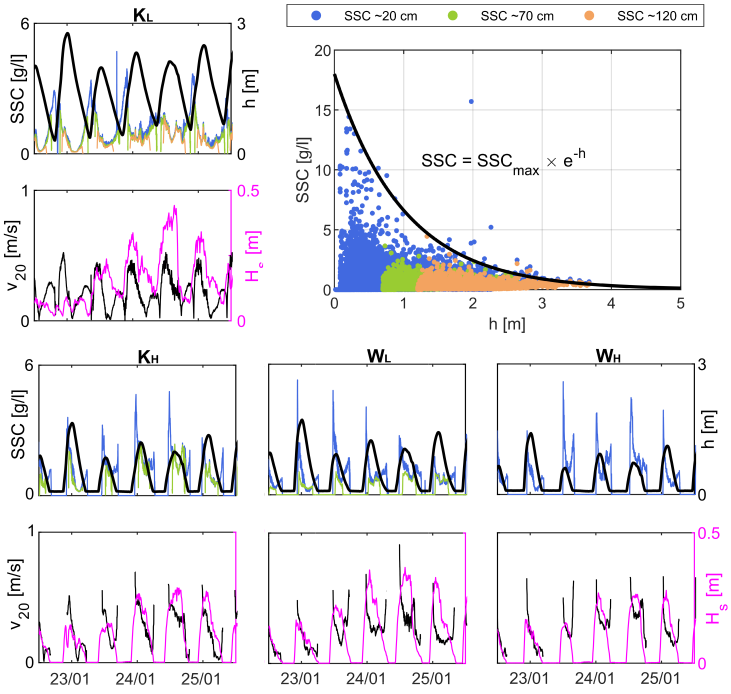

Figure 5.1: Top right panel: logarithmic relation between water depth and (maximum) Suspended Sediment Concentrations. Data-points with 20-minute frequency are displayed. The winter 2018 dataset is used, accounting for a total of 8 sensors measuring SSC for a period of ~60 days, at four different sites and at different elevations above the bed. Variations of flow velocity, significant wave height and sediment concentration over 6 tidal cycles (January 22-26, 2018) are shown per each site: K_L, K_H, W_L, W_H.

The time series (period January 22-26, 2018) of Figure 5.1 confirms this observation. The SSC has two peaks over the tidal cycle: at the beginning of the flood, in concert with a flood flow velocity peak, and at the end of the ebb, with a less pronounced peak. When the tidal flow reaches the measurement sites, the flow velocity is already relatively large (e.g. $v_{20} = 0.5 - 1$ m/s at sites K_H, W_L,W_H), while the wave heights are still relatively small. In the sections hereafter, the relation between SSC and current/wave forcing is further investigated both at tidal (Section 5.3.2) and intra-tidal timescale (Section 5.3.3).

The time series in Figure 5.1 also suggest that the SSC is not significantly stratified over the water column, as the SSC values at different heights above the bed are relatively uniform, especially at site K_L. Overall, the SSC varies significantly during the tidal cycle, but is relatively uniform along the water column. This implies that our methodology to compute the SSF is valid (assuming a vertically constant SSC) (see Section 5.2), with the exception of events of fluid mud formation, as evaluated in Chapter 6.

5.3.2. TIDE AVERAGED SSC

As shown in Chapter 4, the wind direction and magnitude strongly influences the hydrodynamics over the tidal flats. To test whether such wind-driven flows also influence the SSC, in this Section, the tide-averaged sediment concentrations are analyzed as a function of the tide-averaged wind speed (Figure 5.2) and bed shear stress (Figure 5.3).

The linear regression analysis indicates that the correlation between (tide-averaged) SSC and wind speed is higher during spring than during winter conditions. During the spring measurement period, the R^2 equals 0.373 and 0.294, respectively at sites K_H and K_L. Only at site W_H (i.e. the most elevated site) the correlation is higher during winter, with wind speeds alone explaining 30.9% of the SSC variance.

The lower correlation during winter conditions can be explained by storms inducing resuspension (erosion) of large amounts of sediment. The sediment does not directly deposit and consolidate, so it remains available for advection, and the concentration remains relatively high during the calm period following the storm. This is further confirmed by the higher tide-averaged SSC values observed in winter, compared to the spring period.

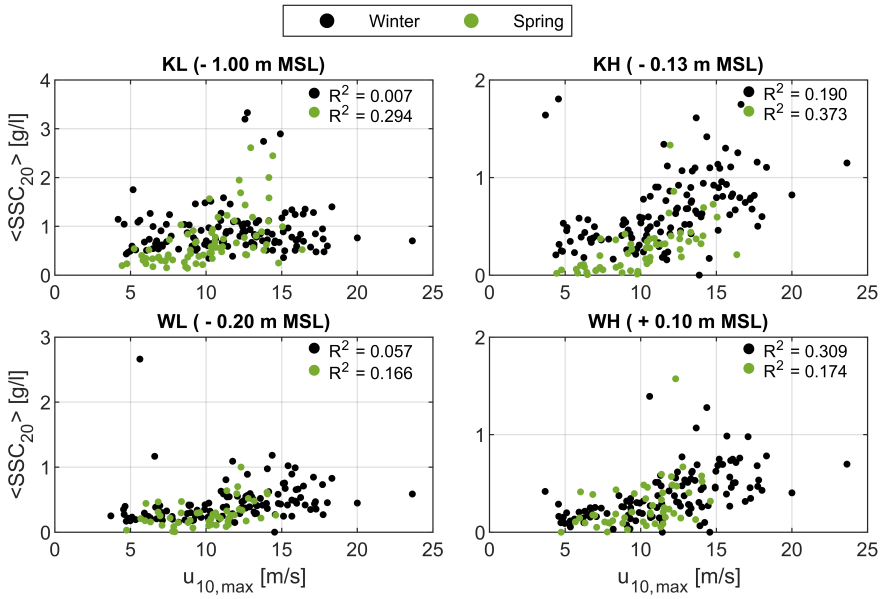

Figure 5.2: Tide averaged SSC measured at 20 cm distance from the tidal flat bed ($< SSC_{20} >$), with respect to wind speed (maximum u_{10} per tidal cycle) at the four measurements sites (K_L, K_H, W_L, W_H). The marker colour indicates the period of measurements (spring and winter). Note the different y-axes.

The different timescales of SSC variation due to storm-induced resuspension and post-storm advection are also suggested by the relatively poor correlation between tide-averaged SSC and tide-averaged bed shear stresses reported in Figure 5.3. Especially in winter, the SSC has no correlation with the bed shear stresses from currents and waves. During spring, on the other hand, the current-induced bed shear stress explains 70% and 66% of the variance in SSC at Koehool, respectively K_L and K_H. At Westhoek sites, W_L and W_H, such correlation is absent. During spring weather conditions, also the relation between wave-induced shear stress and SSC is more clear, with the highest R^2 values of 0.55 at site K_H, and lowest R^2 value of 0.20 at site W_L. Apparently, during spring conditions there is a relatively direct relation between high wind conditions, where both higher waves and currents resuspend sediment, but also deposit relatively rapidly thereafter. In winter, sediment remains in suspension for longer periods of time, and SSC is poorly correlated with hydrodynamic forcing.

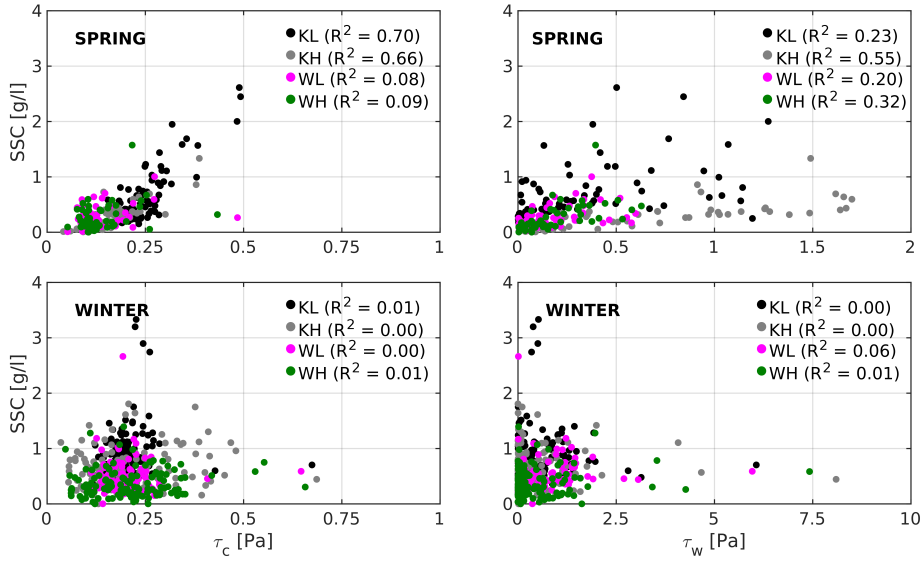

Figure 5.3: Tide averaged SSC measured at 20 cm distance from the tidal flat bed (< SSC_{20} >) as a function of current-induced (left panels) and wave-induced (right panels) tide-averaged bed shear stress. Based on a linear regression analysis, the R-squared value is indicated per each site, during both spring (green markers) and winter (black markers) measurement periods.

The variation of SSC can only partially be explained at tide-averaged timescales. In the next Section we therefore investigate the effect of wind on SSC, bed shear stress and suspended sediment fluxes at intra-tidal timescale.

5.3.3. SSC AND SSF VARIATIONS AT INTRA-TIDAL TIMESCALE

As demonstrated in Chapter 4, the residual flow over a tidal cycle is particularly influenced by specific wind directions. In this section we investigate the role of such wind-dominated conditions on the residual sediment transport. We therefore expand the intra-tidal relationships provided in Figures 4.4 and 4.5, introducing the variations in wave- and current-induced bed shear stress, SSC, SSF and time-integrated SSF, during the three analyzed wind scenarios (S1: absence of wind; S2:

SW wind; S3 NE wind).

The Eulerian asymmetries in the hydrodynamic forcing (Chapter 4) affect the intratidal asymmetries in SSC (Figures 5.4 and 5.5). During no-wind conditions (S1) the wave-induced shear stress is approximately zero. The flow is flood dominant and results in current-induced bed shear stress up to 0.8 Pa during flood, and 0.5 Pa during ebb, at K_L. The SSC is larger during flood (maximum 1.8 g/l) than during ebb (maximum 0.35 g/l). Ebb flows at site K_H instead, resulted in maximum current-induced bed shear stress of 0.2 Pa; such stress is not enough to transport or resuspend sediment, and therefore the SSC is close to zero.

The intratidal variation in SSC is especially asymmetric during scenario S2. The maximum SSC during ebb increases up to 10 g/l and 4 g/l at K_L and K_H, with respect to the S1 scenario. Significant wave heights up to 0.37 m at K_L and 0.30 m at K_H result in a relatively symmetric wave-induced shear stress over the tidal cycle. The flow velocity peaks during ebb result in slightly larger current–induced stress peaks (3% larger at K_L, 25% larger at K_H) compared to the flood phase. The peaks in SSC during the ebb phase – compared to the no-wind scenario – are therefore not fully explained by the increase in shear stress.

During the flow-reversal scenario (S3) the wave-induced stress was high (up to 3 Pa at both sites) but despite these high bed shear stresses the SSC was relatively small. Apparently, despite the much larger wave heights and comparable water levels, the maximum SSC during scenario S3 was much smaller than during S2.

The effect of wind on the SSF variation (lower panels of Figures 5.4 and 5.5) is comparable for the two locations. As the water depth, flow velocity, and SSC are larger at K_L, the resulting SSF is one order of magnitude larger at K_L than at K_H (note the different vertical axes in the two figures). The magnitude of the cross-shore sediment transport (dashed lines) is smaller than the long-shore transport (solid lines), but the response to wind action of the two components is similar. The SSF was considerably higher during scenario S2. At K_L, the time-integrated SSF at the end of the tidal period (representative for the residual transport over the tide) increased up to three orders of magnitude compared to scenario S1. At K_H, the reversed ebb during scenario S3 resulted in a flood-directed residual transport an order of magnitude larger (3.4×10^3 kg/m) compared to scenario S1 (2.5×10^2 kg/m). The (ebb-directed) net flux in scenario S2 (-9.6×10^3 kg/m) was even three orders of magnitude larger compared to S1.

In the next section the SSF and time-integrated SSF are analysed over the full 2016 measurement period (i.e. at monthly timescales) and related to hydrodynamic forcing and bed level changes.

5.3.4. SSF VARIATION AT MONTHLY TIMESCALE

The wind-induced modifications of water depth, flow velocity and SSC lead to a large variability in SSF (Figure 5.6[b],[c]) over the spring 2016 measurement period. The large impact of wind even obscures any spring-neap variation in the SSF. The time-integrated SSF reveals that over the full observation period the net sediment transport was negative (sediment export) at K_L, and slightly positive (sediment import) at K_H.

Figure 5.6[d],[e] reveal that the bed shear stress related to currents is larger at K_L than at K_H (submerged period average 0.25 Pa and 0.17 Pa, respectively) whereas the wave-induced shear stresses are higher at K_H than at K_L (submerged period average 0.63 Pa and 0.33 Pa, respectively). The bed level is more dynamic at the higher mudflat and more stable at the lower mudflat: the bed eroded 1 cm at K_L while it gained 6 cm at K_H (Figure 5.6[f]).

At K_H the time-integrated fluxes are positive during periods that the bed elevation increases (orange boxes in Figure 5.6[c],[f]) and negative during periods that the bed elevation decreases (purple boxes in Figure 5.6[c],[f]). Such a relationship does not exist at K_L (purple and orange boxes in Figure 5.6[b],[f]). Furthermore, at K_L the magnitude of the instantaneous SSF is larger than at K_H; even though the bed level shows less variability over the measurement period. The

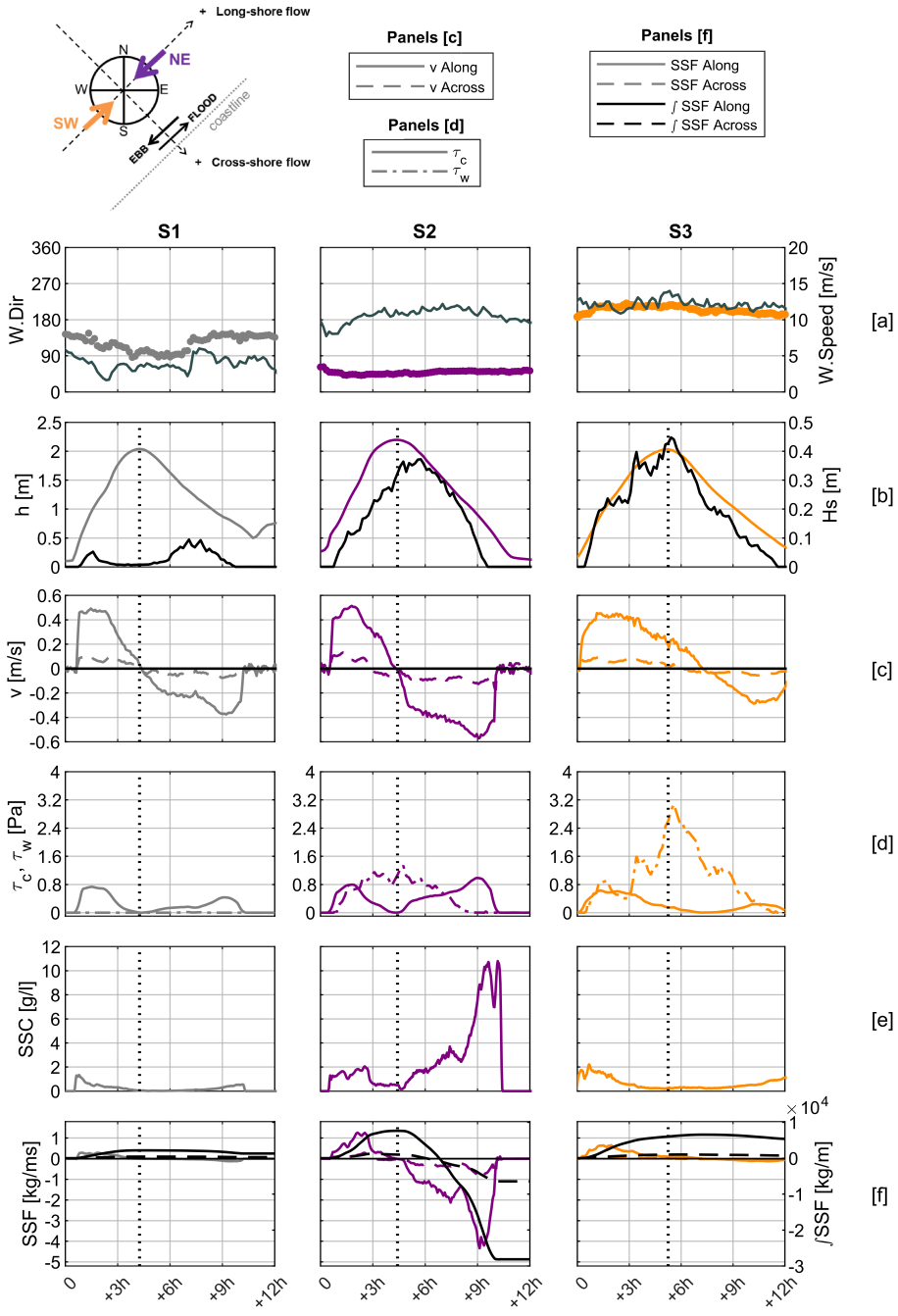

Figure 5.4: Intratidal Variation of the variables measured at K_L during the three wind scenarios.**[a]** Wind speed and direction, **[b]** water level and wave height, **[c]** long-shore and cross-shore flow velocity, **[d]** current and wave induced shear stress,**[e]** SS, **[f]** SSF and time-integrated SSF. The wind scenarios, as analyzed in Figure 4.4, occurred on the following dates: S1 (No-wind) on May 7 2016, S2 (SE wind) on May 12 2016, S3 (SW-wind) on April 29 2016.

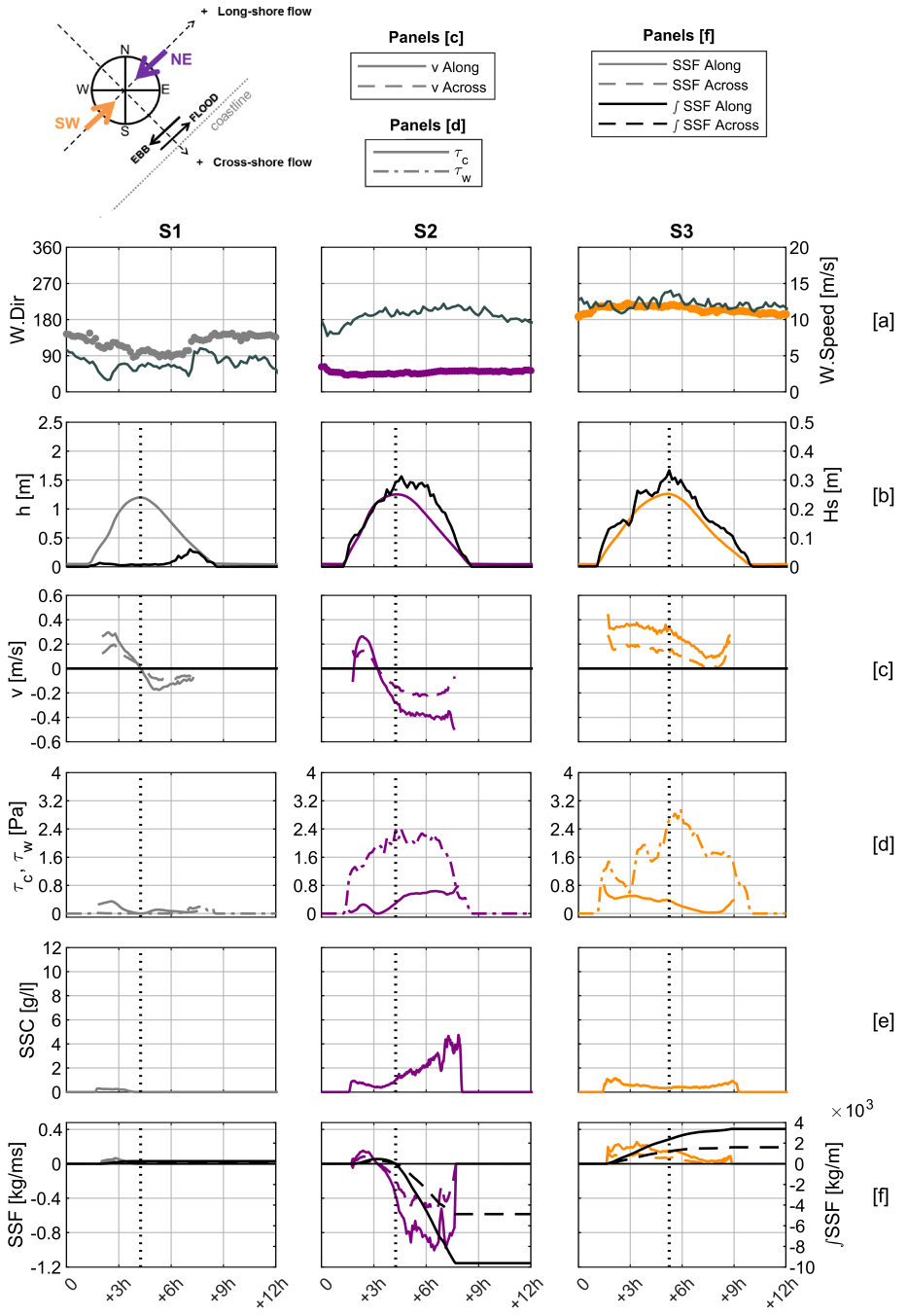

Figure 5.5: Intratidal Variation of the variables measured at K_H during the three wind scenarios.**[a]** Wind speed and direction, **[b]** water level and wave height, **[c]** long-shore and cross-shore flow velocity, **[d]** current and wave induced shear stress,**[e]** SS, **[f]** SSF and time-integrated SSF. The wind scenarios, as analyzed in Figure 4.4, occurred on the following dates: S1 (No-wind) on May 7 2016, S2 (SE wind) on May 12 2016, S3 (SW-wind) on April 29 2016.

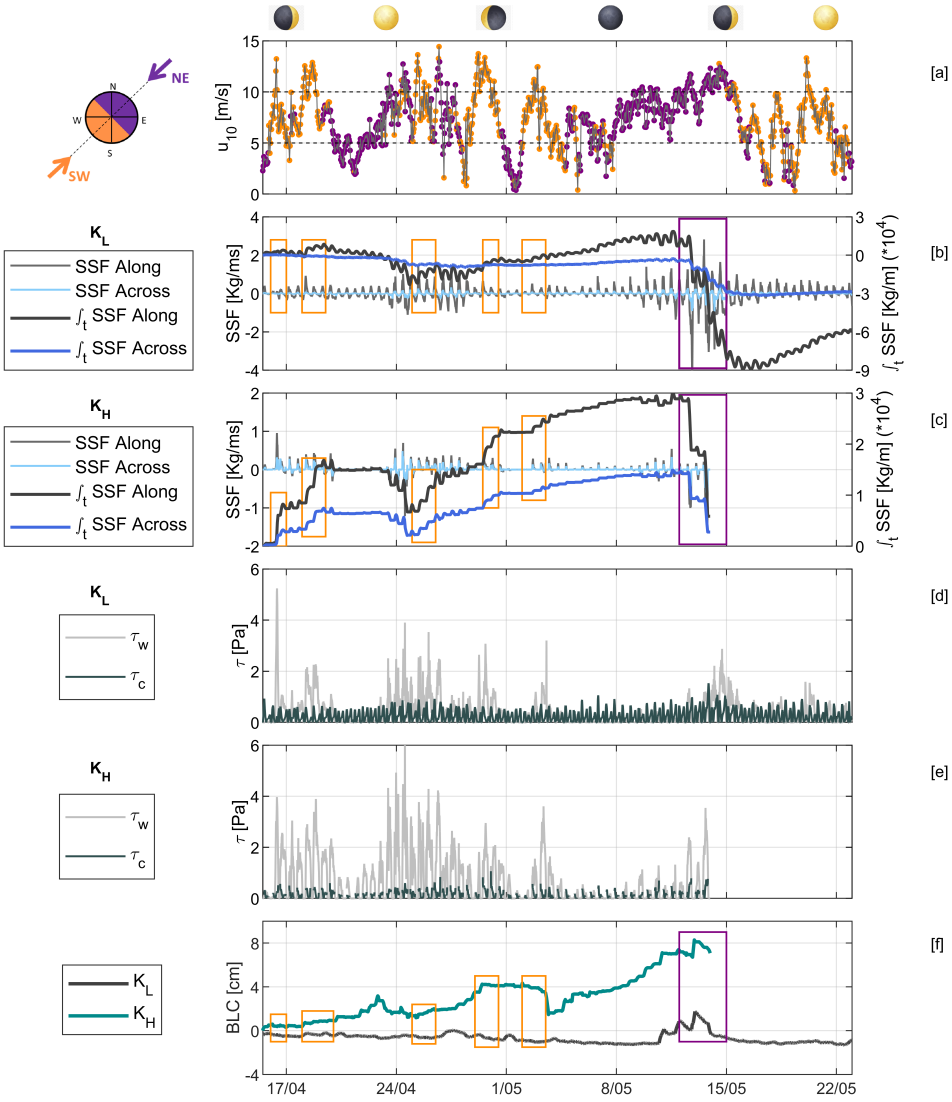

Figure 5.6: **[a]** Wind speed u_{10} and direction (color of the markers); **[b]**,**[c]** Long-shore and cross-shore SSF and time-integrated SSF in the positive (up-channel, representing import) and negative (down-channel, representing export) direction, respectively at K_L and K_H; **[d]**,**[e]** Current and wave induced shear stresses, respectively at K_L and K_H; **[f]** Bed level change at K_L and K_H. The value of the bed elevation is indicated as zero at the beginning of the measurement period. The boxes indicate specific wind events for which the boxes are colored orange in case of SW wind and purple in case of NE wind.

data also suggests a minor effect of waves on bed level changes at K_L: SW wind results in relatively high wave-related bed shear stress (up to 4 pa), but not necessarily in bed erosion.

These effects of the wind direction on the suspended sediment fluxes are also observed during spring 2017 and winter 2018 (Figure 5.7. The SSF during winter is larger compared to spring, due to the larger flow velocities (wind driven flows, see 4) and larger amount of sediment in suspension. NE wind conditions (gray bars) indicate sediment export (i.e. decreasing time-integrated fluxes) similarly to the observations in 2016.

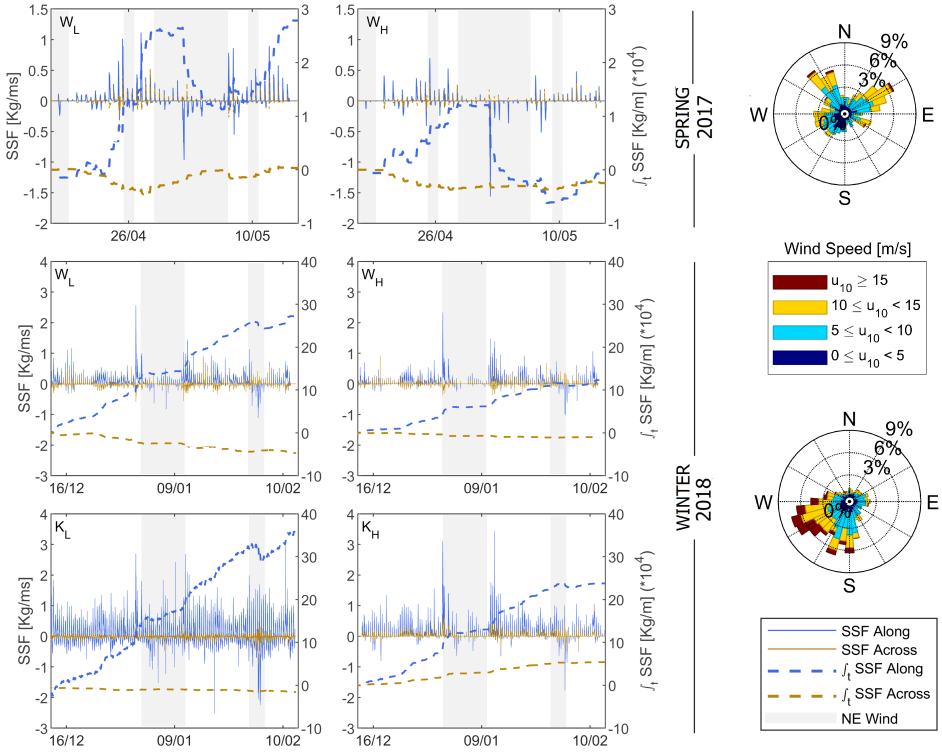

Figure 5.7: Suspended Sediment Fluxes (left y-axis) and time-integrated Suspended Sediment Fluxes (right y-axis) during the 2017 and 2018 measurement periods. Gray bands indicate the period of NE wind inducing down-channel fluxes. Wind roses referred to the 2017 spring measurement period and 2018 winter period are included, showing the different frequency of wind from the NE. During the 2017 spring campaign, a relatively frequent wind from the NE sector generated down-channel sediment fluxes.

Overall this monthly-timescale analysis suggest that different wind directions (at our sites SW and NE) have different effects on residual suspended sediment fluxes, ultimately affecting the (short-term) changes in bed elevations. These short-term changes however, do not only relate to the instantaneous hydrodynamic forcing, but also to the hydrodynamic and sediment transport conditions day to weeks earlier.

5.3.5. THE EFFECT OF WIND DIRECTION ON RESIDUAL TRANSPORT

The effect of wind on residual SSF is further investigated using the 2018 winter time series in Figure 5.8. In contrast to the spring 2016 observations, the residual SSF is estimated using velocity profiles

and observations of SSC at several heights above the tidal flat bed (which were not available in 2016).

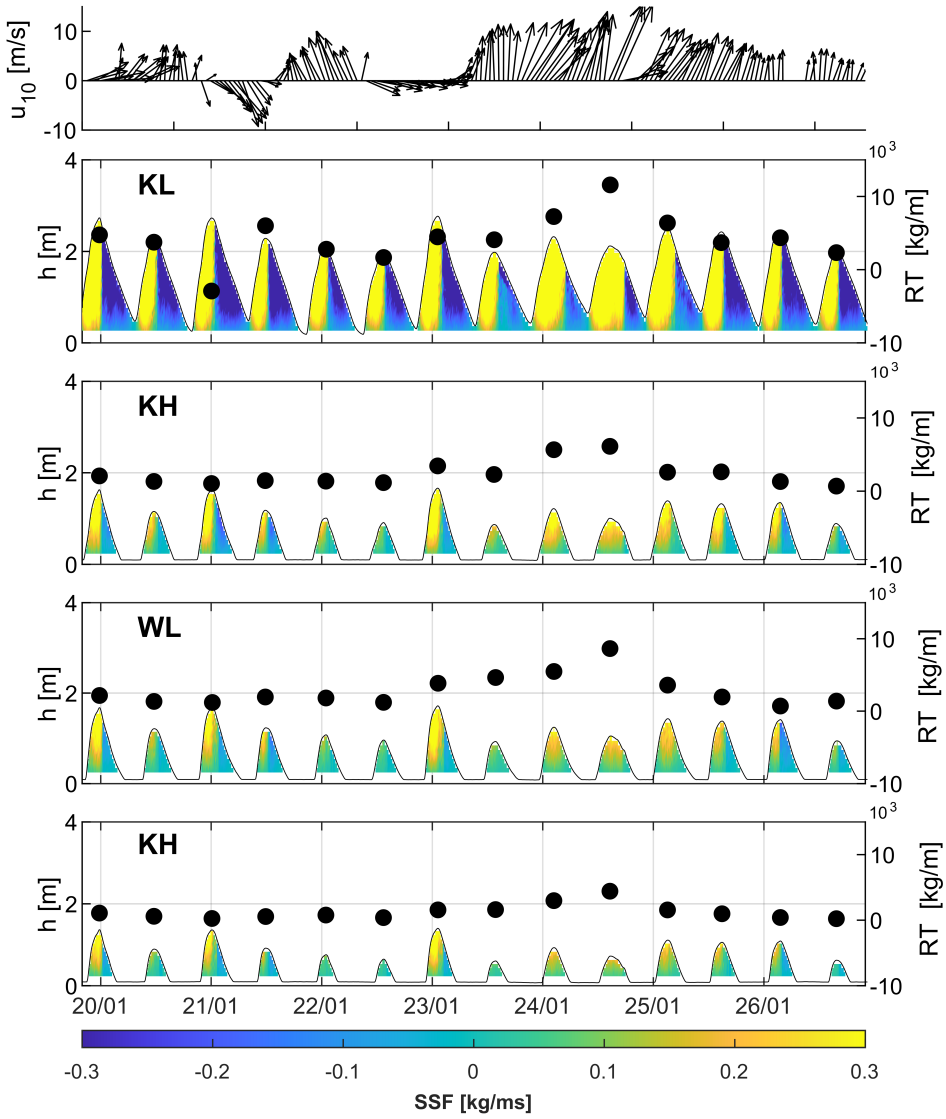

Figure 5.8: Time series of SSF over the full water depth, estimated using the velocity profile (ADCP data), the SSC at different heights above the bed and the water depth. The time series refers to the period January 20-27, 2018. The black markers indicate the Residual Transport (RT). Positive RT indicates sediment import (flood-directed and on-shore directed), negative RT indicates sediment export (ebb-directed and off-shore directed).

The effect of the wind direction on the net sediment transport is similar in winter (Figure 5.8) as in the spring observations discussed earlier (Figures 5.4 and 5.5). The residual transport is positive (i.e. sediment import) during SW wind, e.g. period January 23-27. In particular on January

25, wind speeds up to 20 m/s result in flood directed (positive) flow during the full tidal cycle (i.e. ebb flow reversal) at sites K_H, W_L and W_H. At site K_L these wind conditions resulted in a flood dominant sediment transport with residual transport of $14x10^3$ kg/m. In contrast, the NW wind conditions around January 21 generated sediment export at site K_L (-5 kg/m), due to ebb dominance of the flow velocity and SSC, similar to scenario S2 in Figure 5.4. At the other sites the residual transport was approximately zero: sediment was briefly imported during flood, whereas a long ebb directed flux exported sediment during most of the tidal cycle. The relatively high flow velocity and SSC during flood compensated the longer period with weaker sediment export. All

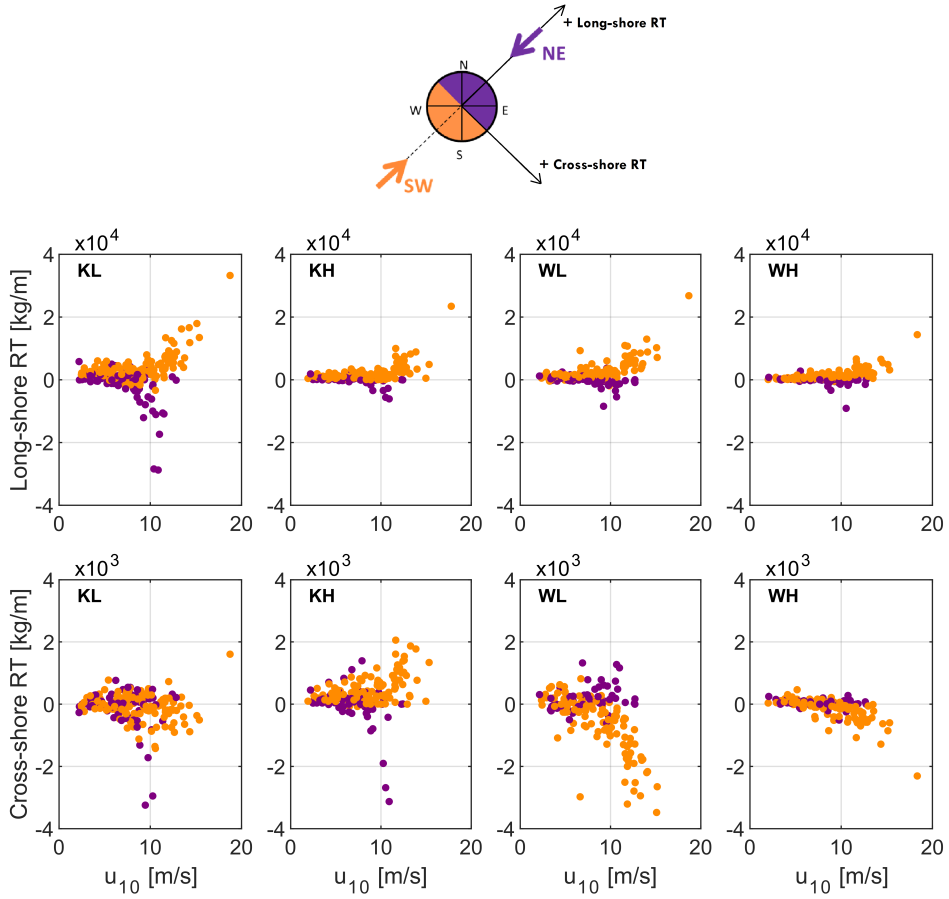

Figure 5.9: Residual transport (RT) in long-shore and cross-shore direction estimated for all tidal cycles measured during the three field campaigns, i.e. totally 716 tidal cycles. The cross-shore RT is one order of magnitude smaller than the long-shore one (notice the different y-axes limits).

residual sediment fluxes collected during the three field campaigns (i.e. a total of 716 tidal cycles) in relation to wind forcing are summarised in Figure 5.9. These observations reveal that the long-shore residual transport is an order of magnitude larger than the cross-shore residual transport. The effect of wind direction on long-shore transport is the same as for long-shore flow (Figures 4.9

and 4.10), with SW winds resulting in sediment import (i.e. up-channel transport), and NE winds resulting in sediment export (i.e. down-channel transport). Figure 5.9 also suggests that a (tide-averaged) 10 m/s wind speeds is, for the residual transport, more or less a threshold value, above which the residual transport increases linearly with the wind speed itself (both cross-shore and long-shore).

The cross-shore component of the residual transport at the Westhoek transect, behave oppositely compared to Koehool transect: negative (i.e. off-shore directed) with SW winds and positive (i.e. on-shore directed) during NE winds. The cross-shore residual transport at K_L is less wind-dependant; at this site the difference in magnitude between the long-shore and cross-shore component is the largest among the four sites. Although the cross-shore components of the residual transport is one order of magnitude smaller, they highlight a local wind-induced circulation, which is discussed in Section 5.4.2.

5.4. DISCUSSION

5.4.1. RESUSPENSION AND ADVECTION BY CURRENTS AND WAVES

In order to generalize the impact of wind on SSC to a wider range of wind conditions, we analyze tide-averaged wind direction and speed, bed shear stresses, and SSC in more detail using SSC-Wind Roses. At both K_L and K_H the SSC increases with wind speed (larger circles at higher wind speed. For low wind speed ($u_{10} < 3$ m/s), the tide-averaged SSC is ~0.8 g/L at K_L, and ~0.3 g/L at K_H. Hence, during tide-only conditions, the sediment concentration is higher on the lower flat than on the higher flat.

At K_L the SSC increases with the current-induced bed shear stress (i.e., darker markers have a larger size in Figure 5.10[c]). Such a trend is present, but less evident, at K_H (Figure 5.10[e]). The effect of the wave-induced stress is instead more evident at K_H (i.e., darker markers have a larger size in Figure 5.10[f]) compared to K_L (Figure 5.10[b]). Apparently, variations in SSC at the higher mudflat are both related to currents and waves, whereas at the lower mudflat variations in SSC are primarily the results of a high current-induced bed shear stress.

The two locations respond differently to wind from the SW and NE. At the lower mudflat, SSC is highest during NE wind (largest circles in the NE quadrant of Figure 5.10[c],[d]), despite higher waves occurring during western winds (blue colors in the NW and SW quadrant of Figure 5.10[d]). The current-induced bed shear stress is comparable for NW and NE winds (Figure 5.10[c]). This suggests that the high sediment concentration during NE winds results from advection, rather than local resuspension. In contrast, both SSC and wave–induced bed shear stress are highest during NW winds at the higher mudflat (Figure 5.10[f]), implying a large relative contribution of local reususpension.

Eventually, the increase in sediment concentration with NE wind (especially for the lower mudflat) suggests the presence of a sediment source east of the observation locations. This may result from transport over the tidal divides, as suggested by *Sassi et al.* (2015) and *Duran-Matute et al.* (2014). Alternatively (or additionally), tidal divides can become temporal sediment sinks (*Bartholdy et al.*, 1998) from which sediment is resuspended during larger winds following a calm period. This will be elaborated in more detail in the next section.

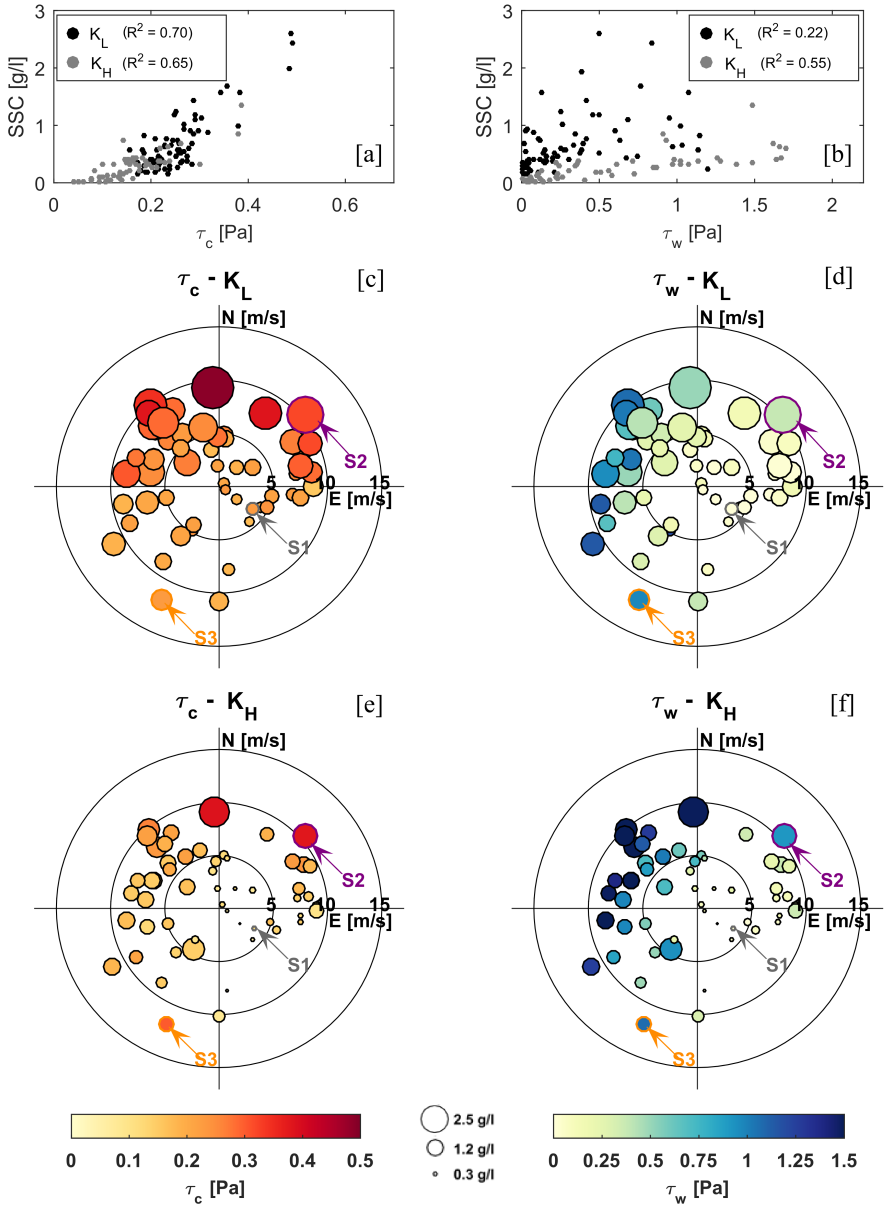

Figure 5.10: SSC-Wind Roses based on 2016 data of tide-averaged wind conditions, bed shear stresses, and SSC. Panels **[a]** and **[b]** show the tide averaged SSC versus the tide-averaged current shear stress and wave shear stress, respectively. The coefficients of determination R^2 for the linear regressions are indicated in the legends. Panels **[c]**, **[d]**, **[e]**, and **[f]** show the SSC-bed shear stress-wind roses: each marker corresponds to one tide (i.e., tide-averaged values are used). The positions of the markers in the rose are representative of the wind conditions during the tide: tide-averaged wind speed and dominant wind direction (e.g., marker position in the upper right quadrant implies a dominant wind from NE). The sizes of the markers scale with the tide-averaged SSC. In panels [c] and [e] the color of the marker indicates the tide-averaged current-induced shear stress; in panels [d] and [f] the color of the marker indicates wave-induced shear stress. The tides of the three wind scenarios are indicated. In the panels dedicated to K_L (i.e. panels [c] and[d]) only the 56 tides measured at K_H are included.

5.4.2. CONCEPTUAL MODEL OF WIND-INDUCED SEDIMENT TRANSPORT AND STORAGE IN INTERTIDAL AREAS

The strong dependency of sediment transport on wind speed and direction is related to the hydrodynamics (Section 4.4.3), but also to sediment concentration (Section 5.3.5). This is illustrated in Figure 5.11.

During dominant wind conditions the residual sediment transport is directed from the tidal channel to the higher flats: the transport is controlled by the channel, and the sediment concentration is relatively low (phase 1). The sediment deposits onto the more elevated intertidal zones including, where present, the tidal divides (phase 2). However, the majority of that sediment is only temporally deposited. Even moderate winds having directions opposite to the dominant winds generate large down-channel residual transport (export; phase 3). In this case the sediment fluxes are characterized by very large sediment concentrations. The observation that sediment is easily eroded from this temporal sediment storage implies that the material is poorly consolidated (even after weeks of phase 1 and phase 2 conditions). This conclusion is relevant for our understanding of the long-term morphodynamics of muddy intertidal flat systems.

Section 5.3.4 revealed that this sediment storage is probably less pronounced in winter than it is during spring conditions. This difference may be explained by hydrodynamic processes and by biologic processes. During winter conditions the overall prevailing hydrodynamic conditions are more energetic than in spring. Sediment therefore remains more or less permanently resuspended, and is transported by the combined tide- and wind-driven flow. Therefore much less sediment settles temporarily east of our observation site, and much less sediment is transported westward during easterly winds than was previously transported eastward. An alternative explanation, however, is that during spring conditions the sediment settles more efficiently due to biostabilisation. *Kornman and Deckere* (1998) and *De Deckere* (2003) observed that the erodibility of mudflats in the nearby Dollard Bay was lowest in the second half of April and in May because the mud was covered by diatoms, reducing the SSC in this period.

Our results are particularly important for muddy areas where the dominant wind direction is, within a certain directional spreading, aligned with the coastline, and the tidal currents are also primarily aligned with the coastline. The role of wind-driven currents is much less pronounced when the dominant wind direction is primarily normal to the coastline, or when the tidal currents are primarily in the cross-shore direction. The angle between wind and coastline depends strongly on the larger-scale geological setting, such as river mouths in estuaries or the large-scale coastal development. The alignment of along-shore tidal currents with respect to the coastline is more strongly influenced by local conditions. Many tidal flats, especially along exposed coastlines with low wave energy, develop extensive, mildly sloping foreshores where cross-shore tidal currents are stronger than long-shore currents. Long-shore tidal currents are more common in estuarine environments where tidal channels encroaching the estuarine embankments lead to steeper cross-shore profiles, or in lagoons where sheltering barriers limit the number of cross-shore tidal channels, leading to the development of long-shore tidal channels.

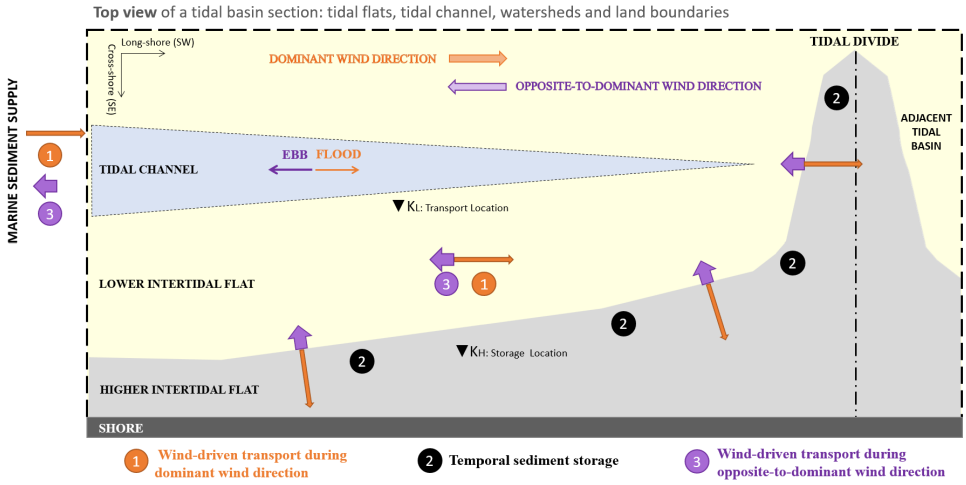

Figure 5.11: Conceptual model of wind-induced sediment transport and storage within our study site. Phase 1 (orange arrows): wind driven transport during dominant wind direction (corresponding to the direction of flood currents). Phase 2: temporal storage following phase 1. Phase 3 (purple arrows, in ebb direction): transport opposite to the dominant wind direction. The widths of the arrows relate to the SSC in the net fluxes (larger for the opposite-to-dominant wind case), whereas the lengths of the arrows relate to the number of occurrences in time (larger for the dominant wind case). The two investigated locations are included in the scheme. The transport location K_L is current dominated (i.e., advection controls the SSC), has large gross fluxes but small net fluxes, and it is characterized by limited bed level changes. At the storage location K_H, where both advection and resuspension contribute to the SSC, the net fluxes are controlled by wind speed and direction and it is characterized by larger and continuous changes in bed level.

5.5. CONCLUSIONS

The present chapter investigated the variation in suspended sediment concentrations at different timescales and spatial scales, and examined the role of specific wind conditions in resuspension and advection of suspended sediments. During non-stormy conditions the intertidal flats are characterized by larger suspended sediment fluxes in winter compared to spring, due to the higher SSC and larger flow velocity; both in turn resulting from the interaction of tidal forcing and wind driven flows. The increase in suspended sediment concentrations follows from wave-induced erosion, and persists also after the storms.

Our results suggest that sediments can be temporarily stored in the shallower areas of the intertidal system, and then easily resuspended and advected during wind events. These storage environments accumulate sediments during conditions of low to moderate winds during which transport is in the same direction as the tide-induced residual transport. This sediment is subsequently resuspended and transported back during events with winds having the opposite direction. Fairly short windy periods opposite to tide-induced residual transport may in this way balance the residual transport of sediment that occurred over longer time periods in calm wind conditions (weeks to months). This temporal storage of sediment in combination with wind-driven transport is crucial for understanding short- and long-term sediment dynamics in muddy systems, but is in general poorly accounted for in literature. During winter conditions much less sediment is temporally stored. This is probably the result of more energetic conditions (preventing sediments to deposit) but may also be attributed to bio-stabilisation of sediments in the spring period.

This study demonstrates that the crucial role of wind on tidal flat sediment dynamics not only

relates to the wave-induced resuspension, but also to the generation of wind-driven flows enhancing the tide-induced advection of sediment, ultimately affecting the net sediment transport and hence the short-term morphodynamic of intertidal areas. We expect that the results provided by this study are especially relevant at locations where the dominant wind direction and the main tidal flow direction is aligned with the coastline (such as in estuaries and lagoons, but less on exposed, broad muddy coastlines).

About the Photo

Bedforms on the upper Koehool intertidal flat are clearly visible at low tide. This photo was taken on May 26, 2016.

Explore more media content using the following QR-code.

6

WIND EFFECTS ON INTERTIDAL FLATS MORPHODYNAMICS

Previous chapters revealed the significant effects of wind on the hydrodyanmics, sediment transport and short-term morphodynamics of intertidal flats. What is the effect of the wind on the long-term developments of intertidal flats? More specifically, what are he conditions leading to a permanent increase of tidal flat elevation? A tidal flat accretes when a new layer of sediment deposits and over–consolidates. The chronological order of sediment deposition and over-consolidation provides what we define, in this chapter, as a 'window of opportunity for tidal flat accretion'. Relating wind speed and direction, with water levels, suspended sediment concentrations, bed shear stresses and bed level changes at diverse timescales, we provide evidence that wind crucially contributes in creating the conditions for the occurrence of such windows of opportunity. The quantitative analyses of consolidation timescales on muddy intertidal flats, presented in this chapter, reveals that large deposition rates substantially increase consolidation timescales, such that the abundance of sediment can be a bottleneck for the accretion of a tidal flat.

Parts of this chapter have been published as: Geomorphology, *Colosimo et al. (2023)*.
Winds of Opportunity: the Effects of Wind on Intertidal Flat Accretion.
co-authors: D.S. van Maren, P.L.M. de Vet, J.C. Winterwerp, B.C. van Prooijen

Ch 6: Wind Effects on Intertidal Flats Morphodynamics

Main Research Question

RQ3: How are phases of accretion and erosion of intertidal flats influenced by wind?

Keypoints

Keypoint 1: The sequence of sediment deposition and over-consolidation phases forms a Window of Opportunity for net tidal flat accretion.

Keypoint 2: Large (small) bed shear stress do not imply erosion (deposition), and vice versa.

Keypoint 3: Large mud deposition rates hamper the vertical accretion of tidal flats.

Keypoint 4: Wind-induced set-down promotes over-consolidation through more aerial exposure.

Implications for Fine Sediment Nourishments

When designing fine sediment nourishments it is advisable to quantify the depositional rate and the related consolidation timescales at the targeted intertidal sites.

6.1. INTRODUCTION

Predicting the morphological evolution of intertidal systems is complex, partly due to the variability in timescales that control sedimentation and erosion, ranging from intra-tidal to seasonal timescales (*Yang et al.*, 2012; *Sassi et al.*, 2015). At the intra-tidal timescale, sediment deposits around high water slack, when the flow is weak and the wave-induced resuspension rates are low. This has been especially observed at intertidal flats bordering macro-tidal estuaries where slack water conditions last several hours (e.g. *Deloffre et al.*, 2007). In micro-to-meso tidal systems, this intratidal variability in wave-induced resuspension is smaller because of smaller fluctuations in the water depth. In these systems the very shallow water depths (smaller than 20-25 cm) represent conditions with the largest changes in bed level (*Shi et al.*, 2017a; *Zhu et al.*, 2017). On the Jiangsu coast (China) changes in bed level during such conditions contribute up to 33% of the changes over a full tidal cycle (*Shi et al.*, 2017a). At seasonal timescales, the alternation of storm and fair weather dictates the changes in bed elevation (*Yang et al.*, 2003; *Fan et al.*, 2006; *Yang et al.*, 2008; *Belliard et al.*, 2019), with storms resulting in erosion (*Yang et al.*, 2023) but also in relatively large sedimentation (*Turner et al.*, 2006; *Li et al.*, 2015). Superimposed on seasonal effects resulting from wave energy are the effects of biota (*Le Hir et al.*, 2007). In muddy areas algae mats may reduce erosion rates in summer due to strengthening of the bed (*Kornman and Deckere*, 1998; *Paterson and Hagerthey*, 2001) but also because bedforms and therefore bed roughness is smaller (*Malarkey et al.*, 2015; *Parsons et al.*, 2016). Erosion can also be enhanced by biota by making sediment available for erosion or modifying the critical shear stress for erosion (*Van Prooijen and Winterwerp*, 2010; *Orvain et al.*, 2012).

Where the erosion of sandy beds mainly depends on the hydrodynamic forcing and grain size, erosion of muddy or mixed sand-mud beds is more complex. In sand-mud mixtures the mud content influences erodibility of the bed, especially influencing the critical shear strength against erosion (*Mitchener and Torfs*, 1996; *Van Ledden et al.*, 2004; *Van Rijn*, 2020). Selective erosion of different particles may also lead to armouring (*Sanford*, 2008; *Le Hir et al.*, 2011) which may lead to vertical layering of sandy and muddy deposits (*Fan and Li*, 2002; *Fan et al.*, 2002). The substrate also influences development of biota which in turn leads to preferential development of a muddy or sandy substrate (*Garwood et al.*, 2015). Crucial to muddy environments is that at a sufficiently high mud content, the density and permeability of the sand-mud mixture will vary over time through consolidation processes (*Torfs et al.*, 1996; *Van Rijn and Barth*, 2019) influencing the shear stress of the bed and therefore influencing its resistance against erosion over time.

In submerged conditions, sediment consolidation is driven by the reduced gravity of the sediment bed (determined by the difference in density between sediment bed and water) controlling the consolidation rate (*Been and Sills*, 1981). Pore water is expelled by the weight of the consolidating sediment bed resulting in particle rearrangement and compaction (decreasing the bed porosity and thickness, while increasing the bulk density) - see e.g. *Merckelbach and Kranenburg* (2004). A submerged sediment bed consolidating under its own weight only slowly develops shear strength and therefore resistance against erosion (for instance during storm events). However, when a tidal flat emerges, it becomes also subject to vertical compaction driven by capillary suction (*Winterwerp et al.*, 2021). This under-pressure is generated by a lowering of the phreatic level within the mudflat bed driven by the falling tide. The suction head (i.e. the difference between bed level and phreatic level) increases with bed elevation due to the asymmetry in ingress and egress of pore water across the tidal flat (*Riedel T. and H.J.*, 2010). As a result, the sediment bed becomes over-consolidated (the bed is more consolidated than could be expected from self-consolidation). The shear strength of the bed is high resulting from larger pressures experienced in the past. The contribution of this phenomenon to bed compaction is crucial, as under-pressures induce stresses in the upper parts of the bed which are orders of magnitude larger than the self-weight stresses by reduced gravity (*Winterwerp et al.*, 2021).

The paragraph above illustrates how bed emergence influences consolidation rates and hence shear strength of the sediment bed. This implies that the erosion rates of intertidal areas (e.g. during storm conditions) is strongly influenced by its inundation history, especially the duration for which the flat is emerged. And although many studies have addressed the morphodynamic behaviour of intertidal areas (*Allen and Duffy*, 1998; *Janssen-Stelder*, 2000; *Bassoullet et al.*, 2000; *Green et al.*, 2000; *Le Hir et al.*, 2000; *Shi et al.*, 2012; *Zhu et al.*, 2017; *Shi et al.*, 2017a), no systematic studies have been executed investigating morphodynamic changes of the bed in response to inundation history. Especially in microtidal environments (with a tidal range less than 2 m) the inundation history may be strongly influenced by meteorological conditions due to storm setup or setdown.

An example of such a microtidal environment is the Dutch Wadden Sea. The tidal range in the Western Wadden Sea is less than 2 meters, while the annually recurring storm surge is 1.88 meter (*Vuik et al.*, 2018) and periods with storm set-down also regularly occur (not yet documented in literature). Winds have a pronounced impact on the residual water flux through the basin (*Duran-Matute et al.*, 2014, 2016; *Sassi et al.*, 2016). Large parts of the Western Wadden Sea are very muddy (see Chapter 3, Chapter 5 or *Colina Alonso et al.* (2021)), therefore providing an example of a system where (1) meteorological effects strongly influence the residual flow as well as inundation frequency and period and (2) erosion processes are influenced by consolidation of the bed. This study aims to advance our understanding of the morphodynamics in this microtidal storm-influenced environment by analysing in detail the hydrodynamic and sedimentary processes over a muddy tidal flat. For this purpose we have collected detailed field observations at four sites during contrasting meteorological conditions covering winter and spring time periods.

6.2. METHODOLOGY

Field data obtained during spring and winter field campaigns (2016, 2017, 2018) is used in this chapter, to analyze the effect of diverse meteorological conditions on bed level changes at different timescales. As reported in detail in Chapter 3 we obtained data for consecutive 73 and 56 tidal cycles, respectively at sites K_L and K_H during spring 2016 (Table 3.3), during 51 and 52 tidal cycles, respectively at sites W_L and W_H during spring 2017 (Table 3.4), and eventually during 124, 122, 120 and 120 tidal cycles respectively at sites K_L, K_H W_L and W_H in winter 2018 (Table 3.5). Totally, we hence measured hydrodynamics and sediment transport over 718 tidal cycles. During 615 tidal cycles (i.e. excluding the 2017 field campaign) we further measured local bed level changes. During 589 tidal cycles (i.e. excluding the 2016 field campaign) the flow velocity along the full water column was further measured. This dataset is combined with publicly available wind dataset, having 1 hour frequency, gathered at the *Koninklijk Nederlands Meteorologisch Instituut, KNMI* meteorological station of Leeuwardeen.

6.3. RESULTS

6.3.1. BED LEVEL CHANGES OVER TIDAL TO YEARLY TIMESCALES

Over a 6-years time period, the maximum bed level increase measured about 20 cm at Westhoek and 30 cm at Koehool (see Figure 3.1[d] of Chapter 3), implying a yearly-averaged (maximum) bed level increase of ~3 cm and ~5 cm, respectively. Throughout this paper we will refer to the settling of particles on the bed as *sedimentation* or *deposition*, whereas a net increase in the bed level over longer timescales is referred to as *accretion*.

At monthly timescales, similar magnitudes in net changes are observed using the ADV bed level observations (Figure 6.1). Over the two-months winter measurement period, the bed erodes at all observation stations. Along each transect, the net erosion is larger at the seaward location

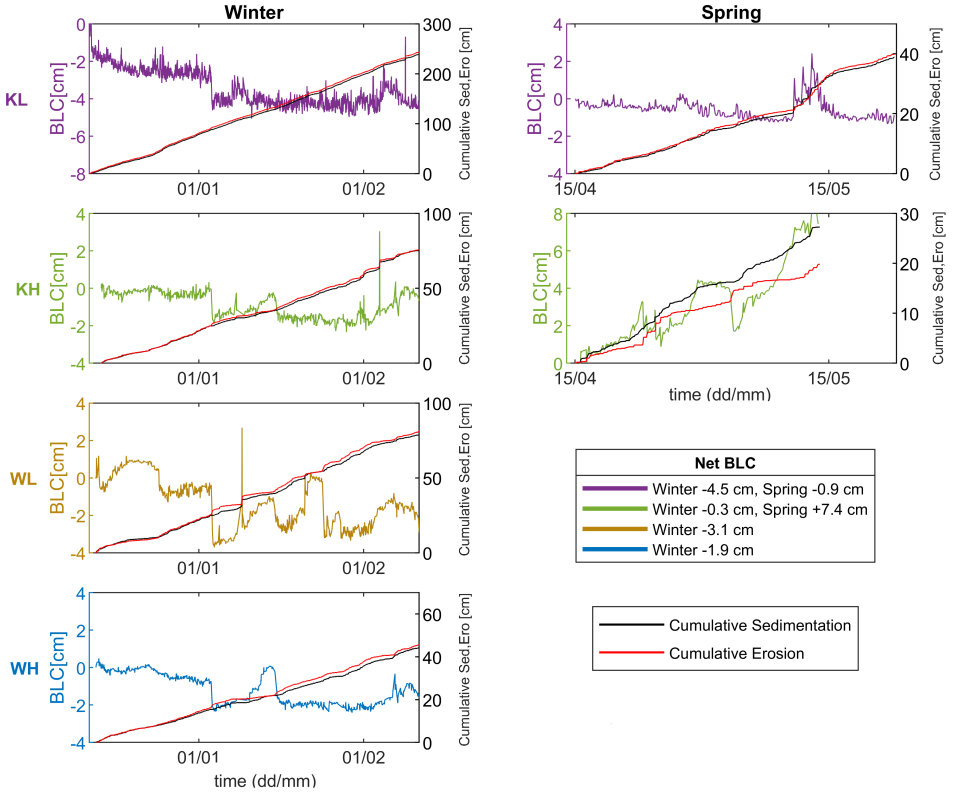

Figure 6.1: Bed levels (BLC, left panel) and cumulative erosion / deposition (right axes) measured in winter (left panels) and spring (right panels) for the four observation stations. One event with 16 cm deposition on January 8 is excluded from site KH (discussed in detail in Section 6.3.3.) Cumulative deposition is defined as the summation of bed level increase (and cumulative erosion the summation of bed level decrease). With bed level data available at 40-minute intervals this differentiation represents tidal variability but not short-term variability resulting from e.g. turbulent fluctuations.

compared to the landward location: -0.3 cm and -4.5 cm (respectively) at KH and KL (Koehool transect); -1.9 cm and -3.1 cm (respectively) at WH and WL (Westhoek transect) - all well within the accuracy range of the ADV (*Shi et al.*, 2015). Over the one-month spring measurement period the bed elevation was rather stable at KL, with a few episodes of sediment deposition around May 15, resulting in a bed level increase of ~2 cm, directly followed by erosion. In contrast, site KH experienced a net accretion of 7.4 cm.

The cumulative sedimentation and erosion per site (Figure 6.1) reveals how bed variability varies over space and time. The bed variability decreases with bed elevation: the cumulative sedimentation and erosion are lowest at the most elevated site WH (45 cm in winter) and highest at the lowest site KL (250 cm in winter, 40 cm in spring), with intermediate values around mid-flat (WL and KH, both 80 cm in winter and 25 cm for KH in spring). The bed is most dynamic in winter. The lower flat (KL) is about 3 times more dynamic in winter compared to spring: both the cumulative (gross) sedimentation and erosion equal ~250 cm in two winter months and ~40 cm in one spring month. The higher flat (KH) is about 1.5 times more dynamic in winter compared to spring: the

cumulative sedimentation is ~80 cm in two winter months and ~25 cm in one spring month.

Over tidal timescales, the largest net bed level changes (both deposition and erosion) occur at relatively small bed shear stress (1-1.5 Pa) - see Figure 6.2. Surprisingly, large erosion rates are not related to large bed shear stresses (4-12 Pa) which typically result from wind speeds above 10 m/s (top right in Figure 6.2). Another important observation is that the bed level changes on tidal timescale decreases up flat, while bed shear stresses increase up flat (Figure 6.2, left panels).

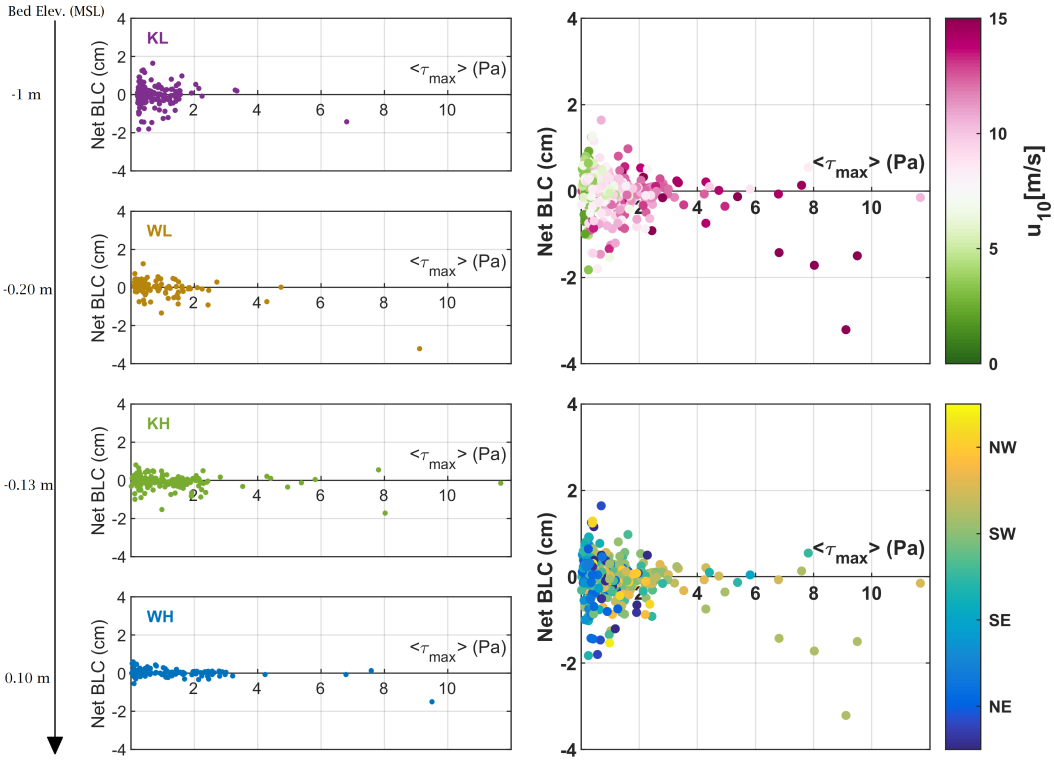

Figure 6.2: Net bed level changes (BLC) per tidal cycle (one marker represents one tidal cycle) as a function of tide-averaged maximum bed shear stress at each site (left panels). The right panels include the net BLC measured at all sites. Upper right panel: BLC as a function of tide-averaged maximum bed shear stress and wind speed; lower right panel: BLC as a function of tide-averaged maximum bed shear stress and wind direction. The combined wave-current bed shear stress has been computed using (*Soulsby*, 1995)'s method.

6.3.2. STORM-INDUCED EROSION AND POST-STORM RECOVERY

Two different erosion types can be observed in the dataset. First, during periods with weak–to–moderate winds ($u_{10} < 10 m/s$) – mainly occurring during Eastern winds – the bed shear stresses are fairly low (maximum 1-3 Pa, depending on the site); these conditions result in sediment deposition (I.e. bed level increase) but also in relatively large bed erosion (up to 2 cm/tide, as already found in Figure 6.2, right panels). The large erosion rates at relatively small bed shear stress suggest that the bed is poorly consolidated. This type of erosion (rapid erosion of poorly consolidated material at low bed shear stress) becomes more prominent in upflat direction (as also suggested

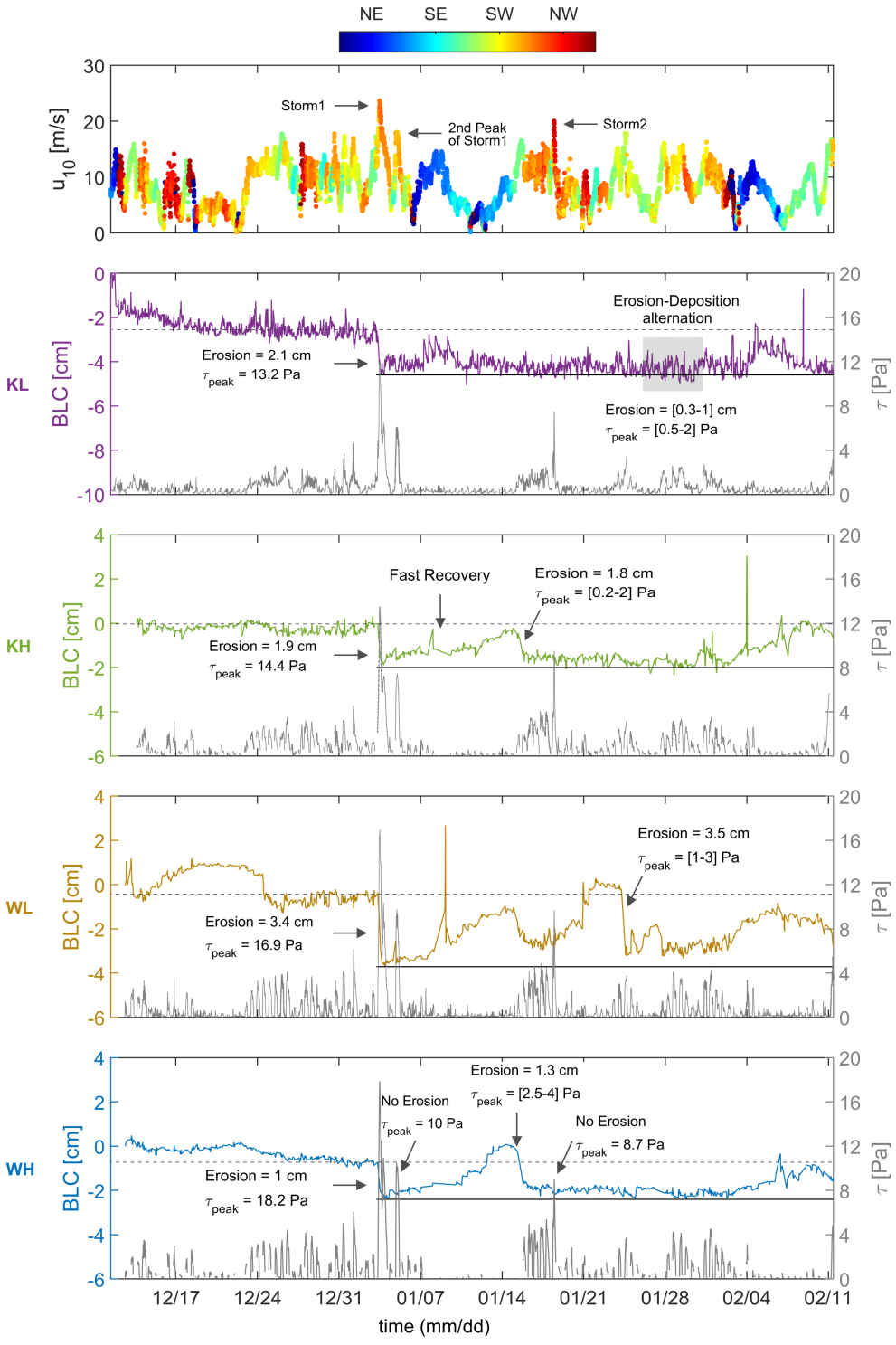

Figure 6.3: Time series of wind, bed level changes (left-axes) and maximum wave-current bed shear stress (right-axes) during the winter measurement period. The dashed vertical lines indicate the moment of the first and second storms (January 3 and 16, respectively).

by the tide-averaged analysis in Figure 6.2).

The second erosion type occurs during periods with relatively strong winds ($u_{10} > 10 m/s$, mainly during Western winds) which lead to bed shear stresses larger than 1.5 Pa (and up to 12 Pa). Erosion rates are large during storm events ('Storm1' resulted in bed erosion of 1-3.5 cm over the flats; see Figure 6.3). Such erosion events have a long-lasting effect (weeks/months) because the sediment deposited after the storm is easily eroded, as will be evaluated hereafter.

Post-storm sediment deposition rates are large: at KL, for instance, the bed elevation increases by 1.5-2 cm during 2-3 days of Eastern wind (January 9-11 and Feb 4-6 with u_{10} up to 15 m/s). In both cases the freshly deposited sediment is eroded again at relatively small bed shear stress (< 1 Pa), resulting in an elevation setback corresponding to the post-storm elevation. At site KL, the bed does not even recover from the storm–induced erosion over the whole subsequent measurement period. At higher bed elevations (sites WL, KH and WH), the bed recovers on average by 95% within the 12 days following the storm (January 3-15), with highest deposition rates (up to 0.5 cm/tidal cycle) occurring during Eastern wind (January 7-15). But also for these higher sites the strength of the bed is weaker than before the storm. An event with a relatively small bed shear stress (1-3 Pa on January 16) occurring directly after the sediment deposition period, completely eroded the bed back to its post-storm level, similar to KL. During the second storm (January 18, 'Storm 2'), western winds up to 21 m/s resulted in bed shear stresses up to 10 Pa but, even under such high bed shear stress none of the sites exhibited erosion. The bed level at all sites remained at the bed level attained after the erosion event of January 16, i.e. approximately the bed elevation after 'Storm 1'.

These observations indicate that storms erode the bed until a level in which the strength of the bed is too large to erode further. Post-storm sediment deposition is large but the strength of these fresh deposits is low. Rapid erosion of the post-storm sediment deposits follows, even during periods of relatively small bed shear stress. No new equilibrium with a stable bed was attained within the observational periods. We hypothesize that such a new equilibrium can be reached after sufficiently long periods of emergence, as will be explained in more detail in section 6.3.5.

6.3.3. DEPOSITION EVENTS

Deposition rates are highest during two specific events: the passage of highly concentrated turbid fringes and fluid mud formation. Their impact on deposition rates will be investigated in more detail below, using observations on intratidal timescales.

DEPOSITIONAL TURBID FRINGES

A satellite picture (September 23, 2017) shows a turbid band near the study area (Figure 6.4). Highly turbid zones are noticed especially at the intertidal areas surrounding the Kimstergat tidal channel. Such turbid bands result in sharp peaks in the SSC typically occurring at the beginning and/or at the end of a submergence period. They are referred to as turbid fringes (*Green*, 2003). In the Wadden Sea, such turbid fringes are particularly observed when calm weather conditions follow relatively energetic tides with considerable wave-induced resuspension. As such they are more common in the more energetic fall/winter period. We will further explore the role of the turbid fringe by examining a period in our dataset (January 10, Figure 6.5) with meteorological conditions very similar to those in Figure 6.4 (southern wind with speed lower than 5 m/s).

The tides are asymmetric with a shorter rising stage than falling stage resulting from the shallow water depth (especially at water depths below 20 cm, which is not recorded by the instruments). As a result the suspended sediment concentration SSC peaks up to 3 g/l shortly after inundation, and rapidly decreases in concert with the rising bed levels (Figure 6.5), suggesting the passage of a depositional turbid fringe. Deposition rates during the passage of the turbid fringe were larger at Westhoek compared to Koehool: 0.45 cm in 1 h (i.e. 0.45 cm/h) at WH, 0.44 cm in 1

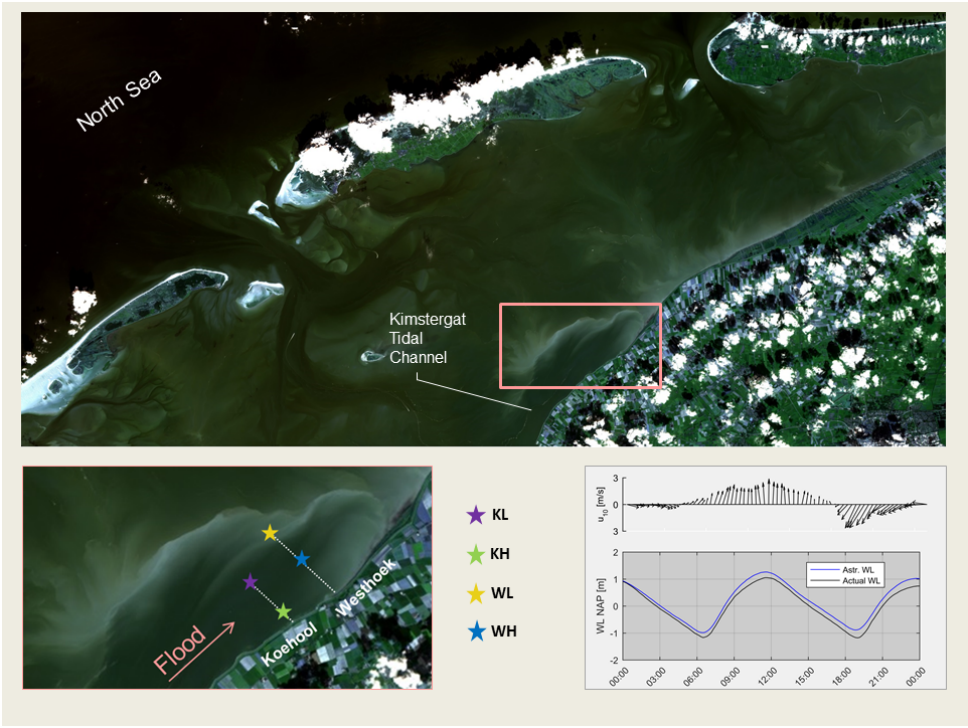

Figure 6.4: Satellite picture of a turbid fringe on September 23, 2017 in our study site: overall view (top), detail (lower left) and water level and wind conditions on September 23 2017 (lower right: wind below 3 m/s from the South and a water level set-down of about 20 cm.)

h and 32 minutes (i.e. 0.28 cm/h) at WL and 0.36 cm in 2 h and 22 minutes (i.e. 0.15 cm/h) at KH. Throughout our dataset, sediment deposition rates are up to 2 cm/tide in winter and 1.3 cm/tide in spring. During the following ebb, these deposits were negligibly resuspended by the weaker flow (below 0.2 m/s). The vertical OBS array at KH and WL reveal pronounced sediment stratification with SSC at 60 cmab (up to 1.5 g/l) about 30-50% smaller compared to SSC at 20 cmab (up to 3 g/l).

In order to understand how the sediment concentration at such turbid fringes relates to the stresses at the bed, we further analyse depositional events resulting in deposition rates exceeding 0.4 cm/tide, using Figure 6.6. The suspended sediment concentrations show a stronger correlation with flow velocity u_h (high SSC at high u_h) than with the wave orbital velocity u_{orb} (highest SSC actually occurring during periods of low u_{orb}). At all sites the largest SSC is observed at the smallest water depths (especially < 0.25 m) indicating the existence of concentrated turbid fringes at the tidal wave front. SSC peaks occur at the beginning of the flood (when flow velocities are highest), except for site KL (closest to the tidal channel) where ebb and flood concentrations are comparable. The observations in Figure 6.5 also indicate that at site KL the turbid fringe has a smaller effect on bed elevation. Apparently, the largest SSC (i.e. the SSC at the turbid fringe) does not occur during conditions with the largest wave-induced orbital motions, but during the period with the highest flow velocities, occurring at the beginning of the flood phase. This is in contrast with the suggestion in *Green* (2003), where the waves are identified as most important.

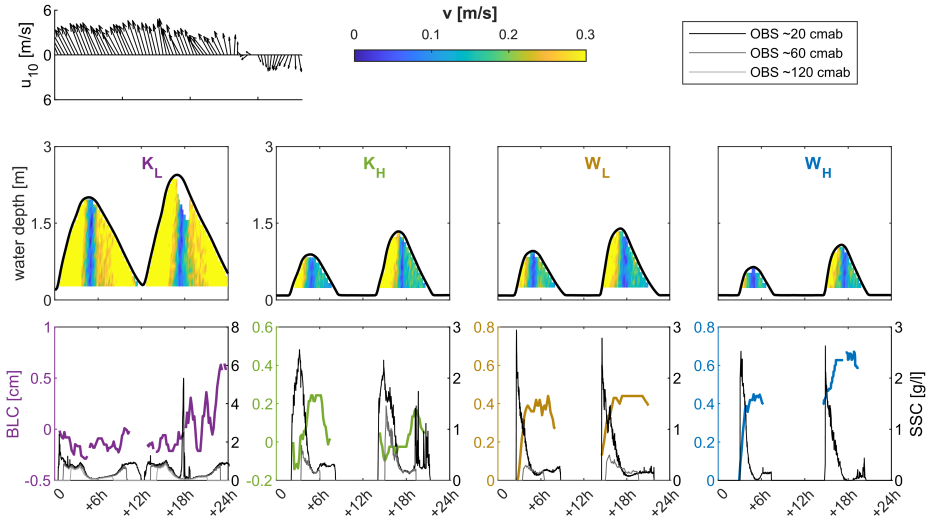

Figure 6.5: SSC (at three heights) and flow velocity observed at the four measurement sites during the passage of a depositional turbid fringe on January 10 2018. Wind conditions (top left panel) reveal that hydrometeorological conditions are similar to those in Figure 6.4.

DEPOSITION OF FLUID MUD

One event resulted in 16 cm sediment deposition at site WH (Figure 6.7). This sedimentation event directly followed the January 3-5 storm ('Storm1' in Figure 6.3), which induced on average 3 cm erosion of the mudflats. Wind conditions in the post-storm period (NE-SE wind) resulted in a set-down. As a consequence the bed remained completely emerged (or only briefly submerged) during several consecutive tidal cycles, especially at WH (Figure 6.3). On January 8 the bed level at WL increased 4 cm in 1 hour and 20 minutes (i.e. a deposition rate of 3 cm/h) during the flood phase, and was followed by stronger erosion during the ebb phase (5.5 cm in 50 minutes). The deposition and erosion rates at WH cannot be inferred from the dataset because the sensors were only shortly submerged. However, the peak in SSC up to 6 g/l and the relatively high flow velocity (~ 0.3 m/s) suggests the passage of a highly concentrated suspension close to the bed. SSC are much lower during the two tidal cycles following the rapid deposition phase (3 g/l vs 6 g/l), and deposition is only 0.5 cm per tidal cycle.

Typically, the thickness of the deposited layer is larger at higher mudflat elevations: 3 cm at KL, 4 cm at WL, 4.2 cm at KH and 16 cm at WH. These relatively high deposition rates, accompanied by peaks in SSC, especially at higher mudflat elevations, suggest that these deposits are formed by fluid mud. Fluid mud deposits up to 20 cm thick have indeed been observed in the salt marshes fringing the mudflat of Westhoek (e.g. *Baptist et al.*, 2019). However, our observations also show that despite the rapid deposition rates, such fluid mud formation has very little impact on the bed levels over longer (days-weeks) time periods (Figure 6.3). Its effect disappears within one tidal cycle (possibly also due to gravity, inducing a fluid mud transport towards the less elevated subtidal zones).

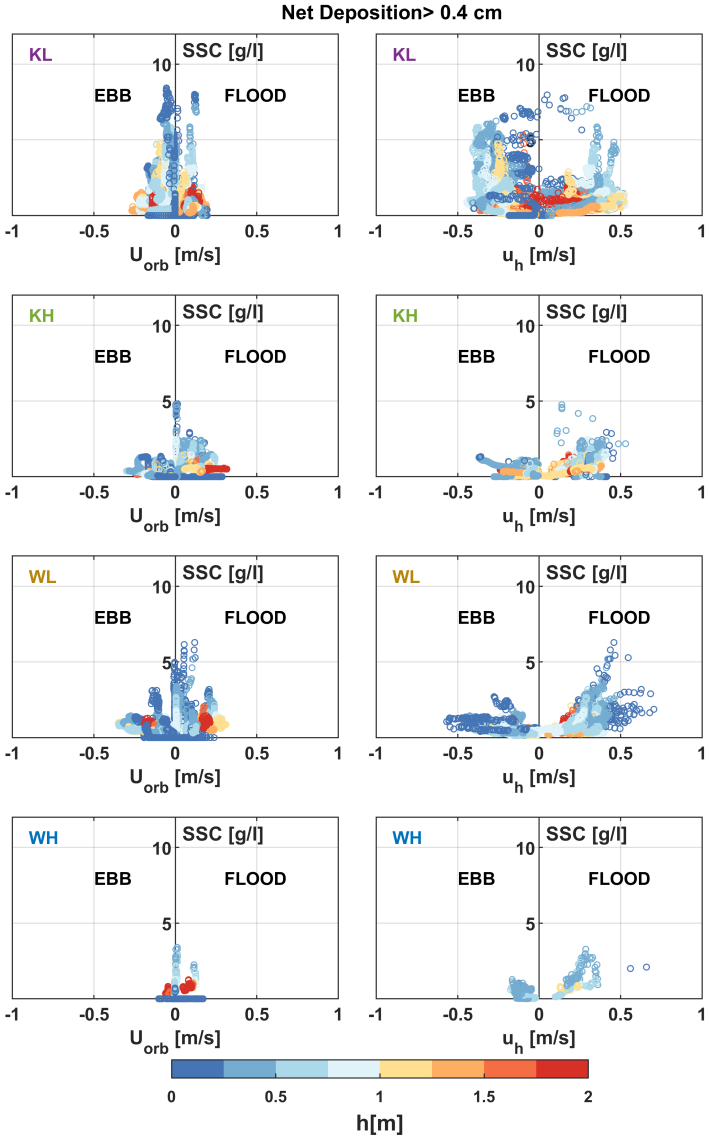

Figure 6.6: SSC versus near-bed wave-orbital velocity (U_{orb}) and horizontal flow velocity at 20 cm above the bed (u_h) for tides with net deposition rates exceeding 0.4 cm (winter measurements). The color of the markers provides the water depth.

6.3.4. WIND-INDUCED EFFECTS ON INUNDATION AND CONSOLIDATION

The morphodynamic development of tidal flats, as presented in the sections above, is strongly influenced by its inundation history (*Reed*, 1990; *Friedrichs and Perry*, 2001). A relatively long inundation duration implies more opportunity for sediment erosion and deposition, whereas a relatively short inundation duration results in longer air exposure, and therefore more opportu-

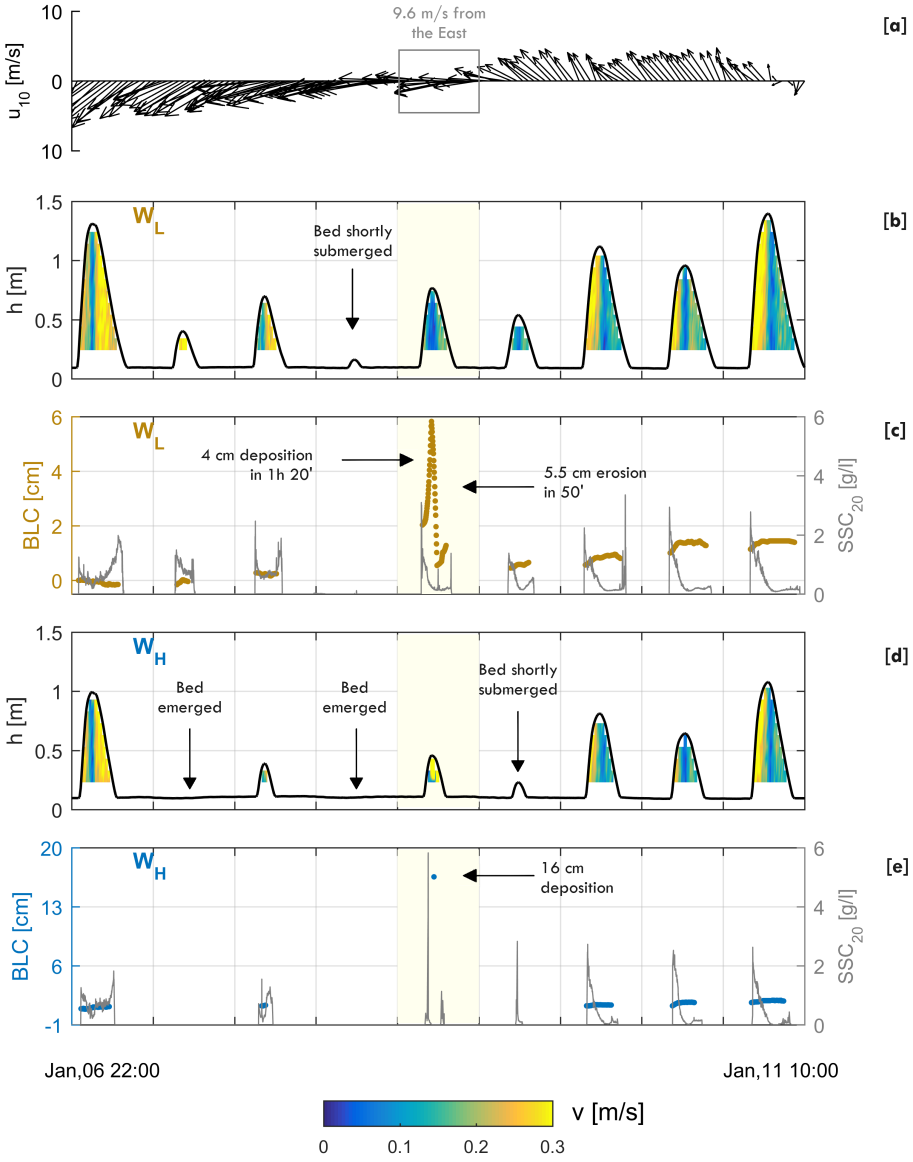

Figure 6.7: Hydro-sedimentary conditions during a fluid formation event at station WL (panels **[b]** and **[c]**) and WH (panels **[d]** and **[e]**). Wind speed and directions are represented in panel **[a]**. Water depth and flow velocity measured are reported in panels **[b]** and **[d]**; bed levels and SSC in panels **[c]** and **[e]**. Emerged conditions imply the absence of data.

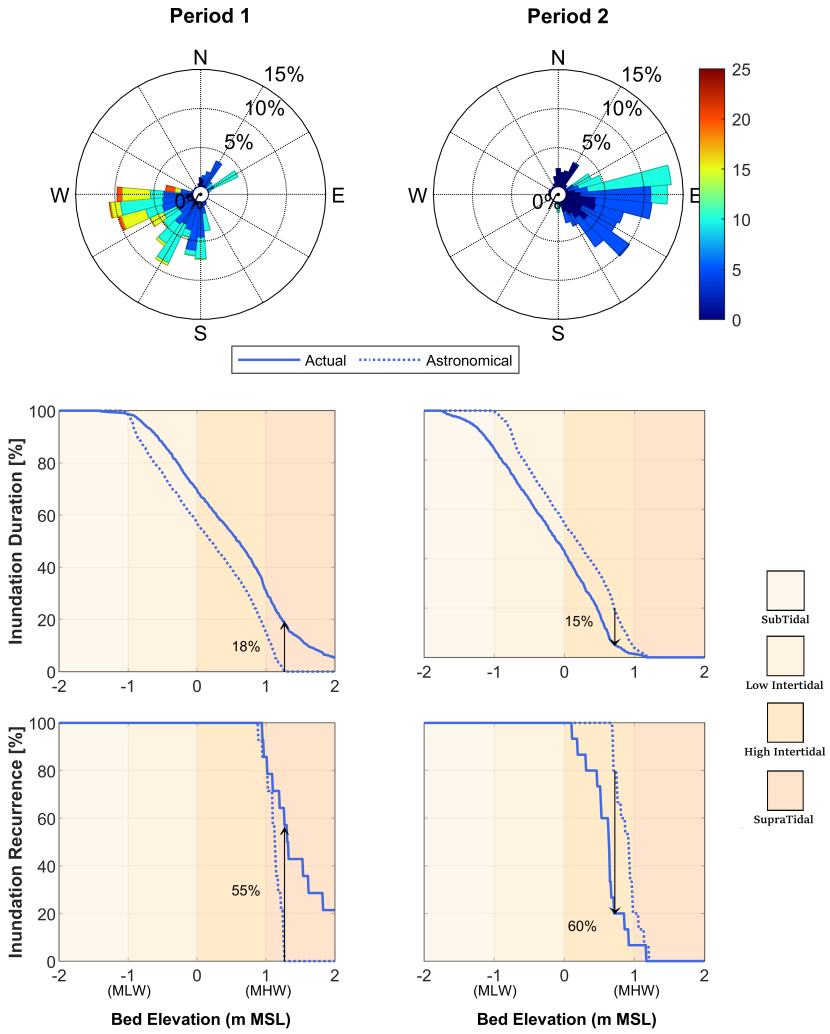

Figure 6.8: Effect of the wind on inundation during Period 1 (left: Dec 31- January 6, strong (u_{10} >15 m/s) western winds, spring tide conditions) and Period 2 (right: January 7-14, moderate (u_{10} <10 m/s) eastern wind, neap tide conditions). The inundation frequency is defined as the percentage of time that a certain bed elevation is inundated at High Water Level (at Harlingen gauging station). The inundation duration is the percentage of time that a certain bed elevation is flooded.

nity for the sediment to over-consolidate. Similarly, frequent inundation of the bed typically leads to a high water content of the muddy bed (and therefore less likely an over-consolidated state). Therefore, both the frequency and duration are important.

We evaluate the effect of wind on the inundation using 2-weeks of actual and astronomical water levels (Dec 31-Jan 14, i.e. winter field campaign). The inundation is governed by tides, but also by wind conditions (exemplified by eastern and western winds in Figure 6.8). The inundation

periods are longer in the period with wind-induced setup (Period 1), compared to the astronomical conditions. For these conditions the bed level at MHW (1.2 mMSL) is inundated for 18% of time, and during 55% of all tides. During a period of set-down (Period 2), the flooding duration and its recurrence decreases, with a maximum decrease of recurrence of 60% at an elevation of 0.8 m. This sharp decrease in recurrence implies that a certain area of the tidal flat is emerged for several consecutive tidal cycles.

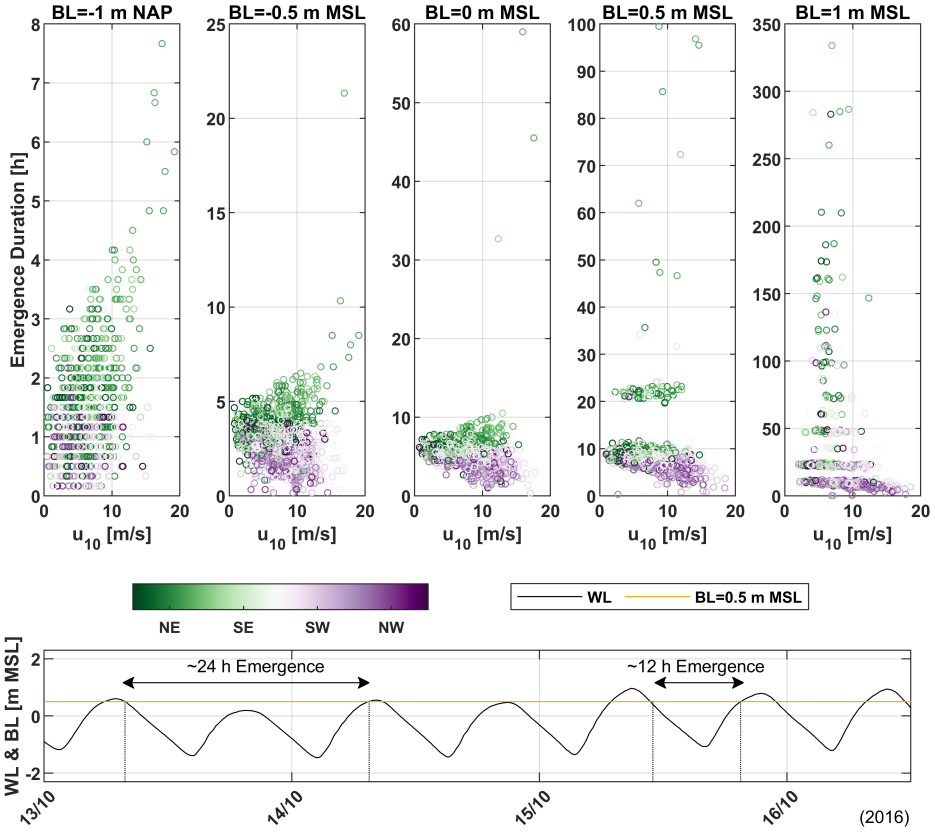

Figure 6.9: Duration of tidal flat emergence at various tidal flat bed levels (BL) as a function of wind velocity u_{10} and direction (measured hourly in Leeuwarden) from January 2016 to December 2018. The emerged duration is determined using water levels (WL) measured every 10 minutes at Harlingen. Each dot corresponds to the time period in-between two consecutive inundations; it varies between 10 minutes (once per tidal cycle, short period of emergence) and multiple tidal cycles (long period of emergence), with wind direction playing a pivotal role. The mean wind speed and the dominant wind direction is computed by averaging meteorological data during the period of emergence. The water levels in the period 13 to 16 October 2016 (lower panel) explain why the emergence duration at bed elevations of 0.5 or 1.0 mMSL is often a multiple of ~12h: a small difference in MHW level doubles the emergence duration (the yellow line representing a bed level of 0.5 mMSL.)

The emergence period is computed at five tidal flat elevations ranging from Mean Low Water (MLW = -1 mMSL) up to Mean High Water (MHW = +1 mMSL) and compared to wind conditions using 2 years of tidal and meteorological data (Figure 6.9). The emergence duration is longer for

wind blowing from the East and shortest for wind from the West. Especially for bed elevations higher than MSL, the emergence duration period becomes a multiple of the dominant tidal period. At BL = 0.5 mMSL the flat is typically emerged for either ~ 10 hours or ~ 22 hours because a small difference in water level may lead to a shift in the the exposure duration from one to two tidal cycles (see bottom panel in Figure 6.9). Around MHW the emergence period may be as long as 334 hours (14 days, corresponding to a spring-neap tidal cycle). These long periods of emergence are crucial for the long-term morphodynamic development because of consolidation processes that take place during periods of emergence.

6.3.5. IMPACT OF AERIAL EXPOSURE ON CONSOLIDATION

The strength of aerially exposed tidal flat beds increase, and this change is generally attributed to evaporation processes (*Fagherazzi et al.*, 2017; *Nguyen et al.*, 2022). Our data shows how the wind influences the water level, flow velocities, sediment concentrations and bed level changes but do not cover in-situ bed shear strength development, as such measurements are extremely difficult in the field. Since strength development is important for understanding how tidal flat dynamics respond to wind conditions, we elaborate on strength development here more conceptually.

The yield strength τ_y of the bed can be described by the fractal model of *Kranenburg* (1994):

$$\tau_y = K_y \left(\phi_s\right)^{\frac{2}{3-n_f}} \tag{6.1}$$

with sediment volume fraction ϕ_s, material parameter K_y and fractal dimension n_f. Since $n_f \approx 2.7$, the strength increases highly non-linear with the volume fraction: a small increase in sediment volume fraction can lead to a substantial increase in strength.

The sediment volume fraction of the bed ϕ_s can be described by Gibson's equation, which has the solution:

$$\frac{\phi_s(z) - \phi_{s,eq}}{\phi_{s,0} - \phi_{s,eq}} = \frac{z}{\sqrt{4\Gamma_{cons} t}} \tag{6.2}$$

where $\phi_s(z)$ is the sediment volume fraction at a specific vertical position z (defined as upwards positive) and time t; the subscripts '0' and 'eq' refer to the initial and equilibrium condition; Γ_{cons} [m^2/s] is the consolidation coefficient.

The associated consolidation time for a mud layer, having thickness δ, is given by:

$$T_{cons} = \frac{\delta^2}{\Gamma_{cons}} \tag{6.3}$$

The consolidation coefficient Γ_{cons} is assumed constant (*Winterwerp et al.*, 2021), with $\Gamma_{cons} \simeq 10^{-8} - 10^{-7}$ m^2/s). The time scale is therefore strongly dependent on the thickness, with thick deposits having much longer consolidation times than thin layers. The equilibrium sediment volume fraction at position z depends on two contributions (*Winterwerp et al.*, 2021): (1) the weight of the sediment above z, scaling with $Z_s - z$, with Z_s being the vertical position of the water-sediment interface and (2) the suction due to under pressures, scaling with the suction head $Z_s - Z_{ph}$ (the vertical distance between the water-sediment interface Z_s and the phreatic level Z_{ph}), resulting in:

$$\phi_{s,e}(z) = \left[\frac{n-1}{n} \frac{(\rho_s - \rho_w) g}{K_p} (Z_s - z) + \left(\frac{\rho_w g (Z_s - Z_{ph})}{K_p} \right)^{\frac{n-1}{n}} \right]^{\frac{1}{n-1}} \tag{6.4}$$

in which $n = 2/(3 - n_f)$. A low phreatic level therefore increases consolidation rates, especially in the upper part of the bed, where $(Z_s - z) \ll (Z_s - Z_{ph})$, leading to over-consolidation. The consolidation rates resulting from underpressures are much larger than self-weight consolidation (the first term in Equation 6.4) due to the small thickness of the sediment deposits.

Next to the capillary suction from the lower phreatic level, evaporation increases the underpressures in the upper part of the bed further - see also *Fagherazzi et al.* (2017) and *Nguyen et al.* (2022). Longer emergence of a tidal flat leads to more evaporation and therefore larger underpressures. The sediment volume fraction will therefore increase with longer emergence and aerial exposure. Because of the non-linear relation between the sediment volume fraction and bed strength, a small increase in aerial exposure (and thus the sediment volume fraction) leads to a substantial increase in strength.

A straightforward example demonstrating the lack of opportunity for consolidation of thick deposited layers of fine sediment is fluid mud formation (Section 6.3.3, Figure 6.7). Layers of several centimeters (4 to 16 cm) thick deposit over time frames of a few hours, during calm conditions following a storm. However, the deposited material is already eroded within the same tidal cycle because the material is very soft and easily erodible. Developing strength for this material to permanently deposit would require a very long period of low-energy or emerged conditions. Similarly, turbid fringes (analyzed in Section 6.3.3) resulting in a relatively rapid (timescales of hours) bed level increases (order of 0.5-1 cm) are effective for a long-term bed level accretion only if followed by relatively long air-exposure (i.e, wind direction inducing set-down is needed).

6.4. DISCUSSION

We identified four key interaction types between the wind and morphodynamics of tidal flats: (i) generation of waves and subsequent resuspension; (ii) generation of wind-driven flow leading to horizontal transport of sediment; (iii) water level set-up, leading to inundation, enabling sediment deposition; (iv) waterlevel set-down, increasing the aerial exposure period, stimulating over-consolidation of previously deposited sediments. The first two interaction types are well identified in previous studies. The role of wind on resuspension of fine sediments through generation of waves has been revealed by publications, see e.g. *Allen and Duffy* (1998); *Ridderinkhof et al.* (2000); *Janssen-Stelder* (2000); *Yang et al.* (2003); *Zhu et al.* (2016); *Shi et al.* (2017b); *Xie et al.* (2018). The importance of wind-driven flow on sediment transport in general is also well established (*Baeye et al.*, 2011; *Xie et al.*, 2018; *De Vet et al.*, 2018; *Yang et al.*, 2023). In the Wadden Sea an eastward directed transport component exists, resulting from wind through both the larger channels (*Nauw et al.*, 2014; *Duran-Matute et al.*, 2014; *Sassi et al.*, 2015; *Duran-Matute et al.*, 2016; *Sassi et al.*, 2016)) and over flats (Chapter 5 and *Van Weerdenburg et al.* (2021)). However, the importance of interaction types (iii) and (iv) are new, especially in combination with (i) and (ii).

As the wind varies both in speed and direction, various sequences of these four interaction types may occur. Based on extensive field experiments presented here, we argue that tidal flat accretion is only possible if: (1) there is a period with sufficient deposition and (2) this period is followed by a period in which the bed can (over)consolidate, thereby developing sufficient strength to withstand the following erosion event. The wind therefore drives the physical processes (resuspension, deposition, consolidation) controlling net accretion. In an analogue to a window of opportunity, we refer to this sequence of events as the 'Winds of Opportunity'. For our measurement location, a period with weak to moderate wind from the southwest can lead to deposition. In order to lead to permanent accretion, this deposition phase should be followed by a period with moderate wind from the southeast to induce water level set-down.

Projecting the concept of these winds of opportunity to a tidal flat, it is expected that the sequential order of deposition, consolidation and erosion cross-sectionally varies as schematized in Figure 6.10. On the lower flat the cumulative changes in bed elevation are larger than on the higher flat (Figure 6.1): a larger submergence duration implies a larger window for deposition. However, due to the short aerial exposure period, over-consolidation and therefore strength development is limited. A relatively small storm will already lead to erosion of the freshly deposited sediments and

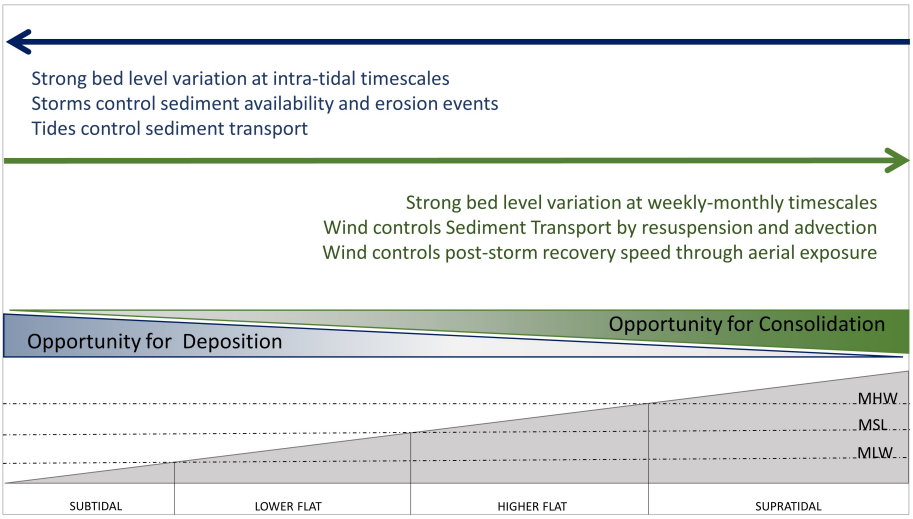

Figure 6.10: The relative importance of the processes controlling tidal flat accretion across a tidal flat, with a strong tidal influence and regular opportunities for deposition over the lower flat and a strong wind-driven influence and opportunities for consolidation over the higher flat. Net accretion requires a temporal sequence of consolidation following deposition.

therefore large deposition rates do not necessarily lead to large accretion rates.

The window for consolidation is larger on the higher flat than on the lower flat for several reasons. Most importantly, the area is exposed longer by tidal action and by variability introduced by the wind (Figure 6.8), leading to (over) consolidation. Secondly, the sediment concentration (and therefore the deposition rate) is lower on the higher flat. Figure 6.6, for instance, shows that the occurrence of large sediment deposition (net bed level change > 0.4 cm) relates to the occurrence of 'depositional' turbid fringes. The maximum SSC measured during the passage of such a turbid fringe decreases at higher bed elevations (Figure 6.6) in concert with a decrease of flow velocity (Figure 6.5). Lower SSC results in thinner bed deposits which consolidate more rapidly. Both aspects result in a relatively uniform bed response to winter storms (erosion everywhere) but spatially varying post-storm recovery (Figure 6.3). The bed of the lower flat did not recover from the storm-induced erosion, whereas at the higher elevations an almost full recovery occurred within the two weeks following the event.

Our conceptual model can also (partly) explain the development of bed stratigraphy and cliffs in fine-grained tidal environments. The development of bed stratigraphy is typically associated with a textural variability reflecting its depositional environment, which in turn determines the erodibility (*Van Rijn*, 2020; *Mitchener and Torfs*, 1996; *Van Ledden et al.*, 2004). In fine-grained environments the bed stratigraphy is often in the form of very fine laminations (e.g. see a photograph taken at Westhoek in Figure 6.11), and we hypothesize that such layering may reflect historic phases in overconsolidation rather than a difference in grain size. The horizontal gradients in sediment deposition and consolidation may give rise to cliff formation. Cliff erosion is caused by mass erosion, induced by waves. As the bed is over-consolidated, "normal" stresses cannot erode the bed (surface erosion). In case evaporation is the dominant over-consolidation agent, the bed is stronger at its surface than at greater depth. The wave-induced stresses are also larger a bit further down within the sediment bed, which explains the erosion of lumps of material (*Winterwerp et al.*, 2012). As discussed, the degree of over-consolidation generally increases up-flat. The inun-

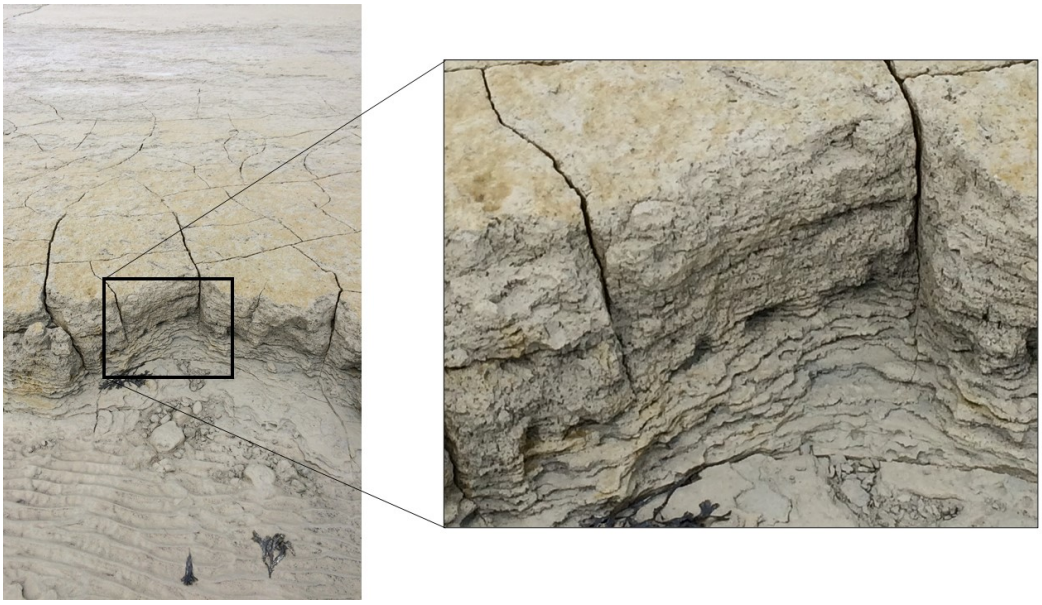

Figure 6.11: Cliff developed in the upper intertdal zone at Westhoek, revealing fine laminations of mud-dominated deposit

dated tidal flat may therefore erode relatively easily and gradually, whereas the higher flat gains strength and is only eroded as mass erosion. This leads to cliff formation at the transition zone from under-consolidated to over-consolidated sediment beds.

A crucial question then arises whether bed level accretion is limited by sediment deposition rates or consolidation rates. For Westhoek and Koehool, periods of deposition led to a bed level increase of centimeters per week. This suggests that there is sufficient sediment available and that the sediment is able to deposit. However, erosion events lead to removal of the freshly deposited sediment. This indicates that over-consolidation is likely the limiting factor for tidal flat accretion. During summer conditions, with generally lower sediment concentrations and less storm setup, deposition rates may become a limiting factor. The limiting factor also varies over the tidal flat profile. Higher parts of the flats (not monitored as part of our surveys) and especially over the supratidal salt marshes, deposition events become progressively more important for accretion. Summarizing, net accretion rates are controlled by (over-)consolidation rates in winter (sediment deposition rates are sufficient) and by deposition rates in summer (especially on the higher flat, where consolidation rates are high).

6.5. CONCLUSIONS

The present study analyzes the processes contributing to the vertical accretion of a tidal flat bed in a fine-grained sediment environment and identifies a 'window of opportunity' for fine sediment accretion over long timescales. This window of opportunity reflects a temporal sequence of sediment deposition and sediment consolidation, resulting in the formation of a new layer of over-consolidated sediment.

Sediment may deposit for several tidal cycles during conditions with relatively large supply and mild hydrodynamic conditions. However, on longer time scales (weeks-months) the com-

bined wave-current forcing easily erodes this relatively fresh material. This implies that although sediment may deposit it does not gain sufficient strength to withstand even minor wave-induced resuspension events. Therefore, erosion resulting from relatively strong storms has a long-lasting effect (months to years). Recovery from such a storm-induced setback is not only dependant on the opportunity for deposition (as abundant sediment is typically available after storms) but especially on the opportunity for consolidation. Crucial hereby is that the strength of the bed resulting from self-weight consolidation is too weak (and requires a very long time) to withstand erosion during subsequent storm conditions; sufficient strength is only attained through over-consolidation resulting from a low water table, evaporation and drying.

Conditions favoring over-consolidation are largely driven by the wind. Winds therefore not only affect the morphological evolution of the mudflats by regulating the bed shear stress, but also by creating favourable conditions for sediment over-consolidation. Winds inducing water level set-down (at our study site, eastern wind) contribute to the reduction of inundation duration and of inundation frequency, favouring aerial exposure of the mudflat and therefore, the over-consolidation process and strength development.

Our study also shows that long-term vertical accretion of tidal flats may even be limited in case of large sediment availability because the resulting mud deposits are too thick to rapidly consolidate and develop strength. As a result, the sediments are continuously deposited and eroded, while net mudflat accretion rates remains small.

About the Photo

Sealife at the lower (-1 m MSL) intertidal flat of Koehool pictured during the winter field campaign, on February 13, 2018.

7

DISCUSSION

The implications of the findings from Chapters 4, 5, and 6 are discussed from two perspectives. Part 1 focuses on highlighting and discussing the main scientific results. Part 2 explores the implications of these findings for seedling dynamics and sediment nourishment strategies.

7.1. PART 1: IMPROVED UNDERSTANDINGS OF HYDRO- & MORPHODYNAMICS OF INTERTIDAL FLATS

7.1.1. WIND-DRIVEN FLOWS IN INTERTIDAL AREAS

Our findings on the role of wind on residual flows over tidal flats provide an important improvement of our understanding of intertidal flat hydrodynamics. A new dataset is made available and a model is developed to unravel the contributions of tides and wind. The hydrodynamics of intertidal flats were always thought to be controlled by the tides – characterized by deterministic fortnightly variation in tidal range with the spring/neap cycle – and by the stochastic action of wind, generating wind-waves, low-frequency water level gradients, and wind-driven flows (e.g. *Le Hir et al.*, 2000; *Bassoullet et al.*, 2000; *O'Callaghan et al.*, 2010; *Friedrichs*, 2012; *Green and Coco*, 2014; *Zhu et al.*, 2014).

The effect of wind-driven flows on residual flows was already shown by the model results of *Sassi et al.* (2015); *Duran-Matute et al.* (2014). Pioneering studies on fringing intertidal flats in the Danish Wadden Sea, highlighted the role of wind on bed level changes of intertidal flats (*Christiansen et al.* (2006); *Andersen et al.* (2006)), but without detailed flow and wave measurements. At the Richmond fringing flats in San Francisco Bay (USA), *Talke and Stacey* (2008) identified the variation in sediment fluxes at intratidal-to-daily timescales, related to changes in wind speed/direction and also to periodical fresh water discharges. However, only a four-day period was considered. Our data set with flow, waves, sediment concentration, measured at high frequency over a total period of 4 months is therefore a valuable contribution to existing datasets. This dataset provided the opportunity to identify various wind events, highlighting the importance of the interaction with the tide. The importance of wind-driven flows on intertidal flats was estimated in *De Vet et al.* (2018): the wind-driven flow was estimated as 1/40 of the wind speed. The non-linear interaction was however not taken into account. We expanded on the work of *De Vet et al.* (2018) by developing an analytical tide-wind interaction model, based on the momentum balance equation (Chapter 4), quantifying the non-linear interaction between tidal flow and wind-driven flows at different tidal flat elevations and under different meteorological conditions. This model revealed that the wind-driven flows strongly influences the magnitude and direction of the residual flow (Chapter 4) and residual sediment transport (Chapter 5) over intertidal flats. The dominance of wind-driven flows over tidal flow increases for decreasing tidal amplitude, i.e. at increasing tidal flat elevations. Wind-driven flows are able to reverse the tidal flow also for consecutive tides, implying prolonged flows in flood or ebb direction. Wind opposing the flood direction affects especially the higher intertidal zone, that emerge for long time periods. Our findings initiated new measurements and analyses on flow and sediment transport over tidal divides in the Wadden Sea (*Van Weerdenburg et al.*, 2021). Similar results were found, indicating the impact of wind on these shallow areas.

7.1.2. SEDIMENT TRANSPORT OVER INTERTIDAL AREAS

Most of the earlier work focused on the role of waves and/or tidal currents on sediment transport over intertidal flats. The sediment is resuspended from the tidal flat via the wave-induced orbital motion at the bottom, and is advected - back and forth over the tidal cycle - by tidal currents (e.g. *Soulsby*, 1995; *Dolphin and Green*, 2009; *Friedrichs*, 2012; *Green and Coco*, 2014; *Hunt et al.*, 2015). Sediment transport is hence dependant on the interaction between these two forcings at varying water depths (i.e. at varying tidal phase). These studies have been fundamental to unravel the distinct contribution of wind waves and tidal currents to the morphodynamic development of tidal flats. Waves generally erode sediment, whereas tidal currents contribute to sedimentation, leading to long-term morphodynamic equilibrium (e.g. *Bassoullet et al.*, 2000; *Janssen-Stelder*, 2000; *Wang and van der Spek*, 2015; *Zhou et al.*, 2017; *Maan et al.*, 2015). However, when wind-driven currents

contribute substantially to the horizontal flow, the combination of tidal currents (promoting sedimentation) and waves (leading to erosion) fails to explain the morphodynamic processes shaping these intertidal environments.

In our study, we demonstrate that wind-driven residual transport and temporary sediment storage significantly influence sediment dynamics in intertidal areas. The strong wind-driven residual flows result in pronounced residual sediment transport, as observed by integrating hydrodynamic and suspended sediment concentration (SSC) measurements. Prolonged periods of residual flow in a particular direction lead to sustained sediment transport in that direction, with limited modulation by tides. A key finding in understanding sediment dynamics in our study area is that sediment transported over an extended period in one direction is temporarily stored (primarily at tidal divides) until it is remobilized and transported back, depending on changing wind conditions. These dynamics are captured in a new conceptual model of wind-induced sediment transport and storage in intertidal areas (Chapter 5).

During average wind conditions, sediment is deposited as relatively thick layers (ranging from millimeters to a few centimeters) on shallow intertidal areas (Chapters 5, 6). These layers do not consolidate due to their thickness and prolonged submersion (Chapter 6). As a result, even minor wind events following the depositional phase resuspend significant amounts of sediment. The sediment fluxes generated by this 'storage-resuspension' mechanism were, in our observations, up to four orders of magnitude larger than those during average conditions. A similar conceptual storage model was proposed by *Bartholdy et al.* (1998).

Of particular importance to sediment transport in intertidal areas are the so-called turbid fringes, which will be evaluated in detail in the following section.

7.1.3. TURBID FRINGES IN INTERTIDAL SYSTEMS

The measurements show that the SSC strongly varies over the tidal period, typically peaking at the beginning of a tidal cycle (Chapter 5). Taking a Lagrangian perspective, the temporal and spatial patterns in wave forcing may generate a fringe of sediment-laden water moving up and down with the tide, and within which wave-orbital motions keep the sediment in suspension (*Green and Coco*, 2014). These so called 'turbid fringes' are therefore generally related to wave-driven processes and are considered noticeable features of estuaries in windy conditions (*Green and Coco*, 2014). However, turbid fringes are also observed in absence of wind. For example, at the macrotidal Skeffling mudflats (Humber estuary, UK) the largest sediment resuspension occurred in absence of waves during the first and last half hours of immersion (*Christie and Dyer*, 1998). *Uncles and Stephens* (2010), analyzed the sediment transport features at the Tavy intertidal flats (Tamar River estuary, UK) and noticed that shortly after immersion and shortly before drying, light wind is able to cause small breaking waves which, combined with flood/ebb tidal current peaks, enhance the turbid fringe.

At the flats that we investigated in the Wadden Sea, the point observations of SSC revealed the occurrence of two SSC peaks during the tidal cycle. Such peaks occur at the beginning of the flood phase and at the end of the ebb phase, when the horizontal flow velocity is at its maximum, while waves are seldom present. Therefore in our site the resuspension of sediment at the tidal front is not controlled by the wave orbital motion, but rather by the relatively fast tidal flows (Chapter 6). At the beginning and at the end of the tidal cycle, the tidal flow velocity is characterized by pronounced peaks (Chapter 4). Our data and visual observations suggest that, especially for windy conditions, the flooding of tidal flats is comparable to a tidal bore. Small bores are sometimes observed at the tidal wave front due to the propagation of the tidal wave in shallow water (*Dronkers*, 1986) strongly influenced by bottom friction (*Friedrichs and Madsen*, 1992). Hence the water surface may present a significant slope (although the very small depth) resulting in a supercritical regime at the tidal front (*Green and Coco*, 2014). We attribute the turbid fringes observed at our

field site to such small tidal bores, that are able to resuspend the fresh (unconsolidated) sediment deposited during the previous tidal cycle(s). Moreover, based on the results presented in Chapter 5, we inferred that winds aligned to the flood direction promote sediment storage in specific zones of the intertidal flat. This temporarily stored unconsolidated sediment can be easily resuspended by tidal (or wind-driven) flows. A similar concept related to the mechanisms controlling turbid fringes, was provided by *Weir and McManus* (1987). The authors identified several zones of recurring high turbidity in the macrotidal Tay estuary (Scotland, UK) and concluded that they were related to wind direction and strength, and also to specific 'source areas' of sediment in the estuary.

Our observations further suggest that the turbid fringes are particularly turbid when calm weather conditions follow wave dominated conditions (Chapter 6). In this case, the flood dominance of the system in terms of water flow results in only one SSC peak (during flood) and hence in the occurrence of only one turbid fringe during the tidal cycle. These turbid fringes have a pronounced effect on the local bed elevation, with a simultaneous local decrease in SSC (following the peak) and increase in bed elevation.

7.1.4. SHORT-TERM AND LONG-TERM DYNAMICS OF MUDDY BEDS

In Chapter 6 we analyze bed level changes at various timescales, and conclude that long-term accretion only limitedly depends on short-term deposition. This is because the consolidation rate of the freshly deposited material is crucial to long-term accretion. Our analysis of erosion and consolidation processes revealed that long-term accretion is so much influenced by periods of resuspension (storms) and subarial exposure (wind-driven set-down) that winds exert a strong control over long-term bed evolution.

Our bed level changes and bed shear stress monitoring highlighted a weak correlation between bed shear stresses and bed level changes over muddy beds (Chapter 6). Relatively small bed shear stresses (< 1.5 Pa) may result in sediment deposition as much as in sediment erosion. Similarly, relatively large bed shear stresses (> 6 Pa), such as those resulting from a storm, do not necessarily lead to bed erosion (Chapter 6). This is because sediment resuspension during a storm does not only relate to the actual bed shear stress exerted on the bed during wave-dominated conditions, but also on strength of the bed and therefore on the history of the mudflat, i.e. the stress previously exerted over the bed (Chapter 6), the hours of drying, sunshine, winds, possible rainfalls and the effect of biota on sediment (*Winterwerp et al.*, 2021).

Our bed level measurements highlighted the occurrence of surface and mass erosion over the two investigated intertidal flats. Surface erosion occurs during drained conditions: the water enters the soil so that the rate of erosion is controlled by the swelling rate of the top layers (*Winterwerp et al.*, 2021). Mass erosion is caused by undrained failures of the soil at horizontal or vertical inhomogeneities in bed strength. Such inhomogeneities are stochastically distributed, and therefore a statistical model was developed to estimate mass erosion by *Van Prooijen and Winterwerp* (2010).

Surface erosion alternates at tidal timescale with sediment deposition. The longer the bed is submerged (i.e. the lower the bed elevation), the larger the cumulative bed level changes over one tidal cycle (Chapter 6). At the lower flat (in proximity of MLW level) the magnitude of the alternating erosion and deposition is similar, so that over longer time periods (weeks-to-months) the averaged bed level changes related to surface erosion is close to zero. At our lowest investigated site, this erosion-deposition pattern may be the result of ripple migration (Figure 7.1, left panel). Ripples were pictured during field surveys at this location, as reported in Figure 2.8. At the other sites (bed elevations between -0.2 m and +0.10 m MSL), surface erosion and sedimentation do not alternate regularly. No specific bedforms were observed at these sites: the bed was relatively smooth and uniform.

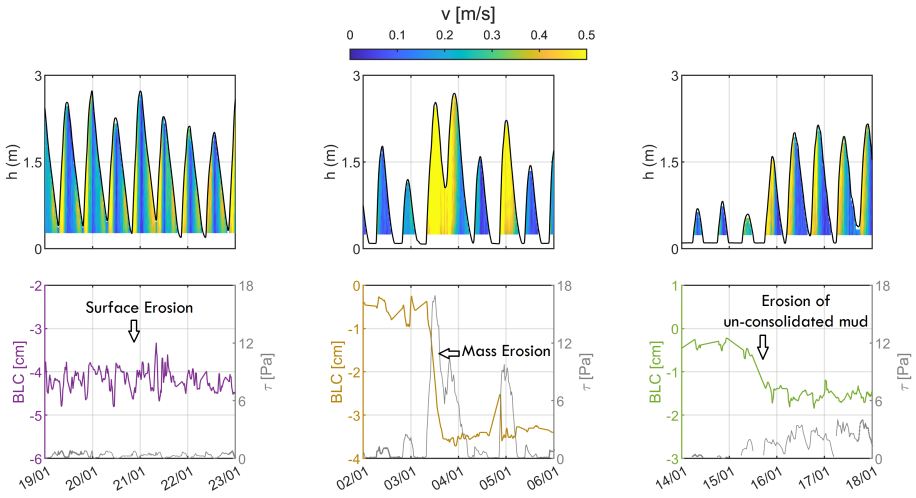

Figure 7.1: Three types of erosion observed during the monitoring. Left panel: Surface erosion alternates with deposition at low bed shear stress. Central panel: Mass erosion removes centimeters of sediment during a storm, i.e at high bed shear stress. Right panel: Erosion of centimeters of sediment at relatively small bed shear stress illustrating erosion of un-consolidated sediment.

Mass erosion is observed during stormy conditions, and involves more consolidated mud layers. Mass erosion generates a temporal reset in the vertical evolution of the tidal flat (Figure 7.1, central panel). Storm-induced erosion may remove, in a few hours, the sediment deposited over multiple years (cm thick layers, Chapter 6), thereby resetting the bed elevation to the elevation of years earlier (see also *De Vet et al.* (2020b)).

This delay can be limited by post-storm bed recovery. Bed recovery after storm is a relatively fast process (*De Vet et al.*, 2020b; *Zhu et al.*, 2019); however, a fast apparent recovery may not be efficient for the long-term recovery (Chapter 6). Sedimentation rates after storms may be high because of the large sediment availability in the system (Chapter 6, *Zhu et al.* (2019)), therefore there is a relatively large opportunity for deposition. However, relatively small bed shear stresses may result in the erosion of the post-storm deposited sediment (making the "fast" post-storm recovery inefficient, Figure 7.1, right panel). Erosion of unconsolidated sediment occurs in drained (or partially drained, depending on the consolidation state) conditions, and results in the removal of centimeters of sediment, inducing a set-back in the evolution of the flat (similarly to mass erosion). An actual (long-term) recovery requires a prolonged period with air exposure (i.e. wind-induced set-down) following a period with sediment deposition. Only during such a sequence of events the newly deposited sediment (over)consolidates and gains sufficient strength (Chapter 6). The occurrence of over consolidation relates to water levels and hence on wind (Chapter 6). Therefore the long-term development of muddy flats (especially in microtidal environments such as the Wadden Sea) is strongly depending on the wind climate.

Our understanding of the consolidation of muddy sediments under emerged conditions has been extensively investigated via laboratory tests by *Barciela Rial* (2019). The consolidation of mud slurries in emerged conditions is characterized by a process of crust formation on the upper bed layers (millimeters thickness). A crust develops because de-watering via evaporation is faster than self-weight consolidation of the layers below the crust. The reduction in permeability due to

crust formation subsequently reduce the consolidation rate of soft layers beneath the crust, which therefore tends to remain in saturated conditions. If this process persists (i.e. if the bed maintains emerged conditions for a relatively long time), desaturation of the soil occurs and cracks appear in the surface. On tidal flats, this process is especially observed at bed elevations above MHW level (See Figure 7.2). At lower elevations, crust formation does not result in crack formation due to the higher inundation frequency. Under such submerged conditions the thin (mm-thick) crust is relatively easily removed, and the saturated layers below eroded. This kind of erosion, which may remove centimeters of layered mud within seconds/minutes, is a combination of mass erosion (removal of the undrained crust) and surface erosion (erosion of the soft, saturated mud below the crust). Based on the laboratory findings of *Barciela Rial* (2019), we infer that over intertidal flats characterized by relatively large deposition rates, the crust formation may play a significant role in erosion processes, as it is responsible for a significant slowdown of the consolidation processes. The erosion of unconsolidated sediment (as observed in our dataset) and the erosion of unconsolidated sediment below an undrained crust (expected based on the laboratory studies of *Barciela Rial* (2019) at higher tidal flat elevations) require further analysis.

7.2. PART 2: IMPLICATIONS

The new physical insights related to the wind-induced residual flow and transport over tidal flats and the role of strength developments during calm conditions have important practical implications. Below we will discuss their impact on the dispersal and establishments of pioneer vegetation and on a fine sediment nourishment.

7.2.1. IMPLICATIONS OF WIND ON VEGETATION ESTABLISHMENT

The hydrodynamics and sediment transport occurring over intertidal flats directly affect the suitability of these areas for saltmarsh development. A key process ensuring the long-term stability of saltmarsh systems is the establishment of annual pioneer vegetation in the transition zone, i.e. at the edge between the existing vegetation and the bare tidal flat. This zone periodically undergoes cliff erosion due to wave action (e.g. *Leonardi et al.*, 2016), re-establishment of vegetation (by pioneer plants) and sedimentation (enhanced by the vegetation trapping).

The colonization by pioneer plants requires, a.o., the availability of (viable) seeds (*Erfanzadeh et al.*, 2010), which are released by the mature plants and transported by hydrodynamic forcing (e.g. *O'Callaghan et al.*, 2010). The period of seed dispersal differs per plant species, with most species dispersing seeds in the autumn-winter periods while seed germination mainly takes place from spring to autumn (*Regteren et al.*, 2019; *Zhu et al.*, 2022). Expansion of plant species is therefore depending on the seasonality in hydrodynamic forcing combined with the seasonality in plant reproduction.

Erosion and sedimentation of the upper bed layers (cm thickness) have a key effect on the establishment of saltmarsh plants, with erosion resulting in loss of seedlings (e.g. *Regteren et al.*, 2019) and deposition in burial of seeds (e.g. *Houwing*, 2000; *Balke et al.*, 2014; *Zhu et al.*, 2014). The burial of seeds - also caused by bioturbation (*Delefosse and Kristensen*, 2012; *Van Regteren et al.*, 2017) - positively affects seed retention (*Zhu et al.*, 2014), provided that the light penetration is enough for the plant to germinate, i.e. the seed is not buried too deep in the soil (*Erfanzadeh et al.*, 2010).

The spatio-temporal variability in sediment dynamics and bed level changes over intertidal flats therefore controls seed dispersal and seed retention processes. The recent study of *Zhu et al.* (2022) indicates the different contribution of tides and wind on seed dispersal and retention on intertidal flats, using field data obtained in various projects conducted in the Western Scheldt and in the Wadden Sea. According to this study, seed dispersal is mainly dependant on tidal forcing,

with spring tides being more efficient than neap tides in dispersing sediment over the flats. On wind-sheltered tidal flats, wind events may import a disproportionate amount of seeds over the flats, whereas wind-exposed tidal flats may be relatively starved of seeds.

The effect of erosion events on seed retention was measured at Westhoek intertidal flat, where experiments on seed availability (in front of the existing marsh) were carried out simultaneously to our 2018 field campaign. Abundant seeds loss occurred during the storm of January 3rd 2018, characterized by almost 2 m water level set up and waves of 1-1.5 m (see Chapter 6). The experiment suggested that although the (biotic and abiotic) boundary conditions are favourable for a lateral marsh expansion at Westhoek, the relatively low seed availability in spring hampers the pioneer vegetation establishment onto the transition zone (*Regteren et al.*, 2019). The limited seed availability is attributed to the relatively large magnitude of storm-induced bed level changes occurring in the winter period. The experiment included manual addition of seeds in March (i.e. after the more severe winter storms); these seeds were retained until the establishment period, in May, confirming that the inundation conditions, and the other environmental variables, are favourable for a lateral expansion of Westhoek saltmarshes.

The analysis of wind effects on currents, sediment transport, and bed level changes executed as part of this thesis, have several implications for seed dynamics in our study area.

(i) Salt marsh plants are sensitive to small changes in inundation frequency and inundation duration, and this effect is enhanced in freshwater marshes (*Delgado et al.*, 2018). The inundation period is affected by spring-neap tidal variations, but also (significantly) by the wind direction (Chapter 6). Our results suggest that: a) the existing salt marshes along the Dutch Frisian coast are resilient to a relatively irregular inundation regime, as it is highly influenced by stochastic forcing of wind, and b) the pioneer establishment in the transition zone may be affected by the relatively large wind-induced variations in the inundation duration and frequency.

(ii) The sediment transport is largely controlled by the wind direction (Chapter 5) and we expect the seed transport to be similarly controlled by wind. We hence infer that in dominant wind conditions (SW wind), the seed transport is directed from Westhoek towards the north-eastern coast. Oppositely, we expect that NE wind enhance the transport of seeds towards the south-west, i.e. towards Koehool intertidal flat. Based on our analyses, the seed dispersal along the Dutch Frisian coast is controlled by the interaction of long-shore tidal and wind-driven flows (Chapter 4).

(iii) Our analysis further suggest that sediment burial most likely occurs during eastern wind due to the large sediment availability at the eastern side of the basin (tidal divides, Chapter 5). Calm-to-moderate wind conditions at our study site result in net deposition in the order of 1-3 mm/tide, implying that 10 days of fair weather induce 2-3 cm deposition over the higher intertidal flats (bed elevation > MSL). Large sediment deposition also occurs over the tidal flats after storms, with highly concentrated turbid fringes "spreading" the recently eroded sediment over the tidal flats (with a relatively high deposition rate, up to 0.5 cm per tidal cycle, Chapter 6).

(iv) Wind-induced set-up increase the sediment import into the upper marsh (*Friedrichs*, 2012; *Zhu et al.*, 2022). On the other hand, prolonged wind-induced set-up results in a longer inundation period subjecting the vegetation to increased stress (*Balke et al.*, 2014), increasing the water content (and the erodibility) of the muddy substrate. Wind-induced set-down offers opportunity for seedling establishment (*Balke et al.*, 2014) and reduces the water content in the substrate. However, prolonged water level set-down induce the formation of superficial mud fractures (see figure 7.2, Westhoek 2016).

Overall, the wind direction controls the duration and frequency of set-ups and set-downs on intertidal areas, highly affecting the opportunity for vegetation establishment. The smaller the slope of the tidal flat, the stronger is this effect, as a difference in water level of a few centimeters affect the inundation frequency and duration of extensive areas of the flats (Chapter 6).

Figure 7.2: Pioneer vegetation on the transition zone at Westhoek intertidal flat (bed elevation close to MHW level). The picture was taken on September 15, 2016. The scarce density in pioneer specie plants (Salicornia Procumbens) is attributed to a poor seed retention, in turn related to relatively large bed level fluctuations.

7.2.2. IMPLICATIONS FOR THE DESIGN OF A FINE SEDIMENT NOURISHMENT

Worldwide, harbours suffer from siltation while channels are continuously dredged to maintain or expand navigational depths. Dredging and disposing sediment is costly and it also can have a negative impact on sensitive coastal ecosystems (e.g. *Erftemeijer and Lewis III*, 2006; *De Vet et al.*, 2020a). Therefore sustainable sediment relocation methodologies are being investigated aiming at minimising dredging volumes while strengthening ecological values by restoring coastal habitats. The establishment of pioneer vegetation requires a sufficiently high bed elevation of the intertidal flats (generally the MHW level is assumed as reference threshold) in order to guarantee the appropriate duration of emerged/submerged conditions of the bed (and so of the vegetation seeds). For low-lying intertidal areas (i.e. bed elevation below MHW level) the vegetation development hence requires, at first, an increase in bed elevation, and so a progradation of the intertidal flat.

The Mud Motor (see *Baptist et al.* (2019)) is an experimental type of nourishment executed in the Dutch Wadden Sea, aimed at promoting the development of pioneer vegetation over fringing intertidal flats, by disposing muddy sediment relatively close to the shore (the tidal channel bordering the targeted intertidal flats). The purpose of this experiment is to strengthen salt marsh expansion by feeding the intertidal area with more fine-grained sediments. The sediment is expected to be transported from the tidal channel towards the flats, and the increase in sediment concentration is expected to lead to the accretion of the intertidal zone.

Three main phases were therefore expected: a) the sediment is transported from the tidal channel towards the targeted tidal flats, i.e. the residual sediment transport is directed towards the flats; b) the sediment leads to permanent accretion on the intertidal flats; c) pioneer vegetation is established. The first two phases have been investigated in Chapters 4,5, 6. The key results of this thesis with respect to the two first phases above are as follows:

- The increase in bed elevation of the targeted flats appears not to be limited by sediment

availability, but by the lack of conditions for this sediment to permanently deposit. Findings from this thesis suggest that adding more sediment may even negatively impact permanent deposition because consolidation times scale non-linearly with the thickness of a deposit. Nourishing sediment during a period when sufficient sediment is already available in suspension (winter) is unlikely to promote salt marsh expansion.

- Crucial to net accretion are periods in which the tidal flat is emerged. Sediment should therefore be preferably nourished in the summer period when the flat is more likely to become emerged and overall sediment concentrations are lower. Sediment should not be nourished during periods of relatively low water levels because during such conditions sediments are not able to deposit on the upper flat. Most successful nourishments should account for meteorological predictions (wind velocity for residual transport, water level for inundation and drying).

About the Photo

Muddy substrate on the upper Westhoek intertidal flat, showing the formation of mud cracks and a small Salicornia procumbens plant. The photo was taken on September 15, 2016.

8

CONCLUSIONS

The primary aim of our research was to enhance the understanding of the mechanisms that govern the transport of fine (muddy) sediments across intertidal flats, and the resulting accretion and erosion processes in these ecologically significant areas. A key knowledge gap was the influence of wind. Therefore, we concentrated on wind-driven processes that affect sediment transport and bed level variability. Our analysis was structured around three main research questions:

1. *What is the role of wind on residual and tidal flows over intertidal flats?*
2. *How do tides and winds influence sediment transport over intertidal flats?*
3. *How are phases of accretion and erosion of intertidal flats influenced by wind?*

This chapter summarizes our conclusions regarding these three main research questions and offers suggestions for future studies.

8.1. GENERAL CONCLUSIONS

This thesis has deepened our understanding of the role of wind in intertidal areas. In line with the three main research questions, we examined the influence of wind on the hydrodynamics, sediment transport, and morphological development of intertidal flats.

The key findings can be summarized as follows: (1) Wind plays a much larger role in residual flow over intertidal flats than previously recognized; (2) Residual sediment transport is driven not only by tides and wind but also by temporary (wind-driven) sediment storage in intertidal systems; and (3) Wind influences both phases of erosion (through wave-induced resuspension) and development of bed strength (due to rapid consolidation during prolonged periods of low water levels).

These findings are elaborated on in the following sections, along with the practical implications of our results and recommendations for future research.

WHAT IS THE ROLE OF WIND ON RESIDUAL AND TIDAL FLOWS OVER INTERTIDAL FLATS?

Wind plays a pivotal role in controlling the residual flow over intertidal flats. Residual flow has been estimated via field measurements and further determined via an analytical model simulating the interaction of a sinusoidal tidal flow and horizontal wind-driven flows. The residual flow increases for increasing wind speeds, and its direction is highly affected by wind direction. Tidal flow amplitudes are larger at the lower intertidal areas, that are submerged for longer time compared to the higher flats. However, the residual flow is larger at the higher flats, due to the flow asymmetries introduced by wind-driven flows.

Our results show that the magnitude of wind-driven flows decreases (increases) for increasing (decreasing) tidal flow amplitude. At sites characterized by a relatively weak tide-induced flow (~0.2 m/s) the wind is able to reverse the direction of the tidal flow also at moderate wind speeds (u_{10} ~10 m/s). As a consequence, wind is the dominant hydrodynamic forcing especially at the higher intertidal areas. These results have provided evidence that wind-induced reversal of the tidal flow (also for consecutive tidal cycles) is a relatively common phenomenon in shallow intertidal environments.

The interaction between tidal and wind-driven flow also depends on the tidal asymmetry. In case of flood dominance, the wind is more effective in modifying the ebb flow, whereas in cases of ebb-dominance the flow velocity during flood is more sensitive to the wind-induced modifications (at the same wind speed). The tide–wind interaction results in modified asymmetries in peak flow velocity during flood and ebb. As a consequence, the effect of the wind on the flow depends on the Eulerian asymmetries in the astronomical signal (being stronger for small tidal asymmetry) and affects the Eulerian asymmetries in the meteorological signal (possibly reversing the flow during flood or ebb).

HOW DO TIDES AND WINDS INFLUENCE SEDIMENT TRANSPORT OVER INTERTIDAL FLATS?

Our study demonstrates that the crucial role of wind on tidal flat sediment dynamics not only relates to the wave-induced resuspension, but also to the generation of wind-driven flows enhancing the tide-induced advection of sediment, ultimately affecting the residual sediment transport and hence the short-term morphodynamic of intertidal areas. The residual sediment transport direction follows wind direction, and its magnitude increases for increasing wind speeds. At tide-averaged wind speeds larger than 10 m/s the residual transport increases linearly with the wind speed (both cross-shore and long-shore direction).

Our dataset, gathered at different location during different seasons, have provided evidence

that during non-stormy conditions the intertidal flats are characterized by larger suspended sediment fluxes in winter compared to spring, due to the higher SSC and larger flow velocity, both in turn resulting from the interaction of tidal forcing and wind–driven flows. The increase in suspended sediment concentrations follows from wave-induced erosion, and persists also after the storms.

Our results suggest that sediments can be temporarily stored in the higher areas of the intertidal system, and then easily resuspended and advected during wind events. These storage environments accumulate sediments during conditions of low to moderate winds during which transport is in the same direction as the tide-induced (flood dominant) residual transport. This sediment is subsequently resuspended and transported back during events with winds having the opposite direction. Fairly short windy periods opposite to tide-induced residual transport may in this way balance the residual transport of sediment that occurred over longer time periods in calm wind conditions (weeks to months). This temporal storage of sediment in combination with wind-driven transport is crucial for understanding short- and long-term sediment dynamics in muddy systems, but is in general poorly accounted for in literature. During winter conditions much less sediment is temporally stored. This is probably the result of more energetic conditions (preventing sediments to deposit) but may also be attributed to bio-stabilisation of sediments in the spring period.

HOW ARE PHASES OF ACCRETION AND EROSION OF INTERTIDAL FLATS INFLUENCED BY WIND?

A tidal flat accretes when a new layer of sediment deposits and over–consolidates. The chronological order of sediment deposition and over-consolidation provides what we define, in this dissertation, as a *'Window of Opportunity for tidal flat accretion'*.

Intense depositional periods tend to occur following stormy conditions, as sediment is made available by erosion processes in the intertidal basin or in the estuary area. During the tidal cycles following a storm, the eroded sediment is distributed by the flooding and ebbing tides over the (especially higher) intertidal areas.

Over-consolidation is promoted by the air exposure of the tidal flat bed, and so by wind-induced set-down. Wind opposes the flooding tides, leaving the bed emerged for prolonged periods (also consecutive tidal cycles). The ideal sequel resulting in opportunity for the tidal flat accretion therefore includes:

1. Stormy conditions resuspending sediments in the intertidal system (W-SW wind at our sites);

2. Calm weather conditions with dominating tidal forcing, spreading the available sediment over the higher intertidal zone (no wind or E-NE wind at our study sites);

3. Prolonged moderate wind conditions favoring water level set-down and hence sediment over-consolidation: wind is directed off-shore and in the long-shore direction opposing the flooding tide (respectively SE and NE wind at our study sites).

The sediment transport measurements conducted at the mudflats of Koehool and Westhoek, located along the Dutch Frisian coast, revealed a relatively large availability of suspended sediment, especially close to the bed, with concentration ranging from a few mg/l up to several g/l and reaching peaks of 10 g/l. Point 1) of the previous list is therefore not necessarily needed at our site,

as sediment is available also during calm weather conditions. Nevertheless, also at our sites the highest deposition rates occurred after stormy periods.

Point 3) of the above list indicates that wind-induced set-down provide opportunity for bed emergence, as the air exposure favours a faster over-consolidation process and so bed strength development. This implies that the erosion rate of intertidal areas (e.g. during storm conditions) is strongly influenced by its inundation history, especially the duration for which the flat is emerged. And although many studies have addressed the morphodynamic behaviour of intertidal areas (e.g. *Allen and Duffy*, 1998; *Janssen-Stelder*, 2000; *Bassoullet et al.*, 2000; *Green et al.*, 2000; *Le Hir et al.*, 2000; *Shi et al.*, 2012; *Zhu et al.*, 2017; *Shi et al.*, 2017a), no systematic studies have been executed investigating morphodynamic changes of the bed in response to inundation history. Especially in microtidal environments (with a tidal range less than 2 m) the inundation history is strongly influenced by meteorological conditions due to wind set–up or set–down.

8.2. IMPLICATIONS

The shift from a bare to a vegetated state for salt marshes is a stochastic process, as the occurrence of disturbance-free period following seeds dispersal (i.e. the "Windows of Opportunity for vegetation development" defined by *Balke et al.* (2014)) is regulated by episodic events.

By applying a similar approach to the study of intertidal flat accretion, we hypothesize that the vertical accretion of tidal flats is regulated by the stochastic action of wind, with wind direction playing a fundamental role in allowing for the over-consolidation process. In case a window of opportunity for a tidal flat accretion occurs, the chance for a relatively quick (days/weeks) increase in tidal flat bed elevation exists. This occurs if the deposited sediment layer is sufficiently thick to allow for a vertical accretion, and sufficiently thin to allow for sediment consolidation, in the available emerged period.

Restoration techniques aiming at reusing fine sediment to restore intertidal flats and salt-marshes should take into account:

1. The effect of wind–driven flows interacting with tidal flows and the result of such interaction on the residual sediment transport direction;
2. The background suspended sediment concentrations and the related deposition rates;
3. The consolidation timescales and the wind-induced elongation of emerged conditions of the tidal flats.

8.3. SUGGESTIONS FOR FUTURE STUDIES

The analytical model presented in this dissertation, aiming at predicting the residual flow resulting from the interaction of tidal and wind-driven currents, still presents some weaknesses. These weaknesses mainly relate to the limitation of the used point-measurements when estimating the terms of the Momentum Balance Equation (MBE). Model limitations and possible improvements are listed hereafter:

- Our MBE excluded the evaluation of the time-variant pressure gradient related to water level gradients in the tidal basin, because it required a spatial water level gradient which was not available from the realized point-measurements. However, the MBE analysis included the local time-varying water levels, which indirectly includes the effect of wind on water levels. The hydrodynamic modelling of *Van Weerdenburg et al.* (2021) involving our study area, interestingly shows that the contribution of large scale set-up/down to the residual flow is minimal compared to the local effect of wind shear on the water level variation. The surge variation facilitate residual sediment transport but the local wind forcing is responsible for its generation. The flow velocity predictions obtained with our model were well

representative of field data also due to this reason. If the wind-related water level variation was not included at all, the analytical model could have not provided such good estimates, as the contribution of water level set-up/-down is relevant in enclosed basins like the Wadden Sea. However, further improvements of the model could be realized including the water level gradients at large spatial scale.

- The friction coefficient $c_{f_{cw}}$ in the bed shear stress formulation results from a wave-current model interaction which also has its uncertainties (*Soulsby*, 1995). Moreover, for each investigated site, we assumed the time-averaged value of the friction coefficient over the measurement period. The model could be improved including a time-variant friction coefficient representative for the current-wave interaction close to the bed. Moreover there are several wave-current interaction models available in literature for the estimation of the bed shear stress (*Zhu et al.*, 2019), therefore the variation of the friction coefficient with different models, could be further analyzed to optimize the predictions.
- We considered the two cases of: a) wind aligned with the tidal wave propagating during flood, and b) wind aligned with the ebb. The model is easily extendable to all wind directions maintaining the simplistic "bimodal" approach of long-shore and cross-shore wind and tide components.
- The variation of the cross-shore advection has been neglected, but the cross-shore advection may become relevant at intertidal areas that are more elevated than our monitored sites, due to the refraction of the tidal wave over the coastal shelf. Moreover, this contribution to the transfer of momentum is expected to be more relevant where cross-shore gradients in bed elevation are relatively large (i.e. on tidal flats characterized by larger slopes).
- High resolution numerical models could provide more insights into the variation of the residual terms of the MBE applied in this study.
- In-situ experiments of consolidation process on soft muddy beds, at different tidal flat elevations and during different meteorological conditions, would contribute to a further understanding of accretion- and erosion-related mechanisms. These experiments should include shear vane tests across the tidal flats (to characterize the sediment over the tidal period) combined with hydrodynamic measurements (to quantify the inundation duration and the bed shear stresses), high-resolution bed level changes (with a resolution sufficient to observe the phenomenon of bed compaction during consolidation as well), water-pressure monitoring within the tidal flat bed (to quantify the suction head driving over-consolidation), SSC along the vertical (to quantify the contribution of residual Suspended Sediment Fluxes to local bed level changes) and the effect of biota and vegetation on sediment stabilization over the (higher) tidal flat. The meteorological contribution via wind forcing, precipitation, evaporation and solar radiation will complement this data to further analyse the relative importance of deterministic and stochastic forcing on the accretion of intertidal flats. The spatial-scales, the time-scales and seasonality of the measured variables will overall control the response of intertidal flats to the challenges imposed by the increasing sea-level rise and modifications in storm frequency and intensity.

REFERENCES

Adam, P. (2002), Saltmarshes in a time of change, *Environmental Conservation*, *29*(1), 39–61, doi:10.1017/S0376892902000048.

Adam, P. (2019), Chapter 23 - salt marsh restoration, in *Coastal Wetlands (Second Edition)*, edited by G. M. Perillo, E. Wolanski, D. R. Cahoon, and C. S. Hopkinson, second edition ed., pp. 817–861, Elsevier, doi:https://doi.org/10.1016/B978-0-444-63893-9.00023-X.

Allen, J., and M. Duffy (1998), Medium-term sedimentation on high intertidal mudflats and salt marshes in the severn estuary, sw britain: the role of wind and tide, *Marine Geology*, *150*(1-4), 1–27.

Andersen, T., and M. Pejrup (2001), Suspended sediment transport on a temperate, microtidal mudflat, the Danish Wadden Sea, *Marine Geology*, *173*(1-4), 69–85, doi:10.1016/S0025-3227(00)00164-X.

Andersen, T. J., M. Pejrup, and A. A. Nielsen (2006), Long-term and high-resolution measurements of bed level changes in a temperate, microtidal coastal lagoon, *Marine Geology*, doi:10.1016/j.margeo.2005.09.016.

Anthony, E., G. Brunier, A. Gardel, and M. Hiwat (2019), Chenier morphodynamics on the amazon-influenced coast of suriname, south america: Implications for beach ecosystem services, *Frontiers of Earth Science*, *7*, doi:10.3389/feart.2019.00035.

Baeye, M., M. Fettweis, G. Voulgaris, and V. Van Lancker (2011), Sediment mobility in response to tidal and wind-driven flows along the Belgian inner shelf, southern North Sea, *Ocean Dynamics*, *61*(5), 611–622, doi:10.1007/s10236-010-0370-7.

Bakker, J. P., P. Esselink, K. S. Dijkema, W. E. Van Duin, and D. J. De Jong (2002), Restoration of salt marshes in the Netherlands, *Hydrobiologia*, doi:10.1023/A:1021066311728.

Balke, T., P. M. J. Herman, and T. J. Bouma (2014), Critical transitions in disturbance-driven ecosystems: identifying Windows of Opportunity for recovery, *Journal of Ecology*, *102*(3), 700–708, doi:10.1111/1365-2745.12241.

Balke, T., M. Stock, K. Jensen, T. Bouma, and K. M. (2016), A global analysis of the seaward salt marsh extent:The importance of tidal range, *Water Resource Research*, pp. 3787–3814, doi:10.1002/2014WR016618.Received.

Baptist, M. J., T. Gerkema, B. C. van Prooijen, D. S. van Maren, M. van Regteren, K. Schulz, I. Colosimo, J. Vroom, T. van Kessel, B. Grasmeijer, P. Willemsen, K. Elschot, A. V. de Groot, J. Cleveringa, E. M. van Eekelen, F. Schuurman, H. J. de Lange, and M. E. van Puijenbroek (2019), Beneficial use of dredged sediment to enhance salt marsh development by applying a 'Mud Motor', *Ecological Engineering*, *127*(December 2018), 312–323, doi:10.1016/j.ecoleng.2018.11.019.

Barbier, E. B., E. W. Koch, B. R. Silliman, S. D. Hacker, E. Wolanski, J. Primavera, E. F. Granek, S. Polasky, S. Aswani, L. A. Cramer, et al. (2008), Coastal ecosystem-based management with nonlinear ecological functions and values, *science*, *319*(5861), 321–323.

Barbier, E. B., S. D. Hacker, C. Kennedy, E. W. Kock, A. C. Stier, and B. R. Sillman (2011), The value of estuarine and coastal ecosystem services, *Ecological Monographs*, *81*(2), 169–193, doi:10.1890/10-1510.1.

Barciela Rial, M. (2019), Consolidation and drying of slurries A Building with Nature study for the Marker Wadden, Ph.D. thesis, Delft university of technology, Delft university of technology, doi:https://doi.org/10.4233/uuid:ae11c3e7-86f2-4c6a-8d53-ee8781d56a72.

Barkowski, J., K. Kolditz, H. Brumsack, and H. Freund (2009), The impact of tidal inundation on salt marsh vegetation after de-embankment on langeoog island, germany—six years time series of permanent plots, *Journal of Coastal Conservation*, *13*(4), 185–206.

Bartholdy, J., C. Christiansen, and H. Kunzendorf (1998), Long term variations in backbarrier salt marsh deposition on the Skallingen peninsula – the Danish Wadden Sea, *Marine Geology*, *203*(1-2), 1–21, doi:10.1016/S0025-3227(03)00337-2.

Bassoullet, P., P. Le Hir, D. Gouleau, and S. Robert (2000), Sediment transport over an intertidal mudflat: Field investigations and estimation of fluxes within the 'Baie de Marennes-Oleron' (France), *Continental Shelf Research*, *20*(12-13), 1635–1653, doi:10.1016/S0278-4343(00)00041-8.

Bauer, E., L. Fischer, H. Joachim, M. M. Kühn, and D. Meier (2001), 4.3 the schleswig-holstein wadden sea region, *Wadden Sea Ecosystem*, *12*, 119–157.

Bazelmans, J., D. Meier, A. Nieuwhof, T. Spek, and P. Vos (2012), Understanding the cultural historical value of the wadden sea region. the co-evolution of environment and society in the wadden sea area in the holocene up until early modern times (11,700 bc–1800 ad): an outline, *Ocean & Coastal Management*, *68*, 114–126.

Been, K., and G. Sills (1981), Self-weight consolidation of soft soils: an experimental and theoretical study, *Geotechnique*, *31*(4), 519–535.

Belliard, J. P., A. Silinski, D. Meire, G. Kolokythas, Y. Levy, A. Van Braeckel, T. J. Bouma, and S. Temmerman (2019), High-resolution bed level changes in relation to tidal and wave forcing on a narrow fringing macrotidal flat: Bridging intra-tidal, daily and seasonal sediment dynamics, *Marine Geology*, doi:10.1016/j.margeo.2019.03.001.

Besset, M., E. J. Anthony, and F. Bouchette (2019), Multi-decadal variations in delta shorelines and their relationship to river sediment supply: An assessment and review, *Earth-Science Reviews*, *193*(March), 199–219, doi:10.1016/j.earscirev.2019.04.018.

Blackmar, P. J., D. T. Cox, and W.-C. Wu (2014), Laboratory Observations and Numerical Simulations of Wave Height Attenuation in Heterogeneous Vegetation, *Journal of Waterway, Port, Coastal, and Ocean Engineering*, *140*(1), 56–65, doi:10.1061/(asce)ww.1943-5460.0000215.

Blew, J., K. Günther, K. Laursen, M. v. Roomen, P. Südbeck, K. Eskildsen, P. Potel, H.-U. Rösner, et al. (2005), Overview of numbers and trends of migratory waterbirds in the wadden sea 1980-2000, in *Wadden Sea Ecosystem*, pp. 7–148, Common Wadden Sea Secretariat.

Bol, R. (2005), Operation of the'maeslant barrier':(storm surge barrier in the rotterdam new waterway), *Flooding and Environmental Challenges for Venice and its Lagoon: State of Knowledge.*, pp. 311–315.

Boorman, L., J. Hazelden, and M. Boorman (2002), New salt marshes for old-salt marsh creation and management, in *Littoral*, vol. 2002, p. 6th.

Boorman, L. A., and J. Hazelden (2017), Managed re-alignment; a salt marsh dilemma?, doi:10.1007/s11273-017-9556-9.

Bouwer, L. M., and P. Vellinga (2007), On the flood risk in the netherlands, *Flood risk management in Europe: Innovation in policy and practice*, pp. 469–484.

Brereton, A. J. (1971), The Structure of the Species Populations in the Initial Stages of Salt-Marsh Succession, *Journal of Ecology*, *59*(2), 321–338, doi:10.2307/2258314.

Bunt, J. A., P. Larcombe, and C. F. Jago (1999), Quantifying the response of optical backscatter devices and transmissometers to variations in suspended particulate matter, *Continental Shelf Research*, *19*(9), 1199–1220, doi:https://doi.org/10.1016/S0278-4343(99)00018-7.

Burden, A., R. Garbutt, C. Evans, D. Jones, and D. Cooper (2013), Carbon sequestration and biogeochemical cycling in a saltmarsh subject to coastal managed realignment, *Estuarine, Coastal and Shelf Science*, *120*, 12–20.

Carniello, L., A. Defina, and L. D'Alpaos (2009), Morphological evolution of the venice lagoon: Evidence from the past and trend for the future, *Journal of Geophysical Research: Earth Surface*, *114*(F4).

Carniello, L., A. D'Alpaos, and A. Defina (2011), Modeling wind waves and tidal flows in shallow micro-tidal basins, *Estuarine, Coastal and Shelf Science*, *92*(2), 263–276, doi:10.1016/j.ecss.2011.01.001.

Chen, Y., J. Dong, X. Xiao, M. Zhang, B. Tian, Y. Zhou, B. Li, and Z. Ma (2016), Land claim and loss of tidal flats in the Yangtze Estuary, *Scientific Reports*, *6*, 1–10, doi:10.1038/srep24018.

Christianen, M. J., J. J. Middelburg, S. J. Holthuijsen, J. Jouta, T. J. Compton, T. van der Heide, T. Piersma, J. S. Sinninghe Damsté, H. W. van der Veer, S. Schouten, and H. Olff (2017), Benthic primary producers are key to sustain the Wadden Sea food web: stable carbon isotope analysis at landscape scale, *Ecology*, *98*(6), 1498–1512, doi:10.1002/ecy.1837.

Christiansen, C., G. Vølund, L. C. Lund-Hansen, and J. Bartholdy (2006), Wind influence on tidal flat sediment dynamics: Field investigations in the Ho Bugt, Danish Wadden Sea, *Marine Geology*, *235*(1-4 SPEC. ISS.), 75–86, doi:10.1016/j.margeo.2006.10.006.

Christie, M., and K. Dyer (1998), Measurements of the turbid tidal edge over the skeffling mudflats, *Geological Society, London, Special Publications*, *139*(1), 45–55.

Coco, G., Z. Zhou, B. van Maanen, M. Olabarrieta, R. Tinoco, and I. Townend (2013), Morphodynamics of tidal networks: Advances and challenges, *Marine Geology*, *346*, 1–16, doi:https://doi.org/10.1016/j.margeo.2013.08.005.

Codiga, D. L. (2011), Unified Tidal Analysis and Prediction Using the UTide Matlab Functions, *Technical Report 2011-01. Graduate School of Oceanography, University of Rhode Island, Narragansett, RI,*, doi:10.13140/RG.2.1.3761.2008.

Colin A., G., T. Jones, J. Kirby, and M. Taej (2014), A review of migratory bird flyways and priorities for management, *Tech. rep.*, UNEP/CMS Secretariat.

Colina Alonso, A., D. S. van Maren, E. P. Elias, S. J. Holthuijsen, and Z. B. Wang (2021), The contribution of sand and mud to infilling of tidal basins in response to a closure dam, *Marine Geology*, *439*(February), 106,544, doi:10.1016/j.margeo.2021.106544.

Colina Alonso, A., D. S. van Maren, A. P. Oost, P. Esselink, R. Lepper, F. Kösters, J. Bartholdy, A. I. Bijleveld, and Z. B. Wang (2024), A mud budget of the wadden sea and its implications for sediment management, *Communications Earth & Environment*, *5*(1), 153.

Colosimo, I., P. L. M. de Vet, D. S. van Maren, A. J. H. M. Reniers, J. C. Winterwerp, and B. C. van Prooijen (2020), The Impact of Wind on Flow and Sediment Transport over Intertidal Flats, *Journal of Marine Science and Engineering*, *8*(11), 910, doi:10.3390/jmse8110910.

Conner, C., and A. De Visser (1992), A laboratory investigation of particle size effects on an optical backscatterance sensor, *Marine Geology*, *108*(2), 151–159.

Cozzoli, F., M. Shokri, T. Gomes da Conceição, P. M. Herman, Z. Hu, L. M. Soissons, J. Van Dalen, T. Ysebaert, and T. J. Bouma (2021), Modelling spatial and temporal patterns in bioturbator effects on sediment resuspension: A biophysical metabolic approach, *Science of the Total Environment*, *792*, doi:10.1016/j.scitotenv.2021.148215, cited by: 13; All Open Access, Green Open Access.

Crosby, S. C., D. F. Sax, M. E. Palmer, H. S. Booth, L. A. Deegan, M. D. Bertness, and H. M. Leslie (2016), Salt marsh persistence is threatened by predicted sea-level rise, *Estuarine, Coastal and Shelf Science*, *181*, 93–99, doi:10.1016/j.ecss.2016.08.018.

Daidu, F., W. Yuan, and L. Min (2013), Classifications, sedimentary features and facies associations of tidal flats, *Journal of Palaeogeography*, *2*(1), 66–80, doi:10.3724/SP.J.1261.2013.00018.

Damen, J. (2004), Land Banking in the Netherlands in the context of land consolidation, *International workshop: Land Banking/Land Funds as an Instrument for Improved Land Management for CEEC and CIS*, pp. 1–5.

Dankers, N., W. van Duin, M. Baptist, E. Dijkman, and J. Cremer (2012), 11 - the wadden sea in the netherlands: Ecotopes in a world heritage barrier island system, in *Seafloor Geomorphology as Benthic Habitat*, edited by P. T. Harris and E. K. Baker, pp. 213–226, Elsevier, London, doi: https://doi.org/10.1016/B978-0-12-385140-6.00011-6.

Davidson, N. C. (2014), How much wetland has the world lost? long-term and recent trends in global wetland area, *Marine and Freshwater Research*, *65*(10), 934–941.

Davy, A. J., M. P. Weinstein, and D. A. Kreeger (2000), *Development and Structure of Salt Marshes: Community Patterns in Time and Space*, pp. 137–156, Springer Netherlands, doi:10.1007/0-306-47534-0_8.

Day, J. W., and J. M. Rybczyk (2019), Chapter 36 - global change impacts on the future of coastal systems: Perverse interactions among climate change, ecosystem degradation, energy scarcity, and population, in *Coasts and Estuaries*, edited by E. Wolanski, J. W. Day, M. Elliott, and R. Ramachandran, pp. 621–639, Elsevier, doi:https://doi.org/10.1016/B978-0-12-814003-1.00036-8.

De Deckere, E. (2003), *Faunal influence on sediment stability in intertidal mudflats*, Netherlands Institute of Ecology.

De Jonge, V., K. Essink, and R. Boddeke (1993), The dutch wadden sea: a changed ecosystem, *Hydrobiologia*, *265*, 45–71.

De Kraker, A. M. (2006), Flood events in the southwestern netherlands and coastal belgium, 1400–1953, *Hydrological Sciences Journal*, *51*(5), 913–929.

De Mulder, E., A. van Bruchem, F. Claessen, G. Hannink, J. Hulsbergen, and H. Satijn (1994), Environmental impact assessment on land reclamation projects in the netherlands: A case history, *Engineering Geology*, *37*(1), 15–23, doi:https://doi.org/10.1016/0013-7952(94)90078-7.

De Vet, P., B. Van Prooijen, I. Colosimo, T. Ysebaert, P. Herman, and Z. Wang (2020a), Sediment disposals in estuarine channels alter the eco-morphology of intertidal flats, *Journal of Geophysical Research: Earth Surface*, *125*(2), e2019JF005,432.

De Vet, P. L., B. C. van Prooijen, I. Colosimo, N. Steiner, T. Ysebaert, P. M. Herman, and Z. B. Wang (2020b), Variations in storm-induced bed level dynamics across intertidal flats, *Scientific Reports*, doi:10.1038/s41598-020-69444-7.

De Vet, P. L. M., B. C. van Prooijen, R. A. Schrijvershof, J. J. van der Werf, T. Ysebaert, M. C. Schrijver, and Z. B. Wang (2018), The Importance of Combined Tidal and Meteorological Forces for the Flow and Sediment Transport on Intertidal Shoals, *Journal of Geophysical Research: Earth Surface*, *123*(10), 2464–2480, doi:10.1029/2018JF004605.

De Vriend, H. J., Z. B. Wang, T. Ysebaert, P. M. Herman, and P. Ding (2011), Eco-morphological problems in the yangtze estuary and the western scheldt, *Wetlands*, *31*, 1033–1042.

Deaton, C. D., C. J. Hein, and M. L. Kirwan (2017), Barrier island migration dominates ecogeomorphic feedbacks and drives salt marsh loss along the Virginia Atlantic Coast, USA, *Geology*, *45*(2), 123–126, doi:10.1130/G38459.1.

Delefosse, M., and E. Kristensen (2012), Burial of zostera marina seeds in sediment inhabited by three polychaetes: laboratory and field studies, *Journal of Sea research*, *71*, 41–49.

Delgado, P., P. Hensel, and A. Baldwin (2018), Understanding the Impacts of Climate Change: an Analysis of Inundation, Marsh Elevation, and Plant Communities in a Tidal Freshwater Marsh, *Estuaries and Coasts*, *41*(1), 25–35, doi:10.1007/s12237-017-0342-y.

Deloffre, J., R. Verney, R. Lafite, P. Lesueur, S. Lesourd, and A. Cundy (2007), Sedimentation on intertidal mudflats in the lower part of macrotidal estuaries: Sedimentation rhythms and their preservation, *Marine Geology*, *241*(1-4), 19–32, doi:10.1016/j.margeo.2007.02.011.

Dijkema, K., R. de Glopper, and I. Mendelssohn (1988), *The use of European marsh-accretion techniques for large-scale marsh creation in Louisiana*, Louisiana State University.

Dolphin, T. J., and M. O. Green (2009), Patter of wave-orbital and skin friction under estuarine (fetch-limited waves), *Journal of Coastal Research*, *2009*(SI56), 178–182.

Downing, J. (2006), Twenty-five years with OBS sensors: The good, the bad, and the ugly, *Continental Shelf Research*, *26*(17-18), 2299–2318, doi:10.1016/j.csr.2006.07.018.

Dronkers, J. (1986), Tidal asymmetry and estuarine morphology, *Netherlands Journal of Sea Research*, *20*(2-3), 117–131.

Druine, F., R. Verney, J. Deloffre, J.-P. Lemoine, M. Chapalain, V. Landemaine, and R. Lafite (2018), In situ high frequency long term measurements of suspended sediment concentration in turbid estuarine system (seine estuary, france): Optical turbidity sensors response to suspended sediment characteristics, *Marine Geology*, *400*, 24–37.

Duran-Matute, M., T. Gerkema, G. J. De Boer, J. J. Nauw, and U. Gräwe (2014), Residual circulation and freshwater transport in the Dutch Wadden Sea: A numerical modelling study, *Ocean Science*, *10*(4), 611–632, doi:10.5194/os-10-611-2014.

Duran-Matute, M., T. Gerkema, and M. Sassi (2016), Quantifying the residual volume transport through a multiple-inlet system in response to wind forcing: The case of thewestern Dutch Wadden Sea, *Journal of Geophysical Research: Oceans*, pp. 6223–6250, doi:10.1002/2016JC011807.

Dyke, P. P. (2007), *Modeling coastal and offshore processes*, Imperial College Press.

Elias, E. P., A. J. Van Der Spek, Z. B. Wang, and J. De Ronde (2012), Morphodynamic development and sediment budget of the Dutch Wadden Sea over the last century, *Geologie en Mijnbouw/Netherlands Journal of Geosciences*, *91*(3), 293–310, doi:10.1017/S0016774600000457.

Erfanzadeh, R., A. Garbutt, J. Pétillon, J.-P. Maelfait, and M. Hoffmann (2010), Factors affecting the success of early salt-marsh colonizers: seed availability rather than site suitability and dispersal traits, *Plant Ecology*, *206*(2), 335–347.

Erftemeijer, P. L., and R. R. R. Lewis III (2006), Environmental impacts of dredging on seagrasses: a review, *Marine pollution bulletin*, *52*(12), 1553–1572.

Fagherazzi, S., C. Palermo, M. C. Rulli, L. Carniello, and A. Defina (2007), Wind waves in shallow microtidal basins and the dynamic equilibrium of tidal flats, *Journal of Geophysical Research: Earth Surface*, *112*(F2), doi:https://doi.org/10.1029/2006JF000572.

Fagherazzi, S., G. Mariotti, P. L. Wiberg, and K. J. McGLATHERY (2013), Marsh collapse does not require sea level rise, *Oceanography*, *26*(3), 70–77.

Fagherazzi, S., T. Viggato, A. Vieillard, G. Mariotti, and R. Fulweiler (2017), The effect of evaporation on the erodibility of mudflats in a mesotidal estuary, *Estuarine, Coastal and Shelf Science*, *194*, 118–127.

Fan, D., and C. Li (2002), Rhythmic deposition on mudflats in the mesotidal changjiang estuary, china, *Journal of Sedimentary Research*, *72*(4), 543–551.

Fan, D., C. Li, A. W. Archer, and P. Wang (2002), Temporal distribution of diastems in deposits of an open-coast tidal flat with high suspended sediment concentrations, *Sedimentary Geology*, *152*(3-4), 173–181.

Fan, D., Y. Guo, P. Wang, and J. Z. Shi (2006), Cross-shore variations in morphodynamic processes of an open-coast mudflat in the changjiang delta, china: with an emphasis on storm impacts, *Continental Shelf Research*, *26*(4), 517–538.

Fan, R., L. Zhao, Y. Lu, H. Nie, and H. Wei (2019), Impacts of Currents and Waves on Bottom Drag Coefficient in the East China Shelf Seas, *Journal of Geophysical Research: Oceans*, *124*(11), 7344–7354, doi:10.1029/2019JC015097.

Faria, A. F. G., E. B. Thornton, T. P. Stanton, C. V. Soares, and T. C. Lippmann (1998), Vertical profiles of longshore currents and related bed shear stress and bottom roughness, *Journal of Geophysical Research: Oceans*, *103*(C2), 3217–3232, doi:10.1029/97JC02265.

Fettweis, M., R. Riethmüller, R. Verney, M. Becker, J. Backers, M. Baeye, M. Chapalain, S. Claeys, J. Claus, T. Cox, et al. (2019), Uncertainties associated with in situ high-frequency long-term observations of suspended particulate matter concentration using optical and acoustic sensors, *Progress in Oceanography*, *178*, 102,162.

Fluet-Chouinard, E., B. D. Stocker, Z. Zhang, A. Malhotra, J. R. Melton, B. Poulter, J. O. Kaplan, K. K. Goldewijk, S. Siebert, T. Minayeva, et al. (2023), Extensive global wetland loss over the past three centuries, *Nature*, *614*(7947), 281–286.

Frazier, S. (1999), Ramsar Sites Overview A Synopsis of the World's Wetlands of International Importance, *Wetland International*.

Friedrichs, C. T. (2012), *Tidal Flat Morphodynamics: A Synthesis*, vol. 3, 137–170 pp., Elsevier Inc., doi:10.1016/B978-0-12-374711-2.00307-7.

Friedrichs, C. T., and D. Aubrey (1996), Uniform bottom shear stress and equilibrium hyposometry of intertidal flats, *Mixing in estuaries and coastal seas*, *50*, 405–429.

Friedrichs, C. T., and O. S. Madsen (1992), Nonlinear diffusion of the tidal signal in frictionally dominated embayments, *Journal of Geophysical Research: Oceans*, *97*(C4), 5637–5650.

Friedrichs, C. T., and J. E. Perry (2001), Tidal Salt Marsh Morphodynamics: A Synthesis, *Journal of Coastal Research*, *1*(27), 7–37.

Friess, D. A., K. Rogers, C. E. Lovelock, K. W. Krauss, S. E. Hamilton, S. Y. Lee, R. Lucas, J. Primavera, A. Rajkaran, and S. Shi (2019), The state of the world's mangrove forests: past, present, and future, *Annual Review of Environment and Resources*, *44*, 89–115.

Fruergaard, M., T. J. Andersen, P. N. Johannessen, L. H. Nielsen, and M. Pejrup (2013), Major coastal impact induced by a 1000-year storm event, *Scientific Reports*, *3*(1), 1051.

Gao, A., S. L. Yang, G. Li, P. Li, and S. L. Chen (2010), Long-Term Morphological Evolution of a Tidal Island as Affected by Natural Factors and Human Activities, the Yangtze Estuary, *Journal of Coastal Research*, *2010*(261), 123 – 131, doi:10.2112/08-1052.1.

Garwood, J. C., P. S. Hill, H. L. MacIntyre, and B. A. Law (2015), Grain sizes retained by diatom biofilms during erosion on tidal flats linked to bed sediment texture, *Continental Shelf Research*, *104*, 37–44.

Gedan, K. B., M. L. Kirwan, E. Wolanski, E. B. Barbier, and B. R. Silliman (2011), The present and future role of coastal wetland vegetation in protecting shorelines: answering recent challenges to the paradigm, *Climatic change*, *106*, 7–29.

Gerkema, T., J. Nauw, and C. van der Hout (2014), Measurements on the transport of suspended particulate matter in the Vlie Inlet, *Netherlands Journal of Geosciences - Geologie en Mijnbouw*, *93*(3), 95–105, doi:10.1017/njg.2014.7.

Gibson, R., M. Barnes, and R. Atkison (2001), Functional group ecology in soft-sediment marine benthos: the role of bioturbation, *Oceanogr Mar Biol Annu Rev*, *39*, 233–267.

Goring, D. G., and V. I. Nikora (2002), Despiking Acoustic Doppler Velocimeter Data, *Journal of Hydraulic Engineering*, *128*(1), 117–126, doi:10.1061/(ASCE)0733-9429(2002)128:1(117).

Graber, F. (2010), David blackbourn, the conquest of nature. water, landscape, and the making of modern germany, new york, norton, 2006, 466 p., isbn 978-0-393-06212-0, *Revue d'Histoire Moderne et Contemporaine*, *57*(3), 177–178.

Gräwe, U., G. Flöser, T. Gerkema, M. Duran-Matute, T. H. Badewien, E. Schulz, and H. Burchard (2016), A numerical model for the entire wadden sea: Skill assessment and analysis of hydrodynamics, *Journal of Geophysical Research: Oceans*, *121*(7), 5231–5251.

Green, M. (2003), The dance of the turbid fringe, *Water and Atmosphere*, *11*(2), 20–21.

Green, M. O., and G. Coco (2014), Review of wave driven sediment resuspension and transport in estuaries, *Reviews of Geophysics*, *52*(1), 77–117, doi:10.1002/2013RG000437.Received.

Green, M. O., R. G. Bell, T. J. Dolphin, and A. Swales (2000), Silt and sand transport in a deep tidal channel of a large estuary (Manukau Harbour, New Zealand), *Marine Geology*, *163*(1-4), 217–240, doi:10.1016/S0025-3227(99)00102-4.

Groot, R., L. Brander, and M. Finlayson (2018), *Wetland Ecosystem Services*, pp. 323–333, Springer Netherlands, doi:10.1007/978-90-481-9659-3_66.

Hazelden, J., and L. Boorman (2001), Soils and 'managed retreat'in south east england, *Soil Use and Management*, *17*(3), 150–154.

Herman, P. M., J. S. Moons, J. W. Wijsman, A. P. Luijendijk, and T. Ysebaert (2021), A mega-nourishment (sand motor) affects landscape diversity of subtidal benthic fauna, *Frontiers in Marine Science*, *8*, 643,674.

Hoeksema, R. J. (2007), Three stages in the history of land reclamation in the netherlands, *Irrigation and Drainage: The Journal of the International Commission on Irrigation and Drainage*, *56*(S1), S113–S126.

Hofstede, J. L. (2003), Integrated management of artificially created salt marshes in the wadden sea of schleswig-holstein, germany, *Wetlands Ecology and management*, *11*(3), 183–194.

Holzhauer, H., B. Borsje, P. Herman, C. Schipper, and K. Wijnberg (2022), The geomorphology of an ebb-tidal-delta linked to benthic species distribution and functionality, *Ocean and Coastal Management*, *216*, 105,938, doi:https://doi.org/10.1016/j.ocecoaman.2021.105938.

Houwing, E.-J. (2000), Morphodynamic development of intertidal mudflats: consequences for the extension of the pioneer zone, *Continental Shelf Research*, *20*(12-13), 1735–1748.

Huismans, Y., A. van der Spek, Q. Lodder, R. Zijlstra, E. Elias, and Z. B. Wang (2022), Development of intertidal flats in the Dutch Wadden Sea in response to a rising sea level: Spatial differentiation and sensitivity to the rate of sea level rise, *Ocean and Coastal Management*, *216*(November 2021), 105,969, doi:10.1016/j.ocecoaman.2021.105969.

Hume, T. M., and C. E. Herdendorf (1988), A geomorphic classification of estuaries and its application to coastal resource management—a new zealand example, *Ocean and Shoreline Management*, *11*(3), 249–274, doi:https://doi.org/10.1016/0951-8312(88)90022-7.

Hunt, S., K. R. Bryan, and J. C. Mullarney (2015), The influence of wind and waves on the existence of stable intertidal morphology in meso-tidal estuaries, *Geomorphology*, *228*, 158–174, doi:10.1016/j.geomorph.2014.09.001.

Janssen-Stelder, B. (2000), The effect of different hydrodynamic conditions on the morphodynamics of a tidal mudflat in the Dutch Wadden Sea, *Continental Shelf Research*, *20*, 1461–1478.

Kabat, P., L. O. Fresco, M. J. Stive, C. P. Veerman, J. S. Van Alphen, B. W. Parmet, W. Hazeleger, and C. A. Katsman (2009), Dutch coasts in transition, *Nature Geoscience*, *2*(7), 450–452.

Kadiri, M., K. L. Spencer, C. M. Heppell, and P. Fletcher (2011), Sediment characteristics of a restored saltmarsh and mudflat in a managed realignment scheme in southeast england, *Hydrobiologia*, *672*(1), 79–89.

Kirwan, M. L., A. B. Murray, J. P. Donnelly, and D. R. Corbett (2011), Rapid wetland expansion during european settlement and its implication for marsh survival under modern sediment delivery rates, *Geology*, *39*(5), 507–510.

Kirwan, M. L., S. Temmerman, E. E. Skeehan, G. R. Guntenspergen, and S. Fagherazzi (2016), Overestimation of marsh vulnerability to sea level rise, doi:10.1038/nclimate2909.

Kobayashi, N. (1993), FORMULATION z Wave Gages, *J. Waterway, Port, Coastal, Ocean Eng*, *119*(1), 30–48.

Kornman, B. A., and E. M. D. Deckere (1998), Temporal variation in sediment erodibility and suspended sediment dynamics in the dollard estuary, *Geological Society, London, Special Publications*, *139*(1), 231–241.

Kranenburg, C. (1994), The fractal structure of cohesive sediment aggregates, *Estuarine, Coastal and Shelf Science*, *39*(5), 451–460.

Laboyrie, P., M. Van Koningsveld, S. Aarninkhof, M. Van Parys, M. Lee, A. Jensen, A. Csiti, and R. Kolman (2018), *Dredging for sustainable infrastructure*, CEDA/IADC The Hague, The Netherlands.

Landin, M. C., E. J. Clairain, and C. J. Newling (1989), Wetland habitat development and long-term monitoring at windmill point, virginia, *Wetlands*, *9*(1), 13–25.

LaSalle, M. W., M. C. Landin, and J. G. Sims (1991), Evaluation of the flora and fauna of a spartina alterniflora marsh established on dredged material in winyah bay, south carolina, *Wetlands*, *11*, 191–208.

Le Hir, P., W. Roberts, O. Cazaillet, M. Christie, P. Bassoullet, and C. Bacher (2000), Characterization of intertidal flat hydrodynamics, *Continental Shelf Research*, *20*(12-13), 1433–1459, doi:10.1016/S0278-4343(00)00031-5.

Le Hir, P., Y. Monbet, and F. Orvain (2007), Sediment erodability in sediment transport modelling: Can we account for biota effects?, *Continental Shelf Research*, *27*(8), 1116–1142, doi:https://doi.org/10.1016/j.csr.2005.11.016, natural Coastal Mechanisms - Flume and Field Experiments on Links between Biology, Sediments and Flow.

Le Hir, P., F. Cayocca, and B. Waeles (2011), Dynamics of sand and mud mixtures: A multiprocess-based modelling strategy, *Continental Shelf Research*, *31*(10), S135–S149.

Leonardi, N., N. K. Ganju, and S. Fagherazzi (2016), A linear relationship between wave power and erosion determines salt-marsh resilience to violent storms and hurricanes, *Proceedings of the National Academy of Sciences*, *113*(1), 64–68.

Li, X., L. Ren, Y. Liu, C. Craft, Ü. Mander, and S. Yang (2014), The impact of the change in vegetation structure on the ecological functions of salt marshes: The example of the Yangtze estuary, *Regional Environmental Change*, *14*(2), 623–632, doi:10.1007/s10113-013-0520-9.

Li, X., R. Bellerby, C. Craft, and S. E. Widney (2018), Coastal wetland loss, consequences, and challenges for restoration, *Anthropocene Coasts*, *15*(January), 1–15, doi:10.1139/anc-2017-0001.

Li, Y., H. Li, L. Qiao, Y. Xu, X. Yin, and J. He (2015), Storm deposition layer on the fujian coast generated by typhoon saola (2012), *Scientific reports*, *5*(1), 14,904.

Lin, J., Q. He, L. Guo, B. C. van Prooijen, and Z. B. Wang (2020), An integrated optic and acoustic (IOA) approach for measuring suspended sediment concentration in highly turbid environments, *Marine Geology*, *421*, 106,062, doi:https://doi.org/10.1016/j.margeo.2019.106062.

Lin, Q., and S. Yu (2018), Losses of natural coastal wetlands by land conversion and ecological degradation in the urbanizing Chinese coast, *Scientific Reports*, *8*(1), 1–10, doi:10.1038/s41598-018-33406-x.

Lin, W., L. P. Sanford, S. E. Suttles, and R. Valigura (2002), Drag Coefficients with Fetch-Limited Wind Waves*, *Journal of Physical Oceanography*, doi:10.1175/1520-0485(2002)032<3058:dcwflw>2.0.co;2.

Lotze, H. K., H. S. Lenihan, B. J. Bourque, R. H. Bradbury, R. G. Cooke, M. C. Kay, S. M. Kidwell, M. X. Kirby, C. H. Peterson, and J. B. Jackson (2006), Depletion, degradation, and recovery potential of estuaries and coastal seas, *Science*, *312*(5781), 1806–1809.

M. Parry, O. C., J. Palutikof, P. van der Linden, and C. Hanson (2007), Ipcc2007: Climate change 2007: Impacts, adaptation and vulnerability. contribution of wirking greoup ii to the fourth assessoment report of the intergovernmental panel on climate change, *Tech. rep.*, Cambridge University Press, doi:10.1016/B978-008044910-4.00250-9.

Maan, C. (2019), Long-term dynamics and stabilization of intertidal flats: A system approach, Ph.D. thesis, Delft University of Technology, doi:10.4233/uuid:cbb5e163-eac7-44b8-b336-deb94106cfce.

Maan, D. C., B. C. Van Prooijen, Z. B. Wang, and H. J. De Vriend (2015), Do intertidal flats ever reach equilibrium?, *Journal of Geophysical Research F: Earth Surface*, *120*(11), 2406–2436, doi:10.1002/2014JF003311.

Mai, S., and A. Bartholomä (2000), The missing mud flats of the Wadden Sea: a reconstruction of sediments and accommodation space lost in the wake of land reclamation, in *Muddy Coast Dynamics and Resource Management*, *Proceedings in Marine Science*, vol. 2, edited by B. W. Flemming, M. T. Delafontaine, and G. Liebezeit, pp. 257–272, Elsevier, doi:https://doi.org/10.1016/S1568-2692(00)80021-2.

Malak, D. A., A. I. Marín, M. Trombetti, and S. S. Roman (2021), Carbon pools and sequestration potential of wetlands in the european union, *Tech. rep.*, European Topic Centre on Urban, Land and Soil Systems; University of Malaga - UMA.

Malarkey, J., J. H. Baas, J. A. Hope, R. J. Aspden, D. R. Parsons, J. Peakall, D. M. Paterson, R. J. Schindler, L. Ye, I. D. Lichtman, et al. (2015), The pervasive role of biological cohesion in bedform development, *Nature communications*, *6*(1), 6257.

Mancheño, A. G., W. Jansen, W. Uijttewaal, A. Reniers, A. van Rooijen, T. Suzuki, V. Etminan, and J. Winterwerp (2021), Wave transmission and drag coefficients through dense cylinder arrays: Implications for designing structures for mangrove restoration, *Ecological Engineering*, *165*, 106,231.

Marani, M., R. Aspden, E. Belluco, M. Camuffo, A. D. Alpaos, J. Korczak, S. Lanzoni, C. Macgregor, A. Marani, D. Mason, M. Menenti, D. Paterson, A. Quirin, R. Rigon, A. Rinaldo, T. Scott, S. Silvestri, S. Vardy, and C. Wang (2004), Observations and ecogeomorphological modelling of tidal environments, *Tech. Rep. January 2014*, University of Padua, Ital), University Ca Foscari Venice, Italy; LSIIT, Universite Luis Pasteur, Strasbourg, France ; ESSC, NERC and University of Reading, United Kingdom; Gatty Marine Laboratory, University of St. Andrews, United Kingdom.

Marfai, M. (2011), Impact of coastal inundation on ecology and agricultural land use case study in central java, indonesia, *Quaestiones Geographicae*, *30*(3), 19–32.

Mariotti, G., and S. Fagherazzi (2011), Asymmetric fluxes of water and sediments in a mesotidal mudflat channel, *Continental Shelf Research*, *31*(1), 23–36, doi:10.1016/j.csr.2010.10.014.

Mariotti, G., and S. Fagherazzi (2012), Modeling the effect of tides and waves on benthic biofilms, *Journal of Geophysical Research: Biogeosciences*, *117*(G4).

Mariotti, G., and S. Fagherazzi (2013), Wind waves on a mudflat: The influence of fetch and depth on bed shear stresses, *Continental Shelf Research*, *60*, S99–S110, doi:10.1016/j.csr.2012.03.001.

McKee, K. L., and W. H. Patrick (1988), The relationship of smooth cordgrass (Spartina alterniflora) to tidal datums: A review, *Estuaries*, *11*(3), 143–151, doi:10.2307/1351966.

Merckelbach, L., and C. Kranenburg (2004), Equations for effective stress and permeability of soft mud–sand mixtures, *Géotechnique*, *54*(4), 235–243.

Merckelbach, L. M. (2006), A model for high-frequency acoustic Doppler current profiler backscatter from suspended sediment in strong currents, *Continental Shelf Research*, *26*(11), 1316–1335, doi:10.1016/j.csr.2006.04.009.

Merten, G. H., P. D. Capel, and J. P. Minella (2014), Effects of suspended sediment concentration and grain size on three optical turbidity sensors, *Journal of Soils and Sediments*, *14*(7), 1235–1241.

Mitchener, H., and H. Torfs (1996), Erosion of mud/sand mixtures, *Coastal engineering*, *29*(1-2), 1–25.

Möller, I., M. Kudella, F. Rupprecht, T. Spencer, M. Paul, B. K. Van Wesenbeeck, G. Wolters, K. Jensen, T. J. Bouma, M. Miranda-Lange, and S. Schimmels (2014), Wave attenuation over coastal salt marshes under storm surge conditions, *Nature Geoscience*, *7*(10), 727–731, doi:10.1038/NGEO2251.

Mossman, H. L., A. J. Davy, and A. Grant (2012), Does managed coastal realignment create saltmarshes with 'equivalent biological characteristics' to natural reference sites?, *Journal of Applied Ecology*, *49*(6), 1446–1456, doi:10.1111/j.1365-2664.2012.02198.x.

Mudd, S. M., A. D'Alpaos, and J. T. Morris (2010), How does vegetation affect sedimentation on tidal marshes? Investigating particle capture and hydrodynamic controls on biologically mediated sedimentation, *Journal of Geophysical Research: Earth Surface*, *115*(3), doi:10.1029/2009JF001566.

Murray, J. M., A. Meadows, and P. S. Meadows (2002), Biogeomorphological implications of microscale interactions between sediment geotechnics and marine benthos: a review, *Geomorphology*, *47*(1), 15–30, doi:https://doi.org/10.1016/S0169-555X(02)00138-1, biogeomorphology.

Murray, N. J., R. S. Clemens, S. R. Phinn, H. P. Possingham, and R. A. Fuller (2014), Tracking the rapid loss of tidal wetlands in the yellow sea, *Frontiers in Ecology and the Environment*, *12*(5), 267–272.

Murray, N. J., S. R. Phinn, M. DeWitt, R. Ferrari, R. Johnston, M. B. Lyons, N. Clinton, D. Thau, and R. A. Fuller (2019), The global distribution and trajectory of tidal flats, *Nature*, *565*(7738), 222–225, doi:10.1038/s41586-018-0805-8.

Nauw, J., L. Merckelbach, H. Ridderinkhof, and H. Van Aken (2014), Long-term ferry-based observations of the suspended sediment fluxes through the marsdiep inlet using acoustic doppler current profilers, *Journal of Sea Research*, *87*, 17–29.

Nguyen, H. M., K. R. Bryan, Z. Zhou, and C. A. Pilditch (2022), Modeling the effects of aerial temperature and exposure period on intertidal mudflat profiles, *Continental Shelf Research*, *245*, 104,802.

O'Brian, D. J. (1998), The sediment dynamics of a macrotidal mudflat on varying timescales, *Continental Shelf Research*, *20*, 1593–1619.

O'Callaghan, J. M., C. B. Pattiaratchi, and D. P. Hamilton (2010), The role of intratidal oscillations in sediment resuspension in a diurnal, partially mixed estuary, *Journal of Geophysical Research*, *115*(C7), C07,018, doi:10.1029/2009JC005760.

on Hydromechanics of the Hydraulics Division, C. (1963), Friction factors in open channels: Progress report of the task force on friction factors in open channels of the committee on hydromechanics of the hydraulics division, *Journal of the Hydraulics Division*, *89*(2), 97–143.

Oost, A., C. Winter, P. Vos, F. Bungenstock, R. Schrijvershof, B. Röbke, J. Bartholdy, J. Hofstede, A. Wurpts, and A. Wehrmann (2017), Geomorphology. in: Wadden sea quality status report. eds.: Kloepper s. et al., *Tech. rep.*, Common Wadden Sea Secretariat, Wilhelmshaven, Germany.

Oost, A. P. (1995), Dynamics and sedimentary development of the dutch wadden sea with emphasis on the frisian inlet, a study of barrier islands, ebb-tidal deltas, inlets and drainage bassins, *PhD Thesis, Utrecht University*.

Orvain, F., P. Le Hir, P.-G. Sauriau, and S. Lefebvre (2012), Modelling the effects of macrofauna on sediment transport and bed elevation: Application over a cross-shore mudflat profile and model validation, *Estuarine, Coastal and Shelf Science*, *108*, 64–75.

Ouyang, X., and S. Y. Lee (2013), Carbon accumulation rates in salt marsh sediments suggest high carbon storage capacity, *Biogeosciences Discussions*, *10*(December), doi:10.5194/bgd-10-19155-2013.

Parsons, D. R., R. J. Schindler, J. A. Hope, J. Malarkey, J. H. Baas, J. Peakall, A. J. Manning, L. Ye, S. Simmons, D. M. Paterson, et al. (2016), The role of biophysical cohesion on subaqueous bed form size, *Geophysical research letters*, *43*(4), 1566–1573.

Pascolo, S., M. Petti, and S. Bosa (2018), On the Wave Bottom Shear Stress in Shallow Depths: The Role of Wave Period and Bed Roughness, *Water*, *10*(10), 1348, doi:10.3390/w10101348.

Paterson, D., and S. Hagerthey (2001), Microphytobenthos in constrasting coastal ecosystems: biology and dynamics, *Ecological comparisons of sedimentary shores*, pp. 105–125.

Pearson, S. G., R. Verney, B. C. van Prooijen, D. Tran, E. C. Hendriks, M. Jacquet, and Z. B. Wang (2021), Characterizing the Composition of Sand and Mud Suspensions in Coastal and Estuarine Environments Using Combined Optical and Acoustic Measurements, *Journal of Geophysical Research: Oceans*, *126*(7), 1–23, doi:10.1029/2021JC017354.

Pendleton, L., D. C. Donato, B. C. Murray, S. Crooks, W. A. Jenkins, S. Sifleet, C. Craft, J. W. Fourqurean, J. B. Kauffman, N. Marbà, et al. (2012), Estimating global "blue carbon" emissions from conversion and degradation of vegetated coastal ecosystems, *PLoS ONE*.

PIANC, E. C. T. G. . (2011), Towards a sustainable waterborne transportation industry, *Tech. rep.*, The World Association for Waterborne Transport Infrastructure.

Pontee, N. (2013), Defining coastal squeeze: A discussion, *Ocean and Coastal Management*, *84*, 204–207, doi:10.1016/j.ocecoaman.2013.07.010.

Postma, H. (1961), Transport and accumulation of suspended matter in the Dutch Wadden Sea, *Netherlands Journal of Sea Research*, *1*(1-2), 148–190, doi:10.1016/0077-7579(61)90004-7.

Reading, C., A. Garbutt, C. Watts, P. Rothery, A. Turk, M. Yates, C. Boffey, J. Saunders, and M. Wolters (2008), Managed realignment at tollesbury, *Tech. rep.*, Environment Angency, Department for Environment, Food and Rural Affairs (Defra), Joint Defra/EA Flood and Coastal Erosion Risk Management RD Programme, Technical Report FD1922/TR.

Reed, D. (1990), The impact of sea-level rise marshes, *Progress in Physical Geography*, *14*(4), 465–481.

Reed, D., B. Van Wesenbeeck, P. M. Herman, and E. Meselhe (2018), Tidal flat-wetland systems as flood defenses: Understanding biogeomorphic controls, *Estuarine, Coastal and Shelf Science*, *213*, 269–282, doi:https://doi.org/10.1016/j.ecss.2018.08.017.

Regteren, M., I. Colosimo, P. Vries, M. E. B. Puijenbroek, V. S. Freij, M. J. Baptist, and K. Elschot (2019), Limited seed retention during winter inhibits vegetation establishment in spring, affecting lateral marsh expansion capacity, *Ecology and Evolution*, *9*(23), 13,294–13,308, doi:10.1002/ece3.5781.

Reise, K., M. Baptist, P. Burbridge, N. Dankers, L. Fischer, B. Flemming, A. Oost, and C. Smit (2010), The wadden sea a universally outstanding tidal wetland, *Wadden Sea Ecosystem*, *29*, 7–24.

Rezaie, A. M., J. Loerzel, and C. M. Ferreira (2020), Valuing natural habitats for enhancing coastal resilience: Wetlands reduce property damage from storm surge and sea level rise, *PLoS One*, *15*(1), e0226,275.

Ridderinkhof, H., R. van der Ham, and W. van der Lee (2000), Temporal variations in concentration and transport of suspended sediments in a channel–flat system in the ems-dollard estuary, *Continental Shelf Research*, *20*(12-13), 1479–1493.

Riedel T., B. M., Lettmann K., and B. H.J. (2010), Tidal variations in groundwater storage and associated discharge from an intertidal coastal aquifer, *Journal of Geophysical Research: Oceans*, *115*(C4).

Sanford, L. P. (2008), Modeling a dynamically varying mixed sediment bed with erosion, deposition, bioturbation, consolidation, and armoring, *Computers & Geosciences*, *34*(10), 1263–1283.

Sanger, D., and C. Parker (2016), Guide to the Salt Marshes and Tidal Creeks of the Southeastern United States, *South Carolina Department of Natural Resources 2016*, *1*, 112.

Sassi, M., M. Duran-Matute, T. van Kessel, and T. Gerkema (2015), Variability of residual fluxes of suspended sediment in a multiple tidal-inlet system: the Dutch Wadden Sea, *Ocean Dynamics*, *65*(9-10), 1321–1333, doi:10.1007/s10236-015-0866-2.

Sassi, M. G., T. Gerkema, M. Duran-Matute, and J. J. Nauw (2016), Residual water transport in the marsdiep tidal inlet inferred from observations and a numerical model, *Journal of Marine Research*, *74*(1), 21–42.

Schoonees, T., A. Gijón Mancheño, B. Scheres, T. Bouma, R. Silva, T. Schlurmann, and H. Schüttrumpf (2019), Hard structures for coastal protection, towards greener designs, *Estuaries and Coasts*, *42*, 1709–1729.

Schulz, K., and T. Gerkema (2018), Corrigendum to 'An inversion of the estuarine circulation by sluice water discharge and its impact on suspended sediment transport.'[Estuarine, Coastal and Shelf Science 200 (2018) 31-40](S0272771417306194)(10.1016/j.ecss.2017.09.031), *Estuarine, Coastal and Shelf Science*, *207*, 510, doi:10.1016/j.ecss.2018.05.003.

Scientific Campbell OBS-3+ (2019), *OBS 3+ and OBS 300 Product Manual*.

Scott, C., S. Hull, and S. Armstrong (2017), White paper: Using dredge sediment for habitat creation and restoration : A cost benefit review, *Tech. rep.*, ABPmer, Quayside Suite, Medina Chambers, Town Quay, Southampton, Hampshire, SO14 2AQ. Report No. R.2865.

Shi, B., S. Yang, Y. Wang, T. Bouma, and Q. Zhu (2012), Relating accretion and erosion at an exposed tidal wetland to the bottom shear stress of combined current–wave action, *Geomorphology*, *138*(1), 380–389.

Shi, B., Y. P. Wang, Y. Yang, M. Li, P. Li, W. Ni, and J. Gao (2015), Determination of critical shear stresses for erosion and deposition based on in situ measurements of currents and waves over an intertidal mudflat, *Journal of Coastal Research*, *31*(6), 1344–1356.

Shi, B., J. R. Cooper, P. D. Pratolongo, S. Gao, T. J. Bouma, G. Li, C. Li, S. L. Yang, and Y. P. Wang (2017a), Erosion and Accretion on a Mudflat: The Importance of Very Shallow-Water Effects, *Journal of Geophysical Research: Oceans*, *122*(12), 9476–9499, doi:10.1002/2016JC012316.

Shi, B., S. Yang, Y. Wang, G. Li, M. Li, P. Li, and C. Li (2017b), Role of wind in erosion-accretion cycles on an estuarine mudflat, *Journal of Geophysical Research: Oceans*, *122*(1), 193–206.

Solanki, P., B. Jain, X. Hu, and G. Sancheti (2023), A review of beneficial use and management of dredged material, *Waste*, *1*(3), 815–840, doi:10.3390/waste1030048.

Soulsby, R. (1995), Bed shear-stresses due to combined waves and currents, *Advanced in Coastal Morphodynamics*, pp. 20–23.

Soulsby, R., and S. Clarke (2005), Bed Shear-stresses Under Combined Waves and Currents on Smooth and Rough Beds, *Hydraulics Research Report*, *1905*(August), TR 137.

Soulsby, R. L., L. Hamm, G. Klopman, D. Myrhaug, R. R. Simons, and G. P. Thomas (1993), Wave-current interaction within and outside the bottom boundary layer, *Coastal Engineering*, *21*(1-3), 41–69, doi:10.1016/0378-3839(93)90045-A.

Speerstra, H. J. (2018), Estimating the roughness of muddy beds, Master's thesis, Delft University of Technology,.

Sternberg, R. W. (1968), Friction factors in tidal channels with differing bed roughness, *Marine Geology*, doi:10.1016/0025-3227(68)90033-9.

Stive, M. J., M. A. De Schipper, A. P. Luijendijk, S. G. Aarninkhof, C. van Gelder-Maas, J. S. Van Thiel de Vries, S. De Vries, M. Henriquez, S. Marx, and R. Ranasinghe (2013), A new alternative to saving our beaches from sea-level rise: The sand engine, *Journal of Coastal Research*, *29*(5), 1001–1008.

Streever, W. J. (2000), Spartina alterniflora marshes on dredged material: A critical review of the ongoing debate over success, *Wetlands Ecology and Management*, *8*(5), 295–316, doi:10.1023/A:1008483203083.

Studds, C. E., B. E. Kendall, N. J. Murray, H. B. Wilson, D. I. Rogers, R. S. Clemens, K. Gosbell, C. J. Hassell, R. Jessop, D. S. Melville, D. A. Milton, C. D. Minton, H. P. Possingham, A. C. Riegen, P. Straw, E. J. Woehler, and R. A. Fuller (2017), Rapid population decline in migratory shorebirds relying on Yellow Sea tidal mudflats as stopover sites, *Nature Communications*, *8*, 1–7, doi:10.1038/ncomms14895.

Suedel, B. C., A. D. McQueen, J. L. Wilkens, C. L. Saltus, S. G. Bourne, J. Z. Gailani, J. K. King, and J. M. Corbino (2022), Beneficial use of dredged sediment as a sustainable practice for restoring coastal marsh habitat, *Integrated Environmental Assessment and Management*, *18*(5), 1162–1173.

Suykerbuyk, W., T. J. Bouma, T. van der Heide, C. Faust, L. L. Govers, W. B. J. T. Giesen, D. J. de Jong, and M. M. van Katwijk (2012), Suppressing antagonistic bioengineering feedbacks doubles restoration success, *Ecological Applications*, *22*(4), 1224–1231, doi:https://doi.org/10.1890/11-1625.1.

Talke, S. A., and M. T. Stacey (2008), Suspended sediment fluxes at an intertidal flat: The shifting influence of wave, wind, tidal, and freshwater forcing, *Continental Shelf Research*, *28*(6), 710–725, doi:10.1016/j.csr.2007.12.003.

Taylor, M. D., T. F. Gaston, and V. Raoult (2018), The economic value of fisheries harvest supported by saltmarsh and mangrove productivity in two Australian estuaries, *Ecological Indicators*, *84*(August 2017), 701–709, doi:10.1016/j.ecolind.2017.08.044.

Temmerman, S., P. Meire, T. J. Bouma, P. M. J. Herman, T. Ysebaert, and H. J. De Vriend (2013), Ecosystem-based coastal defence in the face of global change, *Nature*, *504*(7478), 79–83, doi:10.1038/nature12859.

Torfs, H., H. Mitchener, H. Huysentruyt, and E. Toorman (1996), Settling and consolidation of mud/sand mixtures, *Coastal Engineering*, *29*(1-2), 27–45.

Turner, R. E., J. J. Baustian, E. M. Swenson, and J. S. Spicer (2006), Wetland sedimentation from hurricanes katrina and rita, *Science*, *314*(5798), 449–452.

Uncles, R., and J. Stephens (2010), Turbidity and sediment transport in a muddy sub-estuary, *Estuarine, Coastal and Shelf Science*, *87*(2), 213–224.

Valiela, I. (2006), *Global coastal change.*, Wiley-Blackwell, Oxford. UK.

Van Buuren, A., G. J. Ellen, and J. F. Warner (2016), Path-dependency and policy learning in the dutch delta: toward more resilient flood risk management in the netherlands?, *Ecology and Society*, *21*(4).

van der Krogt, P. C. (2000), Koeman's atlantes neerlandici. new edition. vol. ii, in *Koeman's Atlantes Neerlandici. New Edition. Vol. II*, Brill.

Van der Spek, A. (1995), Reconstruction of tidal inlet and channel dimensions in the frisian middelzee, a former tidal basin in the dutch wadden sea, *Tidal signatures in modern and ancient sediments*, pp. 237–258.

Van Koningsveld, M., and J. P. M. Mulder (2004), Sustainable coastal policy developments in the netherlands. a systematic approach revealed, *Journal of Coastal Research*, *20*(2), 375–385.

Van Ledden, M., W. Van Kesteren, and J. Winterwerp (2004), A conceptual framework for the erosion behaviour of sand–mud mixtures, *Continental Shelf Research*, *24*(1), 1–11.

Van Maren, D., A. Oost, and P. Vos (2016), The effect of land reclamations and sediment extraction on the suspended sediment concentration in the ems estuary, *Marine Geology*, *376*, 147–157.

Van Maren, D., A. Colina Alonso, A. Engels, W. Vandenbruwaene, P. de Vet, J. Vroom, and Z. Wang (2023), Adaptation timescales of estuarine systems to human interventions, *Frontiers in earth science*, *11*, 1111,530.

Van Prooijen, B. C., and J. C. Winterwerp (2010), A stochastic formulation for erosion of cohesive sediments, *Journal of Geophysical Research*, *115*(C1), C01,005, doi:10.1029/2008JC005189.

van Regteren, M. (2020), Pioneering the edges: unravelling how bioturbation, seeds and sediment dynamics affect initial establishment of pioneer vegetation at the salt marsh edge, Ph.D. thesis, Wageningen University.

Van Regteren, M., R. Ten Boer, E. H. Meesters, and A. V. De Groot (2017), Biogeomorphic impact of oligochaetes (Annelida) on sediment properties and Salicornia spp. seedling establishment, *Ecosphere*, *8*(7), doi:10.1002/ecs2.1872.

Van Rijn, L. C. (2020), Erodibility of mud–sand bed mixtures, *Journal of Hydraulic Engineering*, *146*(1), 04019,050.

Van Rijn, L. C., and R. Barth (2019), Settling and consolidation of soft mud–sand layers, *Journal of Waterway, Port, Coastal, and Ocean Engineering, 145*(1), 04018,028.

Van Straaten, L. M. J. U. (1961), Sedimentation in Tidal Flat Areas, *Bulletin of Canadian Petroleum Geology*, *9*(7), 203–226.

Van Straaten, L. M. J. U., and P. H. Kuenen (1957), Accumulation of fine grained sediments in the dutch wadden sea, *Geologie en Mijnbouw*, *19*(1954), 329–354.

Van Weerdenburg, R., S. Pearson, B. van Prooijen, S. Laan, E. Elias, P. K. Tonnon, and Z. B. Wang (2021), Field measurements and numerical modelling of wind-driven exchange flows in a tidal inlet system in the Dutch Wadden Sea, *Ocean and Coastal Management*, *215*(February), 105,941, doi:10.1016/j.ocecoaman.2021.105941.

Van Weerdenburg R., B. v. M., J. Vroom (2019), Transport of mud motor sediment - modelling hydrodynamics and sediment transport - memo: 1209751-000-zks-0001, *Tech. rep.*, Deltares.

Van Wesenbeeck, B., T. Balke, P. van Eijk, F. Tonneijck, H. Siry, M. Rudianto, and J. Winterwerp (2015), Aquaculture induced erosion of tropical coastlines throws coastal communities back into poverty, *Ocean and Coastal Management*, *116*, 466–469, doi:https://doi.org/10.1016/j.ocecoaman.2015.09.004.

Verney, R., J. C. Brun-Cottan, R. Lafite, J. Deloffre, and J. A. Taylor (2006), Tidally-induced shear stress variability above intertidal mudflats in the macrotidal seine estuary, *Estuaries and Coasts*, *29*(4), 653–664, doi:10.1007/BF02784290.

Vroom, J. (2011), Tidal Divides, Master's thesis, Delft University of Technology.

Vuik, V., S. Van Vuren, B. W. Borsje, B. K. van Wesenbeeck, and S. N. Jonkman (2018), Assessing safety of nature-based flood defenses: Dealing with extremes and uncertainties, *Coastal engineering*, *139*, 47–64.

Vuik, V., B. W. Borsje, P. W. Willemsen, and S. N. Jonkman (2019), Salt marshes for flood risk reduction: Quantifying long-term effectiveness and life-cycle costs, *Ocean and Coastal Management*, *171*(February), 96–110, doi:10.1016/j.ocecoaman.2019.01.010.

Wang, C., and S. Temmerman (2013), Does biogeomorphic feedback lead to abrupt shifts between alternative landscape states?: An empirical study on intertidal flats and marshes, *Journal of Geophysical Research: Earth Surface*, *118*(1), 229–240.

Wang, H., Z. Ge, L. Yuan, and L. Zhang (2014), Evaluation of the combined threat from sea-level rise and sedimentation reduction to the coastal wetlands in the yangtze estuary, china, *Ecological Engineering*, *71*, 346–354, doi:https://doi.org/10.1016/j.ecoleng.2014.07.058.

Wang, J. J., X. Z. Li, S. W. Lin, and Y. X. Ma (2022), Economic Evaluation and Systematic Review of Salt Marsh Restoration Projects at a Global Scale, *Frontiers in Ecology and Evolution*, *10*(April), 1–13, doi:10.3389/fevo.2022.865516.

Wang, Z. B., and A. van der Spek (2015), IMPORTANCE OF MUD FOR MORPHOLOGICAL RESPONSE OF TIDAL BASINS TO SEA-LEVEL RISE, in *Coastal Sediments 2015*, doi:https://doi.org/10.1142/9789814689977_0208.

Wang, Z. B., P. Hoekstra, H. Burchard, H. Ridderinkhof, H. E. De Swart, and M. J. Stive (2012), Morphodynamics of the Wadden Sea and its barrier island system, *Ocean and Coastal Management*, *68*, 39–57, doi:10.1016/j.ocecoaman.2011.12.022.

Wei, W., Z. Dai, X. Mei, J. P. Liu, S. Gao, and S. Li (2017), Shoal morphodynamics of the changjiang (yangtze) estuary: Influences from river damming, estuarine hydraulic engineering and reclamation projects, *Marine Geology*, *386*, 32–43, doi:https://doi.org/10.1016/j.margeo.2017.02.013.

Weir, D., and J. McManus (1987), The role of wind in generating turbidity maxima in the tay estuary, *Continental Shelf Research*, *7*(11-12), 1315–1318.

Welp, T., M. Palermo, M. Landin, J. Davis, and T. Prickett (2003), *US Army Corps of Engineers, New Dredging Engineer Manual: Dredging and Dredged Material Placement*.

Whitehouse, R. J., P. Bassoullet, K. R. Dyer, H. J. Mitchener, and W. Roberts (2000), The influence of bedforms on flow and sediment transport over intertidal mudflats, *Continental Shelf Research*, *20*(10-11), 1099–1124, doi:10.1016/S0278-4343(00)00014-5.

Winterwerp, J., P. Erftemeijer, N. Suryadiputra, P. Van Eijk, and L. Zhang (2013), Defining eco-morphodynamic requirements for rehabilitating eroding mangrove-mud coasts, *Wetlands*, *33*(3), 515–526.

Winterwerp, J. C., W. G. Borst, and M. B. De Vries (2005), Pilot study on the erosion and rehabilitation of a mangrove mud coast, *Journal of Coastal Research*, *21*(2), 223–230.

Winterwerp, J. C., G. J. de Boer, G. Greeuw, and D. S. van Maren (2012), Mud-induced wave damping and wave-induced liquefaction, *Coastal engineering*, *64*, 102–112.

Winterwerp, J. C., T. Albers, E. J. Anthony, D. A. Friess, A. G. Mancheño, K. Moseley, A. Muhari, S. Naipal, J. Noordermeer, A. Oost, C. Saengsupavanich, S. A. Tas, F. H. Tonneijck, T. Wilms, C. Van Bijsterveldt, P. Van Eijk, E. Van Lavieren, and B. K. Van Wesenbeeck (2020), Managing erosion of mangrove-mud coasts with permeable dams – lessons learned, *Ecological Engineering*, *158*, 106,078, doi:https://doi.org/10.1016/j.ecoleng.2020.106078.

Winterwerp, J. C., T. van Kessel, D. S. van Maren, and B. C. van Prooijen (2021), *Fine Sediment in Open Water*, *Advanced Series on Ocean Engineering*, vol. 55, advanced s. ed., 644 pp., WORLD SCIENTIFIC, Delft, doi:10.1142/12473.

Wolanski, E., and M. Elliott (2015), *Estuarine ecohydrology: an introduction*, Elsevier.

Wu, J. (1980), Wind-stress coefficients over sea surface near neutral conditions - a revisit., *J. PHYS. OCEANOGR.*, doi:10.1175/1520-0485(1980)010<0727:wscoss>2.0.co;2.

Wu, J. (1982), Wind-stress coefficients over sea surface from breeze to hurricane, *Journal of Geophysical Research*, doi:10.1029/jc087ic12p09704.

Xie, X., M. Li, and W. Ni (2018), Roles of wind-driven currents and surface waves in sediment resuspension and transport during a tropical storm, *Journal of Geophysical Research: Oceans*, *123*(11), 8638–8654.

Yang, S., H. Li, T. Ysebaert, T. Bouma, W. Zhang, Y. Wang, P. Li, M. Li, and P. Ding (2008), Spatial and temporal variations in sediment grain size in tidal wetlands, yangtze delta: On the role of physical and biotic controls, *Estuarine, Coastal and Shelf Science*, *77*(4), 657–671, doi:https://doi.org/10.1016/j.ecss.2007.10.024.

Yang, S., J. Milliman, P. Li, and K. Xu (2011), 50,000 dams later: Erosion of the yangtze river and its delta, *Global and Planetary Change*, *75*(1), 14–20, doi:https://doi.org/10.1016/j.gloplacha.2010.09.006.

Yang, S., B. Shi, T. Bouma, T. Ysebaert, and X. Luo (2012), Wave attenuation at a salt marsh margin: a case study of an exposed coast on the yangtze estuary, *Estuaries and Coasts*, *35*, 169–182.

Yang, S., T. J. Bouma, K. Xu, B. Shi, H. Yang, W. Zhang, X. Luo, P. Li, Y. Huang, M. Tian, et al. (2023), Storms dominate the erosion of the yangtze delta and southward sediment transport, *Science Bulletin*, *68*(6), 553–556.

Yang, S.-l., P.-x. Ding, and S.-l. Chen (2001), Changes in progradation rate of the tidal flats at the mouth of the changjiang (yangtze) river, china, *Geomorphology*, *38*(1-2), 167–180.

Yang, S.-L., C. T. Friedrichs, Z. Shi, P.-X. Ding, J. Zhu, and Q.-Y. Zhao (2003), Morphological response of tidal marshes, flats and channels of the outer yangtze river mouth to a major storm, *Estuaries*, *26*, 1416–1425.

Yozzo, D. J., P. Wilber, and R. J. Will (2004), Beneficial use of dredged material for habitat creation, enhancement, and restoration in new york–new jersey harbor, *Journal of Environmental Management*, *73*(1), 39–52.

Zhou, Z., G. Coco, I. Townend, M. Olabarrieta, M. van der Wegen, Z. Gong, A. D'Alpaos, S. Gao, B. E. Jaffe, G. Gelfenbaum, Q. He, Y. Wang, S. Lanzoni, Z. Wang, H. Winterwerp, and C. Zhang (2017), Is "Morphodynamic Equilibrium" an oxymoron?, doi:10.1016/j.earscirev.2016.12.002.

Zhu, Q., S. Yang, and Y. Ma (2014), Intra-tidal sedimentary processes associated with combined wave–current action on an exposed, erosional mudflat, southeastern Yangtze River Delta, China, *Marine Geology*, *347*, 95–106, doi:10.1016/j.margeo.2013.11.005.

Zhu, Q., B. C. van Prooijen, Z. B. Wang, Y. X. Ma, and S. L. Yang (2016), Bed shear stress estimation on an open intertidal flat using in situ measurements, *Estuarine, Coastal and Shelf Science*, *182*, 190–201, doi:10.1016/j.ecss.2016.08.028.

Zhu, Q., B. C. van Prooijen, Z. B. Wang, and S. L. Yang (2017), Bed-level changes on intertidal wetland in response to waves and tides: A case study from the Yangtze River Delta, *Marine Geology*, *385*, 160–172, doi:10.1016/j.margeo.2017.01.003.

Zhu, Q., B. C. van Prooijen, D. C. Maan, Z. B. Wang, P. Yao, T. Daggers, and S. L. Yang (2019), The heterogeneity of mudflat erodibility, *Geomorphology*, *345*, doi:10.1016/j.geomorph.2019.106834.

Zhu, Z., A. Slangen, Q. Zhu, T. Gerkema, T. J. Bouma, and Z. Yang (2022), The role of tides and winds in shaping seed dispersal in coastal wetlands, *Limnology and Oceanography*, *67*(3), 646–659, doi:10.1002/lno.12024.

A

ANNEX-A: CALIBRATION CURVES OPTICAL BACK SCATTER SENSORS

This Annex is meant to illustrate the calibration curves obtained with the calibration procedures performed in May 2017 and February 2018, following the respective field campaigns. The calibration procedure and the calibration curves obtained for the 2016 campaign were reported in Section 3.7.

Figure A.1 shows the calibration fits (linear up to 1.5 g/l and quadratic for higher concentrations) obtained for maximum SSC of ~ 10 g/l. As mentioned in Section 3.7 this represents only part of the total number of calibration data-points. During the 2017 field campaign four OBS sensors were deployed, respectively two per each site (W_L, W_H). The OBS installed at ~ 60 cm above the bed at W_L (Serial Number T9850) was damaged after the instrumentation retrieve. The data was downloaded from the instrument, but the calibration procedure could not be performed. The calibration curve found for this instrument in 2016 (reported in Figure 3.13) was adopted. The deviation between the calibration curves obtained for the same instrument, through the different calibrations procedures (i.e. 2016, 2017 and 2018) increases for increasing concentrations, as shown in Figure A.2. Maximum deviations of 2 g/l are observed between the 2016 and 2018 curves for ~ 2700 mV. Being the 2017 calibration curves steeper than 2016 curves, we expect that the usage of the 2016's curve, for the damaged OBS, resulted in a slight underestimation of the SSC at site W_L (< 15%).

The 2018 OBS calibration procedure was performed with maximum sediment concentrations of about 5 g/l. In this field campaign, totally eight optical sensors were installed, among which seven OBS-3+ Campbell and one Fluorometer (see Figures A.3 and A.4). The seven OBS sensors were calibrated simultaneously, whereas the Fluorometer was calibrated separately. The curves in Figure A.3 and Figure A.4 indicate a different slope for the linear fit.

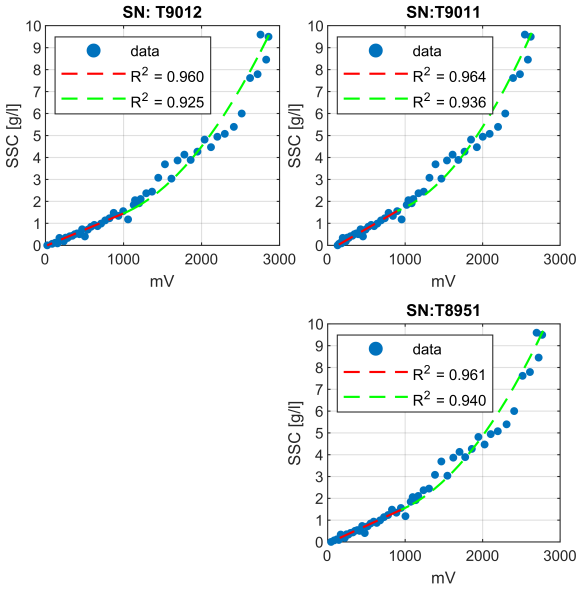

Figure A.1: OBSes Calibration curves obtained after the in-situ sampling at site WH after the **Field Campaign 2017**. Three out of the four deployed instruments, were calibrated. The OBS Serial Numbers (SN) are indicated as panel's title.

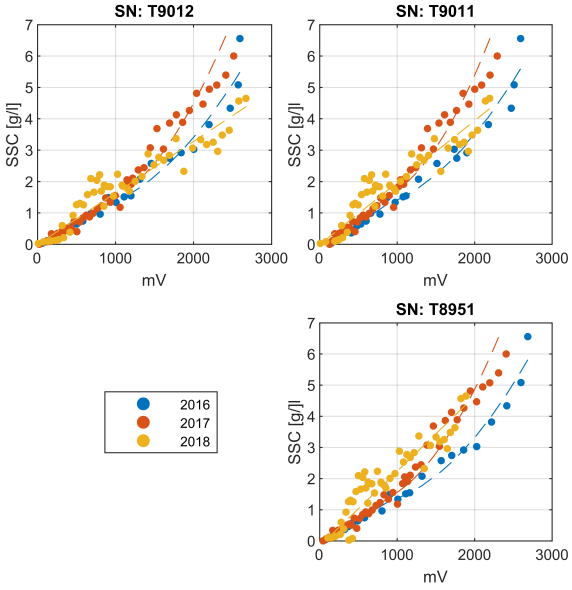

Figure A.2: Three OBS sensors were deployed during the three field campaigns. The calibration points, and the extrapolated linear/quadratic fit) for these sensors are compared. The OBS Serial Numbers are indicated as panel's title).

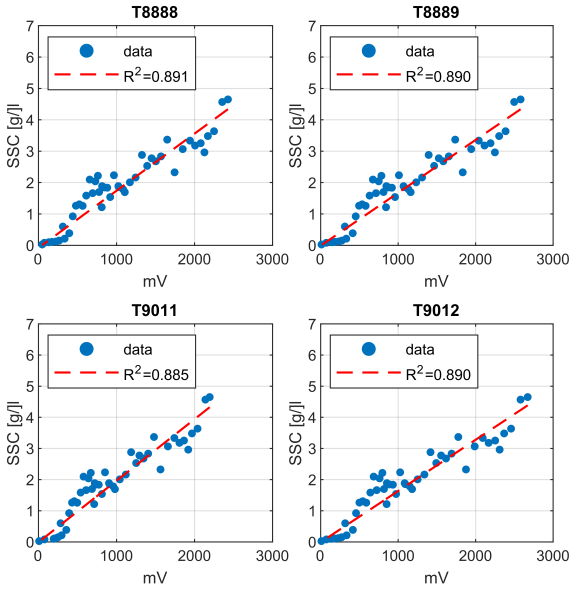

Figure A.3: OBSes Calibration curves, obtained after the **Field Campaign 2018**. The OBS Serial Numbers are indicated as panel's title. The linear fit results in averaged R-Squared values of 0.89.

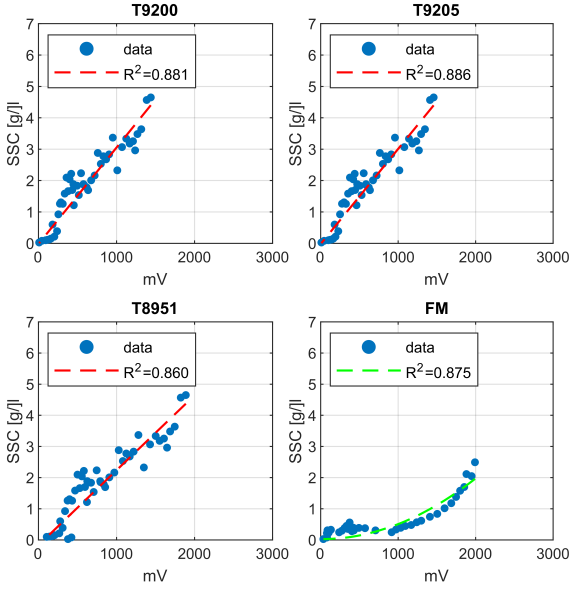

Figure A.4: OBSes Calibration curves, obtained after the **Field Campaign 2018**. The OBS Serial Numbers are indicated as panel's title. The linear fit results in averaged R-Squared values of 0.87. The Fluorometer (FM) shows a different trend in SSC with mV compared to the OBS sensors; a quadratic fit has been adopted for this instrument.

B

ANNEX-B: WIND CLIMATE

This dissertation investigates the effect of deterministic tidal forcing, and stochastic wind forcing on the hydroynamics and morphodynamics of intertidal flats. The results of our research suggest that a fundamental role is played by wind forcing. In this Annex, we provide the results of wind data analysis, performed, as specified in Chapter 3, on the wind speed at 10 m above mean sea level, and wind direction gathered at the Leuwardeen meterological station. The Wind Roses presented hereafter are referred to:

- The specific (about 1 or 2 month-long) periods in which field measurements were conducted in 2016, 2017 ans 2018 (Figure B.1).
- The one year-long period of the years 2016, 2017 and 2018 (Figure B.2).
- Seasonal periods of six months, named in Figure B.3 as "Spring" and "Winter". "Spring" represents the period April 1st - September 30^{th} (of the indicated year) whereas "Winter" represents the period from October 1^{st} (of the indicated year) until March 31^{st} (of the following year).

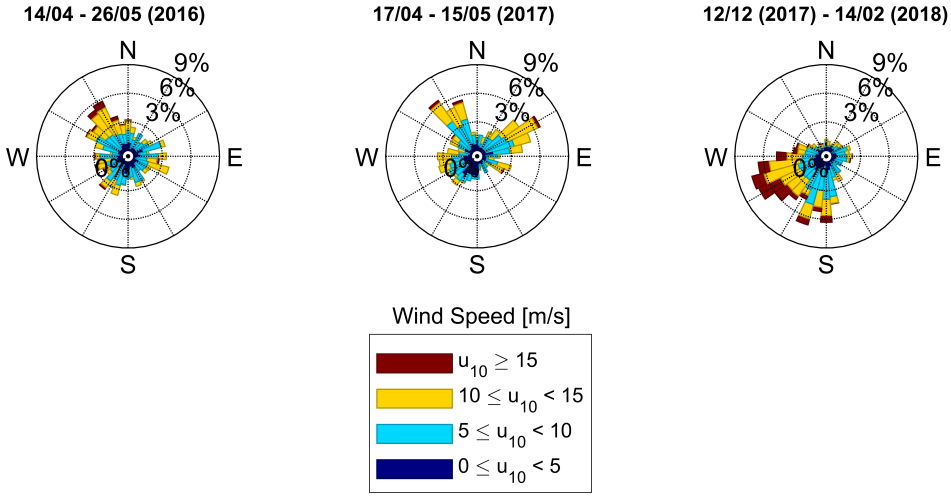

Figure B.1: Wind Roses relative to the three measurement periods: [a] Spring Campaign 2016, [b] Spring Campaign 2017, [c] Winter Campaign 2018.

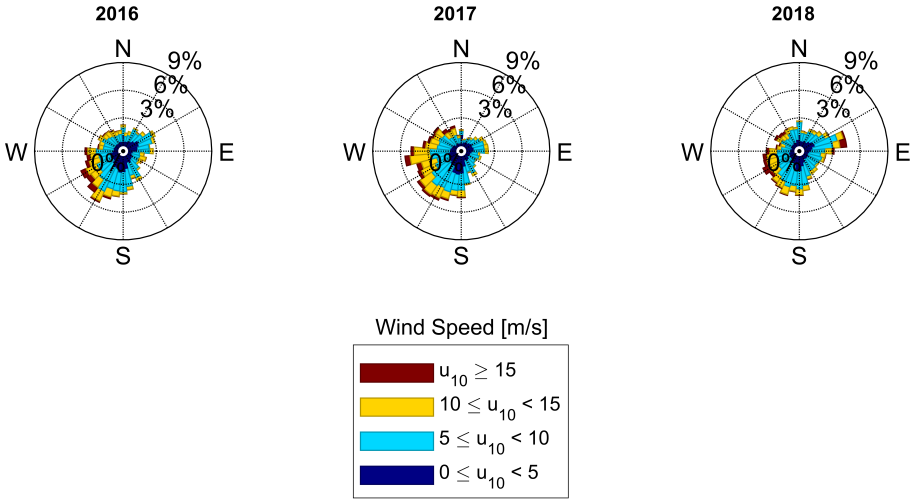

Figure B.2: Wind Roses relative to years (Jan 1^{st} , Dec 31^{st}) of 2016, 2017 and 2018.

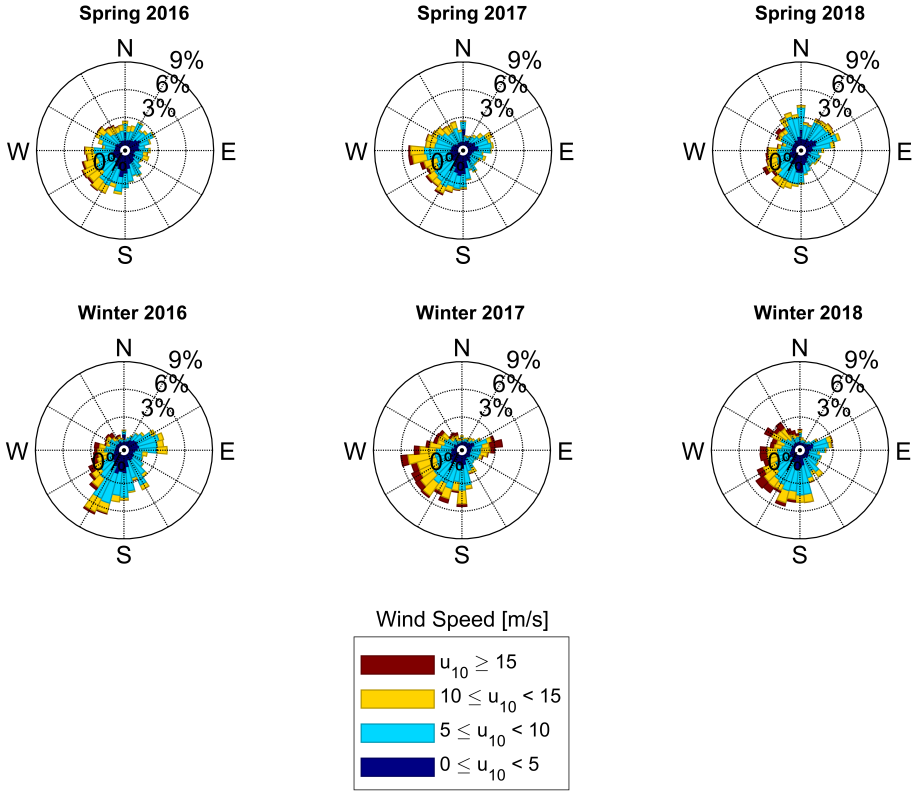

Figure B.3: Wind Roses relative to the "Spring" and to the "Winter" periods of 2016, 2017 and 2018. "Spring" indicates here the period April 1st - September 30th (of the indicated year) whereas "Winter" indicates the period from October 1st (of the indicated year) until March 31st (of the following year).

This wind data analysis suggest that:

- The dominant wind direction at our study site is SW (Figure B.2);
- Most frequently, the highest wind speeds ($u_{10} \geq 15m/s$) are from the SW direction, followed by NW and NE directions. SE wind is relatively weak ($5m/s \leq u_{10} \leq 10m/s$) and the less frequent: this is the wind, at our study site, directed towards the offshore direction (Figure B.2).
- Winds with $u_{10} \geq 15m/s$ from the SW sector mainly occur in winter season. Albeit the lower frequency, these SW storms also occur during the spring semester (Figure B.3).
- During the spring semester NE wind is more frequent compared to the winter semester (Figure B.3). However during the winter semester, high wind speeds ($u_{10} \geq 10m/s$) from the NE also occur relatively frequently.
- The wind conditions during our winter field campaign (2018) were characterized by intense winds from the SW, which were favourable to analyze what happens during the typical storms in our study areas.
- The wind conditions during our spring field campaigns (2016, 2017) were characterized by relatively intense winds from NE and NW but also be weaker winds from all directions. These were helpful to analyze what happens at our study areas when the wind blows in direction that are less "typical" compared to the dominant one, and to compare hydro- and morphodynamics changes in case of windy and non-windy conditions.

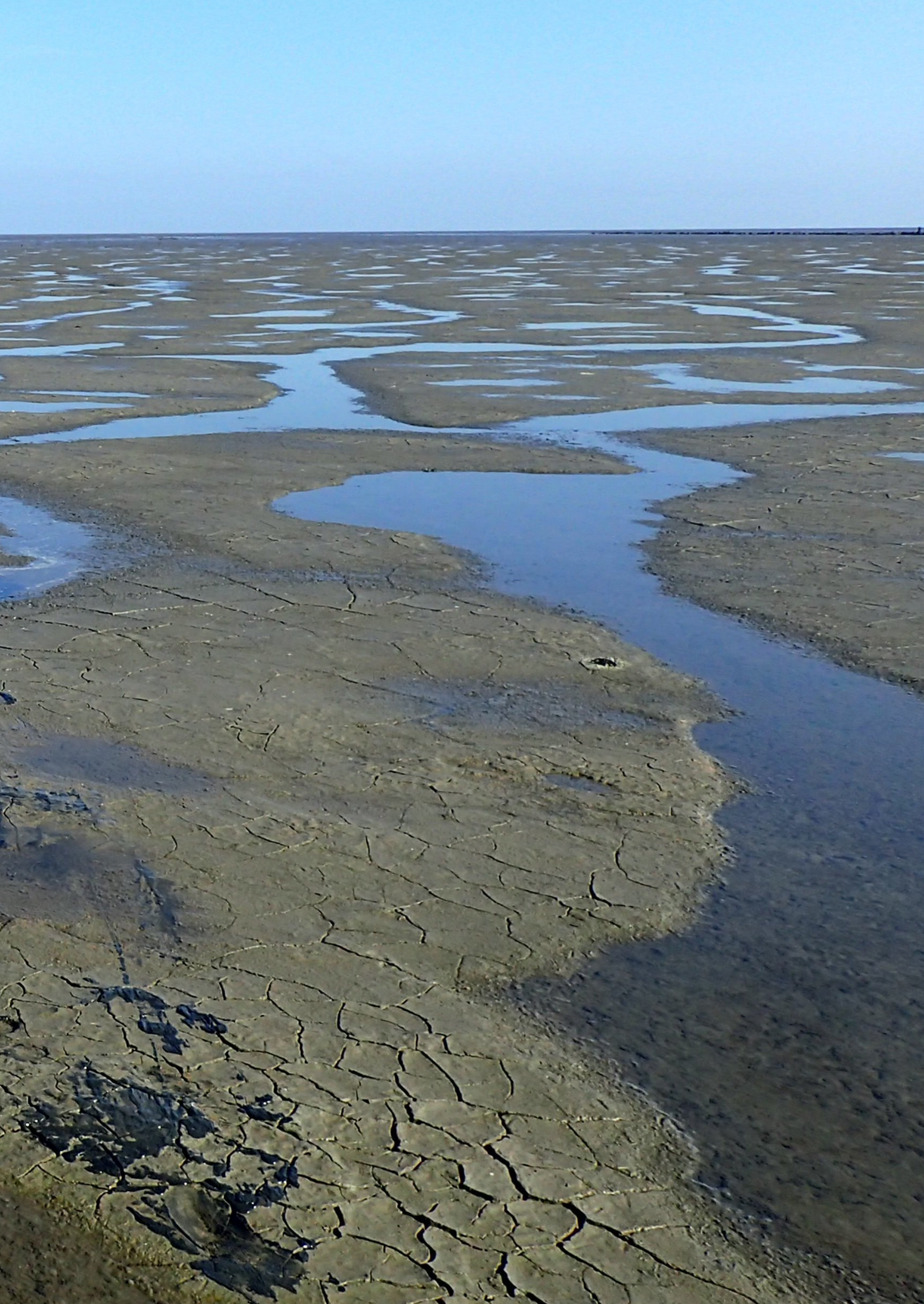

About the Photo

A canoe was used to transport instruments to and from the measurement site. This photo was taken during the spring field campaign at Westhoek on May 15, 2017.

ACKNOWLEDGEMENTS

This PhD journey has been an enriching experience — challenging at times, yet deeply inspiring and fulfilling. While there were moments of doubt and obstacles to overcome, the path was also filled with joy, discovery, and countless opportunities to meet wonderful people who enriched my life. This journey not only allowed me to grow as a researcher but also as a person, teaching me resilience, patience, and the importance of trusting both myself and others. As I sit here in Delft, back in the Netherlands, at a bar overlooking one of my favorite places on earth, I write these final pages with immense gratitude.

This achievement wouldn't have been possible without the support of so many incredible people along the way. First, my heartfelt thanks goes to my two "super-supervisors", **Bram van Prooijen** and **Bas van Maren**. Your guidance throughout my PhD was remarkable — you supported me while giving me the freedom to explore and make decisions, fostering my growth both professionally and personally. Thank you for mentoring me with kindness, humor, and unwavering support. Bram, working with you was not only educational but also immensely enjoyable. You showed me the importance of embracing the joy in one's work. You kept my enthusiasm for science alive and supported me during challenging times. I'll always treasure our fieldwork days, those early morning drives to Koehool and Westhoek tidal flats, while listening to music in the van, already dressed in wetsuits. Bas, I valued so much your ability for transferring your passion and knowledge to others. I enjoyed our fieldwork experience and the many chats we had. Your guidance had a profound impact on my work, and it was vital in helping me finalize my papers and navigate key decisions. I feel immensely proud to have had the privilege of collaborating with you.

A very special thanks goes to **Han Winterwerp**. Your belief in me and my work has been a powerful driving force throughout my journey. Your suggestions have played a crucial role in helping me take important steps forward in my research. I am deeply grateful for your unwavering support, which has given me confidence in my path. I also truly appreciate the warmth and kindness you and Susanna have shown, especially during challenging times. Thank you for everything — I have learned so much from you.

To **Ad Reniers**, your guidance extended beyond science. Meetings with you were a lesson — not just about research but about life. Your ability to communicate wisdom so concisely always impressed me. Thank you for sharing your passion for knowledge with me.

I would also like to express my gratitude to the scientists I had the privilege of working with on the *Mud Motor Project*. **Marin van Regteren**, our days in the mud were great! I feel fortunate to have shared the Mud Motor experience with such a great marine ecologist. I learned a lot from you. Thank you. To **Theo Gerkema**, **Martin Baptist**, **Janine Nauw**, and **Kirstin Schulz**, working with you was an enriching and enjoyable learning experience. Theo, thank you for giving me the opportunity to be on board the *Navicula* research vessel. That experience is unforgettable. I would like to further acknowledge the invaluable contribution to everybody who supported me in the field, among which the *Shore Monitoring & Research* team, the Master student **Han Speerstra**, and the TU Lab technicians, particularly **Jaap van Duin** and **Mohammed Jafar**.

In my PhD journey, I was fortunate to have wonderful colleagues who became like family. The TU Lab was a home away from home, and the support we gave to each other meant the world to me. My heartfelt thanks to **Liselot Arkesteijn** and **María Barciela Rial**, who were not only colleagues but also wonderful friends during my years in Delft. Maria, you were a great example of strength and an inspiring scientist. Our conversations about mud consolidations were key in shaping the Discussion chapter of this book - thank you for your insights and support. I will always cherish our shared adventures, from the Intercoh Conference in Montevideo to the Summer School in Bordeaux.

A big thank you also goes to **Alejandra Gijón Macheño** and **Ana Colina Alonso**. I admire you both so much. Ale, your humility, scientific brilliance, and sharp sense of humor made working with you such a pleasure. I'll never forget the fun we had preparing the video for Lodewijk's defense! Ana, your empathy and emotional intelligence are truly exceptional, qualities I rarely encounter. I feel so lucky to have shared the office with you.

I want to express my gratitude to **Patricia Buffon** for her pure soul and kind heart. Patri, from the moment we met, I felt an instant connection with you. Thank you for always being so kind and supportive. A special thanks also goes to **Stuart Pearson**. Stue, when you joined the TU Lab, your passion and energy for science were so inspiring and left a lasting impression on all of us. Thank you for sharing that enthusiasm with me. I will always remember our trip to Washington DC, our muddy adventure in Friesland's intertidal flats for the web documentary, and the many memorable parties we enjoyed together.

I want to express my gratitude also to **Victor Chavarrias**, **Erik Hendricks**, and **Yorick Broekema**. Victor, you were a constant source of support in the Lab, always ready to help others and foster a strong sense of community. Your dedication to the social life of the group was truly appreciated. You and Elisa's decision to invite us to your wedding in Barcelona was such a kind gesture, and those days remain some of my most cherished memories with the Lab group. Erik, it's no coincidence that I mention you right after Victor's wedding. I have to thank you not only for being a great colleague but also for making that celebration unforgettable. From your endless refilling of my wine glass to the hilarious moments that followed — like me losing my shoes and Bram playing the trumpet on the bus at 6 a.m. — it was an absolute blast. Those memories will always bring me a smile. Yorick, your sense of humor and positivity added so much energy and value to my time in the Lab. Our winter trip to Italy with the group is a memory I will always carry with me — it was truly special.

To **Andrés Vargas-Lunas**, your laughter and optimism were a source of motivation. Your contribution to the Lab music band and our conversations meant a lot to me. To **Gonzalo Durò**, thank you for being not only a wonderful colleague but also a supportive neighbor during this journey.

I want to express my gratitude for being such great colleagues also to **Merel Verbeek**, **Cynthia Maan**, **Jill Hanssen**, **Nicolette Volp**, **Clara Orrù**, **Marco Gatto**, **Sotiria Georgiou**, **Zeinab Safar**, **Clàudia Ylla Arbós** and **Jacob Maljaars** and to extend also my heartfelt thanks to **Otti Kievits** for her valuable support, not only during my time at TU Delft but also as I continued my research remotely from Italy.

A special thanks goes to journalist **Marco Merola** for bringing me into the Adaptation documentary adventure, for inviting me to the Festival della Scienza, and for the many talks and stages we

shared throughout my PhD years. Your dedication provided a wonderful opportunity for the Mud Motor story to be shared across Italy, and I am grateful for the impact your voice brought to this project.

A heartfelt thank you goes to the forever professor of my heart and my dear friend, **Barbara Zanuttigh**. Barbara, you are an extraordinary role model — as a woman, a researcher, and an engineer. Thank you for believing in me as a bachelor student, for giving me the opportunity to carry out my research projects in Spain and Denmark, and for encouraging me to consider Delft University for my PhD studies. You have been a vital mentor in my life, opening my mind to new possibilities and reminding me, time and again, that I could achieve my dreams.

To my lifelong friend, my Sbrufi, and today my paranymph — thank you, **Elena**, for being such a special part of my life. From our days studying together in Bologna to carrying our friendship across Europe, you have always been by my side. Our greatest strength has been our ability to combine a love for learning with a love for celebrating life, always together. Your passion for science and engineering has been a source of inspiration throughout my PhD journey, and you continue to be a shining example to me. Thank you for standing by me in every chapter of my life, and especially today.

Piccy my Piccy, calling you a friend feels far too little after all these years. We chose each other when we were just 13, and from that moment, we have never, ever been apart. I can't even imagine who I would be today without you by my side. Thank you, for always being there to listen (countless times also to my PhD rollercoaster) for sharing every joy and sorrow in our lives, and for giving me the gift of a gorgeous nephew, Valerio. Most of all, thank you for being such a beautiful and irreplaceable part of my soul. I love you.

I would also like to thank two incredible women (and researchers) I had the pleasure of living with during my PhD, **Serena Cunsolo** and **Anna Wronska**. Our time together was invaluable — I learned so much from both of you and deeply cherished our moments cooking together, late-night chats, sharing life experiences, and dreaming about the future. Thank you.

My sincere thanks also go to the friends who stood by my side during this 'new Italian chapter' of my life: **Tota**, **Robi**, **Marta** and **Mary**. We shared the experience of returning to our home-town, forging a special connection and a deep understanding of each other. Your encouragement and help during this challenging period meant the world to me. Robi and Marta, I still can't believe you booked your tickets to the Netherlands for my defense before I even did — truly, you are one of a kind.

And here is a moment I have waited for so long: acknowledging the person with whom I shared my PhD life, someone who has become one of the most important friends in my life, and undoubtedly the greatest gift from my experience in the Netherlands — **Lodewijk**. Lode, we have said "thank you" to each other so many times, but I'm not sure words can ever fully express my gratitude for your kindness, sincerity, and loyalty as a friend. We shared a deep passion for science, a mutual amazement at the beauty of nature, and a "military precision" when designing and executing our field campaigns. I am especially grateful for your support during one of the hardest moments of my PhD — when my hard-drive broke. I can still feel the weight of that pain, and yet, your gentle and motivating words were exactly what I needed to push through. I truly don't know if I could have finished this book without your unwavering support during that time. We were, and still are, "similar enough to understand each other and different enough to surprise each other". It's this

balance of being both incredibly alike and wonderfully different that made our journey together such a rich learning experience in both science and life. Neither distance nor time has altered our friendship over the years. Our shared memories are countless — our first frames built together in the Lab, the time spent in Harlingen, the shared dinners and breakfasts, our walks, your defense, endless van trips. I feel so incredibly lucky to have you in my life, and I look forward to writing many more pages of our friendship in the years to come.

Papà, **Mamma**, **Ely**, nessuno come voi sa quanto difficili siano stati alcuni momenti di questo percorso. Sono grata alla vita per avermi dato una famiglia così unita e forte, e sono grata a voi per il sostegno che mi avete sempre offerto nei momenti più duri. Non dimenticherò mai l'amore e il supporto che mi avete dato quando ho perso tutti i miei documenti per via dell'hard-disk... senza di voi non avrei mai trovato la forza di ricominciare tutto da capo. Papi, sei il più grande esempio di forza e resilienza che potessi avere, e da te continuo a imparare ogni giorno. Grazie per avermi trasmesso, sin da piccola, l'amore per il mare, per la fisica e per l'ingegneria. Mi ricordo quando, seduti a tavola per cena, mi spiegavi la fisica delle cose più semplici, quelle che avevamo di fronte agli occhi. Solo da grande ho capito davvero cosa mi ha fatto innamorare di quello che faccio ogni giorno. Mammina, grazie per ogni parola di stima e incoraggiamento lungo il mio percorso di studi, di lavoro e di vita. Grazie per il sostegno pratico e psicologico e per l'amore che mi dai ogni giorno. Quando penso al "perché sono tornata in Italia" penso alla fortuna di potervi abbracciare ogni volta che voglio, e mi ricordo che ho fatto la scelta migliore che potessi fare. Grazie a entrambi, perché sin da piccola mi avete spronata ad esplorare il mondo, ad essere chi volevo essere e a sognare in grande. Ely, non c'è stato un momento in cui non ci siamo prese per mano e supportate l'un l'altra. Sei il mio esempio, la mia guida, la mia certezza, sei di certo la parte migliore di me. Grazie per il tuo sostegno smisurato ad ogni mia difficoltà, grazie per il tuo amore, grazie per essere la sorella migliore che si possa sognare. Grazie per avermi reso la zia più felice ed innamorata del pianeta.

Andri, amore mio, non ci sono parole che possano davvero racchiudere la mia gratitudine per il tuo sostegno in questo cammino. Grazie per aver creduto in me, per avermi detto di non mollare. Grazie per essermi stato vicino in questi anni segnati da sfide personali e professionali. Completare questo libro ha richiesto sacrifici a entrambi, e ti sono profondamente grata per il tuo supporto e la tua comprensione. Grazie per aver scelto di camminare al mio fianco, per sempre. Grazie per la tua pazienza infinita, per l'amore che non mi hai mai fatto mancare, e per la dolcezza con cui ti sei preso cura di me nei momenti più duri. Grazie perché sai sempre come farmi sorridere, perché mi fai divertire, e perché sei la mia certezza in un mondo così incerto. Ti amo, e non vedo l'ora di scoprire con te tutto ciò che di splendido la vita ha in serbo per noi.

I want to conclude by expressing my deep appreciation for the unique opportunities and experiences I had while studying and exploring the beautiful nature of the Netherlands. I will never forget my days in Friesland's intertidal areas, where the breathtaking landscape left me in awe. Even now, I sometimes close my eyes and imagine myself back there — walking in the mud, watching thousands of birds on the horizon, admiring the richness of sea life. The harmony of science and nature during the days in the field left an indelible mark on me, a memory I will carry with me forever.

List of Publications

Journal Articles

6. **Colosimo I.**, van Maren D. S., de Vet P. L. M., Winterwerp J. C., van Prooijen B. C., *Winds of Opportunity: The Effects of Wind on Tidal Flat Accretion*, Geomorphology, vol. 439, 108840, (2023). doi: 10.1002/ece3.5781.

5. **Colosimo I.**, de Vet P. L. M., van Maren D. S., Reniers, A. J. H. M., Winterwerp J. C., van Prooijen B. C.,*The impact of wind on flow and sediment transport over intertidal flats.*, Journal of Marine Science and Engineering 8(11), 910 (2020). doi: 10.3390/jmse8110910.

4. de Vet P. L. M., van Prooijen B. C., **Colosimo I.**, Ysebaert T., Herman P. M. J., Wang Z. B. *Sediment Disposals in Estuarine Channels Alter the Eco-Morphology of Intertidal Flats.*, Journal of Geophysical Research: Earth Surface, 125(2) (2020). doi: 10.1029/2019JF005432

3. de Vet P. L. M., van Prooijen B. C.,**Colosimo I.**, Steiner N., Ysebaert T., Herman P. M. J., Wang Z. B. *Variations in storm-induced bed level dynamics across intertidal flats.*, Scientific Reports, 10(1), 12877 (2020). doi: 10.1038/s41598-020-69444-7

2. van Regteren M., **Colosimo I.**, de Vries P., van Puijenbroek M. E. B., Freij V. S., Baptist M. J., Elschot K.*Limited seed retention during winter inhibits vegetation establishment in spring, affecting lateral marsh expansion capacity.*, Ecology and Evolution, 9(23), 13294–13308, (2019). doi: 10.1002/ece3.5781.

1. Baptist M. J., Gerkema T., van Prooijen B. C., van Maren D. S., van Regteren M., Schulz K., **Colosimo, I.**, Vroom J., van Kessel T., Grasmeijer B., Willemsen P., Elschot K., de Groot A. V., Cleveringa J., van Eekelen E. M. M., Schuurman F., de Lange H. J., van Puijenbroek M. E. B., *Beneficial use of dredged sediment to enhance salt marsh development by applying a 'Mud Motor'.*, Ecological Engineering, 127, 312–323, (2019). doi: 10.1016/j.ecoleng.2018.11.019.

Conference Proceedings and Talks

11. **Colosimo I.**, van Prooijen B. C., van Maren D. S., de Vet P. L. M., Winterwerp J. C. (2020). Beneficial Reuse of Sediment for Ecological Purposes: Physical Aspects of a Mud Motor. *United States Army Corps of Engineers (USACE)*. Manhattan, NYC, United States. 17 December.

10. de Vet P. L. M, van Prooijen B. C., **Colosimo I.**, Steiner N., Ysebaert T., Herman P. M. J., Wang Z. B. (2019). Long-term morphological evolution of intertidal flats: how do storms affect this?*Symposium on River, Coastal and Estuarine Morphodynamics*. Auckland, New Zeeland. 16-21 November.

9. **Colosimo I.**, van Maren D. S., de Vet P. L. M., van Regteren M., van Prooijen B.C. (2019). Wind-driven flow and sediment transport in intertidal areas. *NCK Theme Day: Morphoodynamics of the Wadden Sea: Recent research and future challenges*, Enkhuizen, The Netherlands, 17 May.

8. de Vet P. L. M, van Prooijen B. C., **Colosimo I.**, Ysebaert T., Herman P. M. J., Wang Z. B. (2019). Eco-morphological changes of intertidal flats initiated by sediment disposals in estuarine channels. *Ems-Scheldt Workshop*, Delft, The Netherlands. 2-3 May.

7. **Colosimo I.**, van Maren D. S., de Vet P. L. M., van Regteren M., van Prooijen B.C. (2019). Winds of Opportunity: the effect of Wind on tidal flat accretion. *Netherlands Center for Coastal Research Conference (NCK days)*, Enkhuizen, The Netherlands, 20-23 March.
6. de Vet P. L. M, van Prooijen B. C., **Colosimo I.**, Steiner N., Ysebaert T., Herman P. M. J., Wang Z. B. (2019). The timing of event matters for the eco-morphology of intertidal flats. *Netherlands Center for Coastal Research Conference (NCK days)*, Enkhuizen, The Netherlands, 20-23 March.
5. **Colosimo I.**, van Maren D. S., de Vet P. L. M., Winterwerp J. C., van Prooijen B. C. (2018). Winds of Opportunity: the influence of wind on mudflat accretion. *American Geophysical Union Fall Meeting, Advancing Earth and Space Science*, Washington D.C., United States, 10-14 December.
4. **Colosimo I.**,van Prooijen B. C., van Maren D. S., Winterwerp J. C., Reniers A. J. H. M., Shultz K., Gerkema T., van Regteren M., Baptist M. (2018). Limiting factors for the application of a Mud Motor. *EcoShape Conference. 'Scaling Up Building with Nature'.Living Lab for Mud, Nature Based Solutions and Harbours*, Utrecht, The Netherlands, 26 June.
3. **Colosimo I.**, van Prooijen B.C., van Maren D. S., de Vet P. L. M., Reniers A. J. H. M.,Winterwerp J.C. (2017). Wind effects on intertidal flat sediment transport 14^{th} *International Conference on Cohesive Sediment Transport Processes, INTERCOH*, Montevideo, Uruguay, 13-17 November.
2. **Colosimo I.**, van Prooijen B.C., van Maren D. S., Reniers A. J. H. M.,Winterwerp J.C. (2017). Field measurements of hydrodynamics and sediment transport on intertidal flats.*Netherlands Center for Coastal Research Conference (NCK days)*, Den Helder, The Netherlands, 15-17 March.
1. **Colosimo I.**, van Prooijen B.C., van Maren D. S., Reniers A. J. H. M.,Winterwerp J.C. (2016). Physical Aspects of a Mud Motor: the Monitoring Campaign. *Netherlands Center for Coastal Research Conference (NCK days)*, Ouddorp, The Netherlands

CURRICULUM VITÆ

Irene COLOSIMO

Irene Colosimo is an Environmental Engineer specialized on coastal morphodynamics, sediment transport, and renewable offshore energy. Her academic and professional journey spans several European countries, including Italy, Denmark, Spain, and the Netherlands. After completing her studies, Irene conducted scientific research at Delft University of Technology (TU Delft), where her work focused on applying nature-based engineering solutions for sustainable coastal development, particularly in response to climate change. Since returning to Italy in 2021, she has worked as a Project Manager, overseeing the design of offshore wind farms. In 2024, Irene was appointed Environmental Councillor for the City of Catanzaro, where she is committed to advancing sustainability, protecting the territory, and fostering initiatives for a greener future. Known for her strong communication and organizational skills, Irene thrives in multidisciplinary teams and values continuous learning, guided by curiosity and a passion for innovation throughout her career.

PROFESSIONAL EXPERIENCE

As a Project Manager at New Developments s.r.l. since May 2022, Irene has led the preliminary and detailed design phases of offshore floating wind and solar projects. She is responsible for coordinating cross-functional teams to advance sustainable energy infrastructure, contributing her technical expertise and project management skills to the growing field of renewable energy.

Irene completed her PhD at Delft University of Technology in the Netherlands. During her doctoral studies, she published scientific articles, presented her research at international conferences, contributed to teaching the course "Building with Nature for Hydraulic Engineers," supervised MSc thesis projects, and led field campaigns in marine environments. Alongside her academic work, Irene worked as a freelance Environmental Engineer, specializing in environmental impact assessments and project planning. She also served as an Innovation Specialist Consultant at Entopan Innovation, supporting startups as part of an incubator and accelerator program.

Since completing her PhD, Irene has worked as a Project Manager in the renewable energy sector, overseeing the design and development of offshore wind farms, combining her technical expertise with strong organizational and leadership skills.

ACADEMIC BACKGROUND

Irene holds a Master's Degree in Environmental Engineering from the *Università degli Studi di Bologna*, Italy, graduating with honors (110/110 cum laude) in 2014. Her Master's thesis, titled *Anchoring Systems for Renewable Marine Energy Offshore Platforms*, was completed as part of the SAEmar project at the *Instituto de Hydraulica Ambiental de Cantabria* in Spain. Her Bachelor's degree, also in Environmental Engineering, was completed at the same university in 2011, where she conducted a thesis on the Physical Modelling of Wave Energy Converters at *Aalborg University's Hydraulic Engineering Lab*, in Denmark.

SKILLS AND COMPETENCIES

Irene's diverse background reflects her proficiency in Coastal and Environmental Engineering with specific expertise in sediment transport and renewable offshore energy systems. Her hands-on experience with field campaigns during her PhD studies honed her organizational and leadership abilities. Her communication skills are well developed, having presented her research at numerous international conferences and contributed to publications in scientific journals. Working across multiple countries, Irene has strengthened her networking and teamwork abilities, fostering collaborations across academic and industry sectors.

PUBLICATIONS, PRESENTATIONS, AND MEDIA

Irene has published peer-reviewed articles in international journals on topics such as coastal engineering, sediment dynamics, coastal morphology and nature-based solutions. She has presented her work at several conferences, including the *American Geophysical Union (AGU) Conference* in Washington DC, and the *International Conference on Cohesive Sediments* in Montevideo, Uruguay. Her research has also been featured in media outlets, such as *National Geographic* and *Corriere della Sera*. Additionally, she contributed to a documentary titled *Adaptation*, dedicated to the topic of the adaptation to climate change, directed by journalist Marco Merola. Irene also presented her research scientific results at the *Festival della Scienza* in Genoa, where she met the artist and illustrator Giancarlo Caligaris, who dedicated a graphic novel to her.


IRENE COLOSIMO, 31 ANNI, VIENE DA UNA FAMIGLIA DI INGEGNERI IDRAULICI, TUTTI UOMINI, SONO ARRIVATI ALLA 5ª GENERAZIONE E IRENE È LA PRIMA DONNA
MAR IONIO
"SONO NATA A CATANZARO, HO STUDIATO A BOLOGNA, HO FATTO TESI IN IDRAULICA AMBIENTALE, SONO ANDATA SEI MESI IN DANIMARCA E POI IN SPAGNA. MI SONO OCCUPATA DEI DISPOSITIVI PER RICAVARE ENERGIA DALLE ONDE DEL MARE."

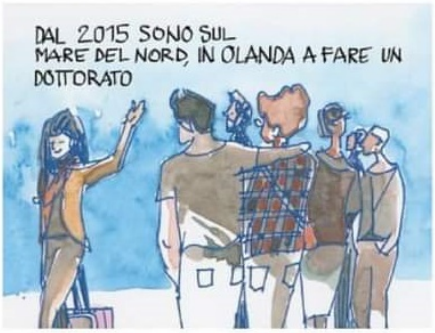
DAL 2015 SONO SUL MARE DEL NORD, IN OLANDA A FARE UN DOTTORATO


MARE DEL NORD
"STUDIO GLI ASPETTI ABIOTICI, IL TRASPORTO DEI SEDIMENTI. LA MIA COLLEGA MARIN STUDIA GLI ASPETTI BIOTICI, LO SVILUPPO DELLA VEGETAZIONE. INGEGNERI E BIOLOGI ECOLOGISTI SI INTEGRANO STRETTAMENTE PER VERIFICARE LE INTERAZIONI DELLA NATURA TRA TERRA E MARE."


"DOPO LA TRAGICA ALLUVIONE DEL 1953 UN SISTEMA IMPONENTE DI DIGHE HA PROTETTO LE COSTE, ADESSO NON SONO PIÙ SUFFICIENTI, ORMAI È TROPPO TARDI, NON TORNEREMO AL PIANETA...
...DI DIECI ANNI FA."
"L'OLANDA HA DECISO DI PREPARARSI IN ANTICIPO CON METODI RESILIENTI."


"BUILDING WITH NATURE"

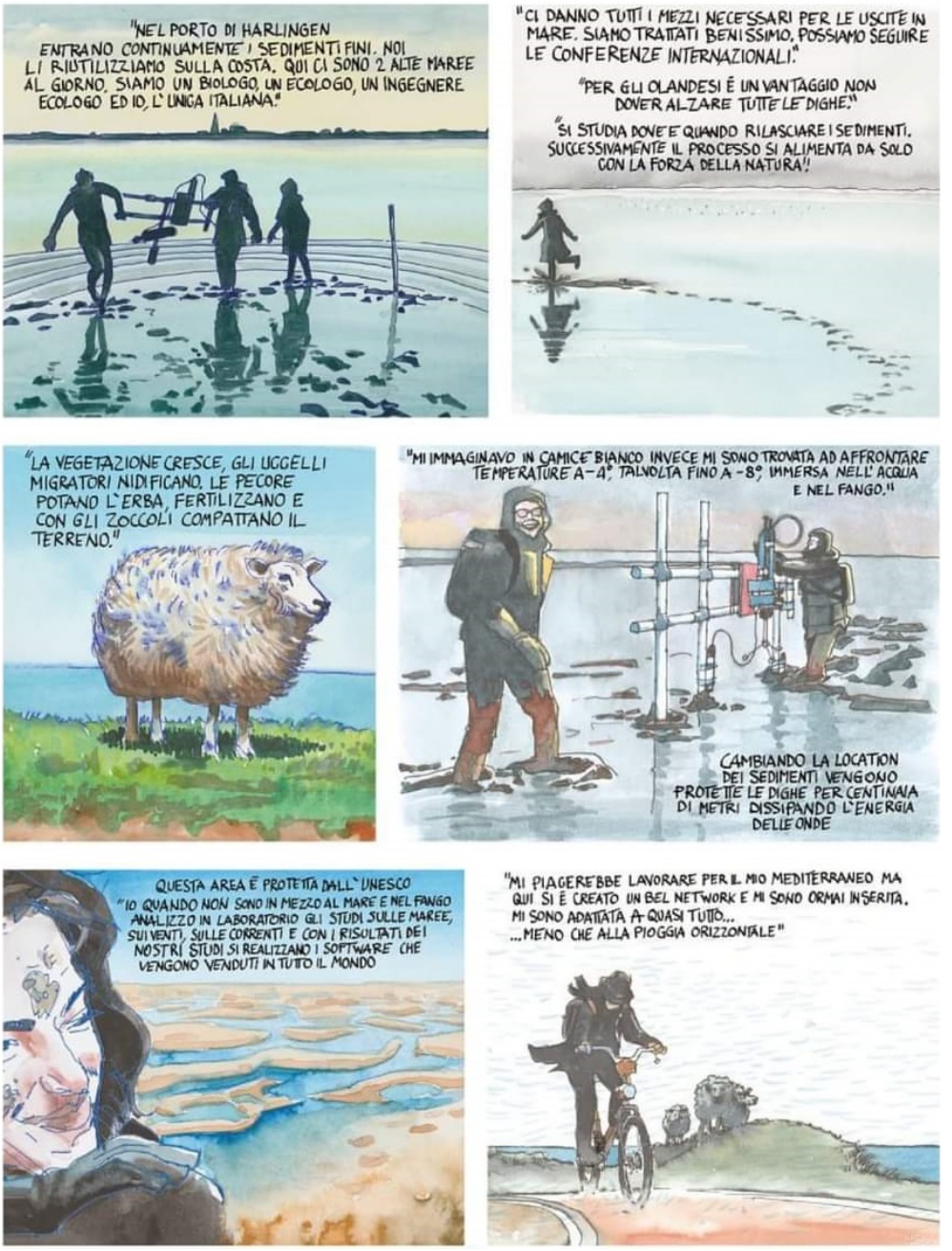

Credit to Giancarlo Caligaris, Corriere della Sera, 02.01.2020.